Fabrication and Characterization of Silicalite-1 Membranes for the Separation of the Greenhouse Gases

David Carter

Thesis submitted in partial fulfillment of the requirements for the Doctorate in Philosophy degree in Chemical Engineering

Department of Chemical and Biological Engineering
Faculty of Engineering
University of Ottawa

ABSTRACT

Membranes composed of zeolite crystals, in which gas molecules are transported by surface diffusion, are promising for gas separation applications. Since this mode of mass transfer mechanism is controlled by synergistic adsorption and diffusion phenomena, the separation of gas mixtures is not solely dependent on molecular size. However, undesirable defect pathways in zeolite membranes are often present due to factors such as incomplete crystal growth and/or thermal stresses during membrane synthesis and calcination. These pathways cause molecules to bypass the selective zeolite crystal layer and adversely affect membrane performance. Since the fabrication of defect-free zeolite membranes is very challenging, their widespread adoption for industrial processes has been impeded. Quantification of defects in zeolite membranes is therefore important to improve synthesis protocols of these membranes.

In this research, zeolite membranes composed of silicalite crystals have been fabricated using the pore plugging method, and their performance was evaluated by developing a method that can be used to describe the selective and non-selective channels that are present in any zeolite membrane. Unlike the other destructive and sophisticated methods, which already exist to discern this information, the proposed method requires only a limited number of in-situ permeation experiments to be conducted using He – a non-adsorbing gas, and N_2 – an adsorbing gas. With this method, the volume fraction, effective length, and size of the selective and non-selective channels of multiple membranes have been quantified, and these parameters were used to predict membrane performance at untested conditions, as well as with untested gases such as CH_4 and CO_2. In addition, by separating surface diffusion from the flow through the defects in gas separation tests with CO_2/N_2 mixture, the respective transport diffusivities and exchange diffusivity coefficients, which account for mass transfer in zeolite crystals were determined using the Maxwell-Stefan model. These determined exchange diffusivity coefficients are not equal to each other and challenge the Vignes correlation. In addition, transport diffusivities determined in mixed gas permeation experiments at University of Ottawa have then been validated by large single crystal transport diffusivities for mixed gases that were determined from

molecular uptake experiments conducted at University of Leipzig in Germany, using Infra-Red Micro-imaging.

RÉSUMÉ

Les membranes qui sont composées de cristaux de zéolithe, dans lesquels les molécules de gaz sont transportées par diffusion superficielle, sont prometteuses pour les applications impliquant la séparation des gaz. Puisque ce mécanisme de transfert de masse est contrôlé par des phénomènes synergiques d'adsorption et de diffusion, la séparation des mélanges gazeux ne dépend pas uniquement des dimensions moléculaires des gaz en question. Cependant, des voies défectueuses et indésirables à travers des membranes en zéolithe sont souvent présentes en raison de facteurs tels que la croissance incomplète des cristaux et les stress thermiques qui ont lieu au cours de la synthèse et calcination des membranes. Ces voies indésirables font en sorte que les molécules contournent la couche sélective de zéolithe et affecte la performance de la membrane de manière négative. Puisque la fabrication des membranes en zéolithe sans défaut est très difficile, l'application de ces membranes aux procédés industriel a jusqu'à date été très limitée. La quantification des défauts dans les membranes en zéolithe est alors importante afin d'améliorer les procédures de synthèse de ces membranes.

Dans cette recherche, des membranes en zéolithe composées de cristaux de silicalite ont été fabriquées par méthode de synthèse "bbcage des pore (pore plugging)", et leur performance a été évalué en développant une méthode qui permet la description des voies sélectives et non-sélectives dans n'importe quelle membrane en zéolithe. Contrairement aux autres méthodes destructives et sophistiquées déjà existantes, la méthode proposée nécessite seulement un nombre limité de tests de perméation in situ en utilisant un gaz non-adsorbant (He) et un gaz adsorbant (N_2). En appliquant cette méthode, la fraction volumique, la longueur effective et les autres dimensions des voies sélectives et non-sélectives de plusieurs membranes ont été quantifiées. Ces paramètres ont par la suite été utilisés afin de prédire la performance des membranes sous des conditions non testées, ainsi qu'avec des gaz non testés tel que le CH_4 et le CO_2. De plus, en séparant la diffusion superficielle et l'écoulement à travers des voies défectueuses lors de la séparation des mélanges CO_2/N_2, le modèle de Maxwell-Stefan a été utilisé afin de déterminer les diffusivités de transport et les coefficients de diffusivité d'échange pour les gaz purs. Ces paramètres représentent le transfert de masse qui a lieu dans les cristaux de zéolithe. Les

coefficients de diffusivité d'échange qui ont été déterminées contestent la corrélation de Vignes. Les diffusivités de transport qui ont été déterminés par les expériences de perméation utilisant des mélanges gazeux à l'Université d'Ottawa ont été validées par des diffusivités de transport dans des larges cristaux individuels. Ces valeurs ont été déterminées en effectuant des expériences d'absorption moléculaire avec des mélanges gazeux à l'Université de Leipzig en Allemagne, en utilisant la micro-imagerie à infra-rouge.

ACKNOWLEDGEMENTS

I would first like to thank Dr Handan Tezel and Dr Boguslaw Kruczek, for sharing their knowledge and passion for separating gas mixtures using zeolite membranes with me. I cannot thank you enough for your guidance, support, and encouragement, and it is because of you that I have learnt so much, and had such an incredible PhD experience.

I would also like to thank Dr Halil Kalipcilar at Middle East Technical University, as well as Dr Christian Chmelik, and Dr Jorg Karger at the University of Leipzig, for sharing their expertise with me, and hosting me at their institutions. I had many wonderful adventures in both Turkey, and Germany, and hope to visit again someday. I would also like to extend my thanks to Dr Douglas Ruthven for his correspondence, and contribution to the Infra-Red Microimaging manuscript.

I would also like to mention the technical staff in the Department of Chemical and Biological Engineering, Louis Tremblay, Franco Ziroldo, Gerard Nina, and James MacDermid. Thank you for your help in bringing my research to life.

Thank you also to my friends in the Department of Chemical and Biological Engineering. I am lucky to have such great friends, and every day has been better than the last thanks to your company and camaraderie. I would like to especially thank Dean Kennedy and Sean Wilson, who have been fellow students of Dr Tezel's, and accompanied me on my PhD journey since I started my research in 2013. And another special thank you to Charbel Atallah for translating my thesis abstract into French.

I would also like to thank my family in both New Zealand and Canada, who have supported me over the years, and instilled in me the belief that anything is possible.

Most of all, I would like to thank my wife Laura for her patience, her love, and her unwavering support. I am looking forward to many more adventures with you, and supporting you on your PhD journey in the future. My final thank you is for my daughter Aylith, who has waited until I finished writing my thesis to celebrate her birthday.

TABLE OF CONTENTS

LIST OF FIGURES

LIST OF TABLES

Chapter 1

Global Introduction

1.1.0 INTRODUCTION

As our global population increases, so too does our demand for energy. This energy is used for heating our homes, manufacturing the goods we use in our daily lives, and transporting the food we eat to the cities we live in. Most of this energy comes from the combustion of fossil fuels (coal, oil, and natural gas), which produces useable energy and a gas mixture called flue gas. Flue gas contains the greenhouse gas carbon dioxide (CO_2), and is typically released to our atmosphere. If this widespread practice of releasing flue gas to our atmosphere continues at the forecasted rates however, there will be catastrophic global warming and climate change in our lifetimes [1]. Also, since natural gas has a lower environmental impact in comparison to oil and coal, there is growing interest in utilizing natural gas for more processes. Natural gas is a mixture of components, and one of these is the greenhouse gas methane (CH_4). Many processes require a high purity of CH_4, and it is therefore necessary to upgrade natural gas by removing the undesirable components.

One of the ways to address these issues is to utilize membranes to divide gas mixtures into two separate product streams with different compositions. Membranes are able to do this by preferentially transporting one of the components in a gas mixture across a semi-permeable layer. For the gas mixture of flue gas fed to a membrane, one of the product streams therefore contains a greater proportion of CO_2 than the original gas mixture. In this situation, the CO_2 rich product stream can then be processed or sequestered more economically than the original gas mixture, and the other stream can be released to the atmosphere. The rate at which each gas is transported across the membrane is dependent on the partial pressures at either side of the membrane layer, as well as the properties of the membrane [2]. When this rate of molecular transport is normalized with respect to the partial pressure difference and membrane area, the resulting parameter is referred to as permeance P [$\mathrm{mol \cdot m^{-2} \cdot s^{-1} \cdot Pa^{-1}}$]. For gas mixtures, the ratio of permeances of two components is then referred to as the permselectivity α [-].

In comparison to other processes that can separate gas mixtures, such as cryogenic distillation, amine absorption and adsorption swing processes, membrane processes contain fewer moving parts, and respond to upstream process disturbances more quickly [3,4]. Because of these benefits, the operating costs of membrane processes can potentially be lower than cryogenic distillation, absorption and adsorption swing processes depending on the product recovery and purity requirements of the process [5]. A wide variety of polymeric, inorganic, and mixed matrix membranes (MMM) have therefore been developed to potentially realize these benefits for a range of different applications [6,7].

In polymeric membranes, which are composed of organic polymers, gases are transported by the solution-diffusion mechanism. More specifically, gas molecules first sorb into the membrane at the high pressure side, then diffuse towards the lower pressure side of the membrane, before finally desorbing at the low pressure side [2,8]. Polymeric membranes can be made into hollow fibres or flat sheets to meet the separation requirements of many chemical processes, however, the polymers used to make these membranes are susceptible to chemical attack under harsh conditions, and thermal degradation. Inorganic membranes by comparison are made up of porous inorganic materials such as zeolites, metal organic frameworks (MOFs), and activated carbons, which are generally able to withstand harsher conditions and higher temperatures than polymers [5]. Gas transport across them depends on the properties of the gas molecules, and the inorganic material's pores. Depending on the pore size, gas transport through these membranes proceeds by Knudsen or surface diffusion flow [2,9,10]. MMMs combine both organic and inorganic membrane attributes as they are composed of porous or nonporous inorganic particles dispersed in a polymeric phase. In doing so, a compromise between the typically observed high selectivity, and lesser permeance of polymeric membranes, with the lower selectivity but higher permeance of inorganic membranes can be realized [2,11,12]. The chemical and thermal stability of MMMs is however limited to that of the polymeric phase. In this research, zeolite type membranes have therefore been investigated due to their superior durability, as well as their high permeances, which are suitable for processing flue gas and natural gas mixtures.

Zeolite type membranes are predominantly fabricated by two methods. These are commonly referred to as the secondary growth method, and in-situ method, which is also known as the pore plugging method. In the secondary growth method, zeolite crystals are first grown in an autoclave, and are then dispersed onto a porous membrane support to become seed crystals. Next, the seeded membrane supports are immersed in zeolite pre-cursor solution, and the seeded support is subjected to a second crystal growth phase. In this method, a fairly thin and uniform layer of crystals is produced on top of the membrane support. In the pore plugging method, an unseeded membrane support is immersed in a zeolite precursor solution, and subjected to a crystal growth phase. In this method, numerous abutting zeolite crystals are synthesized inside the porous region of the membrane support [2,7]. For both fabrication methods, it is also necessary to remove the template molecules (which direct the growth of zeolite crystals), from the pores of the fabricated membranes through calcination. During this process, it is possible to form defects due to differences in the thermal coefficients of expansion between the membrane support and zeolite crystals [13,14]. Although the typically thinner nature of secondary growth membranes results in greater permeances of gases, any defects that are present in these membranes significantly affect membrane performance due to their 2 dimensional crystal arrangement. In pore plugged membranes however, defects may be limited to regions inside the membrane support which do not form a continuous pathway between the high and low pressure sides of the membrane. Consequently, the presence of a limited number of defects in pore plugged membranes may not significantly affect the integrity of the membrane layer. Given this relatively lesser sensitivity to defects, and its simpler fabrication procedure which is easier to control and reproduce, the pore plugging method has been used to fabricate the membranes used in this research.

The zeolite crystal type that was chosen to make membranes with in this research is silicalite-1, henceforth referred to as silicalite. This zeolite is composed of orthosilicate (SiO_4) tetrahedra, which form pentasil units composed of 8 x 5 member rings. These pentasil units then combine to create pentasil chains, and these chains create the 3 dimensional porous structure of silicalite. This porous structure is made up of straight and zig-zag channels which have the size of 5.5 Å, and are slightly larger than the greenhouse gases CO_2 and CH_4. Consequently, silicalite has a large internal surface area that is suitable for the adsorption of CO_2 and CH_4 gases, and has been studied and characterized for these purposes by others [15–18].

Despite these numerous advantages for inorganic membranes to be used for the separation of greenhouse gases from gas mixtures, they have not been adopted by industry for gas separation applications. Their implementation is principally impeded by the fact that it is very challenging to create zeolite membranes that do not contain defects, which compromise the performance of the membrane. Additionally, the process of characterizing newly fabricated membranes to evaluate their quality is also challenging. The two most common methods of characterizing membranes are permporometry analysis, and ideal selectivity measurements using a small molecule type gas (e.g. He, H_2), and a large molecule, which is excluded from or blocks the zeolite pores (e.g. SF_6). Unfortunately these methods can damage the membrane, or irreversibly reduce its performance [13,19]. These two challenges are also linked, as without accurate knowledge of the structure of newly fabricated membranes, changes that have been observed in membrane performance cannot be attributed to changes in the synthesis conditions.

The first objective of this thesis is therefore to fabricate silicalite membranes that are defect free. In this work, defects are defined as pathways through the active layer of the membrane , which bypass the zeolitic pores of the synthesized silicalite crystals. These defect pathways are non-uniform in size, and gas transport through them proceeds by regimes other than by surface diffusion. A summary of the different experimental conditions that were investigated in pursuit of this objective are summarized in Table 7.1 (Chapter 7). Although a procedure to consistently produce membranes of good quality was developed, the objective to fabricate defect free membranes is still in progress. Given these findings, the second objective of this thesis has arisen, to characterize zeolite membranes containing defects and quantitatively describe their structure based on a limited number of in situ pure gas permeation tests. This objective was achieved, and the characterization method, which was developed, is presented in Chapter 5. Although others have developed their own methods to similarly characterize zeolite membranes [20–22], the method in this thesis quantifies the characteristics of both the defect and zeolite pores in a non-destructive way for the first time. Since the characterization method in Chapter 5 was not developed when the manuscripts based on of Chapters 2 and 3 were published, an alternative definition for defects was used. Although contrary to the definition for defects stated for objective 1, pathways through the active layer of the membrane support were not considered to be defects if He was transported through them according to the regime of Knudsen flow. This definition is acknowledged incorrect, but was used as Knudsen flow of He through the pores of silicalite crystals could not at the time be distinguished from Knudsen flow of He through defects. In addition to the second objective, a sub objective of this thesis is to determine the diffusivity and amount of adsorbed CO_2 in the presence of N_2 inside a single crystal of silicalite using Infra-Red Microimaging (IRM). This objective has been achieved for CO_2 at different temperatures, mixture compositions, and pressures with IRM for the first time, and is presented in Chapter 4. These single crystal characteristics have then been compared for validation purposes to the characteristics found using the method proposed in Chapter 5 for membranes. The final objective of this thesis is to use the characterization method from Chapter 5 with the well-established Maxwell-Stefan (MS) model to determine characteristic MS diffusivities and MS exchange diffusivities of defect containing membranes [23–25]. This objective was also achieved, and is presented in Chapter 6. Typically, the MS model is used to characterize newly fabricated membranes by assuming that all molecular transport across a novel membrane occurs through the pores of the zeolite crystals, which is only reasonable for defect free membranes. The research conducted in this thesis continues and builds upon the work of Muhammad Tawalbeh [26]. In Dr. Tawalbeh's thesis, silicalite membranes were also fabricated by the pore plugging method, and characterized using the MS model using binary gas mixtures containing CO_2 and N_2. From the results obtained by Dr. Tawalbeh, it was reasonably assumed that defects were not present, or did not contribute significantly to the performance of the silicalite membranes used in his work. An important distinction between the previous work, and the work in this thesis, is therefore the consideration of defects in the characterization methods used in this thesis. The development of the characterization method in Chapter 5, as well as the application of the MS model in Chapter 6 based on the characteristic parameters determined using the method in Chapter 5 are thus distinguishable contributions to original knowledge.

The research conducted in this thesis has therefore advanced our understanding of zeolite membrane fabrication, characterization, and membrane process design. Although defect free membranes have not been fabricated, several important experimental parameters have been identified, which may help researchers achieve this objective in the future. The characterization method developed in this study can be used to evaluate membrane quality, and complement existing models to fabricate better membranes. Finally, the scope of this thesis, which includes single zeolite crystals, zeolite membranes, and characterization method development, lays the foundation to unify intrinsic zeolite characteristics with membrane performance data. From this foundation, future researchers will be able to characterize single crystals of a zeolite or MOF, and design entire membrane processes based on the approach developed in this work.

1.2.0 THESIS STRUCTURE

This thesis is composed of 8 chapters and 5 appendices. This current chapter is the first chapter, and it covers the context for this research.

In Chapter 2, the permeances and effective diffusivities of He, N_2, CO_2, and CH_4 through a silicalite membrane containing no viscous flow sized defects are presented. This chapter demonstrates the expected behavior of silicalite membranes, which contain few defects. This chapter has been published as a manuscript in the Journal of Fluid Flow Heat and Mass Transfer [27]. It was also presented as an oral presentation at the First International Conference on Fluid Flow Heat and Mas Transfer (Ottawa, ON, 2014).

In Chapter 3, the influence of support pore size on silicalite membrane performance for pure and binary gas mixtures has been investigated, and is presented. For membranes fabricated by the pore plugging method, membrane support pore size plays an important role since crystal growth can be limited by both crystal growth rates, and precursor solution diffusion rates to replenish consumed molecules. From the results of this investigation, membrane support pore sizes of 0.45 µm and 0.8 µm were found to most consistently produce the best membranes, and were used to fabricate subsequent membranes. This chapter has been published as a manuscript in the Canadian Journal of Chemical

Engineering [28]. It was also presented as an oral presentation at the 63rd and 64th Canadian Chemical Engineering Conferences (Fredericton, NB, 2013 and Niagara Falls, ON, 2014).

In Chapter 4, the diffusivities and amounts of adsorbed CO_2 when present as a pure gas and in a binary mixture with N_2 inside a single crystal of silicalite have been measured using Infra-Red Microimaging (IRM), and are presented. This study has been conducted to correlate the observed adsorption and diffusion behavior of CO_2 inside membranes with its single crystal behavior, and was done at the University of Leipzig in Germany. This chapter was submitted as a manuscript to the Journal of Microporous and Mesoporous Materials.

In Chapter 5, the development and demonstration of a novel method to describe the structure of viscous and or Knudsen sized defect containing zeolite membranes are presented. This method utilizes permeances determined using pure He and N_2 gases before and after membrane calcination, which can be determined using the graphite sealed module that is described in Chapter 7, but not the epoxy sealed type module. With this method, the size, volume fraction, and path length of the defect and zeolite channels can be determined. Additionally, the proposed method has been evaluated by comparing predictions of untested gas permeance at different operating pressures with the results of experimental data. This chapter will be submitted as a manuscript to the Journal of Membrane Science. It was also presented in different forms as the model was developed as an oral presentation at the 65th Canadian Chemical Engineering conference (Calgary, AB, 2015), and the 2017 American Institute of Chemical Engineers Annual Meeting (Minneapolis, MN, USA, 2017). It was also presented as a poster at the 2017 International Congress on Membranes and Membrane Technology (San Francisco, CA, USA, 2017), and the 2018 Euro-membrane Conference (Valencia, Spain, 2018).

In Chapter 6, the MS model has been used to characterize CO_2 and N_2 transport through the defect containing silicalite membranes presented in Chapter 5. In doing so, the MS diffusivities for pure CO_2 and N_2, and MS exchange diffusivities for their binary system have been calculated. Unlike most studies, which use the MS model to characterize newly fabricated membranes, the contributions of defects to total membrane permeance have been quantified, and excluded from analysis using the MS model in this study. The results from this research are therefore suitable for comparison with zeolite crystal data from uptake experiments. This chapter will be submitted as a manuscript to the Journal of Membrane Science. It was also presented in different forms as the method was developed as a keynote oral presentation at the 64th Canadian Chemical Engineering Conferences (Niagara Falls, ON, 2014), as a poster at the 6th Diffusion Fundamentals conference (Dresden, Germany, 2015), and the 12th Fundamentals of Adsorption conference (Friedrichshafen, Germany, 2016).

In Chapter 7, the various challenges that were faced while preparing membranes and evaluating their performance are presented. There are two main sections in this chapter. In the first section, the various investigations that were conducted to optimize membrane fabrication, including those that were unsuccessful, are presented. The second section deals with the process of designing a module, and integrating an inorganic membrane into this module with hermetic seals to separate the high and low pressure sides of the membrane. This chapter is intended to be a guide for people who are interested in conducting research in preparing inorganic membranes.

In Chapter 8, conclusions given the results found in the preceding chapters are presented, as well as recommendations, and the contributions of original work.

In Appendix 1, the error analysis for the determination of permeances, as well as the characteristic parameters from Chapter 5 are presented.

In Appendix 2, the Maxwell Stefan equations for a binary gas mixture through a zeolite membrane have been derived and are presented. These equations were derived by Muhammad Tawalbeh [26], and these same equations have been re-derived and used in this work. These equations are featured in this appendix for the convenience of the reader.

In Appendix 3, the experimental method that was used to determine the diffusivities and amounts of CO_2 adsorbed in silicalite using IRM are presented. This chapter was submitted as a manuscript to the MethodsX journal.

In Appendix 4, the abstract for a screening study to evaluate the permeance of silicalite, SAPO-34, and ZIF-8 fillers in Matrimid MMM is presented. This study has been published as a manuscript in the Journal of Membrane Science [29], and does not achieve any of the objectives of this thesis.

In Appendix 5, the abstract for a study to investigate the performance of three different commercially available polymeric membrane films, and their suitability for being used to separate and concentrate ammonia (NH_3) as ammonium sulfate (NH_4SO_4) from anaerobic digester digestate is presented. This study has been published as a manuscript in the journal Desalination [30], and does not achieve any of the objectives of this thesis.

1.3.0 STATEMENT OF CONTRIBUTIONS OF COLLABORATORS AND/OR CO-AUTHORS

I hereby declare that the work presented here is my own effort, and I am the sole author of this thesis. I am the one who performed all the experiments and the analyses unless stated otherwise under the scientific supervision of Dr. F. Handan Tezel, and Dr. Boguslaw Kruczek. I have acknowledged other sources of information and assistance in analyses where applicable. My research project supervisors Dr. F. Handan Tezel, and Dr. Boguslaw Kruczek provided the editorial and scientific reviews of this research.

In Chapters 2, 3, 5, 6, and 7, Dean Kennedy, Tolu Awobusuyi, Cynthia Veitch, Dana Li, Wanqi Jin, Anwuli (Rosemary) Omenogor, and Shaaima Al-Akwaa assisted in fabricating membranes and conducting gas separation experiments. Dean Kennedy assisted for 2 semesters, and all other students assisted for 1 semester each.

In Chapter 3, membrane fabrication and gas separation experiments were conducted by Dean Kennedy and I, with Dean Kennedy as the first author. Sean Wilson conducted and analyzed the gravimetric adsorption experiments.

Chapters 4 and A3 have Dr. Christian Chmelik, Dr. Jörg Kärger, Dr. Douglas Ruthven, and Dr. Reddy Marthala as co-authors. Dr. Reddy Marthala fabricated one of the crystals that I analyzed using IRM, and I synthesized the other. I conducted all of the experiments, and generated the model predictions. These experiments were conducted at Leipzig University (Leipzig, Germany) using their equipment and resources. Dr. Christian Chmelik, Dr. Jörg Kärger, and Dr. Douglas Ruthven helped with the interpretation and understanding of results. Dr Douglas Ruthven re-wrote the original manuscript for this research to be the more concise final version shown in Chapter 4.

Chapter A4 has Dr. Halil Kalipcilar as a co-author, who helped with the interpretation and understanding of the membrane fabrication and gas permeation analysis results. These experiments were conducted at Middle East Technical University (Ankara, Turkey) using their equipment and resources.

In Chapter A5, Lauren Rose, Tolu Awobusuyi, and Matthew Gauthier assisted in conducting liquid permeation experiments.

1.4.0 NOMENCLATURE

α	[-]	Permselectivity
P	$[mol \cdot m^{-2} \cdot s^{-1} \cdot Pa^{-1}]$	Permeance

Abbreviations

CH_4	Methane
CO_2	Carbon dioxide
H_2	Hydrogen
He	Helium
IPCC	International Panel on Climate Change
IRM	Infra-Red Microimaging
N_2	Nitrogen
NH_3	Ammonia
NH_4SO_4	Ammonium Sulfate
MS	Maxwell-Stefan
MOF	Metallic Organic Frameworks
MMM	Mixed Matrix Membrane
SF_6	Sulfur Hexafluoride

SiO_4	Ortho-silicate

1.5.0 REFERENCES

[1] IPCC, Summary for Policymakers, IPCC WGIII AR5. (2014) 1–33. doi:10.1017/CBO9781107415324.

[2] R.W. Baker, Membrane Technology and Applications, 3rd ed., Wiley, 2012.

[3] H. Yang, Z. Xu, M. Fan, R.B. Slimane, A.E. Bland, I. Wright, Progress in carbon dioxide seperation and capture: A review, 20 (2008) 14–27. doi:10.1016/S1001-0742(08)60002-9.

[4] D. Aaron, C. Tsouris, Separation of CO_2 from flue gas: a review, Sep. Sci. Technol. 40 (2005) 321–348. doi:10.1081/SS-200042244.

[5] P. Bernardo, E. Drioli, G. Golemme, Membrane gas separation: 1 review of state of the art, Ind. Eng. Chem. Res. 48 (2009) 4638–4663. doi:10.1021/ie8019032.

[6] L.M. Robeson, The upper bound revisited, 320 (2008) 390–400. doi:10.1016/j.memsci.2008.04.030.

[7] M. Pera-Titus, Porous inorganic membranes for CO_2 capture: Present and prospects, Chem. Rev. 114 (2014) 1413–1492. doi:10.1021/cr400237k.

[8] J.G. Wijmans, R.W. Baker, The solution-diffusion model : a review, 107 (1995) 1–21. doi:10.1016/0376-7388(95)00102-I.

[9] J. Kärger, D.M. Ruthven, D.N. Theodorou, Diffusion in Nanoporous Materials, John Wiley and Sons, 2012.

[10] D. Ruthven, Principles of adsorption and adsorption processes, John Wiley and Sons, 1984.

[11] M. Rezakazemi, A.E. Amooghinb, M.M. Montazer-Rahmati, A.F. Ismail, T. Matsuura, State-of-the-art membrane based CO_2 separation using mixed matrix membranes (MMMs): An overview on current status and future directions, Prog.

Polym. Sci. 39 (2014) 817–861. doi:10.1016/j.progpolymsci.2014.01.003.

[12] T.S. Chung, L.Y. Jiang, Y. Li, S. Kulprathipanja, Mixed matrix membranes (MMMs) comprising organic polymers with dispersed inorganic fillers for gas separation, Prog. Polym. Sci. 32 (2007) 483–507. doi:10.1016/j.progpolymsci.2007.01.008.

[13] H. Maghsoudi, Defects of Zeolite Membranes: Characterization, Modification and Post-treatment Techniques, Sep. Purif. Rev. 45 (2016) 169–192. doi:10.1080/15422119.2015.1103270.

[14] E. Mateo, A. Paniagua, C. Güell, J. Coronas, J. Santamaría, Study on template removal from silicalite-1 giant crystals, Mater. Res. Bull. 44 (2009) 1280–1287. doi:10.1016/j.materresbull.2009.01.003.

[15] L. Tosheva, B. Mihailova, V. Valtchev, J. Sterte, Silicalite-1 macrostructures - preparation and structural features, Microporous Mesoporous Mater. 39 (2000) 91–101. doi:10.1016/S1387-1811(00)00179-7.

[16] P. Li, F.H. Tezel, Pure and Binary Adsorption Equilibria of Methane and Carbon Dioxide on Silicalite, 1 (2007) 3131–3153. doi:10.1080/01496390701512034.

[17] G.K. Papadopoulos, H. Jobic, D.N. Theodorou, Transport diffusivity of N_2 and CO_2 in silicalite: Coherent quasielastic neutron scattering measurements and molecular dynamics simulations, J. Phys. Chem. B. 108 (2004) 12748–12756. doi:10.1021/jp049265g.

[18] J.N. Watson, L.E. Iton, R.I. Keir, J.C. Thomas, T.L. Dowling, J.W. White, TPA−Silicalite Crystallization from Homogeneous Solution: Kinetics and Mechanism of Nucleation and Growth, J. Phys. Chem. B. 101 (1997) 10094–10104. doi:10.1021/jp971531l.

[19] F. Jareman, C. Andersson, J. Hedlund, The influence of the calcination rate on silicalite-1 membranes, Microporous Mesoporous Mater. 79 (2005) 1–5. doi:10.1016/j.micromeso.2004.10.032.

[20] A. Caravella, P.F. Zito, A. Brunetti, E. Drioli, G. Barbieri, Microporous and

Mesoporous Materials A novel modelling approach to surface and Knudsen multicomponent diffusion through NaY zeolite membranes, Microporous Mesoporous Mater. 235 (2016) 87–99. doi:10.1016/j.micromeso.2016.07.049.

[21] P.F. Zito, A. Caravella, A. Brunetti, E. Drioli, G. Barbieri, Knudsen and surface diffusion competing for gas permeation inside silicalite membranes, J. Memb. Sci. 523 (2017) 456–469. doi:10.1016/j.memsci.2016.10.016.

[22] F. Jareman, J. Hedlund, D. Creaser, J. Sterte, Modelling of single gas permeation in real MFI membranes, J. Memb. Sci. 236 (2004) 81–89. doi:10.1016/j.memsci.2004.01.028.

[23] R. Krishna, J.M. Van Baten, M. Stefan, Unified Maxwell – Stefan description of binary mixture diffusion in micro - and meso -porous materials, Chem. Eng. Sci. 64 (2009) 3159–3178. doi:10.1016/j.ces.2009.03.047.

[24] J. Van Den Bergh, M. Mittelmeijer-hazeleger, F. Kapteijn, Modeling Permeation of CO_2/CH_4, N_2/CH_4, and CO_2/Air Mixtures across a DD3R Zeolite Membrane, J. Phys. Chem. 114 (2010) 9379–9389. doi:10.1021/jp101075h.

[25] P.F. Lito, A.S. Santiago, S.P. Cardoso, B.R. Figueiredo, C.M. Silva, New expressions for single and binary permeation through zeolite membranes for different isotherm models, J. Memb. Sci. 367 (2011) 21–32. doi:10.1016/j.memsci.2010.10.034.

[26] M. Tawalbeh, Silicalite-1 Membranes Synthesis, Characterization, CO2/N2 Separation and Modeling, 2013.

[27] D. Carter, D. Kennedy, F.H. Tezel, B. Kruczek, Characterization of Inorganic Silicalite - 1 Membrane to be used for the Separation of Greenhouse Gases, J. Fluid Flow Heat Mass Transf. 1 (2014) 43–47. doi:10.11159/jffhmt.2014.007.

[28] D. Kennedy, D. Carter, S. Wilson, B. Kruczek, F.H. Tezel, Pore plugging synthesis and characterization of silicalite-1 membranes using tubular TiO_2 supports: Effect of support pore size on membrane performance., Can. J. Chem. Eng. (2018). doi:0.1002/cjce.23095.

[29] D. Carter, F.H. Tezel, B. Kruczek, H. Kalipcilar, Investigation and comparison of mixed matrix membranes composed of polyimide matrimid with ZIF – 8, silicalite, and SAPO – 34, J. Memb. Sci. 544 (2017) 35–46. doi:10.1016/j.memsci.2017.08.068.

[30] D. Carter, L. Rose, T. Awobusuyi, M. Gauthier, F.H. Tezel, B. Kruczek, Characterization of commercial RO membranes for the concentration of ammonia converted to ammonium sulfate from anaerobic digesters, Desalination. 368 (2015) 127–134. doi:10.1016/j.desal.2015.03.040.

Chapter 2

This chapter is based on:

Characterization of Inorganic Silicalite-1 Membrane to be used for the Separation of Greenhouse Gases

David Carter[1], Dean Kennedy[1], F. Handan Tezel[1], Boguslaw Kruczek[1]

[1]University of Ottawa, Department of Chemical and Biological Engineering,
161 Louis Pasteur, Ottawa, Ontario, Canada K1N 6N5

In: ***Journal of Fluid Flow, Heat and Mass Transfer*** **(JFFHMT) 1 (2014): 43-47.**

The following chapter is based on the manuscript with the same title published in 2014, and has been modified in accordance with the definition for defects stated in Chapter 1. These changes are in response to the findings of the method in Chapter 5, which suggest that Knudsen sized defects may be present.

ABSTRACT

A Mordenite Framework Inverted (MFI) type silicalite-1 membrane, which does not contain a significant amount and/or number of defects, has been fabricated inside a tubular TiO_2 ceramic support to be used for the separation of greenhouse gases. In this work, single gas permeance experiments have been conducted. The results of which in conjunction with adsorption isotherms for each gas investigated have been used to calculate the effective diffusivities of N_2, CH_4, and CO_2. The permeances at 22 °C and 1 atm of pressure differential for He, N_2, CO_2 and CH_4, were found to be 4.38×10^{-7}, 7.71×10^{-7}, 1.35×10^{-6}, and 1.64×10^{-6} $mol \cdot m^{-2} \cdot s^{-1} \cdot Pa^{-1}$, respectively, giving permeance ratios for the separation of CH_4/N_2, CO_2/N_2, and CH_4/CO_2 equal to 2.13, 1.75, and 1.22, respectively. These permeance ratios are comparable to those found in other studies reported in the literature, whereas the permeances are typically 1 to 2 orders of magnitude greater than those found in the literature at similar conditions.

Chapter 2 – Characterization of Inorganic Silicalite-1 Membrane to be used for the Separation of Greenhouse Gases

Keywords: Inorganic membranes, Silicalite, characterization, Diffusivity, Surface diffusion, Adsorption, Carbon dioxide, Methane, Nitrogen.

2.1.0 INTRODUCTION

In order to mitigate the effects of global warming, a variety of carbon capture technologies are required which are economically favourable [1]. Inorganic membranes and MFI type silicalite-1 membranes in particular can tolerate extremely acidic conditions, and can withstand high pressures which make them suitable for the separation of CO_2 and CH_4 from gaseous process streams [2].

The inorganic membranes used in this study are fabricated by impregnating silicalite-1 crystals into the pores of TiO_2 membrane supports up to a depth of approximately 10 μm to create a thin selective layer. By minimizing the thickness of selective layer, a membrane is produced which has a high permeance, and is able to process large volumes. There exists a trade-off between permeance and permselectivity, the preferential interaction of one component with the membrane. The trade-off can be modelled and used to design membranes for specific processes by characterizing various inorganic membranes [3]. To this end, an understanding of the transport of gas molecules through MFI type silicalite-1 membranes is required, which is investigated in this study.

2.2.0 THEORY

The silicalite-1 crystals synthesized in this study have zeolite type structure. That is, they contain a uniformly distributed network of pores that in this case have a single pore size with no pore size distribution. This 3D lattice structure results in a large internal surface area, with an internal pore size of 5.5 Å. This pore size is less than twice the kinetic diameter of the gases investigated in this study: 3.3 Å, 3.6 Å, and 3.8 Å for CO_2, N_2, and CH_4, respectively, and so it is assumed in this study that monolayer, and not multilayer adsorption is occurring, and that the main mechanism of gas transport at room temperature is surface diffusion. By this mechanism, gas molecules are adsorbed inside the pores of the silicalite-1 crystals, and move in the direction of decreasing surface occupancy.

For monolayer adsorption of N_2, CH_4, and CO_2 into active sites inside a single pore of silicalite-1, a randomly oriented monolayer, similar to a single file system is generated, and in this case, diffusion can be described by Fick's laws [4]. A version of Fick's law has therefore been used to calculate the effective diffusivity using the following equation, and is reasonable for defect free membranes.

$$J = D_e\left(q_f - q_p\right)A \tag{1}$$

In this equation, J represents the membrane flux [mol·m^{-2}·s^{-1}], D_e is the effective diffusivity [m^{2}·s^{-1}], and A is the constant parameter for a single membrane which takes into account the physical characteristics of the membrane including membrane thickness and tortuosity. $q_f - q_p$ represents the driving force, which has been calculated as the gradient of surface occupancy, or working capacity of silicalite-1 from the feed side membrane pressure to the permeate side membrane pressure. Given the dependence of q_f and q_p on temperature, volumetrically determined adsorption capacities found by Li & Tezel [5,6] were modified using the Temperature Dependant Sips model as described by Ahmadpour et al. [7] for the estimation of the adsorption capacities at room temperature. The equations for the Temperature Dependent Sips model are as follows:

$$q = q_s \frac{(bp)^{\frac{1}{n}}}{1 + (bp)^{\frac{1}{n}}} \tag{2}$$

$$b = b_0 \exp\left[\frac{Q}{RT_0}\left(\frac{T_0}{T} - 1\right)\right] \tag{3}$$

$$\frac{1}{n} = \frac{1}{n_0} + \alpha\left(1 - \frac{T_0}{T}\right) \tag{4}$$

$$q_s = q_{s0} \exp\left[\chi\left(1 - \frac{T}{T_0}\right)\right] \tag{5}$$

Where p represents pressure [atm], q_s is the adsorption capacity at saturation [mmol·g^{-1} of adsorbent], and q is the adsorption capacity at a pressure p [mmol·g^{-1} of adsorbent]. b and n are constants which have units of [atm^{-1}] and [dimensionless], respectively. T [K] is temperature, and T_0 [K] is the reference temperature at which parameters q_{s0} [mmol·g^{-1} of adsorbent], b_0 [atm^{-1}], and n_0 [dimensionless] apply. Q [kJ·mol^{-1}] is the isoteric heat of adsorption, and α [dimensionless] and χ [dimensionless] are constants.

The pressure gradient normalized flux is referred to as permeance, and has the units of [mol·m^{-2}·s^{-1}·Pa^{-1}].

2.3.0 EXPERIMENTAL

2.3.1 Membrane Fabrication

The interrupted pore plugging method was used to synthesise MFI type silicalite-1 membranes on TiO_2 ceramic membrane supports as reported by Miachon et al. [8]. Some modifications to the reported procedure were made, and are as follows:

- Following centrifugation of the precursor solution, supernatant liquid is added to the Teflon beaker, and topped up after a period of 3 hours instead of 10 minutes in order to ensure that the membranes' supports have absorbed as much precursor solution as possible at room temperature and pressure.
- For hydrothermal synthesis, the oven was not preheated, and was instead heated up to 170 °C at a rate of 1 °C·min^{-1} with the autoclave module inside the oven from the start.
- The reported standard calcination procedure was used with a heating up rate of 1 °C·min^{-1} instead of 1.7 °C·min^{-1}.

2.3.2 Single Gas Permeation Experiments

Before commencing each single gas permeation experiment, the membrane was purged with He at a flow rate of 100 cc(STP)·min^{-1} and a feed side pressure of 2 atm for 16 hours. Each gas was then investigated in turn for successively greater feed pressures between 1 atm and 5 atm. The gases of interest were tested in order of increasing adsorption capacity on silicalite-1 as found by Li & Tezel [5,6], which is N_2, CH_4, and CO_2.

2.4.0 RESULTS AND DISCUSSION

2.4.1 Adsorption Isotherms for N_2, CH_4, and CO_2

As described in the previous section, adsorption isotherms were generated using the Temperature Dependent Sips model for N_2, CH_4, and CO_2 on silicalite-1 at a temperature of T = 22 °C.

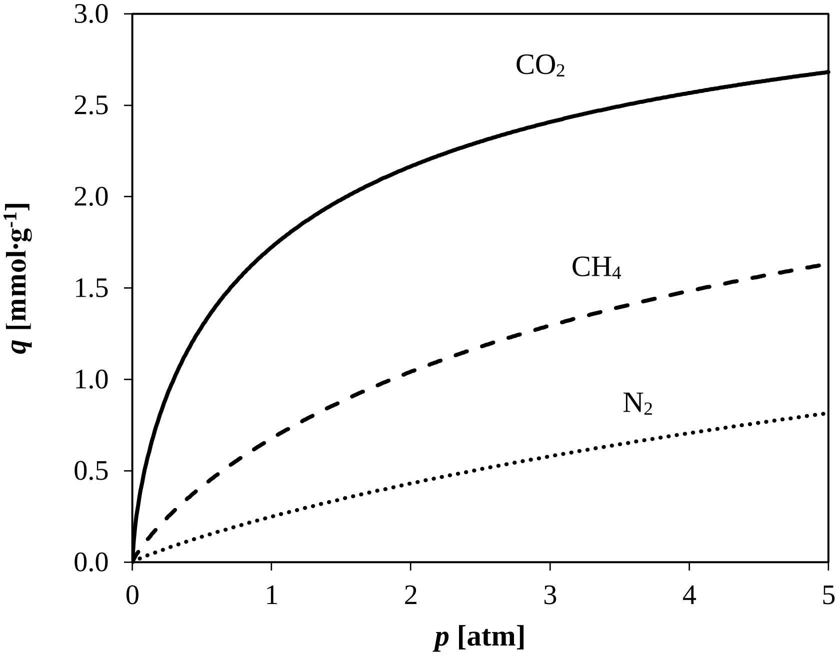

Figure 2.1. Adsorption isotherms for gases on silicalite-1 at T = 22 °C generated using the Temperature Dependent Sips model and the data from Li & Tezel [5,6] as described by Ahmadpour et al. [7].

Figure 2.1 shows the expected order of increasing adsorption capacity *q* for the gases studied in this paper. He gas is assumed to be not adsorbed in silicalite-1. The reported isotherms from which these isotherm curves were generated are for particles and not membranes, however, the constant *A* in Equation 2 is assumed to account for this variation.

2.4.2 Single Gas Permeances for He, N_2, CH_4, and CO_2

The single gas permeances for He, N_2, CH_4, and CO_2 were found for a silicalite-1 membrane on a 0.8 μm TiO_2 support and are shown in Figure 2.2.

The presence of defect pathways through the membrane active layer, and their influence on the performance of the membrane has been considered by analysing the permeance of He and N_2 as a function of pressure differential, which is shown in Figure 2.2. For gas transport at room temperature through silicalite membranes containing no defect pathways, He is transported by Knudsen diffusion through the pores of silicalite, whereas N_2 adsorbs inside silicalite's pores, and is transported by surface diffusion. In the presence of numerous and/ or large defects, the contribution of surface diffusion to N_2 permeance becomes less significant, and either viscous flow or Knudsen diffusion through defects dominates. It should be noted that the experimental procedure used in this study does not allow for the distinction between transport of He by Knudsen diffusion through defects and the pores of silicalite. The presence of Knudsen sized defect pathways therefore cannot be ruled out. In the case of gas transport due to viscous flow, permeance is directly proportional to the average pore pressure, which is not the case as we see that permeance of He and N_2 is independent of pressure. Knudsen diffusion however is independent of pressure, and could be considered present if only He or N_2 permeance is given. It is for this reason that the permeance of both He and N_2 have been measured. In the case where Knudsen diffusion through defects dominates, the contribution of surface diffusion of N_2 through silicalite's pores is reduced, and we would expect to see the He permeance to be greater than that of N_2. This is not the case, which shows that the membrane contains few defects, and Knudsen diffusion through the defects that are present do not significantly contribute to the pure He or N_2 permeances of the membrane. The He and N_2 permeance has been measured at 3 pressure differentials including the extreme pressures of interest as this number of points is sufficient to prove that there is no viscous flow through any defects that are present, and verify the trend in permeance for both He and N_2. In the case of CH_4

and CO_2, more points are needed to verify the trend in permeance, and so more intermediate pressure differentials were investigated.

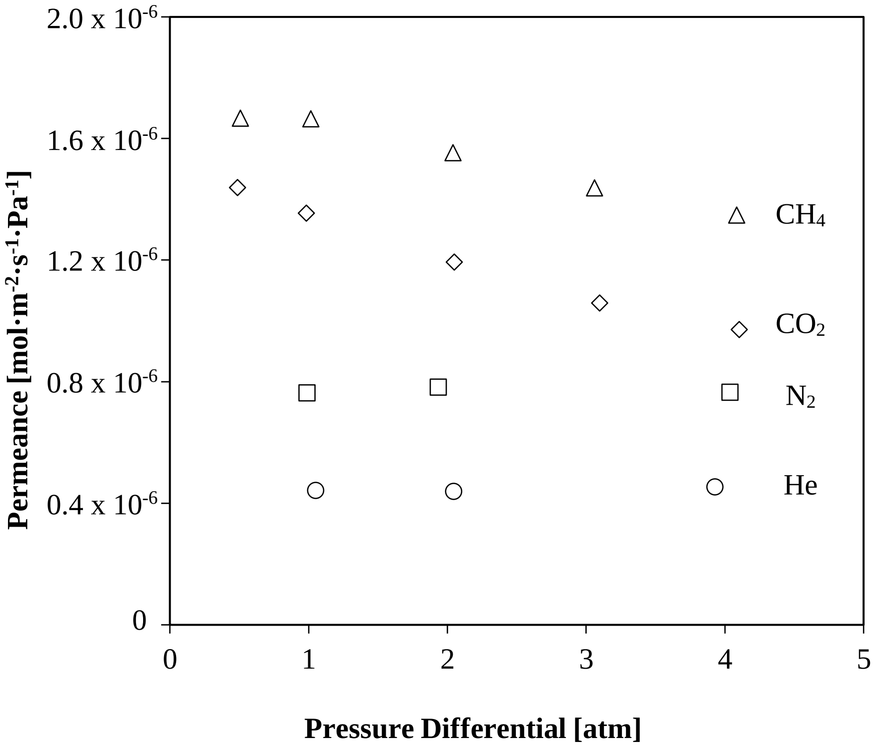

Figure 2.2. Single gas permeances of He, N_2, CO_2, and CH_4 as a function of pressure differential following exposure to each gas in turn followed by a regeneration period of 16 hours during which time the membrane is purged with He at room temperature and a pressure of 2 atm.

The decreasing permeance trends shown by CO_2 and CH_4 in Figure 2.2 can be explained in terms of the shape of their respective isotherms shown in Figure 2.1. More specifically, in the range of the experimental feed and permeate pressures, the CO_2 and CH_4 isotherms are convex (in contrast to the N_2 isotherm which is approximately linear). Thus, the adsorption capacity gradient, which represents the driving force for surface diffusion, is not directly proportional to the pressure gradient. In turn, since the permeance is the pressure gradient normalized flux, in the absence of defects in the membrane structure, permeances of CO_2 and CH_4 are expected to decrease with increasing feed pressure. In other words, the fact that experimentally observed permeances of CO_2 and CH_4 decrease with feed pressure provides additional confirmation that if any defects are present, they do not significantly contribute to the permeance of gases through the membrane. Using the same argument, since the N_2 isotherm is approximately linear in the range of the feed and permeate pressures, its permeance was expected to be independent of the feed pressure.

The permeances shown in Figure 2.2 at a pressure differential of 1 atm for He, N_2, CO_2, and CH_4 are $4.38 \times 10^{-7} \pm 1.0 \times 10^{-9}$, $7.71 \times 10^{-7} \pm 2.8 \times 10^{-9}$, $1.35 \times 10^{-6} \pm 5.5 \times 10^{-9}$, and $1.64 \times 10^{-6} \pm 5.1 \times 10^{-9}$ $mol \cdot m^{-2} \cdot s^{-1} \cdot Pa^{-1}$ respectively. These values are greater than the single gas permeances reported in other studies for silicalite-1 membranes at 25°C. For He, N_2, CO_2, and CH_4, at 25 °C, pressure unspecified, Soydaz et al. [9] found values of 0.75×10^{-7}, 2.1 x 10-7, 3.5×10^{-7}, and 4.8×10^{-7} $mol \cdot m^{-2} \cdot s^{-1} \cdot Pa^{-1}$ respectively. For N_2 and CH_4, Lovallo et al. [10] found values of 5.0×10^{-8} and 7.0×10^{-8} $mol \cdot m^{-2} \cdot s^{-1} \cdot Pa^{-1}$ respectively. For N_2, Miachon et al. [8] found a value of 2×10^{-8} $mol \cdot m^{-2} \cdot s^{-1} \cdot Pa^{-1}$. Higher single gas permeances for N_2, CO_2, and CH_4 were found by Algieri et al. [11], at a pressure differential of 40 kPa, and are 4.6×10^{-6}, 4.3×10^{-6}, and 6.4×10^{-6} $mol \cdot m^{-2} \cdot s^{-1} \cdot Pa^{-1}$. Wirawan et al. [12] was also able to find a greater permeance, but only for CO_2 at a lower pressure differential. For He and CO_2 at a pressure differential of 80 kPa, values of 3.06×10^{-8}, and 1.25×10^{-5} $mol \cdot m^{-2} \cdot s^{-1} \cdot Pa^{-1}$ were found.

From the permeances shown in Figure 2.2, the permeance ratios for CH_4/N_2, CO_2/N_2, and CH_4/CO_2 at a pressure differential of 1 atm are 2.13, 1.75, and 1.22. These permeance ratios are within 50% of the permeance ratios found by the authors of the studies mentioned previously. The separation of CH_4 and N_2 is a particularly difficult separation that is relevant to a range of natural gas upgrading processes, and many research teams are investigating membranes to be used for this separation process [13,14]. The combination of this membrane's comparatively high permeance ratio, and high permeance are therefore indicative that this membrane should be further investigated for this purpose.

2.4.3 Effective Diffusivities for N_2, CH_4, and CO_2

The effective diffusivities have been calculated as a function of the membrane specific constants *A* using the trends found from the single gas permeances shown in Figure 2.2, and using Equation 1.

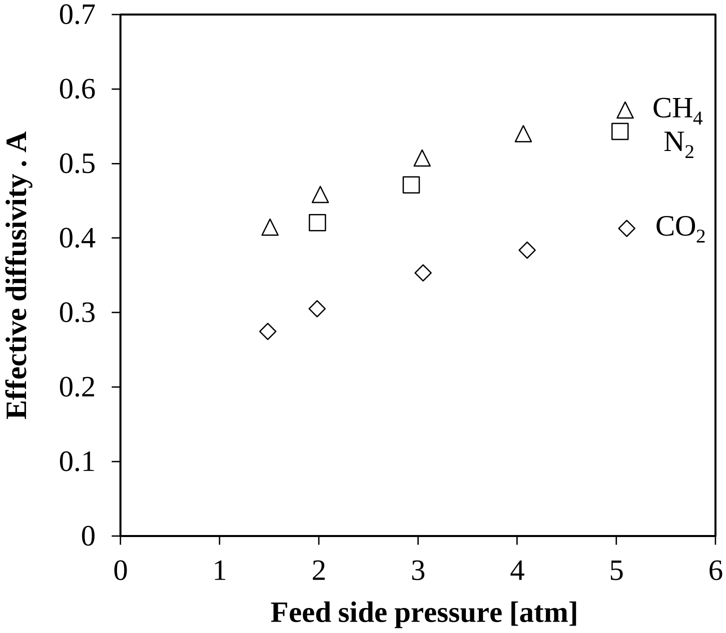

Figure 2.3. Effective diffusivity multiplied by constant A as a function of feed pressure for N_2, CO_2, and CH_4.

By using the adsorption capacities shown in Figure 2.1, Equation 1 was used to calculate the effective diffusivities of CO_2, N_2, and CH_4 as a function of the physical properties of the membrane, represented by *A*. The effective diffusivity ratios for the separation of CH_4/CO_2, N_2/CO_2 and CH_4/N_2 are calculated, and decrease from a feed side pressure of 1 atm to 5 atm as follows, 1.54 – 1.38 ± 0.007, 1.44 – 1.32 ± 0.007, and 1.08 – 1.05 ± 0.004 respectively. The shape of the effective diffusivity curves agree with Figure 2.1 in that as the pressure increases, surface occupancy increases, and so the number of interactions between adjacent molecules increases too. Due to the increased number of interactions, it follows that diffusivity would also increase as shown in Figure 2.3.

Interestingly, the order of increasing effective diffusivities, CO_2, N_2, and CH_4 is not the same as the order of increasing permeance which is N_2, CO_2, and CH_4. According to Equation 1, flux is directly proportional to both the effective diffusivity and the working capacity. In other words, the permeance does not solely depend on the effective diffusivity or the working capacity, but is a combination of both. It should be emphasized that unlike polymer membranes, single gas permeances of adsorbent membranes cannot be used to accurately predict the mixed gas permeation performance. With the limited number of adsorption sites, the molecules having a greater affinity towards the membrane may block access to the pores of those molecules having lower affinity towards the membrane. This blocking effect has been reported in the literature previously for binary mixtures involving CO_2 [15]. To this end, mixed gas permeation experiments will be conducted for membranes of the type used in this study, and their performance will be reported in the near future.

2.5.0 CONCLUSIONS

Single gas permeance experiments for He, N_2, CH_4, and CO_2 were carried out with a fabricated silicalite-1 membrane inside a tubular TiO_2 ceramic support. Their permeances were found to be 4.38×10^{-7}, 7.71×10^{-7}, 1.35×10^{-6}, and 1.64×10^{-6} $mol{\cdot}m^{-2}{\cdot}s^{-1}{\cdot}Pa^{-1}$, respectively at a pressure differential of 1 atm and a temperature of 22°C. Given the pore size of silicalite-1, the greater permeance of N_2 over He, and none of the permeances increasing as a function of pressure, surface diffusion is considered to be the dominant mechanism for gas transport through this silicalite-1 membrane. Although the presence of Knudsen sized defects cannot be ruled out based on these results, their contribution to the permeances of gases through the membrane is not significant. Effective diffusivities were also calculated for the membrane based on the adsorption capacity of each gas on silicalite-1, and the experimentally determined single gas permeances. For the separation of CH_4/N_2, CO_2/N_2, and CH_4/CO_2 the permeance ratios were found to be 2.13, 1.75, and 1.22 respectively. In order to better understand this behaviour and characterize membranes accordingly, future experiments will be conducted using binary gas mixtures.

2.6.0 ACKNOWLEDGEMENTS

The authors would like to acknowledge the financial support received from NSERC (Natural Sciences and Engineering Research Council) and NRCan (Natural Resources Canada).

2.7.0 REFERENCES

[1] J.T. Houghton, G.J. Jenkins, J.J. Ephraums, "Climate change: the IPCC scientific assessment," pp. 365, 1990.

[2] S.M. Auerbach, K.A. Carrado, P.K. Dutta, Handbook of zeolite science and technology, CRC, 2003.

[3] L.M. Robeson, "The upper bound revisited," Journal of Membrane Science, vol. 320, no. 1, pp. 390-400, 2008.

[4] P.H. Nelson, S.M. Auerbach, "Self-diffusion in single-file zeolite membranes is Fickian at long times," Journal of Chemical Physics, vol. 110, no. 18, pp. 9235-9243, 1999.

[5] P. Li, F.H. Tezel, "Pure and binary adsorption equilibria of methane and carbon dioxide on silicalite," Separation Science and Technology, vol. 42, no. 14, pp. 3131-3153, 2007.

[6] P. Li, F.H. Tezel, "Pure and binary adsorption equilibria of carbon dioxide and nitrogen on silicalite," Journal of Chemical & Engineering Data, vol. 53, no. 11, pp. 2479-2487, 2008.

[7] A. Ahmadpour, K. Wang, D.D. Do, "Comparison of models on the prediction of binary equilibrium data of activated carbons," AIChE Journal, vol. 44, no. 3, pp. 740-752, 1998.

[8] S. Miachon, E. Landrivon, M. Aouine, Y. Sun, I. Kumakiri, Y. Li, J. Dalmon, "Nanocomposite MFI-alumina membranes via pore-plugging synthesis preparation

and morphological characterisation," Journal of Membrane Science, vol. 281, no. 1-2, pp. 228-238, 2006.

[9] B. Soydaş, A. Çulfaz, H. Kalipçilar, "Characterization of zeolite membranes by gas permeation," Desalination, vol. 199, no. 1-3, pp. 371-372, 2006.

[10] M.C. Lovallo, A. Gouzinis, M. Tsapatsis, "Synthesis and characterization of oriented MFI membranes prepared by secondary growth," AIChE Journal, vol. 44, no. 8, pp. 1903-1913, 1998.

[11] C. Algieri, P. Bernardo, G. Golemme, G. Barbieri, E. Drioli, "Permeation properties of a thin silicalite-1 (MFI) membrane," Journal of Membrane Science, vol. 222, no. 1–2, 1 pp. 181-190, 2003.

[12] S.K. Wirawan, D. Creasera, J. Lindmark, J. Hedlund, I.M. Bendiyasa, W.B. Sediawan, "H_2/CO_2 permeation through a silicalite-1 composite membrane," Journal of Membrane Science, vol. 375, pp. 313–322, 2011.

[13] X. Ning, W.J. Koros, "Carbon molecular sieve membranes derived from Matrimid polyimide for nitrogen/methane separation," Carbon, vol. 66, pp. 511–522, 2014.

[14] J. Yang, J. Li, W. Wang, L. Li, J. Li, "Adsorption of CO_2, CH_4, and N_2 on 8-, 10-, and 12-Membered Ring Hydrophobic Microporous High-Silica Zeolites: DDR, Silicalite-1, and Beta," Industrial & Engineering Chemistry Research, vol. 52, pp. 17856−17864, 2013.

[15] L. Sandström, E. Sjöberg, J. Hedlund, Very high flux MFI membrane for CO_2 separation, Journal of Membrane Science, vol. 380, no. 1-2, pp. 232-240, 2011.

Chapter 3

This chapter is based on:

Pore Plugging Synthesis and Characterization of Silicalite-1 Membranes Using Tubular TiO_2 Supports:

Effect of Support Pore Size on Membrane Performance

Dean A. Kennedy[1], David Carter[1], Sean Wilson[1], Boguslaw Kruczek[1], F. Handan Tezel[1]

[1]Department of Chemical and Biological Engineering, University of Ottawa
161 Louis Pasteur, Ottawa, ON, K1N 6N5

In: *The Canadian Journal of Chemical Engineering* 96.7 (2018): 1597-1611.

The following chapter is based on the manuscript with the same title published in 2018, and has been modified in accordance with the definition for defects stated in Chapter 1. These changes are in response to the findings of the method in Chapter 5, which suggest that Knudsen and/or viscous flow sized defects may be present in the analyzed membranes.

ABSTRACT

In this study, we present a detailed synthesis procedure and characterization of porous inorganic silicalite-1 membranes. The membranes were synthesized in-situ using a pore plugging method with the inclusion of a 12 hour thermal break promoting secondary growth within the active layer pores of the tubular TiO_2 supports. The effect of the support pore size on membrane performance was examined with pore sizes ranging from 0.3 µm to 1.4 µm. Characterization using Scanning Electron Microscopy (SEM) and Energy Dispersive Spectroscopy (EDS) analysis confirm the penetration and formation of silicalite-1 crystals within porous supports up to a depth of 10 – 12 µm for all membranes. With the exception of the membranes synthesized on the support with 1.4 µm pore size, all membranes were more permeable to probe gas N_2 compared to He. The highest ideal N_2/He selectivity of 2.3 ± 0.5 was observed for the membranes synthesized on supports with 0.8 µm pore size. Single gas permeance for the membranes were high, ranging between 3.7×10^{-7} and 1.3×10^{-5} $mol \cdot m^{-2} \cdot s^{-1} \cdot Pa^{-1}$, and was independent of gas kinematic diameter with the order of permeation being $CH_4 > CO_2 > N_2 > He$. Binary equimolar CO_2/N_2 separation experiments show better membrane CO_2/N_2 permselectivity compared to the ideal selectivity calculated from the single gas experiments. Comparing the observed membrane gas diffusivity and the adsorbate gas uptake rate within the zeolite material alone shows that these favourable selective properties are the result of adsorption surface diffusion and that Knudsen diffusion is minimised.

Keywords: CO_2/N_2 separation, gas permeation, inorganic zeolite membranes, silicalite-1, porous membranes, effect of support pore size

3.1.0 INTRODUCTION

The development of separation processes using membrane technologies is promising due to the potential operational efficiency and predicted flexibility and ease of implementation into a broad array of systems and fields [1]. A current application that has seen great interest in recent years is post-combustion capture and separation of CO_2 from the industrial flue gases. In order to be viable, the addition of separation and sequestration technologies to fossil fuel based processes should not contribute to more than a 35% increase in generation costs [2]. Several different competing gas separation methodologies have been proposed for this application. The most notable of these include: adsorption based separations (temperature and pressure swing adsorption processes), chemical and physical absorption processes, and membrane based processes [1,3–7]. While monoethanolamine (MEA) absorption is the current accepted practice for CO_2 capture, this method is very energy intensive due to multiple process units required for solvent regeneration [8]. Additionally, the potential health and environmental impact of the release of fugitive MEA emissions into the atmosphere is also a major subject of concern for this application [9,10]. Among the competing alternative CO_2 capture methods, membrane based separation technologies are considered an attractive approach based upon the simple modular design and limited regeneration requirements [1,3].

Inorganic zeolite membranes have a high potential to be suitable for separation of gaseous process streams such as for post combustion CO_2 capture. These types of membranes can operate under a wide range of temperatures and pressures and have good solvent stability compared to polymeric membranes [11]. While recent progress with mixed matrix membranes to combine the advantages of polymer and inorganic membranes is promising, the fabrication of robust and defect free mixed matrix membranes is very difficult due to weak polymer – particle adhesion and potential particle agglomeration [12]. Zeolite membranes are generally characterized as a thin layer of crystalline silicates or aluminosilicates formed on the surface of a porous support. Membranes of this type are usually prepared via a seeded or secondary growth method. Different from the traditional seeded approach, zeolite membranes may also be synthesized within the pores of a support via an in situ pore plugging synthesis technique, resulting in a thin composite zeolite layer within the pores of the support [13–17].

The use of Mordenite Framework Inverted (MFI) type zeolites such as ZSM-5 and silicalite-1 have been of great interest due to a three dimensional lattice structure with an internal pore size of 5.1 Å to 5.6 Å (1Å = 0.1nm) [18,19]. The pentasil structure of silicalite-1 leads to a large internal microporous network with high surface area which is conducive to favourable adsorption capacity. The internal aperture of silicalite-1 is larger than the kinetic diameter of the studied gases: 2.6 Å, 3.3 Å, 3.6 Å, and 3.8 Å for He, CO_2, N_2, and CH_4 respectively [20]. Therefore, gas separations may be achieved by exploiting differences in the equilibrium adsorption potential of the adsorbate gases and their differences in the diffusivity within the zeolite pores [21]. These properties are influenced by the electrostatic dispersion within the pore network and energies of adsorption as governed by differences in the dipole moment, quadruple moment, and the molecular polarization energy of the different gases [22]. Adsorption potential for the studied adsorbate gases occurs in the following increasing order for silicalite-1: $He \ll N_2 < CH_4 < CO_2$. The maximum for CO_2 is attributed to high polarizability and a strong quadrupole interaction with the adsorption sites [23–26]. CH_4 has stronger polarizability compared to N_2 contributing to increased adsorption potential. Table 3.1 presents the different molecular properties of the studied adsorbate gases [27–29].

Table 3.1. Molecular properties of the studied adsorbate gases.

Gas	**Molecular Weight [g·mol^{-1}]**	**Kinetic Diamter [Å]**	**Polarizability [x10^{-25} cm^3]**	**Quadrupole moment [x 10^{40}cm^2]**
CO_2	44.01	3.3	29.1	-13.41
CH_4	16.04	3.8	25.9	0
N_2	28.01	3.6	17.4	-4.91
He	4.00	2.6	2.05	0

MFI type zeolite membranes have a larger uniform pore aperture which allows for comparatively greater flux compared to smaller pore sized zeolite membranes such as SAPO-34, DDR, and zeolite T [19]. The ability to achieve both a higher flux and a significant separation is an advantageous property of MFI type zeolite membranes, which make them desirable for investigations into bulk industrial separations that require high gas throughputs. Unlike other MFI type zeolites, such as ZSM-5, the silicalite-1 zeolite does not possess any alumina ions (Al^{3+}) imbedded in the lattice structure of the crystal. This means that silicalite-1 zeolites contain no counterbalancing cations and exhibit more hydrophobic properties compared to their equivalent ZSM-5 type zeolites [15]. Along with zeolite type, the separation performance of the zeolite membrane depends largely on the continuity and thickness of the active zeolite layer. Most of the reported zeolite membranes have been synthesized using alumina in the active layer of the supports, which could lead to the possible incorporation of Al^{3+} ions into the final structure of zeolite membrane. Therefore, the final product would not exhibit the properties of a true silicalite-1. Titanium oxides are more chemically stable than alumina and have been the focus of previous studies

[15,30]. However, little has been investigated regarding the effect of pure TiO_2 active layer pore size on silicalite-1 membrane performance.

The purpose of this study has been to determine the effect of support pore size on the development of high performing silicalite-1 membranes for gas separations. This was achieved by using a pore plugging synthesis method with a thermal break. Silicalite-1 crystals were synthesized within different tubular TiO_2 active layer supports forming thin composite structures. The effect of support pore size on the resultant membrane physical characteristics and gas permeation properties was examined. The physical properties of the membranes were analysed using SEM and EDS. Single gas permeation experiments were performed on all of the membranes using He and N_2 as probe gases to establish the contribution of non - zeolitic pores to gas transport. Single gas permeation behaviour of He, N_2, CO_2, and CH_4 gases was studied for the membrane with the best N_2/He ideal selectivity and the performance was compared to the literature for other silicalite membranes. This membrane was also tested with an equimolar binary CO_2 - N_2 gas mixture.

3.2.0 EXPERIMENTAL

3.2.1 Membrane Fabrication

A silicalite-1 membrane synthesis protocol using the pore plugging method with an 11 hour synthesis interruption was applied in this work [15–17,30,31]. The membranes were fabricated on commercially available ceramic porous tubes with an approximately 10 µm thick active layer containing only TiO_2 purchased from TAMI Industries (Nyons, France). The tubes were 6 cm in length with an outside diameter of 1 cm and thickness of 2 mm. The inside surface of the tube contained the TiO_2 active layer. A range of active layer pore sizes; 0.3 µm, 0.45 µm, 0.8 µm, and 1.4 µm, were investigated. A total of 9 membranes were synthesized in three different batches (batch A, B, and C, respectively) under similar experimental conditions to establish repeatability.

Precursor Solution Preparation

In a Teflon (polytetrafluoroethylene (PTFE)) lined beaker under magnetic stirrer, 9.61g of fumed silica (SiO_2) (Sigma-Aldrich, Oakville, ON, Canada), used as a silicone (Si) source, was dissolved in 72 mL of 1 M tetrapropylammonium hydroxide (TPAOH) solution (Sigma-Aldrich, Oakville, ON, Canada), and 8 mL of deionized water was added. The resultant solution consisted of 2.0 M SiO_2 and 0.90 M TPAOH giving an overall molar ratio of 1 SiO_2 : 0.45 TPAOH : 27.8 H_2O. The solution was left under magnetic stirring for 3 days at room temperature of 295K ± 1K in the Teflon beaker that was covered to prevent any evaporation of the solution. The solution was then centrifuged for 30 minutes at 4000 rpm to remove any undissolved particulates that may act as undesired seeds for zeolite crystallisation.

Hydrothermal Synthesis

The silicalite-1 nanocomposite membranes were prepared using an in situ hydrothermal synthesis pore plugging method and temperature controlled crystallization [16,17]. Hydrothermal synthesis was performed in a 125 ml Teflon beaker, inserted inside a Parr model 4748 stainless steel autoclave (Parr Instrument Co., Moline, IL, USA). A programmable Neytech Vulcan 3-550 furnace purchased from Cole-Parmer Canada (Montreal, QC, Canada) was used for this step. For each batch, 4 ceramic tubular supports were covered with a thin layer of Teflon tape on the external surface to prevent the formation of zeolite crystals on the outside surface. The ceramic supports were inserted into the beaker vertically and were held in place by a home-made cradle to hold them in a vertical position to prevent shifting during the synthesis process. The zeolite precursor solution was poured into the beaker containing the supports until the supports were completely immersed in the solution. The supports were submerged vertically in the solution for 6 hours before hydrothermal synthesis, ensuring sufficient penetration time of the solution into the pores of the support. The autoclave was closed, ensuring that there was less than 1 cm of free height between the solution and the lid of the autoclave.

A standardized temperature program was used during the hydrothermal synthesis procedure. The autoclave was inserted into the programmable oven and heated to 170 ºC at a rate of 1.0 °C·min^{-1} and remained at that temperature for 12 h. To promote secondary growth, a thermal break of 11 hours was used. This was achieved by cooling the mixture in the same oven with the door closed over a period of 8 hours, until the temperature of the mixture reached 50 °C. Following this step, the oven was opened fully until the mixture temperature reached 30 °C over a period of 3 hours. During the period of the thermal interruption, the cooler temperature gives the precursor solution an opportunity to diffuse within the porous network. Replenishing the available precursor solution within the pores promotes further MFI crystal growth and supports pore plugging [17].

Afterwards, the hydrothermal synthesis resumed with a heating rate of 1.0 °C·min^{-1} until the system reached 170 °C, then the temperature was held constant for an additional 72 h, except for batch C which was for 75 h. At the end of the hydrothermal synthesis step, the autoclave was cooled gradually to room temperature within the oven over a period of 12 h. The membranes were removed from the autoclave, rinsed and submerged in distilled water for 24 hours. The washed membranes were then dried at 100 °C for 24 h.

The remaining zeolite solution was collected from the beaker, was washed with distilled water, and was poured into an evaporating dish. The remaining H_2O and TPAOH was evaporated in air inside a fume hood, resulting in a powder.

Calcination

The dried membranes were then subjected to a calcination step performed at 500 °C for 4 h using a programmable oven (Vulcan 3-550) with a heating and cooling rate of 1.0 °C·min^{-1} [15,16,30]. The rate of temperature change should be minimized given the difference in the thermal expansion between the silicalite-1 and the support to prevent the formation of defects [32]. After the membranes were removed from the oven, they were placed in a desiccator until use. The collected zeolite powder was also calcined in the same fashion and kept for subsequent characterization. The properties of synthesized zeolite powder were considered to be same as that of the zeolite synthesized within the supports regardless of the pore size of the active layer.

3.2.2 Membrane and Material Characterization

Membrane Morphology and Particle Microstructure Experiments

A Micromeritrics ASAP-2010 volumetric adsorption analyzer (Micromeritics, Norcross, GA, USA) was used to analyse the zeolite powder in terms of the Brunauer-Emmet-Teller (BET) specific surface area and the Barrett-Joyner-Halenda BJH pore volume and pore size distribution using N$_2$ adsorption-desorption at 77K [33,34]. All samples were degassed under vacuum conditions and heated at 383 K prior to the analysis. The crystallinity of the synthesized silicalite-1 crystals was verified using powdered x-ray diffraction analysis (XRD). The powdered samples were examined at room temperature using a Rigaku Ultima IV powder diffractometer in Bregg-Brentano geometry, using Cu Kα radiation ($\lambda = 1.5418$ A). The 2θ range of 2° to 90° was covered with a 0.02° step width and 6 $°\cdot\text{min}^{-1}$ scan speed.

Scanning electron microscope (SEM) and Electron dispersive spectrometer (EDS) analyses were performed using a JEOL JSM-7500F Field Emission Scanning Microscope (JEOL, Tokyo, Japan) with a Tracor-Northen Series Z-II spectrometer (Zeiss, Oberkochem, Germany) installed. SEM and EDS analyses were used as compositional and morphological verification of the active layer cross section of the synthesized membranes. The synthesized tubular membranes were fractured, and small sections of the membrane cross section were mounted on a specimen holder prior to the analysis.

Single Gas Adsorption Uptake and Equilibria Experiments

Single gas adsorption isotherms and adsorption kinetic behaviour were determined for the synthesized powder using a microgravimetric analyser purchased from VTI Corp. (Hialeah, FL, USA) equipped with a high sensitivity Cahn microbalance with a weighing resolution of ± 1 µg. Single gas adsorption isotherms were conducted at a temperature of 295 K for CO$_2$, CH$_4$, and N$_2$ gases. All gases were purchased from Linde Canada Ltd. (Ottawa, ON, Canada) and were of 99.995, 99.99, and 99.999 % purity respectively. During the adsorption isotherm experiments, the temperature of the system was maintained using a programmable isothermal water bath. The analysed adsorbent sample weight ranged between 30 and 40 mg to minimize adsorption heat and kinetic mass transfer effects.

Samples were regenerated at 573 K under vacuum conditions at approximately 10^{-8} atm for about 1.5 hours. The equilibrium adsorption isotherms for each gas were evaluated at increasing pressures from 0 to 5 atm. For each isotherm point, equilibrium was determined when there was less than a 0.015% sample weight change over a 15 minute period. A buoyancy correction was performed using helium gas at similar pressures and temperatures as silicalite-1 has negligible adsorption capacity for helium.

To elucidate the effect of the intracrystalline diffusion on the rate of gas permeance across the silicalite-1 membrane, the single gas adsorption uptakes on the silicalite-1 powder were also measured. The transient kinetic behavior was analysed under isothermal conditions for constant pressure step changes: (0.5 to 1 atm, 1 to 2 atm, 2 to 4 atm, and 6 to 8 atm). For each gas, the adsorption uptake response curve to a pressure step change was determined as the fractional uptake at different times before adsorption equilibrium was achieved for the silicalite-1 powder.

Single Gas Permeation and Binary Gas Separation Experiments

Single gas permeation and binary gas separation experiments were used to characterize the membrane performance for a feed side pressure between 1.5 atm and 5 atm with the permeate side open to atmosphere at ambient temperature (295 K). For the single gas permeation experiments, the gases that were studied were He, N_2, CH_4, and CO_2. Pure gases He and N_2 were used as probe gases to examine the permeation properties of non-adsorbing small gas (He) and adsorbing larger gas (N_2) on the membrane performance. For the binary gas separation experiments, an equimolar mixture of CO_2 and N_2 gases was used as the feed. Prior to commencing each single gas and binary gas permeation experiment, the membranes were regenerated under helium purge at ambient temperatures (295 K) with a feed side pressure of 2 atm overnight. Single gas permeation experiments were performed in order of increasing gas affinity for the silicalite-1, which is He < N_2 < CH_4 < CO_2 [24–26].

The tubular membranes were attached to tubular stainless steel supports on both ends using epoxy resin. A quick setting epoxy was used initially to fix the tubular supports in place. After 1 hour the membrane was firmly bound to the tubular supports. With the membrane spinning, a second layer of epoxy was used to form an airtight joint between the membrane and the stainless steel support. The epoxy was left to set for a minimum of 2 hours. The spinning motion allowed the epoxy to thinly coat the membrane evenly, which produced smooth rounded joints. The membrane was installed within a custom made membrane module. The dead volume of the permeate side of the membrane module was approximated to be 200 cm^3. One of the main benefits of silicalite-1 membranes is the ability to achieve a high gas flux across the membrane, so that no sweeping gas was required for this setup. The experimental apparatus outlined in Figure 3.1 was used to carry out the single gas permeation and binary gas separation experiments.

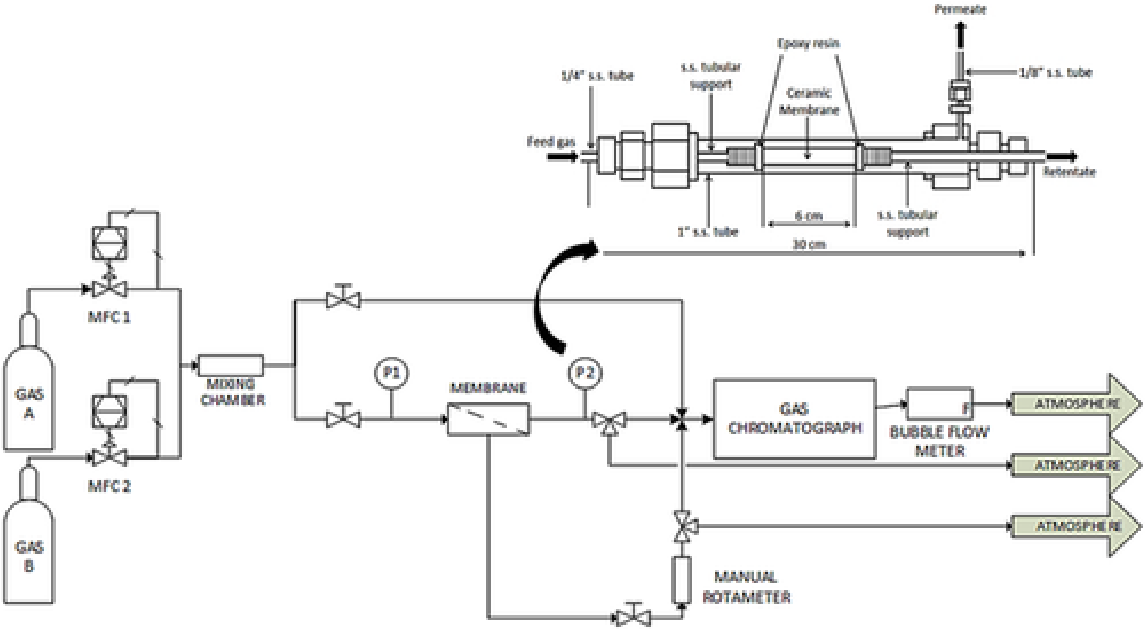

Figure 3.1**.** Single gas permeation and binary gas separation experimental setup (MFC: mass flow controller, P1: feed side pressure transducer, P2: permeate side pressure transducer). The tubular permeation cell is shown in the top right.

The feed gas flow rate and composition were controlled by two mass flow controllers: MFC 1 and MFC 2. Feed pressure was controlled manually using a needle valve. The feed and permeate pressures were measured using electronic pressure transducers P1 and P2, respectively. Permeate flow was measured manually using a 100 mL soap film flow meter. For the binary gas separation experiments, both the feed and permeate gas composition were measured using a Hewlett Packard 5730A gas chromatograph (GC) equipped with a PoropakTM-Q packed column and a thermal conductivity detector (TCD). To measure the mixture gas composition, 1 ml gas samples were injected into the packed GC column with He gas as the carrier gas. The column response to the sample injection was monitored with the TCD, and the corresponding peak areas for the different components were compared to ascertain composition. Prior to the binary gas separation experiments, the feed composition was verified. During the experiments both the feed and permeate side pressures, flow rate, and composition of the permeate were monitored. After approximately 3 hours, the system reached steady state and the feed and permeate side pressures, and the composition and the molar flux of permeate were recorded. A total of 6 consecutive permeate flow measurements were recorded and the average value was used to calculate the molar flux of the permeate.

The membrane performance was evaluated by means of the single gas N$_2$ and He permeances, which are measures of the membrane productivity as described in Equation (1).

$$P_i^{'} = \frac{J_i}{\left(p_{i,F} - p_{i,P}\right)} \qquad (1)$$

where $P_i^{'}$ is the permeance of gas *i*, J_i is the total measured steady state flux of *i* in the permeate, and $p_{i,F}$, and $p_{i,P}$, are the partial pressures of *i* at the feed and permeate side of the membrane, respectively. For the single gas permeation experiments, $p_{i,F}$, and $p_{i,P}$, were simply equal to the absolute total feed and permeate pressures.

The ideal selectivity $\alpha_{i/j}^{*}$ is an estimation of membrane separation performance for a particular gas pair using only the pure gas permeances. It is defined as the ratio of single gas permeance of gases *i* and *j*. (Equation (2a)).

$$\alpha_{i/j}^{*} = \frac{P_i^{'}}{P_j^{'}} \qquad (2a)$$

The permselectivity $\alpha_{i/j}$ refers to membrane separation performance when the feed gas is a gas mixture (Equation (2b)).

$$\alpha_{i/j} = \frac{P_i^{'}}{P_j^{'}} \tag{2b}$$

The membrane performance was evaluated by comparing the N_2/He ideal selectivity and the measured single gas permeance through each membrane. The best performing membrane having the highest N_2/He ideal selectivity was then selected for further analysis using single gases CO_2 and CH_4, and an equimolar binary mixture of N_2 and CO_2 gases. The corresponding permeance and permselectivity values were then determined.

3.2.3 Membrane Transport Characteristics

Gaseous transport through porous membranes involves the contribution of pore flow (viscous flow (Poiseuille flow) and Knudsen flow) and surface flow based on micro-pore diffusion in the silicalite pores and adsorptive surface interactions with the gas adsorbate (Equation (3)) [35–37].

$$J_i = J_i^P + J_i^S \tag{3}$$

Where J_i^P is the flux from pore flow, and J_i^S is the flux from surface flow.

Pore flow consists of both Knudsen flow and viscous flow. The contribution of both of these factors to the total flux from pore flow is expressed in Equation (4) for a homogenous pore structure [35,37].

$$J_i^P = -\frac{\varepsilon}{\tau RT}\left[\left(D_i^{Vis}\right) + \left(D_i^{Kn}\right)\right]\frac{\partial p_i}{\partial x} \tag{4}$$

Where, ε is the membrane porosity, τ is the tortuosity factor, R is the universal gas constant, T is the temperature, p_i is the pressure of component i, and x is the coordinate along the membrane corresponding to the thickness.

Both the viscous flow parameter D_i^{Vis} and the Knudsen diffusive parameter D_i^{Kn} are affected by the defect pore size of membrane. However, D_i^{Kn} is influenced by the molecular weight of the diffusing gas, whereas D_i^{Vis} is independent of this value as defined in Equations (5) and (6) [37]. Viscous flow is thus non selective, whereas selectivity from Knudsen flow is limited to the difference in the molecular weight of the diffusive species.

$$D_i^{Kn} = \frac{2r_p}{3}\sqrt{\frac{8RT}{\pi M_i}} \tag{5}$$

$$D_i^{Vis} = \frac{{r_p}^2 p}{8\eta} \tag{6}$$

Where r_p is the pore radius of the membrane, M_i is the molecular weight of component i and η is the viscosity of the diffusive gas (or gas mixture), and p is the total pressure.

Ideally, the contribution of pore flow to the overall membrane flux may be minimized such that surface flow is the dominating transport mechanism. An advantage of the pore plugging membrane synthesis approach over other methods is that the pore size of the support serves as the maximal size of a potential membrane defect or crack. Therefore, the contribution of pore flow to the total membrane flux may be limited, and surface flow would be dominating the overall mass transport across the membrane.

In considering an ideal zeolite membrane formed through pore plugging synthesis, the dominating transport mechanism is attributed to micro-pore diffusion in the form of surface flow and not pore flow [38,39]. For surface flow, the difference in equilibrium surface coverage between the high pressure feed side and the low pressure permeate side across this membrane is the driving force behind gas transport across the membrane. Gas molecules are adsorbed on the active sites within the micropores of the adsorbent crystals and move in the direction of decreasing surface occupancy, which corresponds to the concentration profile across the membrane [40]. Mass transfer resistance is attributed to the intracrystalline diffusion resistance between the active sites along the length of the membrane [41]. For non-interacting gases such as He, gas transport is governed primarily by activated gaseous diffusion or Knudsen diffusion through the mesopores of the silicalite-1 adsorbent [42]. Since the presence of He permeation across an ideal porous membrane is indicative of Knudson diffusion, the contribution of this transport mechanism for interacting gases such as CO_2, CH_4, N_2, cannot be fully ignored. Since Knudsen diffusion takes place in mesopores of the adsorbent, which in the case of silicalite-1 can easily accommodate not only He, but other, larger gas molecules, it is likely that Knudsen flow will contribute to gas transport regardless.

The affinity of the gases within the pore network of the zeolite membrane plays an important role in the evaluation of membrane performance. With this in mind, it is necessary to quantify both the equilibrium adsorption and the diffusion characteristics of the adsorbent material composing the membrane to effectively describe the gas transport behaviour of the combined sorption and diffusion processes across the membrane. The flux from surface diffusion is derived from Fick's first law in relation to the surface coverage difference across the membrane which represents the driving force for transport (Equation (7)) [35,43,44]. In the case of an ideal defect free membrane, the effective membrane diffusivity, D_e^m, is calculated from the rearrangement of Equation (7), using the experimentally determined membrane flux, J_i^S, and the physical characteristics of the membrane.

$$J_i^S = -\rho(1-\varepsilon)q_i^{sat}\frac{D_e^m}{1-\theta_i}\frac{\Delta\theta_i}{l}, \qquad D_e^m = \frac{J_i^S(1-\theta_i)}{-\rho(1-\varepsilon)q_i^{sat}}\frac{l}{\Delta\theta_i} \tag{7}$$

Where, ρ is the skeletal density of the adsorbent, ε is the porosity of the adsorbent, and q_i^{sat} is the saturation adsorption capacity of component *i*. $\Delta\theta_i$ is the difference in absolute adsorption surface coverage of component *i*, between the high pressure feed side and low pressure permeate side across the length of the membrane. l is the thickness of the membrane, and the θ_i was calculated as the average surface coverage across the membrane.

The Sips isotherm model is used to represent the experimental isotherm data to calculate the surface coverage related to the single gas adsorption behavior [21,22].

$$\theta_i = \frac{q_i}{q_i^{sat}} = \frac{\beta_i {p_i}^n}{1+(\beta_i p_i)^n} \tag{8}$$

Where, q_i is the amount adsorbed of component i, β_i is the affinity constant, and n is the constant parameter. The Sips model parameters may be optimized from the minimization of the sum of the squared residuals between the model fit and the experimental data for the pure component adsorption isotherms.

The membrane effective diffusivity may be determined from single gas permeation experiments. However, due to the variability between different membrane sets composed of composite materials, it is difficult to determine this value appropriately [35,41]. Therefore the transport performance properties of the zeolite membrane may be evaluated by comparing the effective diffusivity of the membrane, D_e^m, with the effective adsorption transport diffusivity evaluated from the zeolite material alone D_e. This link between the gas adsorption behaviour of the zeolite material and the membrane permeation experiments establishes the performance parameters for an ideal zeolite membrane.

The adsorption mass transfer rate can be approximated using the Linear Driving Force (LDF) model proposed by Glueckauf and Coates and discussed in the literature [22,45–48] (Equation (9)).

$$\frac{\partial q}{\partial t} = k_{LDF}\left(q_e - q(t)\right) \tag{9}$$

In this model, the single gas adsorption uptakes are determined experimentally and the amount adsorbed is monitored at different times as $q(t)$. The change in q as a function of time gives the slope, dq/dt, that is plotted as a function of $q(t)$ for different times. Since the q_e value is known as the amount adsorbed at equilibrium, the slope of this plot would give the value of k_{LDF} according to Equation (9).

The LDF diffusion model is valid in the uptake region of $\frac{q(t)-q_0}{q_e - q_0} > 0.6$ [49] or 0.7 [22]. The kinetic rate constant mechanism as shown with the LDF model only considers the surface resistance as a barrier to mass transfer. In reality the silicalite-1 crystals are known to be microporous with a characteristic cuboid shape. To reflect the contribution of diffusion limitation within the micropores of the adsorbent, the LDF model may still be employed when considered as the reduced form of the Fickian Diffusion model for the isothermal diffusion gradient through a homogeneous spherical crystal, thus relating the effective intracrystalline transport diffusion term, D_e, to k_{LDF} [22,48].

$$k_{LDF} \approx \frac{15D_e}{R_c^2} \tag{10}$$

Here D_e is the effective transport diffusivity, and R_C is the radius of the crystal. The inverse of k_{LDF} is the diffusion time constant.

While the crystal size may be approximated to a certain degree of accuracy using SEM micrographs, it may not be directly correlated to the actual path length of the diffusing species within the membrane. Depending on the tortuosity of the micropores and the orientation of the zeolite crystals formed within the porous membrane support, these values may be different from the crystals formed in the free volume during the hydrothermal synthesis. As such, the values of the diffusion time constant of the adsorbing silicalite material alone, and the effective membrane transport diffusivity calculated from the permeation experiments may not be explicitly compared. However, an implicit comparison may be drawn from the selectivity ratios of D_e and D_e^m between the individual components i and j (Equation (11)).

$$\frac{D_{ei}}{D_{ej}} \approx \frac{D_{ei}^m}{D_{ej}^m} \tag{11}$$

An ideal zeolite formation within the porous membrane support is thought to have the same diffusivity characteristics and gas selectivity ratios as the zeolite material alone since surface diffusion would be dominant. The contribution of pore diffusion from non zeolitic pores results in reduced effective membrane transport diffusivity selectivity.

3.3.0 RESULTS AND DISCUSSION

3.3.1 Morphological and Compositional Analysis

The XRD patterns obtained (Figure 3.2) on the zeolite powder collected from the bulk solution in the autoclave following the hydrothermal synthesis and calcination, correspond well to the XRD patterns of MFI type zeolite previously reported in the literature [15,50–52], therefore confirming successful formation of silicalite-1 zeolite. Analysis of the N_2 volumetric adsorption measurements at 77 K showed an average BET surface area of 471.5 $m^2 \cdot g^{-1}$. The BJH micropore area and the micropore volume were 21.89 $m^2 \cdot g^{-1}$ and 0.302 $cm^2 \cdot g^{-1}$, respectively. These values correspond well with literature values for silicalite-1 crystals [53–56].

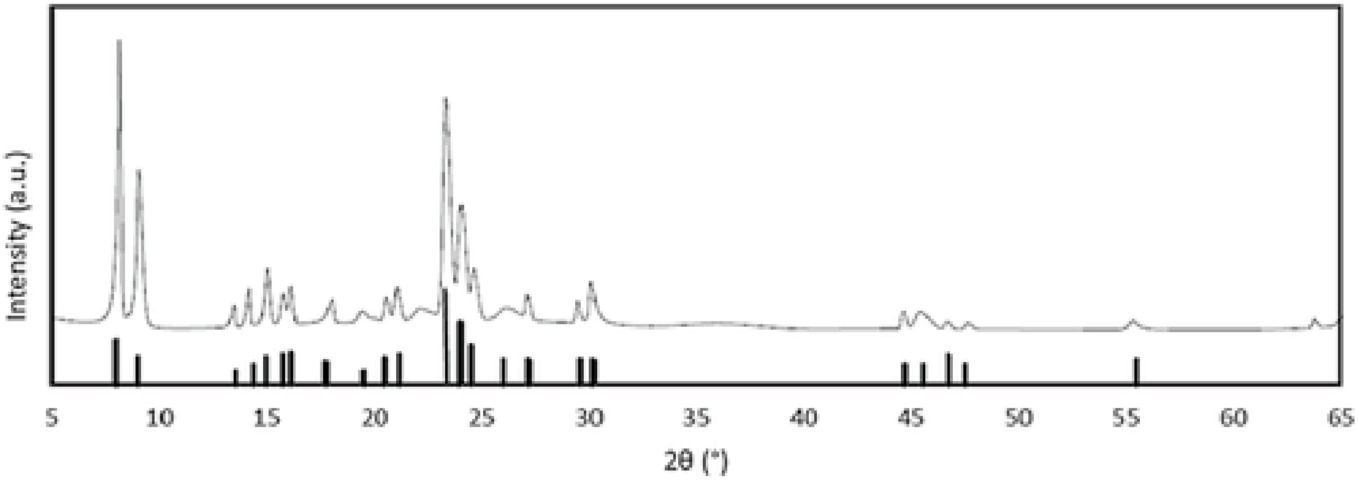

Figure 3.2. XRD patterns corresponding to the silicalite-1 powder recovered from the synthesis solution. The intensity response is equivalent to the characteristic XRD patterns for randomly orientated MFI type silicalite-1 crystals reported in the literature [15, 50-52] represented by the lines at the base of the chart.

The extent of membrane formation through silicalite-1 pore plugging synthesis was examined using SEM (Figure 3.3) and EDS (Figure 3.4) analysis of the cross section for four different support pore sizes. Cross-sectional analysis of the membrane is an effective assessment of the formation of the zeolite selective layer via pore plugging synthesis, since the formation of a zeolite film on the surface is not the goal of this approach. With respect to the pore plugging method, the idea is that a nanocomposite silicalite-1 membrane structure is formed within the pores of the support active layer, as such only a non-selective layer of randomly oriented crystal outgrowth is present on the surface.

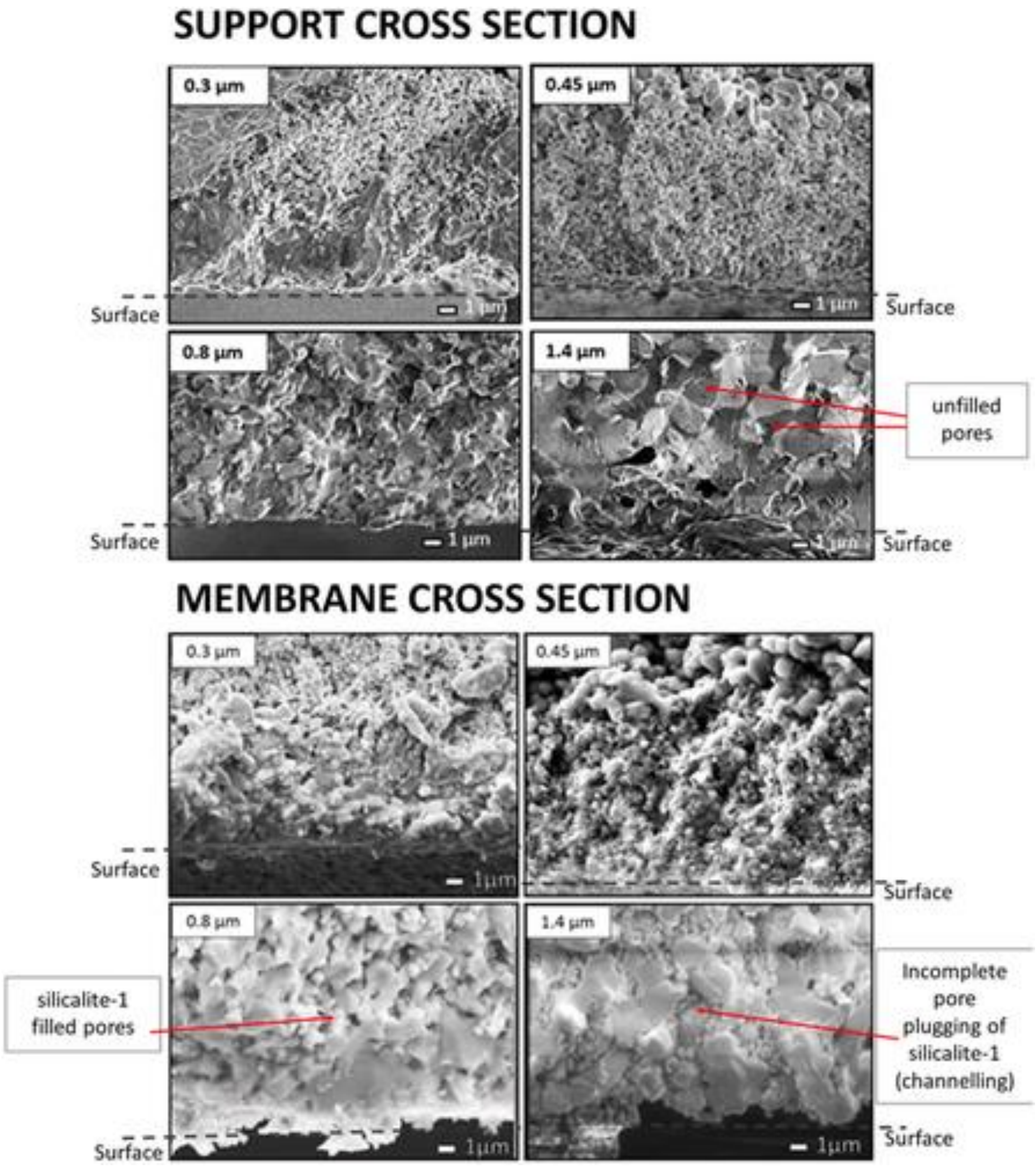

Figure 3.3**.** Cross-sectional SEM images of membrane supports (top) and synthesized silicalite-1 membranes (bottom) for supports with pure TiO_2 in the active layer and pore sizes of 0.3, 0.45, 0.8, and 1.4 µm (magnification 4000×). The dashed line is the membrane surface in contact with the feed gas.

In Figure 3.3, the bottom part of each figure represents the surface of the tubular membrane that is exposed to the feed gas. Following hydrothermal synthesis, the pore network is occupied by zeolite crystals inter-grown within this porous active layer. This is evident by the lower observed porosity for the synthesized membranes compared to the supports. Pore plugging is observed for the three membranes synthesized within the 3 smallest support pore sizes as indicated by a fairly continuous active layer agglomeration composed of composite silicalite-1 crystals formed within the pores of the support. The membrane synthesized on the support with a pore size of 1.4 µm shows incomplete pore blocking by the silicalite-1 crystals grown within the pores as evident by distinct voids forming visible channels within the pores of the support.

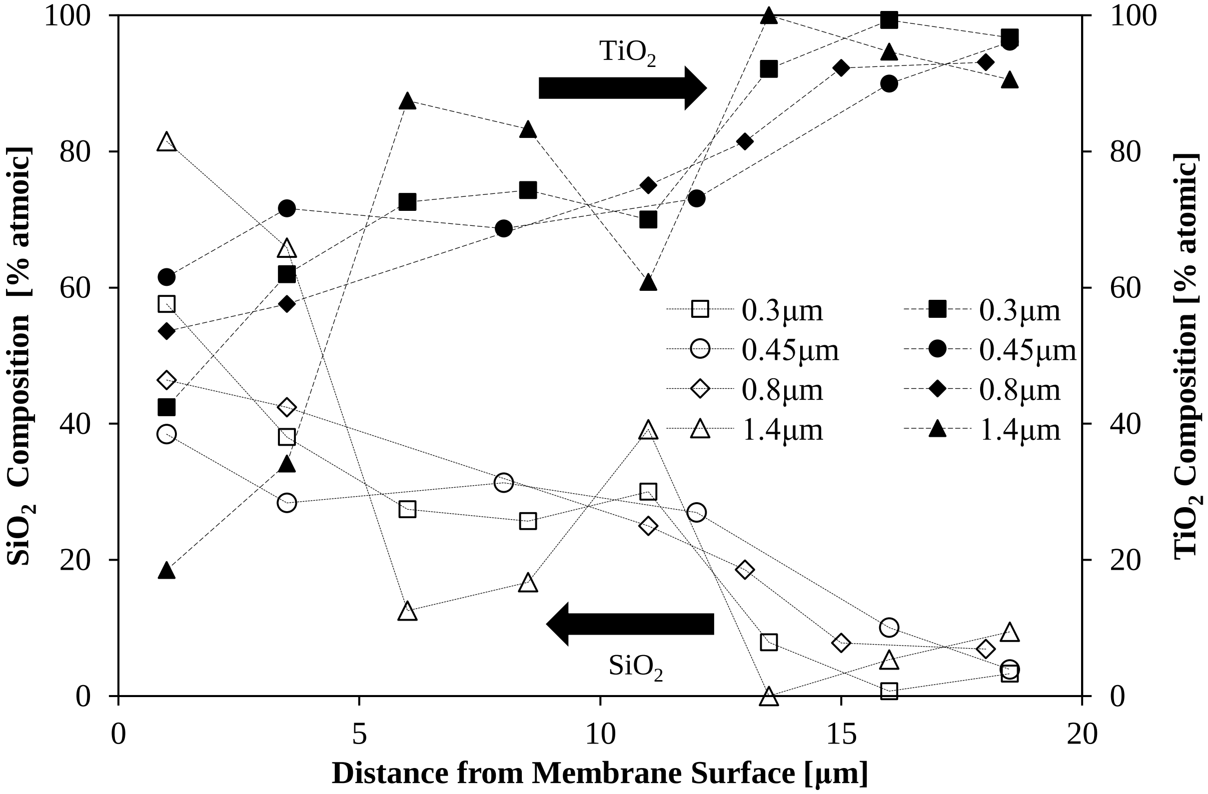

Figure 3.4. Cross-sectional EDS analysis showing SiO_2 and TiO_2 composition as a function of distance from the top membrane surface for synthesized silicalite-1 membranes on supports with TiO_2 in the active layer for support pore sizes of 0.3, 0.45, 0.8, and 1.4 µm.

Compositional analysis of the composite membranes' cross section determined using EDS shows the SiO_2 and TiO_2 composition as a function of distance from the membrane surface (Figure 3.4). Since silicalite-1 zeolite is composed of SiO_4 tetrahedra, the presence of SiO_2 serves to quantitatively support the visual observations from the SEM imagery with respect to zeolite crystal growth. Crystal outgrowth is observed in the first top layers less than 2 μm from the membrane surface as the Si content is about 60% and 80% in this region for the membranes with support pore sizes of 0.3 and 1.4 μm, respectively. The variable thickness is consistent with other studies in the literature which report crystal outgrowth in the range of fractions of a micrometer to tens of micrometers [15,57–59]. The EDS analysis in Figure 3.4 supplements the SEM observations. Silicalite-1 penetration of approximately 30% up to the first 10 - 12 μm is observed within the composite TiO_2 layer for membranes with support pore sizes of 0.3, 0.45, and 0.8 μm. A consistent layer of SiO_2 within the first 10-12 μm from the membrane surface is observed, and is indicative of the presence of silicalite-1 crystals occupying the pores of the membrane active layer. A more uneven distribution of SiO_2 is observed in the active layer for the membrane with a support pore size of 1.4 μm, which is indicative of incomplete pore plugging and the presence of defects within the membrane as supported by the SEM imagery [17].

Not depicted on the SEM images is porous alumina support that begins approximately 30 μm from the membrane surface. EDS analysis showed only the presence of SiO_2 and TiO_2 at a distance of up to 20 μm from the membrane surface. While the accuracy of EDS does not completely capture the presence of very small quantities of Al^{3+}, it is important to mention that no Al^{3+} was detected within this range. The absence of alumina within the support active layer indicates that it is likely that only silicalite-1 zeolite was synthesized within the active layer of the support. This observation is in agreement with previous studies supporting the development of pure silicalite-1 membranes with no significant incorporation of Al^{3+} from the porous alumina support into the membrane active layer [15].

3.3.2 Silicalite-1 Single Gas Adsorption Isotherms and Diffusion Kinetics

Single gas adsorption equilibrium isotherms for CO_2, CH_4, and N_2 gases on the synthesized silicalite-1 powder were determined and are shown in Figure 3.5a. The adsorption capacity for CO_2 is the highest, followed by CH_4 and N_2. This is expected due to the strong quadrupole moment and greater polarizability of CO_2 contributing to increased adsorption potential [23,29]. The adsorption isotherms are in agreement with previous studies in the literature for the adsorption of these gases on silicalite-1 [15,24,25]. Using the adsorption equilibrium isotherms, the corresponding ideal adsorption selectivity for CO_2/N_2, CO_2/CH_4, and CH_4/N_2 gases were determined from the ratio of the equilibrium adsorption capacities, and the results are presented in Figure 3.5b. The ideal adsorption selectivity is the highest for CO_2/N_2 which approaches values greater than 25 and the lowest for CH_4/N_2 at 3.5 as pressure approaches 0 atm. However, from the perspective of membrane gas permeation and separation, 1 atm total pressure is the limiting value for the permeate side for a practical membrane. At that pressure, ideal CO_2/N_2 and CH_4/N_2 selectivity values are 9 and 3, respectively. Although the adsorption capacities for all the gases increase with pressure, the rate of increase gradually decreases for both CO_2 and CH_4. This compares to a relatively steady increase in N_2 adsorption capacity. As a result, this leads to a decrease in the ideal selectivity for CO_2/N_2 and CH_4/N_2 at increasing pressures. The ideal selectivity presents the equilibrium separation potential of silicalite-1 zeolite. However since molecular transport of these gases may occur by means of adsorptive surface diffusion within the pores of zeolite, the diffusivity of the gases must also be a considering factor for evaluating the separation potential [40].

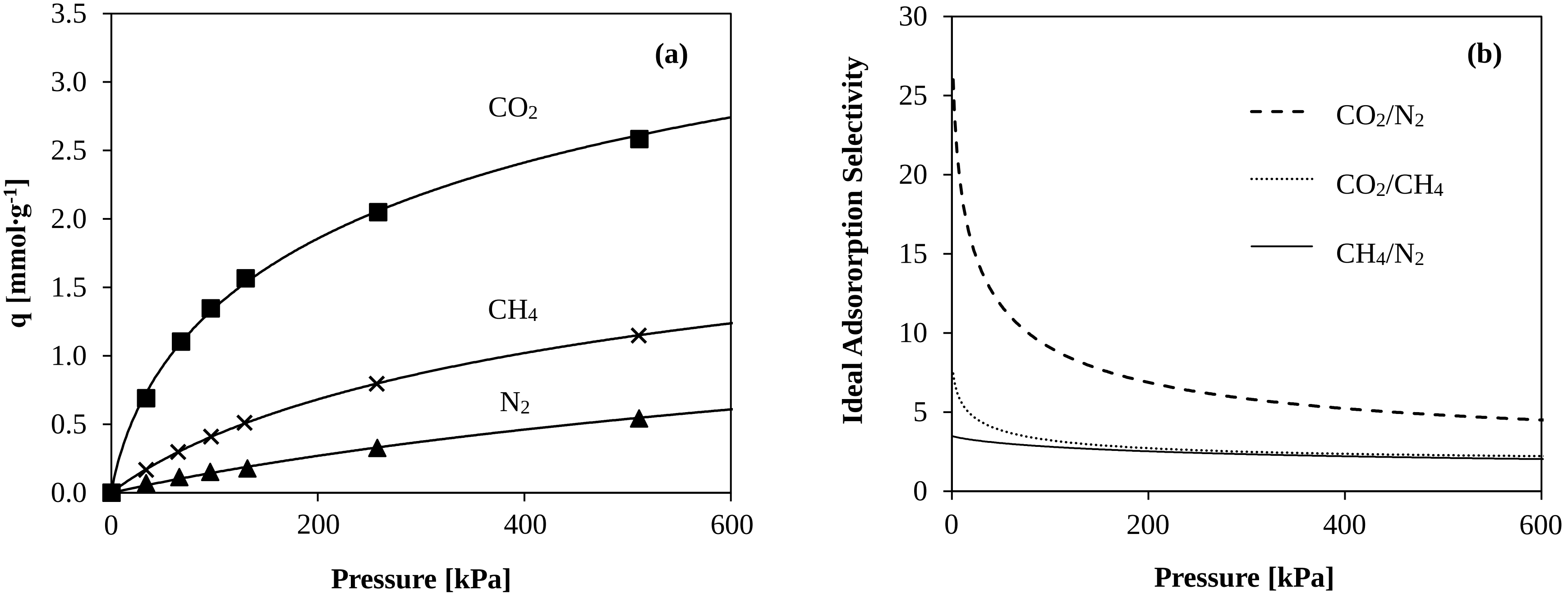

Figure 3.5**.** (a) Single component adsorption equilibrium isotherms and Sips model fit for CO_2, N_2, and CH_4 at 295 K for the synthesized silicalite-1 powder. (b) Ideal adsorption selectivity for CO_2, CH_4, and N_2 gases as determined from the single component adsorption equilibrium isotherms in Figure 3.5a.

The experimental single gas uptake curves were modelled with the LDF model and effective diffusivity for different pressure steps have been determined from Equation (9). These effective diffusivity values are shown for different gas loadings in Figure 3.6. CH_4 has the fastest uptake on the silicalite-1 zeolite, and it has the highest transport diffusion time constant, followed by N_2, and CO_2. Interestingly, this means that although CO_2 has the highest adsorption capacity on silicalite-1 as shown in Figure 3.5a, it also has the highest resistance to intracrystalline transport diffusion within the micro-pores. As expected, the observed transport diffusivity values increase as loading increases for all three gases. The effective diffusivity in the order from the highest to the lowest is: $CH_4 > N_2 > CO_2$ which is in agreement with the trends previously reported for silicalite-1 [60,61]. This behaviour is consistent with the fact that microporous materials initially induce a resistance on the movement of gas particles to the adsorbent sites due to the small porous structure. At higher loadings, the transport of the gases tends to increase due to increases in the frequency for both intermolecular and surface interactions with the zeolite due to higher molecular concentrations.

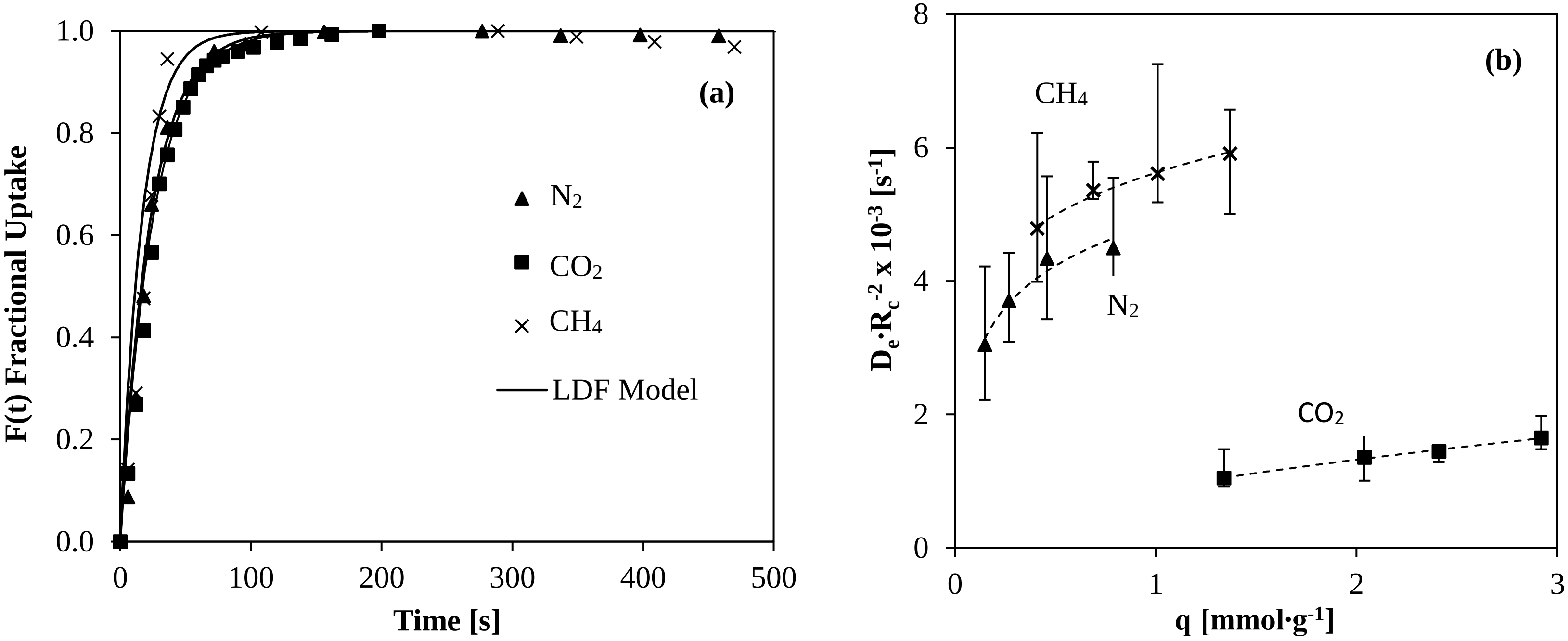

Figure 3.6**.** (a) Single component N_2, CH_4, and CO_2 gas uptake curves on synthesized silicalite-1 powder for a pressure step change of 50 kPa to 100 kPa at 295 K. (b) Experimental transport diffusion time constants as a function of adsorption surface loading on synthesized silicalite-1 at 295 K for pressure step changes of 50–100 kPa, 100–200 kPa, 200–400 kPa, and 600–800 kPa.

3.3.3 Single Gas Membrane Permeation

Single gas permeation experiments were performed using N_2 and He gases to characterize the membrane performance with respect to effective pore plugging of the synthesized silicalite-1 inside the pores of the TiO_2 active layer. Four TiO_2 active layer pore sizes were studied: 0.3 µm, 0.45 µm, 0.8 µm, and 1.4 µm. A total of 9 membranes were fabricated from 3 different batches under similar conditions (batch A, B, and C, respectively). He and N_2 gases are of interest for characterization purposes as He is assumed to have little or no interaction within the zeolitic pores, whereas N_2 has some affinity to the silicalite-1 zeolite as observed from the adsorption equilibrium capacities shown in Figure 3.5. If the pores of the membrane support are sufficiently plugged with zeolite, N_2 gas transport across the membrane would occur by surface diffusion and to a lesser extent by Knudsen flow. However, the transport of the non-adsorbing He gas is limited to only Knudsen diffusion. For the surface diffusion, the driving force is the gradient of surface occupancy within the zeolite membrane caused by a pressure differential. This is why it was expected that N_2 gas, which has a higher adsorption capacity compared to He, would have a greater flux than He gas despite having a significantly larger kinetic diameter (3.6 Å for N_2 vs. 2.6 Å for He).

The single gas permeance values of He and N_2 gases are presented in Figure 3.7 as a function of the pressure differential across the different synthesized silicalite-1 membranes. He permeances were observed to be between 2×10^{-7} and 2×10^{-5} $mol \cdot m^{-2} \cdot s^{-1} \cdot Pa^{-1}$, whereas N_2 permeances were observed to be between 4×10^{-7} and 2×10^{-5} $mol \cdot m^{-2} \cdot s^{-1} \cdot Pa^{-1}$. In all cases, the permeance values for N_2 are higher than those for He, with the exception of the membranes synthesized using the 1.4 µm pore size support. Since this is the case, it can be concluded that the membranes with support pore sizes of 0.3 µm, 0.45 µm, 0.8 µm are indeed sufficiently plugged with silicalite-1 zeolite, suggesting that the presence of defects has been minimized to the extent that surface diffusion is the dominant transport mechanism. The higher N_2 permeance over He is attributed to the interaction of N_2 with the silicalite-1 adsorption sites within the membrane. The relative linearity of the pure component adsorption equilibrium isotherms for N_2 (Figure 3.5), reinforces the fact that the gradient in pressure contributes to the adsorption driving force across the membrane through surface flow. He is an inert gas and is assumed to not interact with the zeolite, therefore the contribution of surface diffusion as a means of gas transport is quite small and Knudsen flow is the dominate transport mechanism for this gas. This results in N_2 selective membranes for the three smallest support pore sizes.

Figures 3.8a and 3.8b show the average single gas He and N_2 permeance and corresponding ideal N_2/He selectivity as a function of the support active layer pore size for all of the prepared membranes. The average single gas permeances ranged between 3.7 x 10^{-7} and 1.3 x 10^{-5} $mol \cdot m^{-2} \cdot s^{-1} \cdot Pa^{-1}$ with N_2 gas being more permeable than He gas (with the exception of the membranes synthesized on the 1.4μm pore size support where He gas was more permeable). This observation is consistent with previous studies that reported the likelihood of the MFI crystals' plugging the pores being inversely proportional to the support pore size [15,17]. The membranes synthesized within the 0.8 um support show both the lowest gas permeance and the highest N_2/He selectivity.

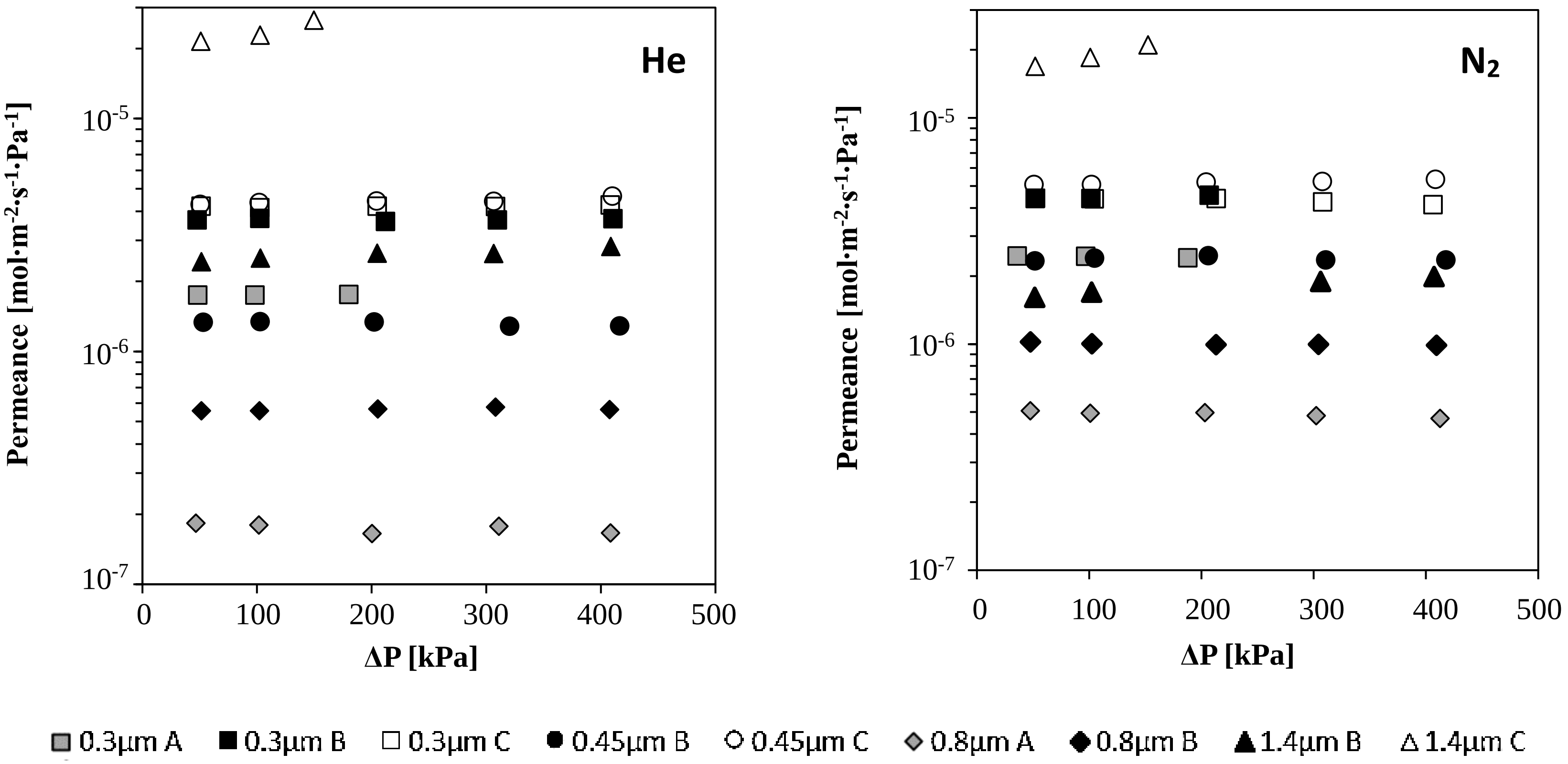

Figure 3.7. Single gas He (left) and N$_2$ (right) permeances as a function of differential pressure for synthesized silicalite-1 membranes with pure TiO$_2$ in the active layer with support pore sizes of 0.3, 0.45, 0.8, and 1.4 µm. Experiments were performed at 293 K with the permeate side open to atmospheric pressure.

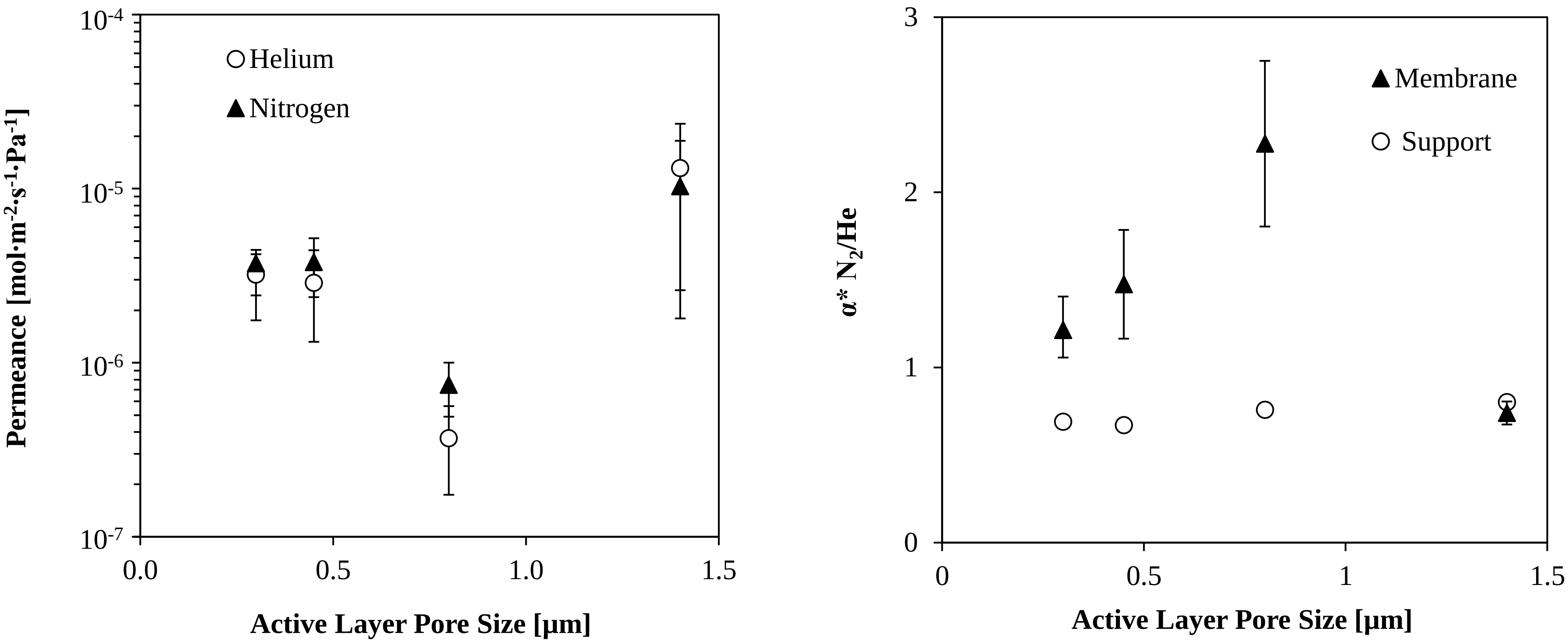

Figure 3.8**.** (a) Average single gas He and N_2 permeances as a function of active layer pore size for synthesized silicalite-1 membranes with pure TiO_2 in the active layer. (b) Average single gas N_2/He permeance ideal selectivities as a function of active layer pore size for synthesized silicalite-1 membranes compared to the unsythesized supports. Experiments were performed at 293 K with a feed pressure range of 150–500 kPa and the permeate side open to atmospheric pressure.

The permeance of N_2 and He gases for the non-synthesized supports were also examined as a reference and are shown in Figure 3.9. The average permeance of the porous supports with no membrane is in the order of 1.0 x 10^{-4} mol·m^{-2}·s^{-1}·Pa^{-1} with He being more permeable than N_2. With respect to Knudsen flow, the square root of the inverse ratio of the molecular weights gives the ideal separation factor, whereas mass transfer through viscous flow is not selective at all [62]. The experimental permeance measurements for the supports correspond to an ideal He/N_2 selectivity ranging from 1.25 to 1.53 (corresponding to the numbers shown in Figure 3.8b as the inverse of the ideal N_2/He values from 0.8 to 0.65 for the supports). This value is lower than the He/N_2 selectivity of 2.65 expected for gas transport by Knudsen diffusion alone suggesting a significant contribution from viscous flow.

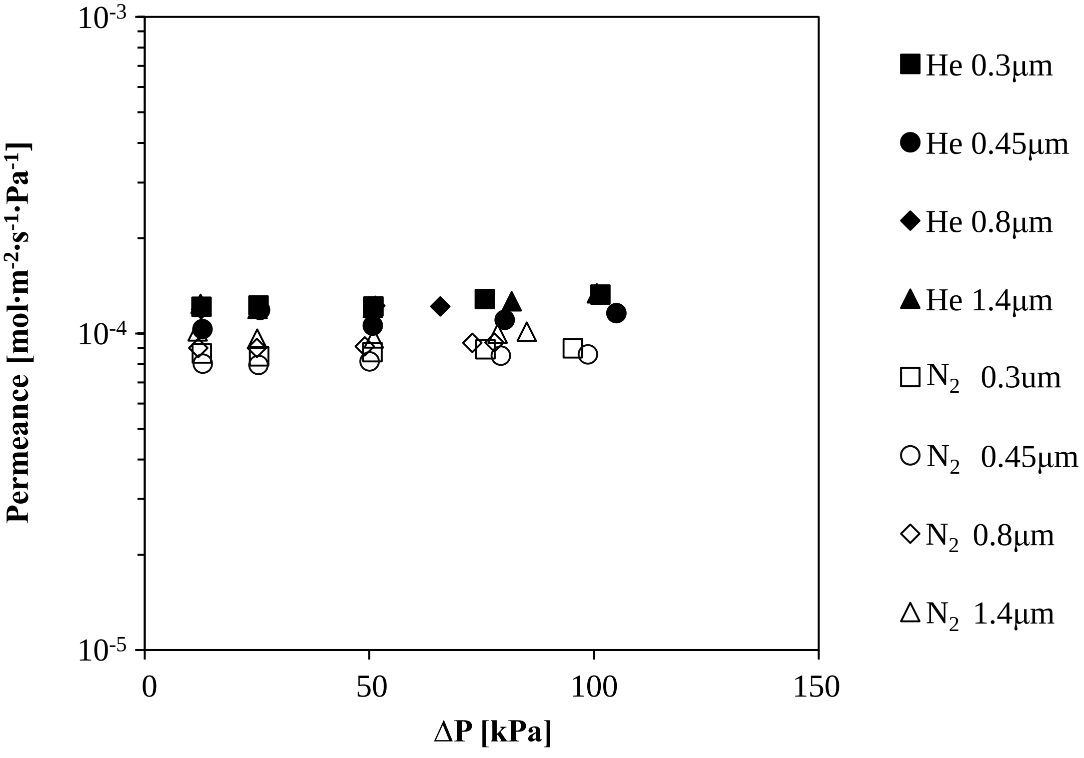

Figure 3.9. Single gas He (filled points) and N_2 (unfilled points) permeances as a function of differential pressure for membrane supports only, with pure TiO_2 in the active layer with pore sizes of 0.3, 0.45, 0.8, and 1.4 μm. Experiments were performed at 293 K with the permeate side open to atmospheric pressure.

The TiO_2 active layer pore size influences the amount of precursor zeolite solution diffusing into the support active layer during the pore plugging synthesis. Intuitively, the smaller support pore sizes are thought to be more conducive to easier pore plugging. However, because of lower penetration of the precursor solution within the pores following the initial nucleation step, the formation of the final zeolite active layer may actually be inhibited due to the smaller pore size. Conversely, larger pore sizes may result in a more consistent composite membrane structure up to a certain pore size, at which point zeolite crystal growth may not be sufficient to completely fill the pores, leading to an increased presence of defects [15,63]. Previous studies have shown that the formation of the silicalite-1 zeolite crystal size and orientation is highly dependent on the synthesis parameters such as: temperature, solution concentration, and length of the synthesis time [16,17,64]. While the zeolite crystal properties may be modified by altering these conditions, as can be observed with the apparent lack of N_2/He selectivity for the 1.4 µm membranes, there likely exists a maximum physical limitation of support pore size in order to achieve effective pore blocking.

As can be seen in Figure 3.8a and 3.8b, for the 1.4 µm membranes, He permeance is higher than N_2 resulting in similar N_2/He selectivity as the unsynthesized supports. This indicates that for the 1.4 µm membranes, gas transport through the non zeolitic pores is the primary means of permeation across the membrane. These results support the initial findings from the SEM and EDS analysis, which indicated the likely presence of defects due to incomplete pore plugging, allowing alternative pathways for gas transport.

The average ideal selectivity approaches a maximum value of 2.3 ± 0.5 for the membranes synthesized on the support with the pore size of 0.8 µm. The observed N_2/He ideal selectivity ratios are comparable to the values reported in the literature which range from 1.6 to 3 for MFI type membranes reported in the literature [61,65–69]. However, the corresponding N_2 and He permeances in this study are substantially higher than most other membranes of this type, with the exception of Hedlund et al., where N_2/He ideal selectivity was reported to be about 1.59 [66].

Silicalite-1 membranes synthesized using the supports with 0.8 µm pore size showed the highest N_2/He ideal selectivity indicating the most effective pore plugging and minimal defects amongst the membranes studied. Therefore, additional single gas permeation experiments for He, N_2, CH_4, and CO_2 were performed on this membrane type, and results are given in Figure 3.10. As expected, the He and N_2 permeances remained relatively consistent with previous experimental results in this study and those reported in the literature [61,70,71]. Unlike He and N_2, the permeances of CO_2 and CH_4 decreased with increasing pressure difference. Adsorption diffusion across the membrane is the main mechanism for gas transport as these observations can be explained in terms of the shape of their respective isotherms shown in Figure 3.5a. The silicalite-1 adsorption capacity gradient (i.e. the slope of the adsorption isotherms) for CO_2 and CH_4 decreases with increasing pressure; this gradient represents the driving force that facilitates adsorptive surface flow across the membrane. In the absence of defects in the membrane structure, the permeance of CO_2 and CH_4 are expected to decrease with increasing feed pressure. On the other hand, since the N_2 isotherm has a more linear tendency, the permeance is expected to remain constant with increasing pressure differential. As can be observed from Figure 3.10, the decrease in permeance for CO_2, as the pressure difference increases is more than that of CH_4. This is due to the fact that the CO_2 isotherm is more rectangular which results in a greater decrease in isotherm slope as pressure difference increases compared to CH_4.

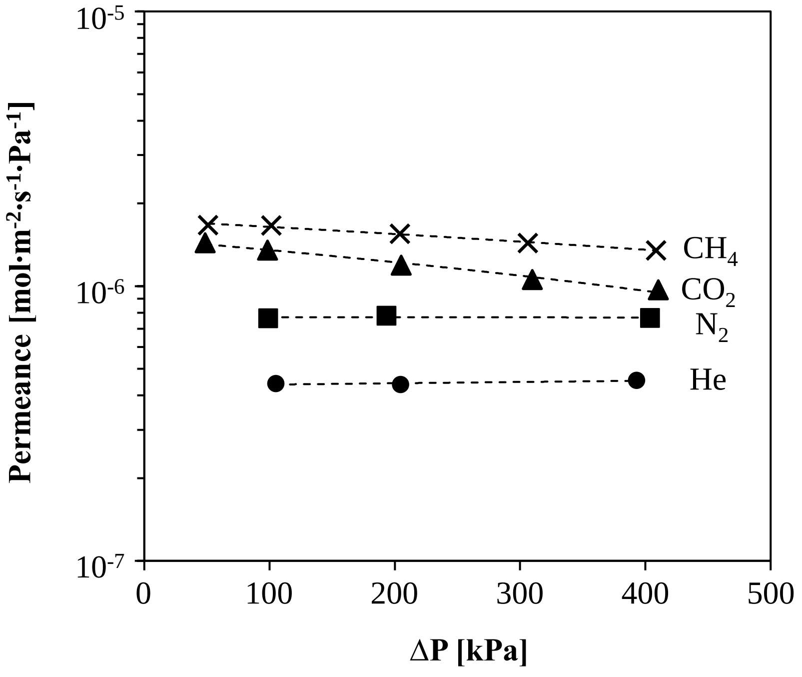

Figure 3.10**.** Single gas permeance of He, N_2, CO_2, and CH_4 gases as a function of pressure differential for the synthesized silicalite-1 membrane with pure TiO_2 in the active layer and support pore size of 0.8 μm from Batch A. Experiments were performed at 293 K with the permeate side open to atmospheric pressure.

Figure 3.11 compares the diffusivity ratios D_e and D_e^m for the different gases CH_4/CO_2, N_2/CO_2, and CH_4/N_2. D_e was determined from the silicalite powder adsorption uptake experiments (Figure 3.6b). The D_e^m values were calculated from the single gas permeance data presented in Figure 3.10, and the membrane parameters shown in Table 3.2. While the absolute value of the different diffusion coefficients (D_e and D_e^m) for each gas may not be directly compared, comparing diffusion selectivity ratios shows the effectiveness of silicalite formation within the membrane pores compared to an ideal case where a membrane is assumed to be a single crystal. As expected, the increased surface occupancy at higher average pressures results in increased diffusivity in all cases due to an increase in the number of interactions between adjacent gas molecules [31]. It follows that the order of the diffusivity ratios are in the order of increasing selectivity: $CH_4/N_2 < N_2/CO_2$

< CH_4/CO_2, and are the same for both methods. However, in all cases, the D_e^m gas diffusivity ratios are lower than that of the D_e ratios. This indicates that while adsorption surface flow through the zeolite material is present in the membrane, there is still a sizeable contribution to flow through the non-zeolite pores.

Figure 3.12 presents the single gas permeance as a function of gas kinetic diameter for the studied gases observed at 293K for a pressure differential of 1 atm in this work compared to those reported in the literature under similar conditions [61,65–67,71–74]. It is evident that the pore plugging method used in this study results in high gas permeance, while maintaining favourable gas permeation ratios consistent with the results from the literature (Table 3). Comparison with our previous work [15] shows that the gas permeation rate is significantly higher. The experimental single gas permeance is not related to the gas kinetic diameter. Since the pores of the silicalite-1 membrane are greater than the kinetic diameter of all of the studied gases, if adsorption diffusion was not a mechanism of gas transport, smaller gases would be expected to have a higher permeance. However, this is not the case as CH_4 is the most permeable (even though it is the largest) followed by CO_2, N_2, and He, which is indicative of adsorption surface flow across the membrane. It should be stressed that both the diffusivity and the equilibrium capacity for adsorption play key roles in determining the permeance of the components through the zeolite membrane. As such, this explains that although silicalite-1 has a lower equilibrium adsorption capacity for CH_4 compared to CO_2 (Figure 3.5a), the transport diffusivity for CH_4 gas across the membrane is higher compared to CO_2 as indicated by the effective diffusivity values shown in Figure 3.6b. The experimental observations show combined high gas permeance and good ideal selectivity compared to the previous results in the literature. This is indicative of the ability to achieve synthesis of highly ordered silicalite crystals within the pores of the support, thus resulting in productive membranes in terms of both flux and separation potential, which are imperative to applications in industrial gas separations. The CO_2/N_2 and CO_2/CH_4 ideal selectivity are 1.77 and 1.23, respectively, these values are comparable to other silicalite-1 membranes reported in the literature (Table 3.3).

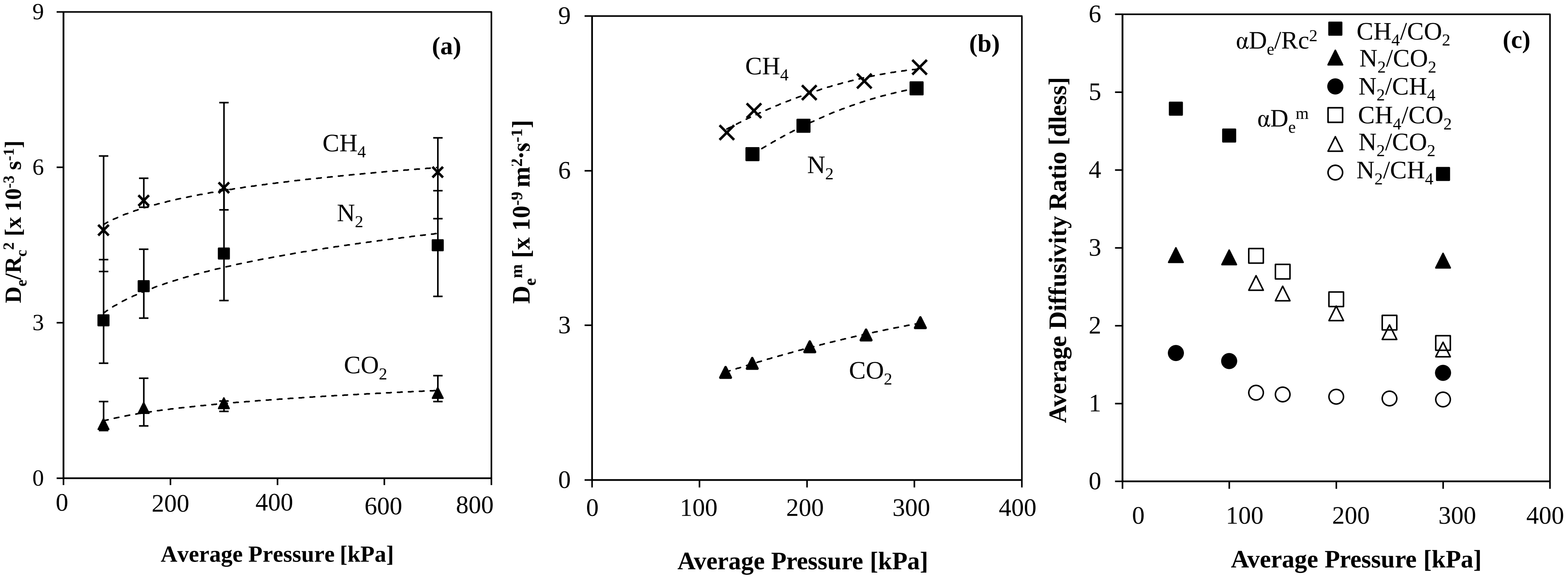

Figure 3.11. Single gas diffusivity coefficients determined from (a) the single gas adsorption uptake experiments for pure N_2, CO_2, and CH_4 gases on synthesized silicalite-1 shown in Figure 3.6 and (b) the single gas permeance of N_2, CO_2, and CH_4 gases shown in Figure 3.10. (c) Comparison of the experimental diffusivity ratios.

Table 3.2. Sips adsorption isotherm parameters determined in this study at 295 K for silicalite-1 for single gas CH_4, N_2, and CO_2; and estimated membrane parameters used for calculating the single gas diffusive property of the membrane, D_e^m.

Sips Model Parameters		**CH_4**	**N_2**	**CO_2**
q^{sat}	($mmol\cdot g^{-1}$)	2.426	2.325	3.605
β	(atm^{-1})	0.180	0.076	0.870
n	(dless)	0.955	0.997	0.592
membrane thickness (x)	(μm)		~10-12†	
silicalite-1 skeletal density (*ρ*) [71]	($g\cdot cm^{-3}$)		1.785	
Silicalite-1 porosity (*ε*) [48]	(dless)		0.428	
† the membrane thickness was estimated from EDS analysis of the membrane cross section given in Figure 4.				

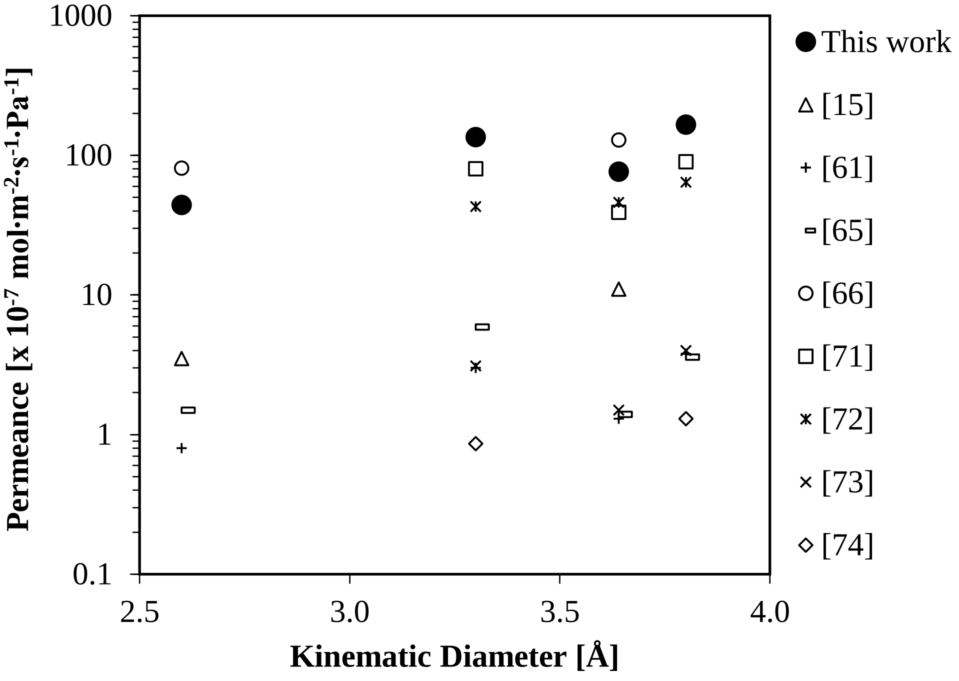

Figure 3.12. Single gas permeance of He, N_2, CO_2, and CH_4 gases at 100 kPa pressure differential as a function of gas kinetic diameter for a synthesized silicalite-1 membrane with pure TiO_2 in the active layer and support pore size of 0.8 μm compared those reported in the literature [15,61,65,66,71-74]. Experiments were performed at 293 K with a 100 kPa pressure differential and the permeate side open to atmospheric pressure.

Table 3.3. Comparison of single gas permeance and ideal selectivity with literature for a silicalite-1 membrane synthesized with pure TiO_2 in the active layer and pore size of 0.8 µm. Experimental conditions for this work were evaluated at 293 K with a 100 kPa pressure differential and the permeate side open to atmospheric pressure.

Reported Synthesis Description	**Support type**	**T (K)**	**x [µm]**	**Permeance *P'* [x 10^{-7} mol·m^{-2}·s^{-1}·Pa^{-1}]**					**Ideal Selectivity α* [-]**			**Ref.**
				H_2	**He**	**CO_2**	**N_2**	**CH_4**	**N_2/He**	**CO_2/N_2**	**CO_2/CH_4**	
Pore plugging and secondary growth	**TiO_2 layer, α-Al_2O_3 tube**	**293**	**~12**	**-**	**44.2**	**135.0**	**76.3**	**166.0**	**1.72**	**1.77**	**0.81**	**This work**
pore plugging	TiO_2/ZrO_2 layer, α-Al_2O_3 tube	296	5	-	3.5	-	11	-	3.14	-	-	[10]
seeded growth	α-Al_2O_3 disc	298	10	2.9	1.5	5.9	1.4	3.6	0.93	4.20	1.80	[58]
seeded growth	α-Al_2O_3 disc	298	0.5	210	81	-	129	-	1.59	-	-	[59]
steam-assisted crystallization	α-Al_2O_3 tube	298	5.5	-	1-18	-	0.43-20	-	~1	-	-	[61]
unseeded growth	α-Al_2O_3 tube	300	10	44	26.7	-	15.6	-	0.58	-	-	[60]
unseeded growth	SS disc	300	50-60	2.5	0.8	3.0	1.3	3.8	1.62	2.31	0.79	[55]
seeded growth	α-Al_2O_3 disc	298	17	86	-	80	39	90	-	2.05	0.89	[64]
in situ nucleation and secondary growth	α-Al_2O_3 tube	298	2	79	-	43	46	64	-	1.07	0.67	[65]
unseeded growth	SS disc	298	50	2.5	-	3.1	1.5	4.0	-	2.06	0.78	[67]
pore plugging	TiO_2/ ZrO_2 layer, α-Al_2O_3 tube	293	6.5	-	-	0.5	0.4	-	-	1.20	-	[24]
secondary growth	α-Al_2O_3 disc	298	3	0.96	-	0.86	-	1.3	-	-	0.66	[68]
secondary growth	SS disc	303	20	-	-	2.3	-	0.7	-	-	3.28	[35]
seeded growth	α-Al_2O_3 disc	300	10	-	1.4	-	-	-	-	-	-	[36]

3.3.4 Mixture Gas Membrane Permeation

The single gas permeance of zeolite adsorbent membranes cannot be used to accurately predict mixed gas permeation performance. This is due to the fact that zeolites have a finite number of adsorptive sites which results in changes in zeolite mixture selectivity when compared to the single gas behaviour. Permeation experiments for the membrane with a support pore size of a 0.8 μm synthesized in batch A were carried out using an equimolar binary CO_2-N_2 feed. The results are presented in Figure 3.13. The CO_2 permeance observed from the binary mixture is similar to the single gas permeance values shown in Figure 3.10. The N_2 permeance is lower for the binary CO_2-N_2 system at 1.8×10^{-7} to 2.0×10^{-7} $mol \cdot m^{-2} \cdot s^{-1} \cdot Pa^{-1}$ compared to the single gas system at 8.0×10^{-7} $mol \cdot m^{-2} \cdot s^{-1} \cdot Pa^{-1}$. The CO_2/N_2 permselectivity ranges from 3 to 9 (Figure 3.13b) and decreases with increasing pressure differential which is consistent with the trends observed with respect to the ideal adsorption selectivity given in Figure 3.5b. CO_2 has a much greater affinity towards the zeolite compared to N_2, therefore it will be preferentially adsorbed to a site which may block access to N_2. This is favourable for increasing CO_2/N_2 permselectivity compared to the single gas CO_2/N_2 ideal selectivity. These results are consistent with results that have been reported in the literature for binary mixtures involving CO_2 and N_2 on silicalite-1 pellets [26], and MFI type membranes [30,75]. The permeance of N_2 in the mixture is affected much more than the permeance of CO_2 compared to their pure component permeance. Therefore, the presented permselectivity values for the mixtures are much higher than the ideal selectivity.

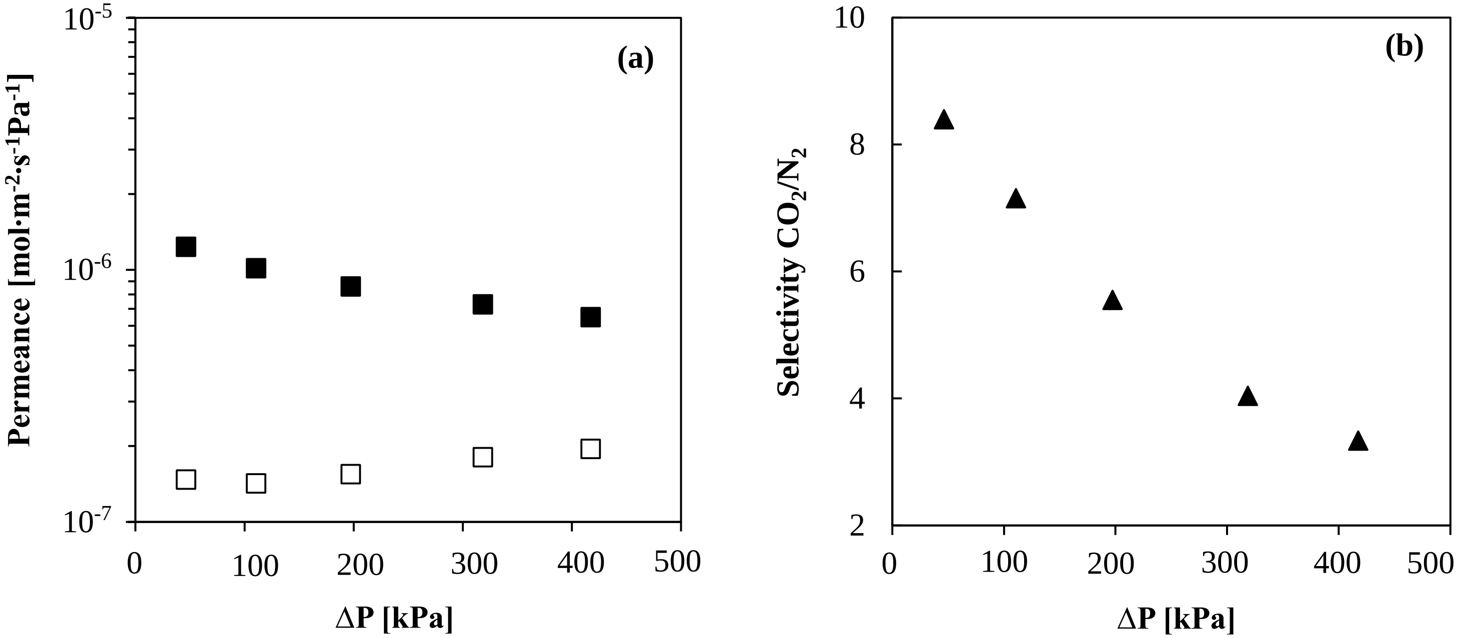

Figure 3.13. (a). Permeance and (b) CO_2 /N_2 permselectivity of CO_2 and N_2 as a function of total pressure differential for a synthesized silicalite-1 membrane with pure TiO_2 in the active layer and support pore size of 0.8 µm. Experiments were performed at 293 K with the permeate side open to atmospheric pressure using an equimolar binary CO_2-N_2 feed.

3.4.0 CONCLUSIONS

Silicalite-1 membranes have been successfully synthesized in-situ within tubular supports with TiO_2 in the active layer using a modified pore plugging synthesis method with a thermal break of 11 hours. SEM and EDS analyses confirm the synthesis of silicalite-1 membranes with a thickness of approximately 10 - 12 µm with no Al^{3+} detected within the membrane composite structure in the active layer. The permeation properties of the membranes show that the potential for gas transport across the membrane through surface flow is governed by both the surface occupancy of the components and the resistance to gas transport. These characteristics can be determined using the adsorption equilibria and diffusion measurements obtained from the zeolite material alone and compared to the performance of the membrane. Evaluating the adsorbent material with respect to adsorption equilibria and diffusion kinetics may serve to establish the upper limit of membrane surface flow diffusivity, particularly for porous membranes formed from adsorbent materials.

Single gas He and N_2 permeation experiments confirm the minimization of defects for membranes synthesized on supports with pore sizes of 0.3µm, 0.45µm, and 0.8 µm, with calculated membrane permeances ranging from 3.7×10^{-7} and 1.3×10^{-5} $mol \cdot m^{-2} \cdot s^{-1} \cdot Pa^{-1}$. Ideal N_2/He permeance ratio was observed to be the highest at 2.3 ± 0.5 for the membranes with the support pore size of 0.8 µm which is equivalent to other MFI type membranes.

Single and mixed gas permeation experiments show that adsorption surface diffusion is the primary method for gas transport across the synthesized membranes. He and N_2 permeances were observed to be constant, whereas single gas CO_2 and CH_4 permeances decrease with increasing pressure differential across the membrane. Permeance was shown to be independent of gas kinematic diameter, with CH_4 being the most permeable (although it is the largest), followed by CO_2, N_2, and He.

The effect of competitive adsorption within gas mixtures and surface diffusion was shown to induce favourable separation of CO_2 over N_2 with actual mixture permselectivity higher than the ideal gas selectivity calculated from the pure component data. A CO_2/N_2 permselectivity value as high as 9 was attained for an equimolar CO_2 – N_2 feed mixture.

High gas permeability (calculated to be equivalent to about 33000 Barrer for CO$_2$ using the membrane thickness of about 10 – 12 μm determined from the EDS and SEM analysis) were observed which results is a similar material performance as described by the Robeson upper bound for CO$_2$/N$_2$ separations for polymeric materials [76]. The CO$_2$/N$_2$ permselectivities of these membranes are lower than reported equilibrium selectivities of competing adsorption based separations involving zeolite 13X or activated carbons [77]. However, the observed high permeances of these membranes coupled with the thermal and chemical stability silicalite-1 zeolite may show potential as an initial bulk separation step following industrial flue gas treatment, where polymeric materials are thought to be less stable and are subject to rapid physical aging.

3.5.0 NOMENCLATURE

A_m	Membrane area	$[\mathrm{m^2}]$
D_e	Effective transport diffusivity	$[\mathrm{m^2 \cdot s^{-1}}]$
D_e^m	Effective membrane diffusivity	$[\mathrm{m^2 \cdot s^{-1}}]$
D_i^{Kn}	Knudsen diffusivity parameter	$[\mathrm{m^2 \cdot s^{-1}}]$
D_i^{Vis}	Viscous flow parameter	$[\mathrm{m^2 \cdot s^{-1}}]$
J	Membrane flux	$[\mathrm{mol \cdot m^2 \cdot s^{-1}}]$
k_{LDF}	Kinetic rate constant	$[\mathrm{s^{-1}}]$
l	Thickness of the active layer of the membrane	[m]
n	Dimensionless Sips model parameter	[dless]
M	Molar mass	$[\mathrm{g \cdot mol^{-1}}]$
p	Pressure	[atm] (1atm =101325 Pa)
P'	Permeance	$[\mathrm{mol \cdot m^2 \cdot s^{-1} Pa^{-1}}]$

q	Adsorption capacity	[mmol·g^{-1} of adsorbent]
$q(t)$	Amount absorbed at time t	[mmol·g^{-1} of adsorbent]
q_e	Adsorption capacity at equilibrium	[mmol·g^{-1} of adsorbent]
q^{sat}	Adsorption capacity at saturation	[mmol·g^{-1} of adsorbent]
R	Universal gas constant	[m^3·Pa·K^{-1}·mol^{-1}]
R_c	Radius of crystal	[m]
t	Time	[s]
T	Temperature	[K]
X	Membrane thickness	[μm]

Greek Symbols

$\alpha_{A/B}$	Permselectivity	[dless]
$\alpha^*_{A/B}$	Ideal selectivity	[dless]
β	Adsorption affinity constant	[atm^{-1}] (1atm =101325 Pa)
ε	Porosity of the silicalite in the membrane	[dless]
θ_i	Adsorption surface coverage of component I	[dless]
ρ	Skeletal density of the adsorbent	[g·cm^{-3}]
τ	Tortuosity factor	[dless]

Abbreviations

BET	Brunauer-Emmett-Teller
BJH	Barrett-Joyner-Halenda
EDS	Energy dispersive spectroscopy

GC	Gas chromatograph
LDF	Linear driving force model
MEA	Monoethanolamine
MFC	Mass flow controller
MFI	Mordenite Framework Inverted
PTFE	Polytetrafluoroethylene
SEM	Scanning electron microscopy
TCD	Thermal conductivity detector
TPAOH	Tetrapropylammonium hydroxide
XRD	X-ray diffraction spectroscopy

3.6.0 ACKNOWLEDGEMENTS

The authors gratefully acknowledge financial support received from the Natural Sciences and Engineering Research Council of Canada (NSERC) and Natural Resources Canada (NRCan).

3.7.0 REFERENCES

[1] D. Aaron, C. Tsouris, Separation of CO_2 from flue gas: a review, Sep. Sci. Technol. 40 (2005) 321–348.

[2] J.P. Ciferno, T.E. Fout, A.P. Jones, J.T. Murphy, Capturing Carbon from Existing Coal-Fired Power Plants, Chem. Eng. Prog. 105 (2009) 33–41.

[3] S.D. Kenarsari, D. Yang, G. Jiang, S. Zhang, J. Wang, A.G. Russell, Q. Wei, M. Fan, Review of recent advances in carbon dioxide separation and capture, RSC Adv. 3 (2013) 22739. doi:10.1039/c3ra43965h.

[4] M.T. Ho, G.W. Allinson, D.E. Wiley, Reducing the Cost of CO$_2$ Capture from Flue Gases Using Pressure Swing Adsorption, Ind. Eng. Chem. Res. 47 (2008) 4883–4890. doi:10.1021/ie070831e.

[5] P. Xiao, J. Zhang, P. Webley, G. Li, R. Singh, R. Todd, Capture of CO$_2$ from flue gas streams with zeolite 13X by vacuum-pressure swing adsorption, Adsorption. 14 (2008) 575–582. doi:10.1007/s10450-008-9128-7.

[6] A.D. Ebner, J.A. Ritter, State-of-the-art Adsorption and Membrane Separation Processes for Carbon Dioxide Production from Carbon Dioxide Emitting Industries, Sep. Sci. Technol. 44 (2009) 1273–1421. doi:10.1080/01496390902733314.

[7] E.S. Kikkinides, R.T. Yang, S.H. Cho, Concentration and recovery of carbon dioxide from flue gas by pressure swing adsorption, Ind. Eng. Chem. Res. 32 (1993) 2714–2720. doi:10.1021/ie00023a038.

[8] A. Nuchitprasittichai, S. Cremaschi, Sensitivity of amine-based CO$_2$ capture cost: the influences of CO$_2$ concentration in flue gas and utility cost fluctuations, Int. J. Greenh. Gas Control. 13 (2013) 34–43.

[9] E. Gjernes, L.I. Helgesen, Y. Maree, Health and environmental impact of amine based post combustion CO$_2$ capture, Energy Procedia. 37 (2013) 735–742. doi:10.1016/j.egypro.2013.05.162.

[10] B. Thitakamol, A. Veawab, A. Aroonwilas, Environmental impacts of absorption-based CO$_2$ capture unit for post-combustion treatment of flue gas from coal-fired power plant, Int. J. Greenh. Gas Control. 1 (2007) 318–342. doi:10.1016/S1750-5836(07)00042-4.

[11] S.M. Auerbach, K.A. Carrado, P.K. Dutta, Handbook of Zeolite Science and Technology, CRC Press, New York, 2003.

[12] M.A. Aroon, A.F. Ismail, Performance studies of mixed matrix membranes for gas separation : A review, Sep. Purif. Technol. 75 (2010) 229–242. doi:10.1016/j.seppur.2010.08.023.

[13] B. Soydaş, A. Çulfaz, H. Kalıpçılar, Characterization of zeolite membranes by gas permeation, Desalination. 199 (2006) 371–372. doi:10.1016/j.desal.2006.03.084.

[14] Z.A.E.. Vroon, K. Keizer, A.. Burggraaf, H. Verweij, Preparation and characterization of thin zeolite MFI membranes on porous supports, J. Memb. Sci. 144 (1998) 65–76. doi:10.1016/S0376-7388(98)00035-0.

[15] M. Tawalbeh, F.H. Tezel, B. Kruczek, S. Letaief, C. Detellier, Synthesis and characterization of silicalite-1 membrane prepared on a novel support by the pore plugging method, J. Porous Mater. 20 (2013) 1407–1421. doi:10.1007/s10934-013-9726-y.

[16] S. Miachon, E. Landrivon, M. Aouine, Y. Sun, I. Kumakiri, Y. Li, O.P. Prokopová, N. Guilhaume, a. Giroir-Fendler, H. Mozzanega, J. a. Dalmon, Nanocomposite MFI-alumina membranes via pore-plugging synthesis. Preparation and morphological characterisation, J. Memb. Sci. 281 (2006) 228–238. doi:10.1016/j.memsci.2006.03.036.

[17] Y. Li, M. Pera-titus, G. Xiong, W. Yang, E. Landrivon, S. Miachon, J. Dalmon, Nanocomposite MFI-alumina membranes via pore-plugging synthesis: Genesis of the zeolite material, 325 (2008) 973–981. doi:10.1016/j.memsci.2008.09.030.

[18] X. Zhang, H. Liu, K.L. Yeung, Influence of seed size on the formation and microstructure of zeolite silicalite-1 membranes by seeded growth, Mater. Chem. Phys. 96 (2006) 42–50. doi:10.1016/j.matchemphys.2005.06.031.

[19] J. Caro, M. Noack, P. Kölsch, R. Schäfer, Zeolite membranes – state of their development and perspective, Microporous Mesoporous Mater. 38 (2000) 3–24. doi:10.1016/S1387-1811(99)00295-4.

[20] D.W. Breck, Zeolite molecular sieves: structure, chemistry, and use, R.E. Krieger, 1984.

[21] D.D. Do, Adsorption Analysis: Equilibria and Kinetics Vol. 2, Imperial College Press, 1998.

[22] D. Ruthven, Principles of adsorption and adsorption processes, John Wiley and Sons, 1984.

[23] P.S. Yaremov, N.D. Scherban, V.G. Ilyin, Adsorption of nitrogen, hydrogen, methane, and carbon oxides on micro- and mesoporous molecular sieves of different nature, Theor. Exp. Chem. 48 (2013) 394–400. doi:10.1007/s11237-013-9287-9.

[24] P. Li, F.H. Tezel, Pure and binary adsorption equilibria of carbon dioxide and nitrogen on silicalite, J. Chem. Eng. Data. 53 (2008) 2479–2487. doi:10.1021/je700183y.

[25] P. Li, F.H. Tezel, Pure and Binary Adsorption of Methane and Nitrogen by Silicalite, J. Chem. Eng. Data. 54 (2009) 8–15. doi:10.1021/je7005902.

[26] D. Kennedy, F. Handan Tezel, Improved method for determining binary adsorption isotherms by using concentration pulse chromatography: Adsorption of CO_2 and N_2 by silicalite at different pressures, Adsorption. 20 (2014) 189–199. doi:10.1007/s10450-013-9562-z.

[27] S. Sircar, Basic Research Needs for Design of Adsorptive Gas Separation Processes, Ind. Eng. Chem. Res. 45 (2006) 5435–5448. doi:10.1021/ie051056a.

[28] A.D. Buckingham, P.G. Hibbard, Polarizability and Hyperpolarizability of the Helium Atom, Symp. Faraday Soc. 2 (1968) 41–47.

[29] P. Rallapalli, K.P. Prasanth, D. Patil, R.S. Somani, R. V. Jasra, H.C. Bajaj, Sorption studies of CO_2, CH_4, N_2, CO, O_2 and Ar on nanoporous aluminum terephthalate [MIL-53(Al)], J. Porous Mater. 18 (2011) 205–210. doi:10.1007/s10934-010-9371-7.

[30] M. Tawalbeh, F.H. Tezel, S. Letaief, C. Detellier, B. Kruczek, Separation of CO_2 and N_2 on zeolite silicalate-1 membrane synthesized on novel support, Sep. Sci. Technol. 47 (2012) 1606–1616.

[31] D. Carter, D. Kennedy, F.H. Tezel, B. Kruczek, Characterization of inorganic silicalite-1 membrane to be used for the separation of greenhouse gases, J. Fluid Flow, Heat Mass Transf. 1 (2014) 43–47.

[32] M. Pan, Y.S. Lin, Template-free secondary growth synthesis of MFI type zeolite membranes, Microporous Mesoporous Mater. 43 (2001) 319–327. doi:10.1016/S1387-1811(01)00212-8.

[33] E.P. Barrett, L.G. Joyner, P.P. Halenda, The determination of pore volume and area distributions in porous substances. I. computations from nitrogen isotherms, J. Am. Chem. Soc. 73 (1951) 373–380. doi:10.1021/ja01145a126.

[34] S. Storck, H. Bretinger, W.F. Maier, Characterization of micro- and mesoporous solids by physisorption methods and pore-size analysis, Appl. Catal. A Gen. 174 (1998) 137–146. doi:10.1016/S0926-860X(98)00164-1.

[35] J.-H. Moon, Y.-S. Bae, S.-H. Hyun, C.-H. Lee, Equilibrium and kinetic characteristics of five single gases in a methyltriethoxysilane-templating silica/α-alumina composite membrane, J. Memb. Sci. 285 (2006) 343–352. doi:10.1016/j.memsci.2006.09.003.

[36] A.J. Burggraaf, Transport and separation properties of membranes with gases and vapours, in: Membr. Sci. Technol., 1996: pp. 331–433. doi:10.1016/S0927-5193(96)80012-X.

[37] A.J. Burggraaf, L. Cot, Fundamentals of inorganic membrane science and technology, Elsevier, 1996.

[38] D.M. Ruthven, Diffusion through porous media: Ultrafiltration, Membrane Permeation and Molecular Sieving, Diffusion-Fundamentals.Org. 11 (2009) 1–20.

[39] L.J.P. van den Broeke, W.J.W. Bakker, F. Kapteijn, J.A. Moulijn, Transport and separation properties of a silicalite-1 membrane—I. Operating conditions, Chem. Eng. Sci. 54 (1999) 245–258. doi:10.1016/S0009-2509(98)00241-3.

[40] P.H. Nelson, S.M. Auerbach, Self-diffusion in single-file zeolite membranes is Fickian at long times, J. Chem. Phys. 110 (1999) 9235. doi:10.1063/1.478847.

[41] W. Zhu, P. Hrabanek, L. Gora, F. Kapteijn, J.A. Moulijn, Role of Adsorption in the Permeation of CH_4 and CO_2 through a Silicalite-1 Membrane, Ind. Eng. Chem. Res. 45 (2006) 767–776. doi:10.1021/ie0507427.

[42] J.M. Van De Graaf, F. Kapteijn, J.A. Moulijn, Permeation of weakly adsorbing components through a silicalite-1 membrane, Chem. Eng. Sci. 54 (1999) 1080–1092. doi:10.1016/S0009-2509(98)00326-1.

[43] R.S.A. de Lange, K. Keizer, A.J. Burggraaf, Analysis and theory of gas transport in microporous sol-gel derived ceramic membranes, J. Memb. Sci. 104 (1995) 81–100. doi:10.1016/0376-7388(95)00014-4.

[44] F. Kapteijn, J.M. van de Graaf, J.A. Moulijn, One-component permeation maximum: Diagnostic tool for silicalite-1 membranes?, AIChE J. 46 (2000) 1096–1100. doi:10.1002/aic.690460521.

[45] E. Glueckauf, Theory of chromatography, part 10. Formulae for diffusion into spheres and their application to chromatography, Trans. Faraday Soc. 51 (1955) 1540. doi:10.1039/tf9555101540.

[46] E. Glueckauf, J.I. Coates, Theory of chromatography, part IV. The influence of incomplete equilibrium on the front boundary of chromatograms and on the effectiveness of separation, J. Chem. Soc. (1947) 1315. doi:10.1039/jr9470001315.

[47] S. Sircar, J.R. Hufton, Why Does the Linear Driving Force Model for Adsorption Kinetics Work?, Adsorption. 6 (n.d.) 137–147. doi:10.1023/A:1008965317983.

[48] R. Yang, Gas Separation by Adsorption Processes, Butterworth Publishers, Toronto, 1987.

[49] C.R. Reid, K.M. Thomas, Adsorption of gases on a carbon molecular sieve used for air separation: Linear adsorptives as probes for kinetic selectivity, Langmuir. 15 (1999) 3206–3218.

[50] L. Rouleau, G. Pirngruber, F. Guillou, C. Barrère-Tricca, A. Omegna, V. Valtchev, M. Pera-Titus, S. Miachon, J.A. Dalmon, Nanocomposite MFI-alumina and FAU-alumina Membranes: Synthesis, Characterization and Application to Paraffin Separation and CO_2 Capture, Oil Gas Sci. Technol. - Rev. l'IFP. 64 (2009) 745–758. doi:10.2516/ogst/2009036.

[51] M.R. Othman, S.C. Tan, S. Bhatia, Separability of carbon dioxide from methane using MFI zeolite–silica film deposited on gamma-alumina support, Microporous Mesoporous Mater. 121 (2009) 138–144. doi:10.1016/j.micromeso.2009.01.019.

[52] G. Reding, T. Mäurer, B. Kraushaar-Czarnetzki, Comparing synthesis routes to nano-crystalline zeolite ZSM-5, Microporous Mesoporous Mater. 57 (2003) 83–92. doi:10.1016/S1387-1811(02)00558-9.

[53] L. Tosheva, B. Mihailova, V. Valtchev, J. Sterte, Silicalite-1 macrostructures – preparation and structural features, Microporous Mesoporous Mater. 39 (2000) 91–101. doi:10.1016/S1387-1811(00)00179-7.

[54] J. Hua, Y. Han, One-step preparation of zeolite silicalite-1 microspheres with adjustable macroporosity, Chem. Mater. 21 (2009) 2344–2348. doi:10.1021/cm803366k.

[55] S.P. Naik, A.S.T. Chiang, R.W. Thompson, F.C. Huang, Formation of silicalite-1 hollow spheres by the self-assembly of nanocrystals, Chem. Mater. 15 (2003) 787–792. doi:10.1021/cm020786v.

[56] H. Zhou, J. Mouzon, A. Farzaneh, O.N. Antzutkin, M. Grahn, J. Hedlund, Colloidal defect-free silicalite-1 single crystals: preparation, structure characterization, adsorption, and separation properties for alcohol/water mixtures, (n.d.). doi:10.1021/acs.langmuir.5b02520.

[57] Z.A.E.P. Vroon, K. Keizer, M.J. Gilde, H. Verweij, A.J. Burggraaf, Transport properties of alkanes through ceramic thin zeolite MFI membranes, J. Memb. Sci. 113 (1996) 293–300. doi:10.1016/0376-7388(95)00128-X.

[58] E.R. Geus, M.J. Den Exter, H. Van Bekkum, Synthesis and characterization of zeolite (MFI) membranes on porous ceramic supports, J. Chem. Soc. Faraday Trans. 88 (1992) 3101–3109. doi:10.1039/FT9928803101.

[59] G.E. Romanos, T.A. Steriotis, E.S. Kikkinides, N.K. Kanellopoulos, V. Kasselouri, J.D.F. Ramsay, P. Langois, S. Kallus, Innovative methods for preparation and testing of Al2O3 supported silicalite-1 membranes, J. Eur. Ceram. Soc. 21 (n.d.) 119–126.

[60] R. Babarao, J. Jiang, Diffusion and Separation of CO_2 and CH_4 in Silicalite, C_{168} Schwarzite, and IRMOF-1: A Comparative Study from Molecular Dynamics Simulation, Langmuir. 24 (2008) 5474–5484. doi:10.1021/la703434s.

[61] W.J.W. Bakker, L.J.P. Van Den Broeke, F. Kapteijn, J. a Moulijn, Temperature Dependence of One-Component Permeation through a Silicalite-1 Membrane, AICHe J. 43 (1997) 2203–2214. doi:10.1002/aic.690430907.

[62] M.-B. Hagg, L. Deng, Membranes in Gas Separation, in: A. Pabby, S. Rizvi, A.M. Sastre (Eds.), Handb. Membr. Sep. Chem. Pharm. Food, Biotechnol. Appl., Second, CRC Press, 2015.

[63] L. Liu, Gas separation by poly(ether block amide) membranes, University of Waterloo, 2008.

[64] Z.W. and, Y. Yan*, Controlling Crystal Orientation in Zeolite MFI Thin Films by Direct In Situ Crystallization, (2001). doi:10.1021/CM000849E.

[65] M.E. Welk, T.M. Nenoff, F. Bonhomme, Defect-free zeolite thin film membranes for H_2 purification and CO_2 separation, Stud. Surf. Sci. Catal. 154 (2004) 690–694. doi:10.1016/S0167-2991(04)80871-1.

[66] J. Hedlund, J. Sterte, M. Anthonis, A. Bons, B. Carstensen, N. Corcoran, D. Cox, H. Deckman, W. De Gijnst, P. De Moor, F. Lai, J. Mchenry, High-flux MFI membranes, 52 (2002) 179–189.

[67] M.D. Jia, B. Chen, R.D. Noble, J.L. Falconer, Ceramic-zeolite composite membranes and their application for separation of vapor/gas mixtures, J. Memb. Sci. 90 (1994) 1–10. doi:10.1016/0376-7388(94)80029-4.

[68] M.G. Hernández, E. Salinas-Rodríguez, S.A. Gómez, J.A.E. Roa-Neri, S. Alfaro, F.J. Valdés-Parada, Helium permeation through a silicalite-1 tubular membrane, Heat Mass Transf. 51 (2015) 847–857. doi:10.1007/s00231-014-1460-8.

[69] Y. Takata, T. Tsuru, T. Yoshioka, M. Asaeda, Gas permeation properties of MFI zeolite membranes prepared by the secondary growth of colloidal silicalite and application to the methylation of toluene, Microporous Mesoporous Mater. 54 (2002) 257–268. doi:10.1016/S1387-1811(02)00386-4.

[70] S. Gopalakrishnan, T. Yamaguchi, S. Nakao, Permeation properties of templated and template-free ZSM-5 membranes, J. Memb. Sci. 274 (2006) 102–107. doi:10.1016/j.memsci.2005.08.005.

[71] B. Soydaş, A. Çulfaz, H. Kalipçilar, Effect of soda concentration on the morphology of MFI-Type zeolite membranes, Chem. Eng. Commun. 196 (2008) 182–193.

[72] C. Algieri, P. Bernardo, G. Golemme, G. Barbieri, E. Drioli, Permeation properties of a thin silicalite-1 (MFI) membrane, J. Memb. Sci. 222 (2003) 181–190. doi:10.1016/S0376-7388(03)00286-2.

[73] W.J.W. Bakker, F. Kapteijn, J. Poppe, J.A. Moulijn, Permeation characteristics of a metal-supported silicalite-1 zeolite membrane, J. Memb. Sci. 117 (1996) 57–78. doi:https://doi.org/10.1016/0376-7388(96)00035-X.

[74] A. J. Burggraaf, Z. A E.P. Vroon, K. Keizer, H. Verweij, Permeation of single gases in thin zeolite MFI membranes, J. Memb. Sci. 144 (1998) 77–86. doi:10.1016/S0376-7388(98)00036-2.

[75] L. Sandström, E. Sjöberg, J. Hedlund, Very high flux MFI membrane for CO_2 separation, J. Memb. Sci. 380 (2011) 232–240. doi:10.1016/j.memsci.2011.07.011.

[76] L.M. Robeson, The upper bound revisited, 320 (2008) 390–400. doi:10.1016/j.memsci.2008.04.030.

[77] K.T. Chue, J.N. Kim, Y.J. Yoo, S.H. Cho, R.T. Yang, Comparison of Activated Carbon and Zeolite 13X for CO_2 Recovery from Flue Gas by Pressure Swing Adsorption, Ind. Eng. Chem. Res. 34 (1995) 591–598. doi:10.1021/ie00041a020.

[78] D.H. Olson, G.T. Kokotailo, S.L. Lawton, W.M. Meier, Crystal structure and structure-related properties of ZSM-5, J. Phys. Chem. 85 (1981) 2238–2243. doi:10.1021/j150615a020.

Chapter 4

This chapter is based on:

Equilibrium Isotherms and Transport Diffusivities for CO_2 and CO_2/N_2 Mixtures in Silicalite measured by Infra-Red Micro-imaging

D. Carter[a], F.H. Tezel[a], B. Kruczek[a], J. Kärger[b], D. Ruthven[c], R. Marthala[d], C. Chmelik[b*]

[a]University of Ottawa, Department of Chemical and Biological Engineering
161 Louis Pasteur, Ottawa, Ontario, Canada K1N 6N5
[b]University of Leipzig, Department of Interface Physics
Linnestrasse 5, Leipzig, Germany, 04103
[c]University of Maine, Department of Chemical and Biological Engineering
Jenness Hall, Orono, Maine, USA, 04469
[d]Friedrich-Alexander University, Erlangen Catalysis Resource Centre
Egerlandstrasse 3, Erlangen, Germany, 91058
*Corresponding author

To be submitted to: ***The Journal of Microporous and Mesoporous Materials***

ABSTRACT

Large crystals of silicalite (0.1 - 1 mm) were synthesized and used to study the kinetics and equilibrium of CO_2 adsorption (at room temperature), both as a pure component and as a binary mixture with nitrogen, using Infra-Red Microscopy (IRM) coupled with Fourier Transform Infra-Red (FTIR) Spectroscopy. The use of such large crystals permits the measurement of fast intra-crystalline diffusion processes, beyond the range normally accessible by macroscopic techniques. As expected, the effect of N_2 on the CO_2 equilibrium was minimal but the effect on the intra-crystalline diffusivity was significant. Diffusivities (at 300 K) range from 4×10^{-9} to 4×10^{-8} $m^2 \cdot s^{-1}$ for CO_2, decreasing with increasing total concentrations of CO_2 and N_2 in the adsorbed phase.

Chapter 4 – Equilibrium Isotherms and Transport Diffusivities for CO_2 and CO_2/N_2 Mixtures in Silicalite measured by Infra-Red Micro-imaging

Keywords: Silicalite, adsorption kinetics, binary adsorption isotherms, carbon dioxide adsorption, adsorption equilibrium.

HIGHLIGHTS

- Silicalite crystals with side lengths from several 100 μm up to 1 mm were synthesized.
- Adsorption and diffusion characteristics of CO_2 in mixtures with N_2 were measured.
- The diffusion of CO_2 in silicalite was slowed down in the presence of N_2.

4.1.0 INTRODUCTION

This paper reports the results of an experimental study of adsorption and diffusion of CO_2 in large silicalite crystals, both as a single component and in the presence of N_2. This system is of practical interest since silicalite is one of only a few hydrophobic CO_2 selective adsorbents, making it potentially useful for the capture of CO_2 from humid stack gas. This study was carried out at room temperature using infra-red microscopy (IRM) and Fourier transform infra-red (FTIR) microscopy to follow the uptake of CO_2 in large single crystals of silicalite, thus avoiding any intrusion of both inter-particle diffusion and heat transfer resistances on the kinetics.

4.2.0 EXPERIMENTAL

The large silicalite crystals were synthesized by Reddy Marthala (FAU Erlangen) and David Carter (U.Ottawa / U. Leipzig) according to the procedure described by Kida et al [1]. The largest and most regularly shaped crystal from each of these synthesis batches (designated respectively as MFI-1 and MFI-2) was used for the present study.

The schematic diagram of the apparatus used for the uptake rate measurements via IR microscopy (IRM, see ref [2]) is shown in Fig. 4.1. Gas mixtures of pre-set composition were prepared by mixing the pure components in the stainless steel reservoirs and then delivered at a pre-set pressure to the sample cell of the IRM, thus exposing the pre-conditioned crystal to a well defined step change in CO_2 pressure. The transient uptake curve and the final equilibrium loading were then determined from the intensity of the IR absorbance over the frequency range 3550 – 3740 cm^{-1}. The calibration procedure for this method has been described elsewhere [3]. The equilibrium isotherms were determined from the end points of the uptake curves and diffusivities were determined by matching the uptake curve to the appropriate solution of the transient diffusion equation for a system with a constant diffusivity.

The images of crystals taken using the IRM in optical mode are shown in Fig. 4.2.

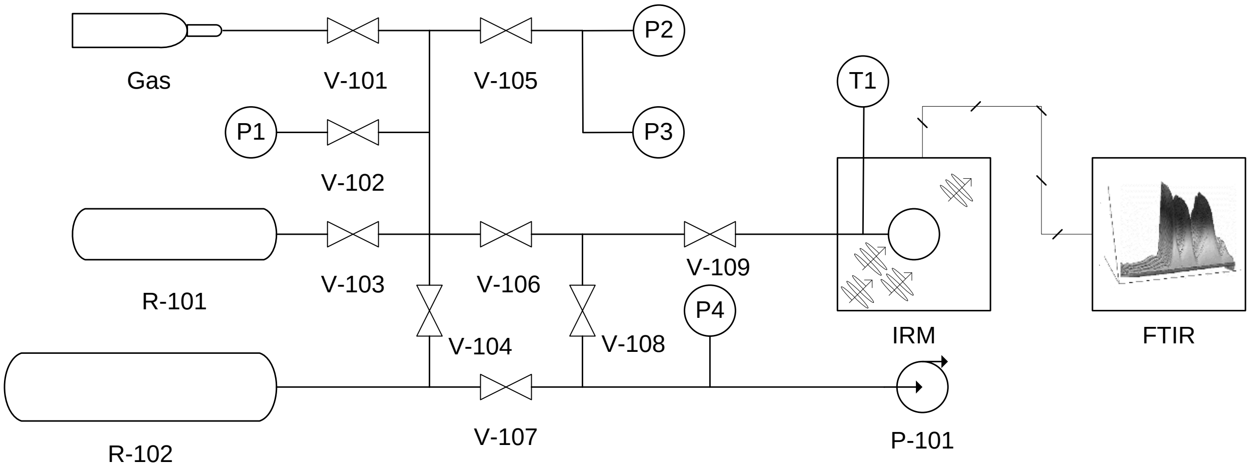

Figure 4.1. Schematic diagram showing the experimental setup used for uptake rate measurements. The sample cell containing a single silicalite crystal is located on the stage of the IRM, and the absorbance of IR light by the sample is analyzed by the FTIR. P1 – P4 are pressure transducers with different operating ranges, and T1 is a thermocouple. V-101 – V-109 are gate valves. R-101 and R-102 are stainless steel reservoirs and P-101 is the vacuum pump. Regeneration furnace is not shown.

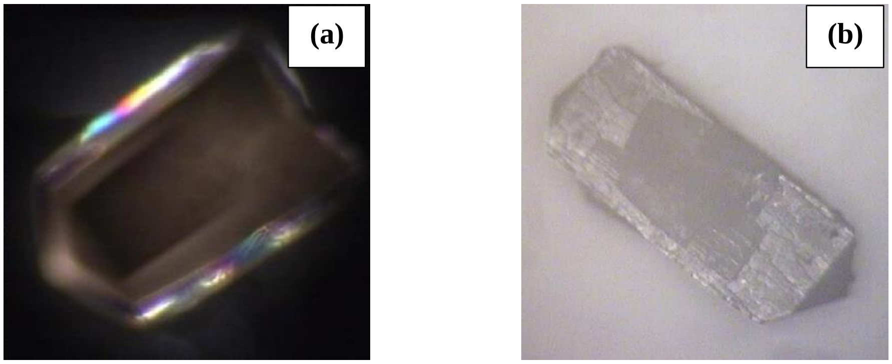

Figure 4.2. Images of rectangular parallelepiped crystals of (a) MFI-1 and (b) MFI-2 taken using the IRM in optical mode. MFI-1 has average *x*, *y*, and *z* dimensions of 493 µm, 445 µm, and 910 µm respectively. MFI-2 has average *x*, *y*, and *z* dimensions of 510 µm, 490 µm, and 1200 µm respectively.

4.3.0 RESULTS AND DISCUSSION

4.3.1 Adsorption Isotherms

The adsorption isotherms for CO_2 are shown in Fig. 4.3 for different compositions in the gas phase. The Henry constants K (mol·kg^{-1}·kPa^{-1}) derived from the initial slopes are summarized in Table 4.1. The single component CO_2 isotherms and the binary CO_2 –N_2 isotherms are similar to those previously determined by gravimetric, volumetric, piezometric and chromatographic methods [4–9].

It is evident that the isotherms for both samples (MFI-1 and MFI-2) are very similar and the presence of nitrogen has only a very minor effect on the CO_2 isotherm. This is confirmed by the Henry constants (derived from the initial slopes) which are summarized in Table 4.1. The minimal effect of N_2 on the CO_2 isotherms is to be expected since nitrogen is adsorbed much less strongly than CO_2 – see Supplementary Material 4.7.1. This was also observed by others in the literature [9].

Table 4.1. Summary of Henry Constants ($mol{\cdot}kg^{-1}{\cdot}Pa^{-1}$) for CO_2 in Silicalite at 300 - 305 K.

Mole Fr. CO_2	MFI-1	MFI-2
0.15	2.47×10^5	1.77×10^5
0.3	1.85×10^5	1.61×10^5
0.5	1.64×10^5	1.55×10^5
0.7	1.54×10^5	1.55×10^5
0.85	1.52×10^5	1.48×10^5
1.0	1.60×10^5	1.45×10^5
Graham and Hughes [8] (Pure CO_2)	3.1×10^5	
Rees, et al. [7]	2.5×10^5	
Vidoni [10] (Pure CO_2)	3.4×10^5	
Vidoni [10] Theoretical (DFT)	2.63×10^5	

Also included in Table 4.1 are the Henry constants for CO_2 predicted from density functional theory (DFT) for an ideal silicalite structure as well as the values measured experimentally in several studies using polycrystalline samples of small silicalite crystals (≈ 10 μm) [10]. Vidoni's measurements were carried out with three different samples with different hydroxyl contents. The CO_2 isotherms for the three samples showed significant differences in the saturation loading but the Henry constants were essentially the same and close to the theoretical value. The Henry constants for the present samples are somewhat smaller but show no obvious trend with N_2 pressure. The isosteric heats for Vidoni's three samples are all very similar (≈ 24.5 $kJ{\cdot}mol^{-1}$) and essentially independent of loading (at least up to 1.5 $mol{\cdot}kg^{-1}$). Graham and Hughes's data, determined from experimentally measured isosteres, show similar trends but with a slightly smaller value for the isosteric heat (23 $kJ{\cdot}mol^{-1}$) [8]. They also measured isotherms for nitrogen and for CO_2 – N_2 mixtures on the same silicalite sample and showed that the mixture isotherms conform to the ideal adsorbed solution theory (IAST).

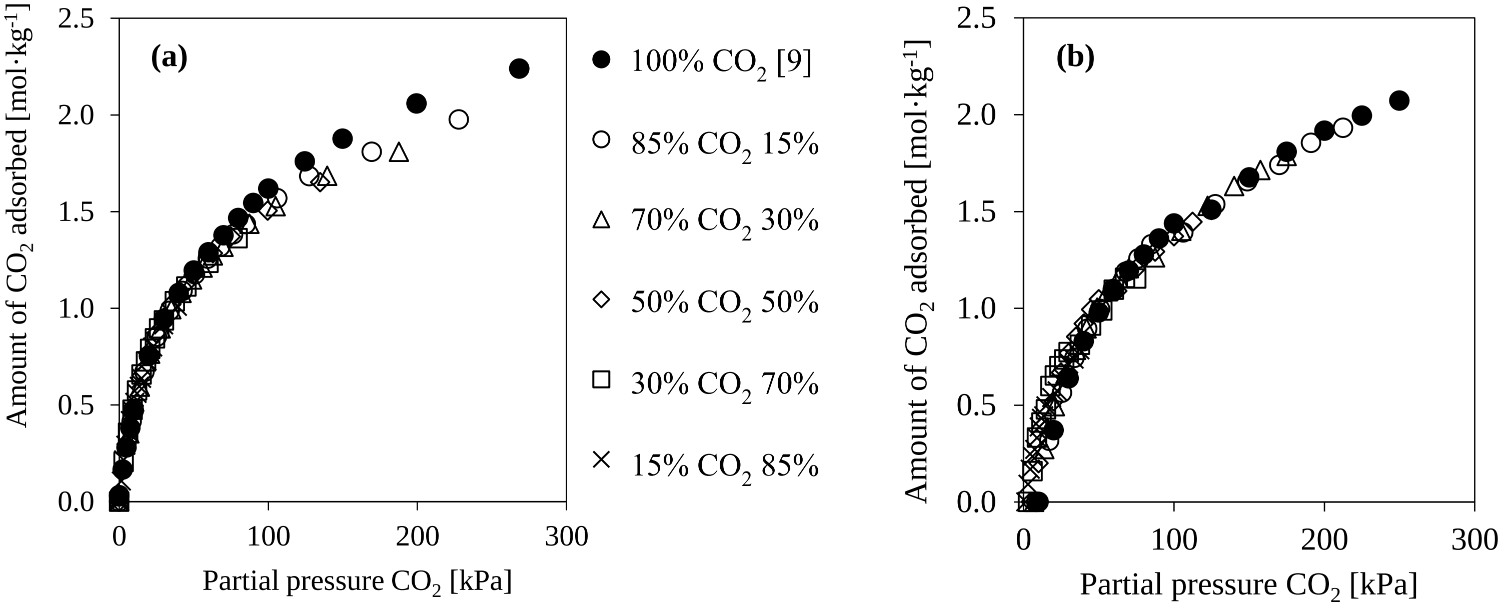

Figure 4.3. Equilibrium isotherms for CO_2 on (a) MFI-1 and (b) MFI-2 at different gas mixture compositions for CO_2 and N_2. Experiments were conducted at a temperature of at 299 ± 2 K for MFI-1, and 305 ± 2 K for MFI-2. Total pressures were between 0 and 270 kPa.

4.3.2 Transport Diffusivities

It is well established from previous studies that diffusion in the longitudinal direction (*z*) is much slower than in the transverse directions (*x*,*y*) [11]. Considering the dimensions of the crystals it is therefore logical to assume that the uptake rate is controlled by diffusion in the *x* and *y* directions (perpendicular to the long axis of the crystal). The transport diffusivity D_T ($m^2 \cdot s^{-1}$) was therefore determined by matching the uptake curve to the solution of the transient diffusion equation for an infinite rectangular parallelepiped [12]:

$$\frac{M_t}{M_\infty} = 1 - \frac{64}{\pi^4} \sum_{r=1}^{\infty} \sum_{s=1}^{\infty} \frac{\exp\left\{ -\frac{\pi D_T t}{4} \left[\frac{1}{a_x^2} (2r-1)^2 + \frac{1}{a_y^2} (2s-1)^2 \right] \right\}}{(2r-1)^2 (2s-1)^2} \tag{1}$$

where M_t/M_∞ is the fractional uptake at time *t* (s), and a_x (m) and a_y (m) are half thicknesses of the crystal in the *x* and *y* directions, respectively.

The resulting diffusivities are shown in Fig. 4.4. Since the data show that the diffusivity decreases with increasing concentration of both CO_2 and N_2, we have plotted the diffusivity as a function of total concentration (CO_2 + N_2) in the adsorbed phase. The CO_2 concentration in the adsorbed phase was measured directly but the N_2 concentration at each point was estimated from the Extended Langmuir model as shown in Supplementary Material 4.7.1, assuming the ratio of Henry constants given by Rees et al. [7], as specified in the figures. It appears that the retarding effect of N_2 is stronger than that of CO_2 and the magnitude of this effect appears to be too large to be explained by errors in the estimation of the nitrogen concentration. The trends are similar for the two samples but the diffusivities for MFI-2 are approximately double those for MFI-1.

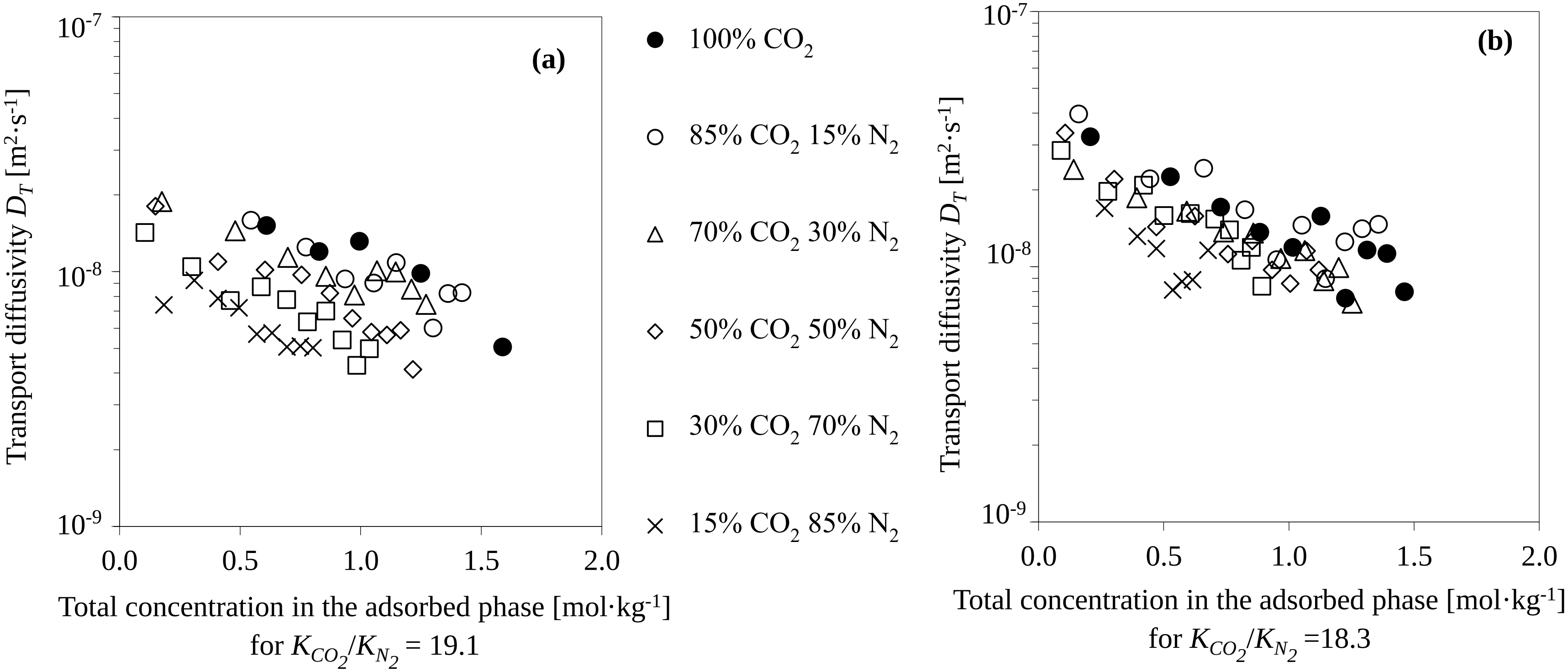

Figure 4.4. Transport diffusivities for CO_2 as a function of total concentration in the adsorbed phase for (a) MFI-1 and of (b) MFI-2. Experiments were conducted at total pressures between 0 and 100 kPa using a range of mixture compositions. CO_2 concentrations are the average amounts of CO_2 adsorbed between the initial and final uptake conditions. The temperature was 299 ± 2 K for MFI-1 (a_x = 246 µm, a_y = 222 µm) and 305 ± 2 K for MFI-2 (a_x = 245 µm, a_y = 255 µm).

The diffusivities ($\approx 10^{-8}\,m^2{\cdot}s^{-1}$) are similar to the values derived by Babarao and Jiang [13] from Molecular Dynamic (MD) simulations and slightly larger than the self-diffusivities reported previously for small molecules in silicalite [11]. The variation with loading is similar to that observed previously for self-diffusivites – see for example Caro et al. [14]. Transport diffusivities at room temperature for CO_2 and N_2 in silicalite at low loadings (1 - 2 molecules per unit cell) have been measured by Papadopoulos et al. using the coherent Quasi Elastic Neutron Scattering (QENS) technique [15]. Their values (0.9 x 10^{-8} and 0.5 x 10^{-8} $m^2{\cdot}s^{-1}$ respectively, for N_2 and CO_2) are about half the values obtained in this study. Self-diffusivities for CO_2 in HZSM-5 at low loading, measured by Kärger et al. [16] by PFG NMR, are even smaller (2.2 x 10^{-9} $m^2{\cdot}s^{-1}$). This difference is probably attributable to the difference between silicalite and ZSM-5. The presence of small amounts of Al in ZSM-5 has been shown to retard diffusion significantly [17].

Large crystals of silicalite have a complex twin-structure – see Fig. 4.5 [18]. The agreement between the present transport diffusivities and the values determined by other techniques, notably coherent QENS which measures over a length scale of a few unit cells, strongly suggests that the transport process in these large crystals does indeed reflect diffusion within the intra-crystalline pores. However, the difference in diffusivities between the two crystals is significant and this suggests that there may be some contribution from rapid transport along the twin planes (which would reduce the effective crystal size thereby increasing the apparent diffusivity).

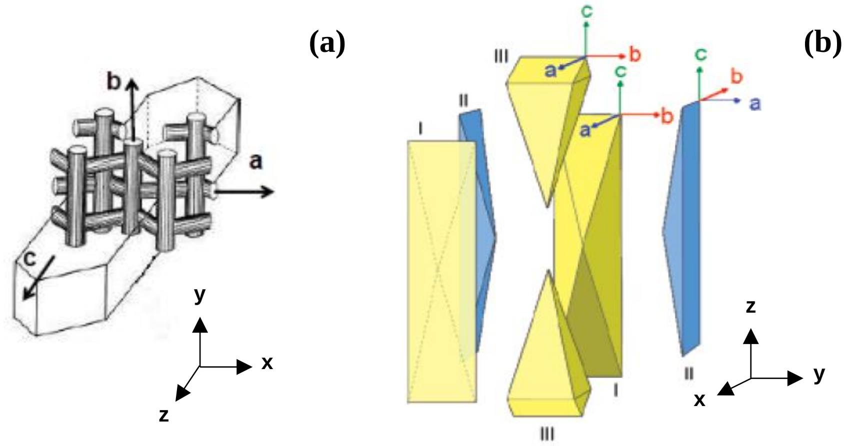

Figure 4.5. Representations of the channel directions a, b, and c that are present in an un-twinned coffin shaped MFI crystal [18]. (a), and a twinned MFI crystal which is made up of three segment types labelled I, II and III (b).

4.4.0 CONCLUSIONS

The equilibrium data obtained from the IR measurements confirm that, except at high loadings (> 1.5 $mol \cdot kg^{-1}$), competitive adsorption of N_2 has only a minor effect on the CO_2 isotherms, in accordance with previous studies carried out by classical methods.

Transport diffusivities for CO_2 in these large silicalite crystals at room temperature are in the order of 10^{-8} $m^2 \cdot s^{-1}$ which is consistent with short range measurements by coherent QENS and MD simulations as well as with self-diffusivities measured by PFG NMR. This implies that the complex twin structure has only a minor effect on the transport rate.

The transport diffusivity decreases with loading of both CO_2 and N_2. We did not calculate thermodynamically corrected diffusivities, but as the correction factor increases with the loading of both components, one can say that the corrected diffusivity will decrease even more with increasing loading. The effect of N_2 in reducing the diffusivity of CO_2 appears to be stronger than that of CO_2 itself. That might suggest that N_2 molecules are preferentially located in the channels while the longer CO_2 molecules prefer the channel intersections. Of course, without more direct evidence, any such suggestion is highly speculative.

With respect to the possible application of silicalite in carbon capture, it appears that the competitive adsorption of N_2 is unlikely to be a serious issue. Under the relevant conditions the impact on the equilibrium is minor. Although the effect on the intra-crystalline transport diffusivity is significant, intra-crystalline diffusion is still very rapid and is unlikely to be rate limiting in small commercial crystals. The limited equilibrium capacity for CO_2 at the relevant partial pressures for post combustion flue gas applications is a more serious issue.

4.5.0 ACKNOWLEDGEMENTS

This research project was financially supported by German Science Foundation, the Natural Sciences and Engineering Research Council of Canada (NSERC), and the University of Ottawa Student Mobility program.

4.6.0 REFERENCES

[1] T. Kida, K. Kojima, H. Ohnishi, Synthesis of large silicalite-1 single crystals from two different silica sources, 30 (2004) 727–732. doi:10.1016/j.ceramint.2003.08.011.

[2] J. Kärger, T. Binder, C. Chmelik, F. Hibbe, H. Krautscheid, R. Krishna, J. Weitkamp, monitor mass transfer in nanoporous materials, Nat. Publ. Gr. 13 (2014) 333–343. doi:10.1038/nmat3917.

[3] D. Carter, F.H. Tezel, B. Kruczek, J. Karger, C. Chmelik, Determination of the adsorption isotherms and transport diffusivities of gases in mixtures inside zeolitic crystals using Infra-Red Micro-imaging., Submitted to MethodsX. (2019).

[4] P. Li, F.H. Tezel, Pure and binary adsorption of carbon dioxide and nitrogen on silicalite, J. Chem. Eng. Data. 53 (2008) 2479–2487. doi:10.1021/je7005902.

[5] J.A. Dunne, M. Rao, S. Sircar, R.J. Gorte, A.L. Myers, Calorimetric Heats of

Adsorption and Adsorption Isotherms 2. O_2, N_2, Ar, CO_2, CH_4, C_2H_6, and SF_6 on NaX, H-ZSM-5, and Na-ZSM-5 Zeolites, Langmuir. 12 (1996) 5896–5904. doi:10.1021/la960496r.

[6] M.S. Sun, D.B. Shah, H.H. Xu, O. Talu, Adsorption Equilibria of C_1 to C_4 Alkanes, CO_2, and SF_6 on Silicalite, J. Phys. Chem. B. 102 (1998) 1466–1473. doi:10.1021/jp9730196.

[7] L.V.C. Rees, P. Bruckner, J. Hampson, Sorption of N_2, CH_4 and CO_2 in Silicalite-1, Gas Sep. Purif. 5 (1991) 67–75. doi:10.1016/0950-4214(91)80003-N.

[8] P. Graham, A.D. Hughes, Sorption of binary gas mixtures in zeolites, 3 (1989) 56–64.

[9] D. Kennedy, F.H. Tezel, Improved method for determining binary adsorption isotherms by using concentration pulse chromatography: Adsorption of CO_2 and N_2 by silicalite at different pressures, Adsorption. 20 (2014) 189–199. doi:10.1007/s10450-013-9562-z.

[10] A. Vidoni, Adsorption and Diffusion of Light Hydrocarbons in DDR Zeolite, University of Maine, 2011.

[11] J. Kärger, D.M. Ruthven, D.N. Theodorou, Diffusion in Nanoporous Materials, John Wiley and Sons, 2012.

[12] J. Crank, The Mathematics of Diffusion, Oxford University Press, 1975.

[13] R. Babarao, J. Jiang, Diffusion and Separation of CO_2 and CH_4 in Silicalite, C_{168} Schwarzite, and IRMOF-1: A Comparative Study from Molecular Dynamics Simulation, Langmuir. 24 (2008) 5474–5484. doi:10.1021/la703434s.

[14] J. Caro, M. Bülow, W. Schirmer, J. Kärger, W. Heink, H. Pfeifer, S. Petrowitsch Ždanov, Microdynamics of methane, ethane and propane in ZSM-5 type zeolites, J. Chem. Soc. Faraday Trans. 81 (1985) 2541–2550. doi:10.1039/F19858102541.

[15] G.K. Papadopoulos, H. Jobic, D.N. Theodorou, Transport diffusivity of N_2 and CO_2 in silicalite: Coherent quasielastic neutron scattering measurements and molecular dynamics simulations, J. Phys. Chem. B. 108 (2004) 12748–12756. doi:10.1021/jp049265g.

[16] J. Kärger, H. Pfeifer, F. Stallmach, N.N. Feoktistova, S.P. Zhdanov, 129Xe and 13C PFG n.m.r. study of the intracrystalline self-diffusion of Xe, CO_2, and CO, Zeolites.

13 (1993) 50–55. doi:10.1016/0144-2449(93)90022-U.

[17] M. Noack, P. Kölsch, V. Seefeld, P. Toussaint, G. Georgi, J. Caro, Influence of the Si/Al-ratio on the permeation properties of MFI-membranes, Microporous Mesoporous Mater. 79 (2005) 329–337. doi:10.1016/j.micromeso.2005.01.004.

[18] L. Karwacki, M.H.F. Kox, D.A. Matthijs De Winter, M.R. Drury, J.D. Meeldijk, E. Stavitski, W. Schmidt, M. Mertens, P. Cubillas, N. John, A. Chan, N. Kahn, S.R. Bare, M. Anderson, J. Kornatowski, B.M. Weckhuysen, Morphology-dependent zeolite intergrowth structures leading to distinct internal and outer-surface molecular diffusion barriers, Nat. Mater. 8 (2009) 959–965. doi:10.1038/nmat2530.

4.7.0 SUPPLEMENTARY MATERIAL

4.7.1 Competitive Adsorption of Nitrogen

Graham and Hughes [8] have shown that the adsorption of CO_2 – N_2 mixtures on silicalite conforms to the Ideal Adsorption Solution Theory (IAST). Furthermore Vidoni [10] has shown that the equilibrium isotherms for CO_2 on an ideal crystal of silicalite conform closely to the Langmuir model, with a saturation capacity of 3.5 $\text{mol}\cdot\text{kg}^{-1}$. One may therefore assume that, at least at low fractional loadings, the equilibrium isotherms can be represented by the Langmuir model. This model is shown by equation S.1 for a pure gas system containing component *A*, and by equation S.2 for binary mixtures composed of components *A* and *B*.

$$\frac{q_A}{q_S} = \frac{b_A p_A}{1 + b_A p_A} \tag{S.1}$$

$$\frac{q'_A}{q_S} = \frac{b_A p_A}{1 + b_A p_A + b_B p_B} \tag{S.2}$$

Similar expressions can be written for component B. q_A ($\text{mol}\cdot\text{kg}^{-1}$) is the amount adsorbed for component A, q_s ($\text{mol}\cdot\text{kg}^{-1}$) is the amount adsorbed at saturation for component A, and q'_A, ($\text{mol}\cdot\text{kg}^{-1}$) is the amount of component A adsorbed when it is present in a mixture with B. b (Pa^{-1}) is the adsorption affinity constant. p (Pa) is pressure for pure gas sytems, and partial pressure for gas mixtures with subscripts *A* and *B* indicating the components.

The ratio of adsorbed phase concentrations for Langmuir model is therefore given by equation S.3.

$$\frac{q'_A}{q'_B} = \frac{q_{SA} b_A p_A}{q_{SB} b_B p_B} = \frac{K_A p_A}{K_B p_B} \tag{S.3}$$

where K (mol·kg^{-1}·Pa^{-1}) is the Henry constant.

For such a system, at a given partial pressure of component A, the ratio of the loading of A in the presence of B to the loading of A as a single component is given by equation S.4.

$$\frac{q'_A}{q_A} = \frac{1 + b_A p_A}{1 + b_A p_A + b_B p_B} = \frac{1 + b_A p_A}{1 + b_A p_A \left(1 + \frac{b_B p_B}{b_A p_A}\right)} \tag{S.4}$$

The effect of competitive adsorption of nitrogen will be the most severe when the pressure ratio of N_2/CO_2 has its highest value. For the present system (A = CO_2 , B = N_2) for the highest N_2 partial pressure (85% N_2), $p_B/p_A = 5.67$ and with $b_A/b_B = 17.2$ (from data of Rees et al. [7]) Eq S.2 reduces to:

$$\frac{q'_A}{q_A} = \frac{1 + b_A p_A}{1 + 1.329\, b_A p_A} \tag{S.5}$$

The maximum fractional loading of CO_2 present in a mixture of 15% CO_2 and 85% N_2 at a total pressure of 1 atm is about 0.2 (which corresponds to an amount of adsorbed CO_2 of 0.7 mol·kg^{-1} as shown in Fig. 3) corresponding to $b_A\, p_A \approx 0.25$ so, over the relevant range, the minimum value of the ratio q'_A/q_A will be about 0.94 (at the highest CO_2 loading). Under the experimental conditions competitive adsorption of nitrogen is therefore expected to lead to a reduction of the nitrogen loading by less than 6%. This is of the same order as the experimental uncertainty and would not be noticeable. However, competitive adsorption would be expected to become evident at higher loadings and this has indeed been observed in a previous study [9].

Chapter 5

This chapter is based on:

In-Situ Characterization of Inorganic Membranes Subject to Viscous, Knudsen and Surface Diffusion Flow Regimes

D. Carter[1], S. Al-Akwaa[1], F.H. Tezel[1], B. Kruczek[1*]
[1]University of Ottawa, Department of Chemical and Biological Engineering
161 Louis Pasteur, Ottawa, Ontario, CANADA, K1N 6N5

To be submitted to: ***Journal of Membrane Science***

ABSTRACT

Synthesis of defect-free zeolite gas separation membranes is challenging. In addition to the desired transport by surface and Knudsen diffusion through the zeolitic pores, the undesired transport by Knudsen and viscous flows through the defects are typically present to different extent. In this paper, we propose a method to assess the extent of the undesirable defect-transport in zeolite membranes, which is important for fine-tuning of membrane synthesis protocols. In addition, knowing the contribution of the undesirable defect transport allows determining intrinsic transport properties of the zeolite crystals incorporated in the membrane. The proposed method is based on single gas permeation tests with He and N_2 before and after calcination of the membrane, and the knowledge of the adsorption isotherms of these gases on the zeolite crystals incorporated into the membrane. The validity of the parameters, which characterize the crystal and defect transport can be verified at two different levels. First, by comparing the experimental and predicted permeances of He and N_2 before and after membrane calcination at different pressures. Secondly, knowing surface diffusivity ratios CO_2 and CH_4 with respect to N_2, evaluated in parallel dynamic adsorption experiments, the experimental and predicted permeances of CO_2 and CH_4 at different pressures can also be compared. In this case, agreement between the experimental and predicted permeances is indicative that the membranes have been characterized accurately. The application of the proposed method is demonstrated using two silicalite zeolite membranes prepared by a pore-plugging method inside porous TiO_2 support.

Keywords: Zeolites, Silicalite, Membranes, Knudsen flow, Surface Diffusion

HIGHLIGHTS

- Quantification of crystal and defect transport contributions to total gas transport in zeolite membranes.
- Prediction of single gas permeances of He, N_2, CO_2 and CH_4 at different pressures.
- Determination of gas transport properties of defect containing zeolite membranes.

5.1.0 INTRODUCTION

Zeolite particles have an extraordinary ability to separate gas mixtures due to differences in the adsorption-diffusion behaviour of guest molecules inside their highly ordered pore networks at modest temperatures and pressures [1]. For the continuous separation of gas mixtures, zeolites can be used as membranes, and the general advantages of separating mixtures using membranes realized, if a thin and continuous layer of zeolite crystals can be assembled [2,3]. Despite these advantages, a significant barrier to the adoption of zeolitic membranes is that their performance is compromised by the unoccupied regions which surround the zeolite crystals of the membrane. These regions are henceforth referred to as defects, and can be attributed to experimental factors such as incomplete zeolite crystal growth, or the different rates of linear expansion for zeolite crystals and the membrane support during heating and cooling.

Both the number of defects and the size of defects affect membrane performance, and therefore numerous techniques have been developed to quantify these characteristics in novel membranes. These techniques have been summarized recently by Maghsoudi [4], and include polymer sphere permeation experiments, the bubble point method, and permporometry. These techniques require exposing the membrane to solid and or liquid materials, as well as dedicated equipment, and consideration of the regeneration conditions that are required to restore membrane performance for gas separation applications. Although these limitations can be overcome at the lab scale, they are often not scalable for larger membranes. Technological advances in 3D laser microscopy show promise to be used as an alternative method to determine defect characteristics, however, the resolution of this technology is not yet sufficient to discriminate between differently sized Knudsen defects [5,6].

The simplest parameter that can be determined experimentally to describe membrane performance is ideal selectivity α. This characteristic parameter is determined by conducting pure gas permeation experiments with 2 different gases, and dividing the permeance of the more permeable gas (P_i) by the permeance of less permeable gas (P_j):

$$\alpha = \frac{P_i}{P_j} \tag{1}$$

The two gases that are used to determine α are typically a small molecule, which can pass through the narrow channels of the zeolite (such as He, H_2, or N_2), and a larger molecule, which is excluded from or blocks the zeolite's pores (such as SF_6). Membranes containing few defects will therefore be highly selective for the smaller gas molecule, which will be able to permeate through both defects and the zeolite channel network, whereas the larger molecule will be transported through the defects only. For silicalite membranes, selectivities of $\alpha(N_2/SF_6)$ up to 108 at 298 °K, and $\alpha(H_2/SF_6)$ of 136 and 155 at 298 °K have been found by others [7–9]. Although ideal selectivities can be used to effectively rank newly fabricated membranes, they do not quantify the change in membrane structure that has occurred by changing the membrane fabrication conditions. Furthermore, adsorption of SF_6 by silicalite crystals has been found to induce crystal expansion, which affects the physical structure of the membrane [7,10]. Given this behaviour, characterized membranes may not have the same properties as they did prior to characterization.

Novel membranes can also be characterized with the Maxwell-Stefan (MS) model, which does not require the use of dedicated materials or equipment as required for permporometric or bubble point characterization methods. In the MS model, the diffusivity of gas molecules is determined with consideration of adsorption phenomena and isotherm data, which can be used to predict the performance of membranes at untested conditions. This model and its variations have been used for a number of different gas and membrane combinations by several research groups [11–13]. The Maxwell-Stefan model does not however discriminate between the transport of gases through defects and the selective layer of membranes. Therefore, MS diffusivities are the most reliable when the contributions of defects to membrane performance have been excluded. Consequently, Maxwell-Stefan diffusivities can be used to compare different membranes of the same type, but they cannot be used to reliably describe defective membranes. A simpler model that can be used in combination with transient permeation values to determine MS diffusivities has been proposed by Gardner et al. [14]. Like the MS model however, this model could only be used to more simply compare different membranes of the same type. Kangas et al. [15] have alternatively proposed characterizing defective membranes with the MS model in combination with permporometric analysis, however, this type of investigation is very rigorous.

Some noteworthy alternatives to the MS model have been developed by other researchers and are pertinent to this study. Caravella et al. [16] proposed a model which combined surface diffusion and Knudsen flow transport through the zeolitic pores of NaY membranes, and was followed up by Zito et al. [17] for silicalite membranes. This model does not however allow the characterization of defects that are present in addition to the zeolite crystals which make up the membrane. Also, Jareman et al. [18] combined defect sizes determined by permporometry with flux equations which take into account substrate effects. The resulting model is well suited for applications where substrate effects are likely to be present and permporometry analysis can be conducted, but is less desirable for applications where this is not possible.

Recently, we have characterized silicalite zeolite membranes, prepared by a pore plugging method on titanium dioxide supports, by a combination of single gas permeation tests with He, N_2, CH_4 and CO_2 at different feed pressures, and dynamic adsorption experiments on zeolite crystals collected from an autoclave in which the zeolite membranes were synthesized [19]. Based on the fact that permeances of He and N_2 were independent of pressure we concluded that the membranes were either defect-free, or the defects were very small so that viscous flow through the defects was negligible. Using single N_2, CH_4 and CO_2 permeances along with the respective isotherms of these gases on silicalite crystals, the effective diffusivity coefficients of N_2, CH_4 and CO_2 in the synthesized membranes were determined. These effective diffusivity coefficients were subject to unquantified morphological attributes of the membrane structure, and so the magnitude of the effective diffusivity coefficients could not be compared with diffusivities determined by others. The resulting N_2/CH_4 and N_2/CO_2 diffusivity coefficient ratios are however normalized with respect to the morphological attributes of the membrane structure, and so were compared with the respective values determined from dynamic adsorption experiments. Since the ratios determined from gas permeation experiments were slightly smaller than those determined from the dynamic adsorption experiments, it was concluded that not all gas transport proceeded through the zeolite crystal channels of the membrane. From the permeance trends as a function of pressure for the gases tested, the reduced ideal selectivity could be attributed to some of the gas transport occurring through defect channels by Knudsen diffusion. However, the contribution of defect transport to the total gas transport through the membranes could not be evaluated.

The objective of this paper is to develop a method to distinguish between the crystal and defect transport in zeolite membranes based on single gas permeation experiments in conjunction with adsorption experiments on zeolite crystals incorporated into the pores of the support for the zeolite membranes. Knowing the contribution of the undesirable defect transport will help in determining intrinsic transport properties of the zeolite crystals. The proposed method is based on single gas permeation tests with He and N_2 before and after calcination of the membrane, and the knowledge of the adsorption isotherms of these gases on the zeolite crystals. The validity of the proposed method is verified by comparing the experimental and predicted permeances of He and N_2 before and after membrane calcination at different pressures. In addition, using the surface diffusion coefficient ratios of N_2 with CO_2 and CH_4, the experimental and predicted permeances of CO_2 and CH_4 at different pressures can also be compared. The application of the proposed method is demonstrated using two silicalite zeolite membranes prepared by a pore-plugging method inside porous TiO_2 support.

5.2.0 THEORETICAL BACKGROUND

The transport of gas molecules through zeolite membranes proceeds through two pathways. These pathways are firstly the defined pore network of the zeolite crystals, and secondly defects, which surround the zeolite crystals. In the former transport pathway, gas molecules are transported by surface diffusion or Knudsen flow, subject to the physico-chemical properties of the gas molecules and the zeolite's pore characteristics. In the latter transport pathway, gas molecules are transported by Knudsen and/or viscous flow subject to the size of the defect pathways in comparison to the size of the gas molecules.

In the regime of surface diffusion, gas molecules are adsorbed into the zeolite's pores as described by their isotherms at the experimental conditions, and diffuse in the direction of decreasing surface occupancy (i.e. decreasing pressure) by continuously adsorbing and desorbing through the zeolite pore network [20,21]. The separation of gas mixtures by surface diffusion is therefore a function of both adsorption and diffusion phenomena, and can be responsible for significant separation selectivities. Transport by Knudsen flow is a result of more frequent collisions between gas molecules and pore walls, leading to the separation of gas mixtures based on molecular mass differences [20,21]. When gas molecules collide more frequently with other gas molecules than they collide with pore walls, the regime of viscous flow occurs, in which all gas molecules move with the same velocity.

The proposed method is based on single gas permeation tests performed before and after calcination of the membrane. The key assumption of the proposed characterization method is that before membrane calcination, zeolite crystalline pathways are not accessible to penetrating gas molecules because they are filled with a template used in the synthesis of the zeolite membrane [8,22–25]. Consequently, before calcination gas molecules can only permeate through the defects, in which gas transport occurs by a combination of Knudsen and viscous flows. The contributions of each transport mode depend on the pore size of the defects. The size of the shape of defects are not uniform; however, for the modelling purposes the defects can be assumed to be straight cylinders of diameter (d_d) and the effective length (l_d). There are *n* defects per unit volume of the membrane so that the volume fraction of the defects in the membrane ε_d is simply:

$$\varepsilon_d = n\frac{\pi}{4}d_d^2 l_d \tag{2}$$

It can be shown that the total gas flux through an uncalcined membrane, that is the defect flux (J_d), is given by Eq. (3) [26]:

$$J_d = \left\{\frac{\varepsilon_d}{l_d}d_d^2\frac{(p_h + p_l)}{64\mu RT} + \frac{\varepsilon_d}{l_d}d_d\frac{1}{3}\sqrt{\frac{8}{\pi MRT}}\right\}(p_h - p_l) \tag{3}$$

where: p_h and p_l are the pressures at the high and low pressure sides of the membrane, respectively, *T* is the absolute temperature, *R* is the universal gas constant, and μ and *M* are the dynamic viscosity and the molecular weight of the gas, respectively. Dividing Eq. (3) by the pressure gradient leads to:

$$P_d = P_{d,v} + P_{d,K} = \frac{\varepsilon_d}{l_d}d_d^2\frac{(p_h + p_l)}{64\mu RT} + \frac{\varepsilon_d}{l_d}d_d\frac{1}{3}\sqrt{\frac{8}{\pi MRT}} \tag{4}$$

where P_d is the total defect permeance, which is the sum of the defect permeance due to the viscous flow ($P_{d,v}$) and the defect permeance due to the Knudsen flow ($P_{d,K}$). There are three unknowns in Eq. (4): ε_d, d_d, and l_d. Combining ε_d and l_d into a lumped term *x* = ε_d / l_d, Eq. (4) is re-written to:

$$P_d = xd_d^2\frac{(p_h + p_l)}{64\mu RT} + xd_d\frac{1}{3}\sqrt{\frac{8}{\pi MRT}} \tag{5}$$

Therefore, performing single gas permeation tests with two different gases at the same conditions (*T*, p_h, p_l) should allow determination of d_d and *x*. One could choose any two gases differing significantly by the molecular weight, but we selected helium and nitrogen as the test gases. Knowing d_d and *x* determined at a given *T*, p_h, p_l one should be able to predict J_d at any other *T*, p_h, p_l. Out of these three operating conditions, the easiest to control is p_h. Therefore, the validity of the proposed method can be verified by comparing the experimental and calculated J_d (or P_d) at different p_h while keeping p_l and *T* constant.

After membrane calcination, it is assumed that the precursor is completely removed from the pores of zeolite crystals and these pores become accessible to permeating gases. Moreover, it is assumed that calcination does not affect ε_d. The advantage of using He as one of the testing gases comes from the fact that it is practically not adsorbed by zeolites at ambient temperature [27–29]. Therefore, the transport through the zeolite pores is governed exclusively by Knudsen diffusion. Consequently, the total helium permeance of after calcination (P_{He}) is given by:

$$P_{He} = P_{He,d} + P_{He,z} = \left\{ x d_d^2 \frac{(p_h + p_l)}{64\mu_{He} RT} + x d_d \frac{1}{3}\sqrt{\frac{8}{\pi M_{He} RT}} \right\} + y d_z \frac{1}{3}\sqrt{\frac{8}{\pi M_{He} RT}} \qquad (6)$$

where $P_{He,d}$ and $P_{He,z}$ are the helium permeances due to transport through the defects and zeolite, respectively, d_z is the effective zeolite pore size and *y* is the equivalent to *x* for the zeolite pores, i.e. $y = \varepsilon_z / l_z$ in which ε_z is the volume fraction of zeolite pores and l_z is the effective length of zeolite pores. Normally, for a given zeolite d_z is known. Therefore, knowing *x* and d_d from single gas permeation tests of the uncalcined membrane and using a reliable value for d_z allows to determine the lumped parameter *y* from Eq. (6).

It is important to note that if in addition to He, another non-adsorbing gas were used (e.g. hydrogen) to test the membrane after calcination, it would lead to another independent equation in the form of Eq. (6), which would allow the determination of d_z experimentally. However, in the proposed method the second gas to be used for membrane testing is to be adsorbed on a zeolite. For molecular sieve silica membranes which are similar to the silicalite membranes characterized in this work, this assumption was found to be reasonable for N_2 [30]. Then, it can be shown that the total permeance of an adsorbing gas in the calcined membrane is given by:

$$P = P_d + P_z = \left\{ x d_d^2 \frac{(p_h + p_l)}{64\mu RT} + x d_d \frac{1}{3}\sqrt{\frac{8}{\pi MRT}} \right\} + y\left(\frac{q_h - q_l}{p_h - p_l}\right)\rho D_T \qquad (7)$$

where q is the surface loading, D_T is the transport diffusion coefficient in zeolite crystals and ρ is the zeolite density. Eq. (7) requires the adsorption isotherm, $q = f(p)$, of the permeating gas on zeolite crystals incorporated into the support of the membrane, which can be determined in parallel adsorption experiments, or can be taken from the literature. Then, knowing x and d_d from gas permeation experiments with uncalcined membrane, y from the gas permeation experiment with He after membrane calcination, Eq. (7) can be used to determine D_T or a lumped ρD_T, if ρ is not available.

The transport diffusion coefficient, which is normally determined from a dynamic adsorption experiment using a packed bed of crystals of known size range, requires the characteristic length for diffusion in zeolite crystals. Since the sizes of each individual crystal in the packed bed can vary, the characteristic length for diffusion can be associated with a considerable uncertainty. On the other hand, although the absolute individual transport diffusion coefficients are uncertain, their ratios should be accurate, because of cancelation of the characteristic length [19,31]. In turn, knowing the ratio of transport diffusion coefficients for a pair of gases, one of which is the absorbing gas used in the proposed characterization method, the permeance of the other adsorbing gas can be predicted from Eq. (7) and compared with an experimentally determined value. This provides another level for the verification of the proposed method. Moreover, if the proposed method is correct, the experimentally determined D_T (or ρD_T) might be more accurate than D_T from a dynamic adsorption test. This is because D_T (or ρD_T) determined from a membrane does not depend on the knowledge of the characteristic length, and it is also decoupled from any geometrical parameters, which are lumped in $y = \varepsilon_z / l_z$. The diffusion coefficients determined from dynamic adsorption tests by comparison are calculated as a lumped parameter with the crystal size, which is subject to uncertainty for packed beds of crystals as mentioned previously. In other words, the proposed characterization method takes into account the complex morphology of the membrane layer and calculates D_T (or ρD_T) based on average geometrical parameters, which lead to the observed results.

5.3.0 MATERIALS AND METHODS

The selection of a system to demonstrate the validity of the proposed characterization method follows from our previous work, in which the synthesized silicalite membranes were characterized by a combination of membrane single gas permeation tests and dynamic adsorption experiments on silicalite crystals incorporated into the support of the membranes [19]. New silicalite membranes were synthesized and tested, while the previously published adsorption data was used along with new permeance data.

5.3.1 Membrane Fabrication Procedure

Silicalite zeolite membranes were synthesized using the pore-plugging method [21,32,33] on 6 cm long on Filtanium^{TM} tubular ceramic membrane supports (TAMI Industries, Nyons, France). The membrane supports' active layers were composed of TiO_2, and contained an active layer pore size of 0.45 μm. Before the zeolite synthesis, both axial faces and the outer surface of the membrane support 1 cm from each end were glazed using the Aremco 617 glaze solution (Aremco Products Inc, Valley Cottage, NY, USA). After applying a layer of the glaze solution, the support was dried at 573 K for 2 hours, followed immediately by curing at 1148 K for 1 hour, with 1 $K \cdot min^{-1}$ heating and cooling ramps. A total of 5 coats of glaze were applied.

Silicalite zeolite membranes M1 and M2 were fabricated inside the active layer of the glazed membrane supports according to the interrupted hydrothermal synthesis method, which has been reported by Miachon et al. [32]. The molar composition of the solution, as well as the temperatures and hold times for the procedure are shown in Table 5.1. The precursor solution was composed of 99.8% purity silicon dioxide (SiO_2), 20 wt% tetrapropyl ammonium hydroxide (TPAOH), and deionized water (H_2O). SiO_2 and TPAOH were purchased from Sigma (Oakville, ON, Canada). The only difference between membranes M1 and M2 was the free volume in the autoclave above the solution (i.e. the volume in the autoclave not occupied by the precursor solution) during the hydrothermal synthesis. For a given temperature, as the free volume in the autoclave decreases, the pressure during the hydrothermal synthesis increases. In turn, crystal growth during hydrothermal synthesis depends on the temperature and pressure, which affect the solubility and diffusivity of solute molecules [34].

Table 5.1. Selected properties of the synthesis parameters for the membranes M1 and M2 that have been fabricated in this study. Interruption time begins when the oven starts to cool down at the end of hold time 1, and ends when the oven commences heating up to the hold temperature for hold time 2. After synthesizing silicalite crystals, each membrane was dried at 373 K for 20 hours, and calcined at 773 K for 4 hours. The heating and cooling rates for drying and calcination were 1 K·min^{-1}.

Memb.	Precursor solution molar ratio	Heating ramps	Cooling ramps	Hold Temp.	Hold Time 1	Interruption Time	Hold Time 2	Free Volume
	Si:TPAOH:H_2O							
	[mol]	[K·min^{-1}]	[K·min^{-1}]	[K]	[h]	[h]	[h]	[%]
M1	1 : 0.45 : 27.8	1	1	443	12	11	72	< 1.0
M2	1 : 0.45 : 27.8	1	1	443	12	11	72	5.6

5.3.2 Gas Permeation Experiments

A process flow diagram (PFD) showing the experimental setup used to conduct gas permeation experiments is shown in Fig. 5.1. The heart of the testing system is a membrane module, which connects the glazed ends of a tubular ceramic supported membrane with stainless steel process lines. In the present study, a gas tight seal between these materials has been achieved using single use compressible graphite gaskets. These gaskets are positioned concentrically over the glazed ends of the tubular membrane, and form a hermetic seal when they expand radially due to axial compression from the membrane module flanges. The membrane module shown in Fig. 5.1 has been made in house at the University of Ottawa, using stainless steel stock, brass flange bolts, and compressible graphite from McMaster Carr (Elmhurst, IL, USA). In comparison to epoxies, and elastomeric or fluorinated polymers, the graphite used in this study contains practically no solvents which could outgas and poison the zeolite crystals, and can be heated up to temperatures greater than 750 K.

The configuration of the experimental setup allows pure gases to be fed to the membrane at chosen constant feed flow rates using mass flow controllers MFC1 and MFC2. For feed flow rates below 1,000 mL(STP)·min^{-1}, MFC1, the mass flow controller made by Bronkhorst (Burlington, ON, Canada) was used, whereas MFC2, the mass flow controller made by MKS (Andover, MA, USA) with a range of 0 – 10 L(STP)·min^{-1} was used when higher feed flow rates were required. The flow rates of the permeate and retentate streams were then measured using bubble flow meters F1 and F2.The pressures on the feed (high pressure side) and the permeate (low pressure side) side were measured with pressure transducers P1 and P2 respectively. The pressure transducers were made by Cole Parmer, (Montreal, QC, Canada) and have operating ranges of 0 – 250 psig and 0 – 10 psig for P1 and P2, respectively. Additionally, the gas temperature was measured in line using a K type thermocouple T1 made by Omega (Laval, QC, Canada). He with a purity of 99.999%, N_2 with a purity of 99.998%, CH_4 with a purity of 99.99%, and CO_2 with a purity of 99.99% used as test gases were purchased from Linde (Missisauga, ON, Canada).

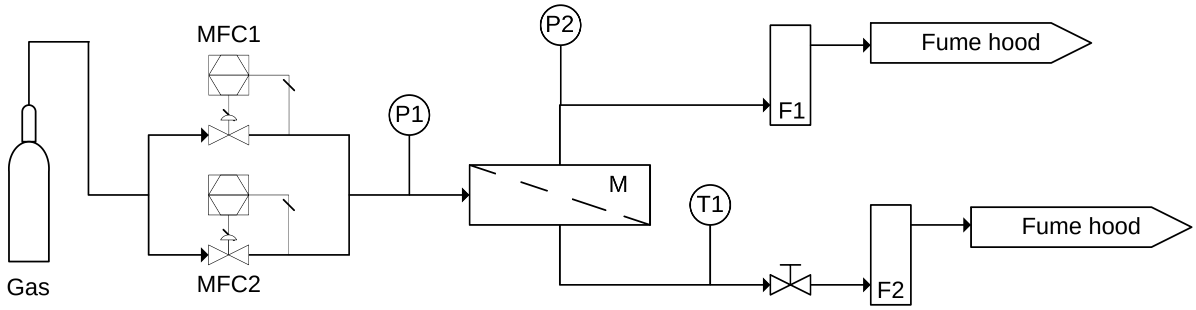

Figure 5.1. A schematic showing the experimental setup used in this investigation. MFC1 and MFC2 are mass flow controllers, P1 and P2 are pressure transducers, M is the module containing the membrane, T1 is a temperature thermocouple, and F1 – F2 are bubble flow meters.

Pure gas permeation experiments were conducted at three different absolute feed pressures of 170, 300 and 450 kPa absolute. The permeate side of the membrane was open to atmosphere. However, since some of the gases needed to be vented into the fume hood for safety considerations, the permeate side pressure was greater than the atmospheric pressure, ranging from 109 kPa to 175 kPa absolute depending on the gas permeation rate. Unlike, the feed pressure, which was controlled, the permeate pressure could not be directly controlled, but nevertheless it was carefully monitored.

The membranes were tested with single gases before and after calcination. Before calcination the membranes were tested with pure He and N_2 at the three feed pressures listed above, and after calcination they were retested with pure He and N_2 as well as with pure CH_4 and CO_2 at the same feed pressures. The testing with calcined membranes were carried out in the following order: He, N_2, CH_4, CO_2. Then a test with He at one pressure was repeated, in order to rule out potential contamination of the membranes with residual impurities of tested gases, in particular CH_4 and CO_2.

5.3.3 Parameters for the Proposed Method

In addition to experimentally measured gas permeances of uncalcined and calcined zeolite membranes, the proposed characterization method relies on adsorption parameters, which can be determined by independent adsorption experiments, or are available in the literature. In this paper we rely on the adsorption parameters of silicalite zeolite powder determined experimentally in our lab and reported previously [19,35,36].

Single gas adsorption isotherms of N_2, CH_4 and CO_2 on silicalite zeolite crystals are adequately described using the Langmuir model [36,37]:

$$q = q^s \frac{bp}{1+bp} \tag{9}$$

where q is the equilibrium adsorption capacity of zeolite at pressure p, q^s is the maximum adsorption capacity of zeolite, and b is the affinity constant [19]. The values of these constants for the gases considered in this study are summarized in Table 5.2. In addition,

Table 5.2 lists the ratios of the transport diffusivity of CO_2 and CH_4 with respect to N_2, as well as other properties of gases required by the gas transport equation.

Table 5.2. Constant parameters required for demonstration of the proposed characterization method using silicalite zeolite membranes at temperature 295 K. The adsorption and diffusion properties are taken from Ref [19].

Property		He	N_2	CH_4	CO_2
M	[kg·mol^{-1}]	0.004	0.028	0.016	0.044
μ	[Pa·s^{-1}]	1.973 x 10^{-5}	1.755 x 10^{-5}	1.096 x 10^{-5}	1.473 x 10^{-5}
q^s	[mol·kg^{-1}]	-	1.930	2.303	4.490
b	[Pa^{-1}]	-	0.072	0.194	0.301
D_T / D_{TN_2}	[-]	-	1	0.65 ± 0.06	0.35 ± 0.01

5.4.0 RESULTS AND DISCUSSION

5.4.1 Experimental Pure Gas Permeances

The single permeances of membranes M1 and M2 at different feed pressures before and after membrane calcination are presented in Figs. 5.2a and 5.2b, respectively. The corresponding permeance ratios (ideal selectivities) for N_2/He before and after membrane calcination, as well for CH_4/N_2 and CO_2/N_2 after calcination for M1 and M2 are shown in Figs. 5.3a and 5.3b, respectively. Uncertainties associated with gas permeances, calculated using standard error equations in combination with the dimensional variation of each membrane and instrument sensitivities, were less than 9% of the respective reported values. The details of uncertainty calculations are presented in Appendix 1.

It can be noticed that before calcination both membranes are permeable to He and N_2, which means that M1 and M2 are not defect-free. The corresponding defect permeances (P_d) of He and N_2 increase with pressure, and at a given feed pressure, M2 is more permeable than M1, which indicates more defects in M2 than in M1. The fact that defect permeance of both membranes increases with pressure suggests that the first term in Eq. (5) is not negligible. In other words, the transport through the defects must include the viscous flow, which is proportional to $p_h + p_l$. In addition, for both M1 and M2 the defect permeance of He is greater than that of N_2, which indicates that in addition to the viscous flow, there must also be Knudsen flow through the defects; the latter favors the transport of the lighter He molecules over the heavier N_2 molecules as can be seen in Eq. (5). The difference between the defect permeances of He and N_2 is greater for M1 than for M2. Consequently, before calcination the ideal N_2/He selectivity of M1 is slightly smaller than that of M2 as can be seen in Fig. (5.3). The ideal N_2/He selectivity of both M1 and M2 slightly increases with feed pressure while remaining less than unity. This is consistent with Eq. (5) which indicates that the contribution of non-selective viscous flow to the total transport through the defects increases with increase in $p_h + p_l$. On the other hand, since Knudsen flow is independent of pressure, its contribution to the total flow must decrease with increasing p_h.

As expected, the He and N_2 permeances of both M1 and M2 increase significantly after calcination. This is because calcination removes the template from the zeolite crystals, thus opening additional pathways for the transport of He and N_2 through the calcined membranes. As expected, the increase of N_2 permeance is much greater than that of He, and as a result the calcined membranes become N_2-selective, i.e. the ideal N_2/He selectivity for both M1 and M2 becomes greater than unity. Although He is smaller than N_2 it is practically not adsorbed by the silicate crystals and its transport through the zeolite pores is limited to Knudsen flow. The fact that N_2 permeance of the calcined membranes is several times greater than that of the uncalcined membranes indicates that permeation through the calcined membranes is dominated by transport through the zeolite crystals. Comparing M1 and M2, it can be noticed that the increase in N_2 permeance after calcination is greater for M1 (Fig. 5.2a) than for M2 (Fig. 5.2b). Therefore, the ideal N_2/He selectivity of the calcined M1 (Fig. 5.3a) is greater than that of M2 (Fig. 5.3b). The observed results suggest that the contribution of the transport through zeolite crystals to the total transport is greater in M1 than in M2. Assuming that calcination removes all templates from the silicalite crystals, one could conclude that during the hydrothermal synthesis more silicalite crystals were formed in the active layer of M1 than in the active layer of M2 even though both membranes were prepared using the same support. This suggests that increasing the pressure in the autoclave by increasing the volume of the precursor solution (i.e. decreasing the free volume in the autoclave), while maintaining the same temperature, favors diffusion of the zeolite precursor components into the pores of the membrane active layer, which promotes the formation of more zeolite crystals. This finding may support the work of Li et al., which found that diffusion of the zeolite precursor components into the pores of the membrane support active layer during an interruption in hydrothermal synthesis plays a key role in growing sufficient crystals to plug the pores of the active layer [38].

Considering the effect of feed pressure on the ideal N_2/He selectivity of the uncalcined and calcined membranes, one can observe in Fig. 5.3 that the ideal N_2/He selectivity of the uncalcined membranes increases with feed pressure, while the opposite is true for the calcined membranes. In both cases, pressure-dependence of the ideal selectivity is a result of an increasing contribution of non-selective viscous flow to the total transport at higher pressures. At higher feed pressures, more viscous flow occurs, which reduces the relative contribution of selective transport through zeolite channels. Although the trends are opposite, in both cases the ideal selectivity at higher pressures is closer to unity than at the lower pressures.

For both M1 and M2, the CO_2 and CH_4 permeance of the calcined membranes is greater than the N_2 permeance, and $P_{CO_2} < P_{CH_4}$ which is in agreement with the findings of others [39–42]. It is interesting to note, that unlike P_{N_2} of the calcined membrane, which increases with pressure, P_{CO_2} and P_{CH_4} are either approximately constant (Fig. 5.2b), or decrease with p_h (Fig. 5.2a). Moreover, the effect of feed pressure appears to be a little bit stronger for P_{CO_2} than for P_{CH_4}. These qualitative observations can be explained based on the transport mechanism through the pores of zeolite crystals. The transport of adsorbing gases such as N_2, CH_4 and CO_2 occurs by surface diffusion, which the driving force is a surface occupancy gradient across the membrane. In turn, the surface occupancy for a given gas is directly related to its adsorption isotherm. In the pressure range of interest, the N_2 isotherm is linear while those of CO_2 and CH_4 are both concave. Moreover, the CO_2 isotherm is more concave than the CH_4 isotherm (i.e. the slope of the isotherms increases in the following order: $CO_2 < CH_4 < N_2$). If there were no viscous flow, P_{N_2} of the calcined membranes would be independent of pressure, while the P_{CO_2} and P_{CH_4} would decrease with increasing pressure. However, since calcination does not eliminate the contribution of viscous flow, P_{N_2} of the calcined membranes increases with pressure. Meanwhile, relatively constant P_{CO_2} and P_{CH_4} are influenced by the combined effects of a decreasing contribution of surface diffusion while there is an increasing viscous flow contribution with feed pressure.

Despite a greater affinity of CO_2 to silicalite crystals compared to CH_4, i.e. for a given feed pressure the driving force for CO_2 diffusion is greater than that for CH_4, the permeance of CO_2 is less than the permeance of CH_4, $P_{CO_2} < P_{CH_4}$. This order of permeance can be attributed to the greater diffusivity of CH_4 in comparison to CO_2 in silicalite crystals, which is related to permeance and the surface loading at the high and low pressure sides of the membrane as shown in Eq. (7). The surface diffusion coefficient of CH_4 in silicalite pores must therefore be greater than that of CO_2, which is consistent with the data given in Table 5.2 and the work of others [19,39–43].

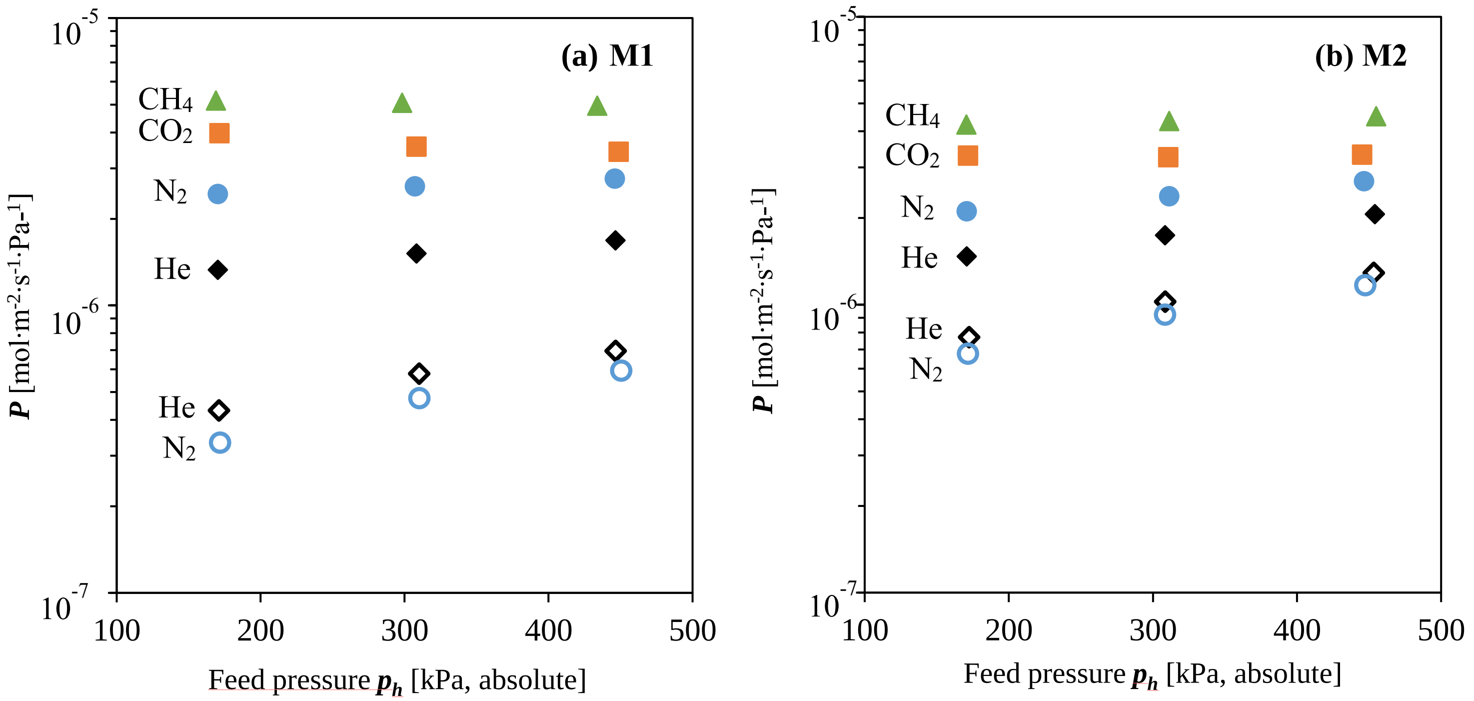

Figure 5.2. Experimentally determined permeances for M1 (a) and M2 (b). Hollow and filled points denote permeances determined from permeation experiments conducted prior to and following membrane calcination respectively. Permeation experiments were conducted at a temperature of 295 ± 2 K. Membrane length and area were 6.0 ± 0.1 cm and 10.5 ± 0.1 cm^2, respectively.

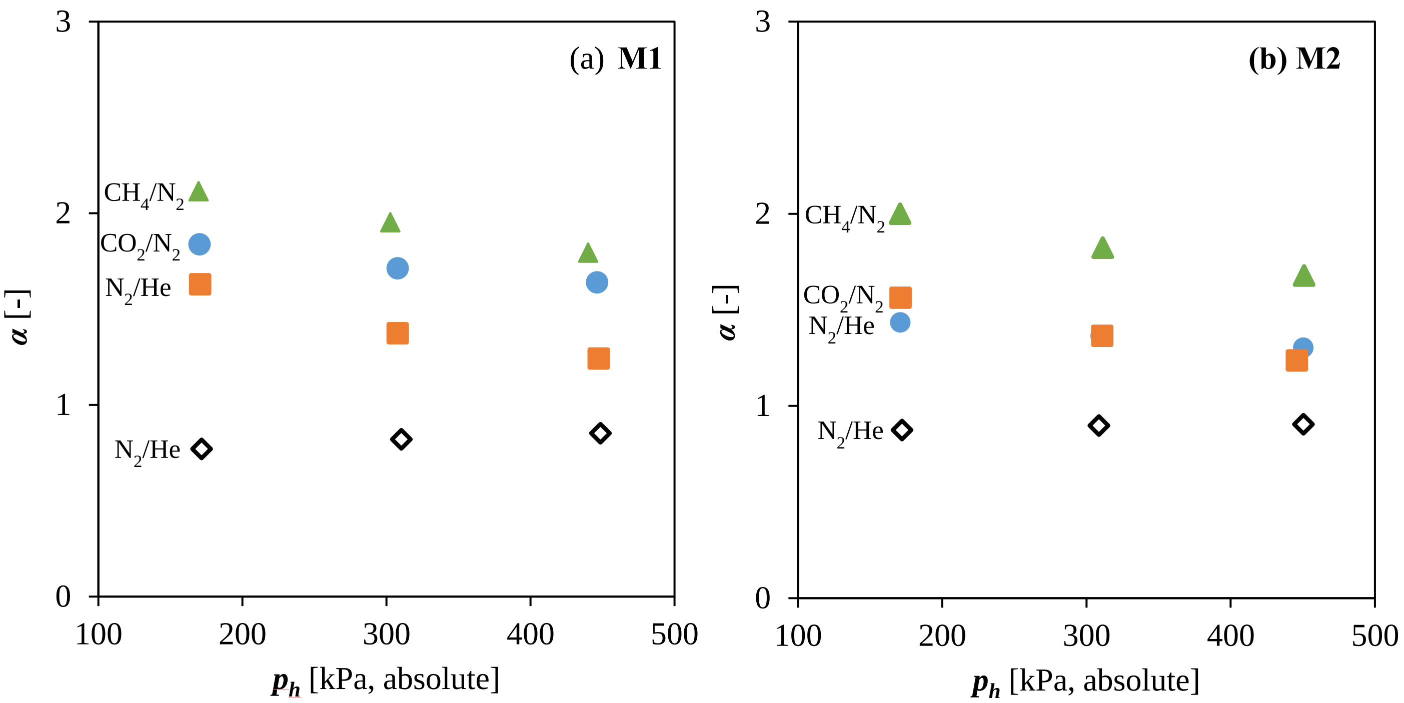

Figure 5.3. Ideal selectivities determined using the permeances shown in Fig. 5.2 for M1 (a) and M2 (b). Hollow and filled points denote ideal selectivities determined from permeation experiments conducted prior to and following membrane calcination respectively. Permeation experiments were conducted at a temperature of 295 ± 2 K. Membrane length and area were 6.0 ± 0.1 cm and 10.5 ± 0.1 cm^2, respectively.

5.4.2 Quantification of the Defect Transport

As discussed in the previous section, a non-zero permeance through the uncalcined membranes indicates the existence of defects in both M1 and M2, and the transport through the defects occurs by both viscous and Knudsen flow. These qualitative observations can be quantified using the proposed characterization method. Using experimental P_{He} and P_{N_2} of the uncalcined membrane for a given p_h and the corresponding p_l into Eq. (5) for He and N_2 separately, which results in a system of two independent equations and allows the determination of $x = \varepsilon_d / l_d$, and d_d.

Table 5.3 presents the calculated values of x and d_d determined at low (170 kPa), medium (300 kPa) and high (450 kPa) feed pressures along with the corresponding confidence ranges. The latter were determined by combining standard error analysis equations for sums and products as necessary to the independent equations used to calculate x and d_d. A sample calculation for determining these confidence ranges is shown in Appendix 1. In principle, for a given membrane the values of x and d_d should be independent of the feed pressure. On the one hand, considering the confidence ranges associated with x and d_d, one could argue that both x and d_d are independent of the feed pressure, but on the other hand, the dependence of x and d_d on the feed pressure is quite evident. More specifically, for both membranes M1 and M2, as the feed pressure increases, x increases while d_d decreases. According to Eq. (5), an increase in either x or d_d increases P_d. Therefore, the opposite effect of the feed pressure on x and d_d may suggest that these two parameters are coupled.

The values of d_d in Table 5.3 range from 1.6 µm to 3.8 µm. Since the pore size of the active layer of the support provided by the manufacturer is 0.45 µm, the calculated d_d appear to be very large. On the other hand, the pore size distribution of the active layer is unknown. It is possible that the active layer, in addition to small regular pores, may contain some large pores, which in turn would be difficult to plug during the hydrothermal synthesis.

The calculated ε_d / l_d in Table 5.3 ranges from 0.39 m^{-1} to 0.96 m^{-1}. Assuming that l_d has a magnitude comparable to the thickness of the active layer, which has been found to be approximately 10 – 12 μm previously [19], the corresponding ε_d is in the order of 10^{-6}. In other words, according to the results reported in Table 5.3 the uncalcined membranes contain very few, but relatively large defects. In turn, this suggests that the vast majority of regular pores in the active layer of the support were adequately plugged during the hydrothermal synthesis.

Table 5.3. Comparison of characteristic values for M1 and M2 when different data sets are used. Permeation experiments were conducted at a temperature of 295 ± 2 K. Both membranes had a length of 6.0 ± 0.1 cm and an area of 10.5 ± 0.1 cm^2.

Feed pressure [kPa]	Characteristic parameter			
	$x = \varepsilon_d / l_d$ [m^{-1}]		d_d [μm]	
	M1	M2	M1	M2
170	0.58 ± 0.20	0.39 ± 0.21	2.1 ± 0.8	3.8 ± 2.1
300	0.76 ± 0.25	0.63 ± 0.29	1.8 ± 0.6	2.9 ± 1.3
450	0.96 ± 0.34	0.90 ± 0.46	1.6 ± 0.6	2.4 ± 1.1

The values of x and d_d at a given feed pressure, can be used for the prediction of P_d of He and N_2 at the other feed pressures. The predictions of P_d of He for M1 and M2 are shown in Figs. 5.4a and 5.4b, respectively, while the predictions of P_d of N_2 for M1 and M2 are shown in Figs. 5.4c and 5.4d, respectively. In addition to the total defect permeance, which is indicated by the solid line, the dotted line shows the corresponding contribution of the Knudsen permeance ($P_{d,K}$). Thus, the difference between these lines represents the viscous permeance ($P_{d,v}$). Different line types in Figs. 5.4a – 5.4d correspond to different sets of x and d_d used (i.e. low, medium, or high pressure sets) for the prediction of defect permeances. It should be emphasized that as indicated by Eq. (5) the prediction of defect permeance requires permeate pressure, which was not constant. However, for a given membrane and gas, p_l increased linearly with p_h. The respective relationships between p_l and p_h for He and N_2 using M1 and M2 are shown graphically in Fig. S.5.1. These empirical relationships were used to predict P_d of He and N_2 in Fig. 5.4.

Despite the variation of x and d_d with feed pressure, the predicted P_d based on different sets of x and d_d are remarkably close to each other, in particular for N_2. Moreover, the predicted P_ds are very close to the experimental values. Any discrepancies between the experimental and predicted permeances are within the 9% experimental uncertainty that has been mentioned previously. Although the total defect permeances based on different sets of x and d_d are very close to each other, the Knudsen and viscous contributions to the total permeance depend on the set of x and d_d used for the predictions. The Knudsen contribution to the total permeance of the uncalcined membranes is the highest when using x and d_d determined at the high feed pressure and the lowest when using x and d_d determined at the low feed pressure. For the viscous contribution to the total permeance, the situation is exactly the opposite. As previously observed, for both membranes x increases whereas d_d decreases with increasing feed pressure. While the two parameters are coupled, a decrease in d_d increases the contribution of the Knudsen flow to the total flow through the defects, which follows from Eq. (5).

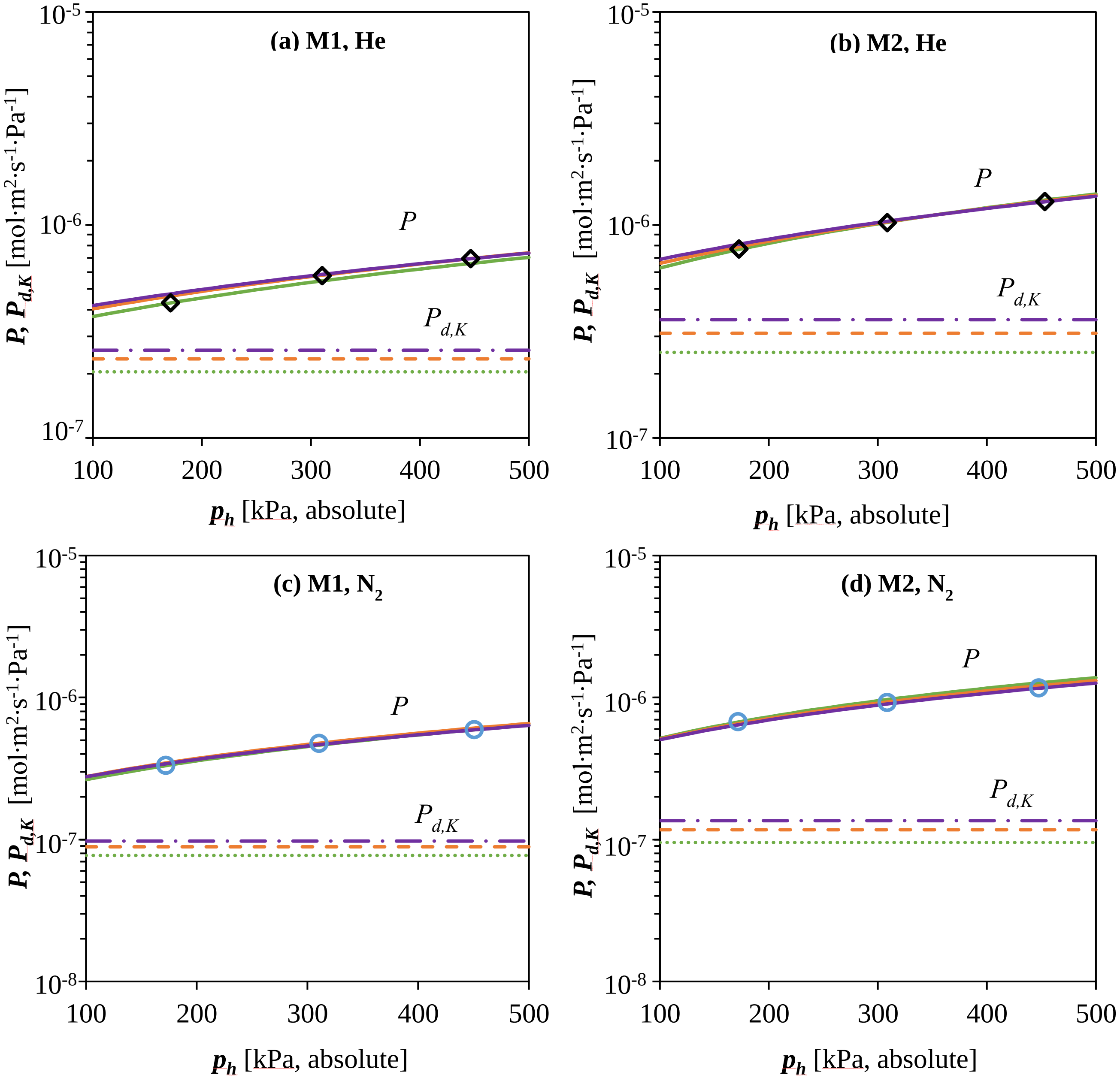

Figure 5.4. Experimentally determined and predicted permeances of He and N_2 through uncalcined M1 and M2. Parameters *x* and d_d as required to predict permeances have been determined using the 170 kPa (**green**), 300 kPa (**orange**), and 450 kPa (**purple**) feed pressure data values shown in Table 5.3. For defect permeances by Knudsen flow, the dotted, dashed, and dash-dotted lines denote predictions determined using the 170 kPa, 300 kPa, and 450 kPa feed pressure data values shown in Table 5.3 respectively.

5.4.3 Quantification of the Zeolite Transport

Assuming that calcination does not introduce any additional defects but only opens the zeolite pores, the previously determined *x* and d_d values can be used to calculate the defect transport contributions to total membrane permeance through the calcined membranes. Thus, Eq. (6) can be used to determine $y = \varepsilon_z / l_z$ based on the experimental total permeance of the non-adsorbing gas (He). Then knowing *y*, Eq. (7) can be used to determine D_T of the adsorbing gas (N_2) based on the experimental total permeance of that gas. Table 5.4 presents the calculated values of *y* and D_{TN_2} determined at low (170 kPa), medium (300 kPa), and high (450 kPa), feed pressures along with the corresponding confidence ranges, for which a sample calculation is shown in Appendix 1. Similarly to the values of *x* and d_d, *y* should be independent of feed pressure, but as shown in Table 5.4, it actually increases as feed pressure increases. This increase; however, is very small compared to the changes in *x* and d_d with feed pressure and is well within the corresponding confidence range. Based on experimental single gas permeances presented in Fig. 5.2, we concluded a greater contribution of zeolite transport in M1 compared to M2. Since at a given feed pressure, *y* for M1 is greater than *y* for M2, this parameter can be used to quantify the transport through the zeolite pores and ultimately the quality of the pore-plugged membranes. Considering D_{TN_2}, which should be constant, it also slightly increases with feed pressure. While this increase is well within the corresponding confidence range, it nevertheless might indicate the actual dependence of D_{TN_2} on pressure. An increase in transport diffusivity of adsorbing gases such as N_2 in zeolites with pressure was reported previously [20]. Irrespective of this, for a given feed pressure, D_{TN_2} in M1 and M2 are similar to each other. This is because at given conditions, D_{TN_2} should be a property of the silicalite-1 crystals and should not depend on the contribution of surface diffusion to the total permeance of the calcined membranes. Considering the values of D_{TN_2} in Table 5.4, which range from $0.8\text{x}10^{-8}$ and $1.2\text{x}10^{-8}$ $m^2 \cdot s^{-1}$, they are in agreement with the values that have been determined by others [17,39,44].

In comparison to $x = \varepsilon_d / l_d$, the values of $y = \varepsilon_z / l_z$ are more than four orders of magnitude greater (see Tables 5.3 and 5.4). As previously discussed, ε_d is in the order of 10^{-6}. On the other hand, ε_z should much greater than this. More specifically, in the limiting case when the pores of the active layer are completely plugged with zeolite crystals, ε_z is the product of the silicalite's porosity (7.5%) [45], and the membrane support's porosity (23%, as given by TAMI), which is equal to 1.7%. If the pores are not completely plugged, ε_z < 1.7% In addition, while l_d should be comparable to the thickness of the active layer of the support, l_z could be a small fraction of that. This is illustrated in Fig. 5.5, which presents the examples of a defective pore (Fig. 5.5a) and a selective pore (Fig. 5.5b) in a pore-plugged membrane.

The pore is selective as long as there is a continuous layer of zeolite crystals within the pore, which could be much thinner than the thickness of the active layer of the membrane support. On the other hand, if there is no continuous layer of zeolite crystals, permeant molecules will bypass the zeolite crystals, and in this case l_d must be at least equal, or more likely greater than the thickness of the active layer. With the limiting value of $\varepsilon_z = 0.1725$, l_z estimates of 1.7 µm and 2.3 µm are obtained for M1 and M2 when values of *y* equal to 10,000 and 7,600 (from Table 5.4) are used, respectively. Therefore, indeed for our experimental data, l_z is only a fraction of the thickness of the active layer of the membrane. It should be emphasized that such estimated l_z likely overestimate the actual effective thickness of the zeolite layer within the pores, because in reality membranes are not defect free as previously discussed.

The values of *y* at a given feed pressure were substituted into Eq. (6) to predict the total helium permeance of M1 and M2 at the other pressures. Similarly, the values of *y* and D_{TN_2} at a given feed pressure were substituted into Eq. (7) to predict the total nitrogen permeance of M1 and M2 at the other feed pressures. Fig. 5.6 presents the comparison of these predicted and experimental permeances. In addition to the predicted total permeance, which is indicated by the solid line, the dashed and dotted lines shows the corresponding predicted contribution of the Knudsen permeance of He through zeolite pores (Figs. 5.6a and 5.6b for M1 and M2, respectively), and the corresponding predicted surface diffusion permeance of N_2 through zeolite pores (Figs. 5.6c and 5.6d for M1 and M2, respectively). It should be emphasized that as indicated by Eq. (7) the prediction of the total permeance requires permeate pressure, which was not constant, but rather increased with feed pressure (Fig. S.5.1). Consequently, although the adsorption isotherm of N_2 in silicalite crystals is practically linear in the pressure range of interest [19], the predicted surface diffusion permeances of N_2 in Figs 5.6c and 5.6d decrease with increasing feed pressure.

Considering predictions of the total He permeance of the calcined M1 and M2 (Figs. 5.6a and 5.6b), it can be noticed that the three lines are very close to each other. This is because the predicted Knudsen permeance in zeolite crystals depends solely on the value of y, which as shown in Table 5.4 was not very sensitive to the feed pressure. The total predicted He permeances are very close to each other, as well as to the experimental values. In case of the total predicted N_2 permeances of the calcined M1 and M2 (Figs. 5.6c and 5.6d) the three lines are further apart from each other than those for He in Figs. 5.6a and 5.6b. This is because in addition to y, the predicted total N_2 permeance also depends on D_{TN_2}, and both y and D_{TN_2} increase slightly with increasing feed pressure. This is why the prediction of the total N_2 permeance is sensitive to even small variation in y and D_{TN_2}. Despite this sensitivity, the experimental total permeance of N_2 at a given feed pressure is generally well predicted based on y and D_{TN_2} determined at other feed pressures. Considering the predicted permeances of M1 and M2, it can be noticed that total permeance of N_2 is slightly better predicted for M2 than for M1. This is because the contribution of the defect permeance, which can be very well predicted (Fig. 5.4), to the total permeance is greater for M2 than for M1.

Table 5.4. Comparison of characteristic values for M1 and M2 when different data sets are used. Permeation experiments were conducted at a temperature of 295 ± 2 K. Both membranes have a length of 6.0 ± 0.1 cm, and an area of 10.5 ± 0.1 cm^2.

Feed Pressure [kPa]	Characteristic parameter			
	$y = \varepsilon_z / l_z$ [m^{-1}]		D_T [m$^2 \cdot$s^{-1}]	
	M1	M2	M1	M2
170	9600 ± 2300	7600 ± 5800	1.0 ± 0.3 x10^{-7}	0.8 ± 0.7 x10^{-7}
300	10000 ± 2700	7600 ± 6600	1.1 ± 0.3 x10^{-7}	1.0 ± 1.0 x10^{-7}
400	10600 ± 3500	8200 ± 9100	1.2 ± 0.5 x10^{-7}	1.1 ± 1.4 x10^{-7}

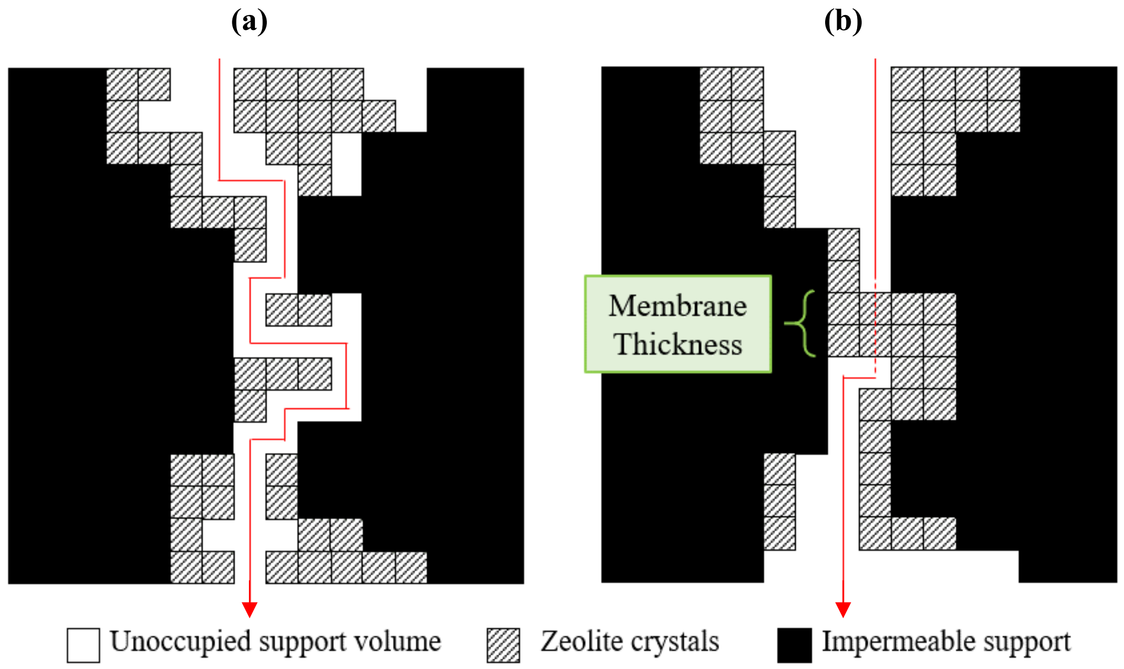

Figure 5.5. Schematic diagrams showing zeolite crystal occupancy configurations inside membrane support pores of pore plugged membranes. The molecular pathway is denoted by the line. Fig. 5.5a shows a continuous defect pathway, and Fig. 5.5b shows the pathway through a continuous zeolite layer made up of zeolite crystals which have a thickness less than the thickness of the membrane support pores. Through the zeolite crystals the molecular pathway line becomes dashed.

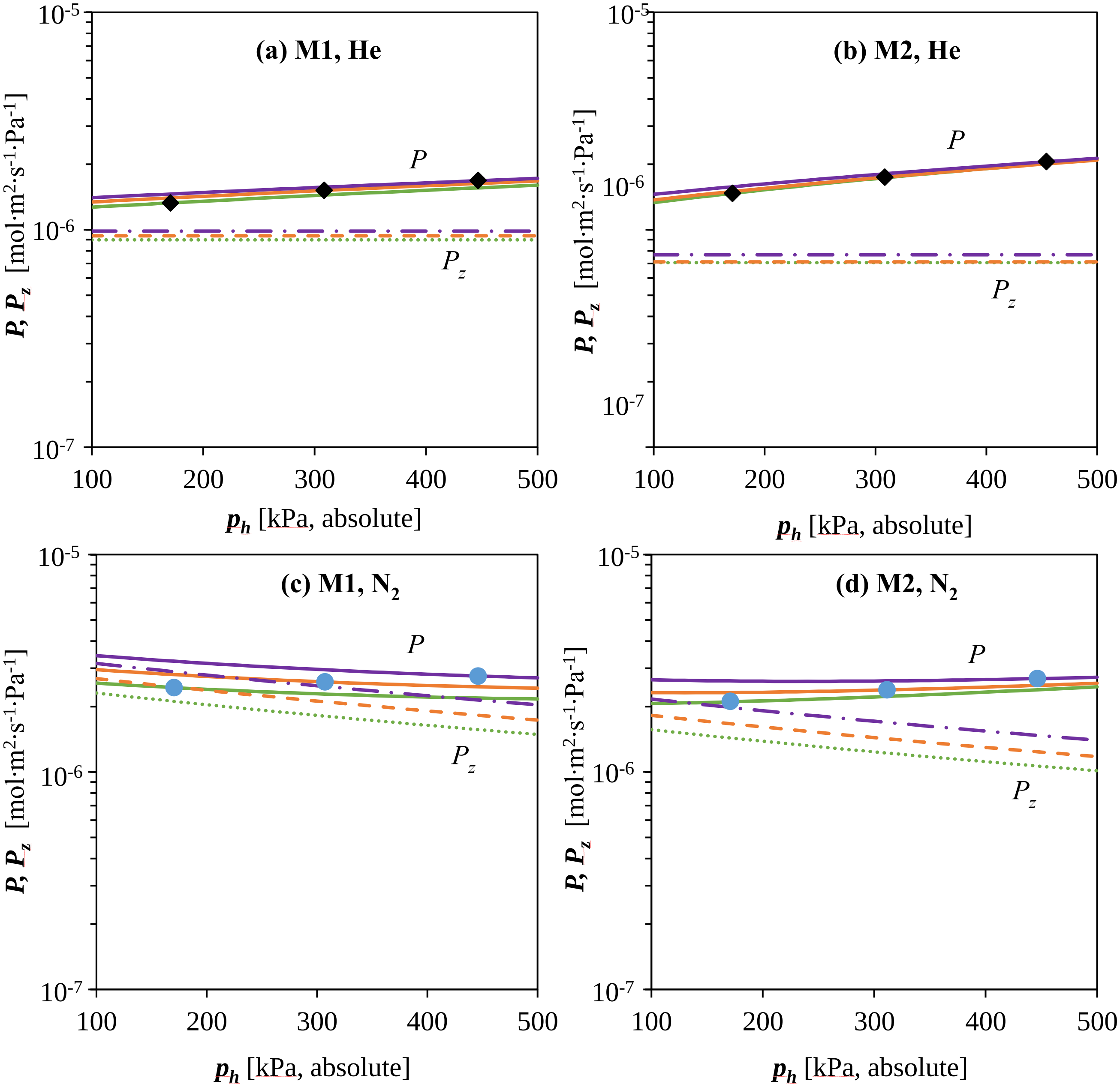

Figure 5.6. Experimentally determined and predicted permeances of He and N_2 through calcined M1 and M2. Parameters x, d_d, y, and D_T as required to predict permeances have been determined using the 170 kPa (**green**), 300 kPa (**orange**), and 450 kPa (**purple**) feed pressure data values shown in Table 5.3. For silicalite permeance predictions, the dotted, dashed, and dash-dotted lines denote predictions using the 170 kPa, 300 kPa, and 450 kPa feed pressure data values shown in Table 5.3 and Table 5.4 respectively.

5.4.4 Validation of the Proposed Method

In addition to the prediction of the total permeance of the probe gases (He and N_2), the proposed method allows predicting the total permeance of any adsorbing gas, provided the ratio of its transport diffusivity over that of N_2, and its adsorption isotherm is known. We have recently reported D_{TCH_4}/D_{TN_2} and D_{TCO_2}/D_{TN_2}, determined in dynamic adsorption experiments [19], and these ratios are listed in Table 5.2. A comparison of the predicted permeances of an adsorbing gas with experimentally determined values represents the ultimate verification of the proposed method.

The respective total permeances in M1 and M2 were calculated using Eq. (7), as well as x, d_d, y and D_{TN_2} summarized in Tables 5.3 and 5.4, along with the ratios D_{TCH_4}/D_{TN_2}, D_{TCO_2}/D_{TN_2} and adsorption isotherm constants for CO_2 and CH_4 listed in Table 5.2. As previously noted, calculation of the permeance requires the pressure gradient ($p_h - p_l$), which should be an independent variable. In our testing system, however we could directly control p_h but not p_l. Consequently, the experimental data generated to verify the proposed method was also used to determine a relationship between p_l and p_h. As shown in Fig. S.5.1, for a given gas and membrane p_l appears to be directly proportional to p_h. Knowing the empirical relationship between p_l and p_h has allowed generating Fig. 5.7, which presents the predicted permeances of CH_4 (Figs. 5.7a & 5.7b) and CO_2 (Figs. 5.7c & 5.7d) in M1 and M2 as a function of feed pressure, and compares them to the respective experimental permeances. For a given gas and membrane, there are three theoretical lines representing the predicted permeances, each corresponding to different set of x, d_d, y and D_{TN_2} values determined from low (170 kPa), medium (300 kPa), and high (450 kPa) feed pressure data. The difference between the theoretical lines for different sets of x, d_d, y values in Fig. 5.7 is greater compared to Fig. 5.6. While for M1, the difference between the theoretical lines appears to be independent of p_h (Figs. 5.7a & 5.7c), for M2 (Figs. 5.7b & 5.7d) the theoretical lines are getting closer to each other at higher feed pressures. As the feed pressure increases, the contribution of defect transport, to the total transport increases.

Moreover, as previously concluded, the proportion of the defect transport is greater in M2 than in M1.

The theoretical permeance lines, in particular for M1, show a greater dependence on the feed pressure (a decrease with increasing feed pressure) than the experimental values; the latter show only a little variation with feed pressure. On the one hand, as the feed pressure increases, the surface diffusion permeance decreases, because of the shape of the CO_2 and CH_4 adsorption isotherms (As pressure increases, the slope of the isotherm decreases, which decreases the surface diffusion permeance). On the other hand, as the feed pressure increases the viscous permeance through the defects increases. In the case of the experimental permeances, these two opposite effects appear to counterbalance. This is not the case for the theoretical permeances, which decrease with feed pressure. There are two possible explanations, (1) the theoretical permeances underestimate the viscous contributions, and/or (2) D_T / D_{TN_2} are not constant as assumed, but rather decrease with feed pressure. However, despite different shapes of the theoretical and experimental permeances, the experimental CO_2 permeances, determined at different feed pressures fall on the corresponding theoretical lines, in particular in case of M1. On the other hand, the experimental CH_4 permeances are greater than the theoretical values at the corresponding feed pressure. This could indicate that the value of D_{TCH_4} / D_{TN_2} ratio not only depends on feed pressure, but is also greater than the value listed in Table 5.2.

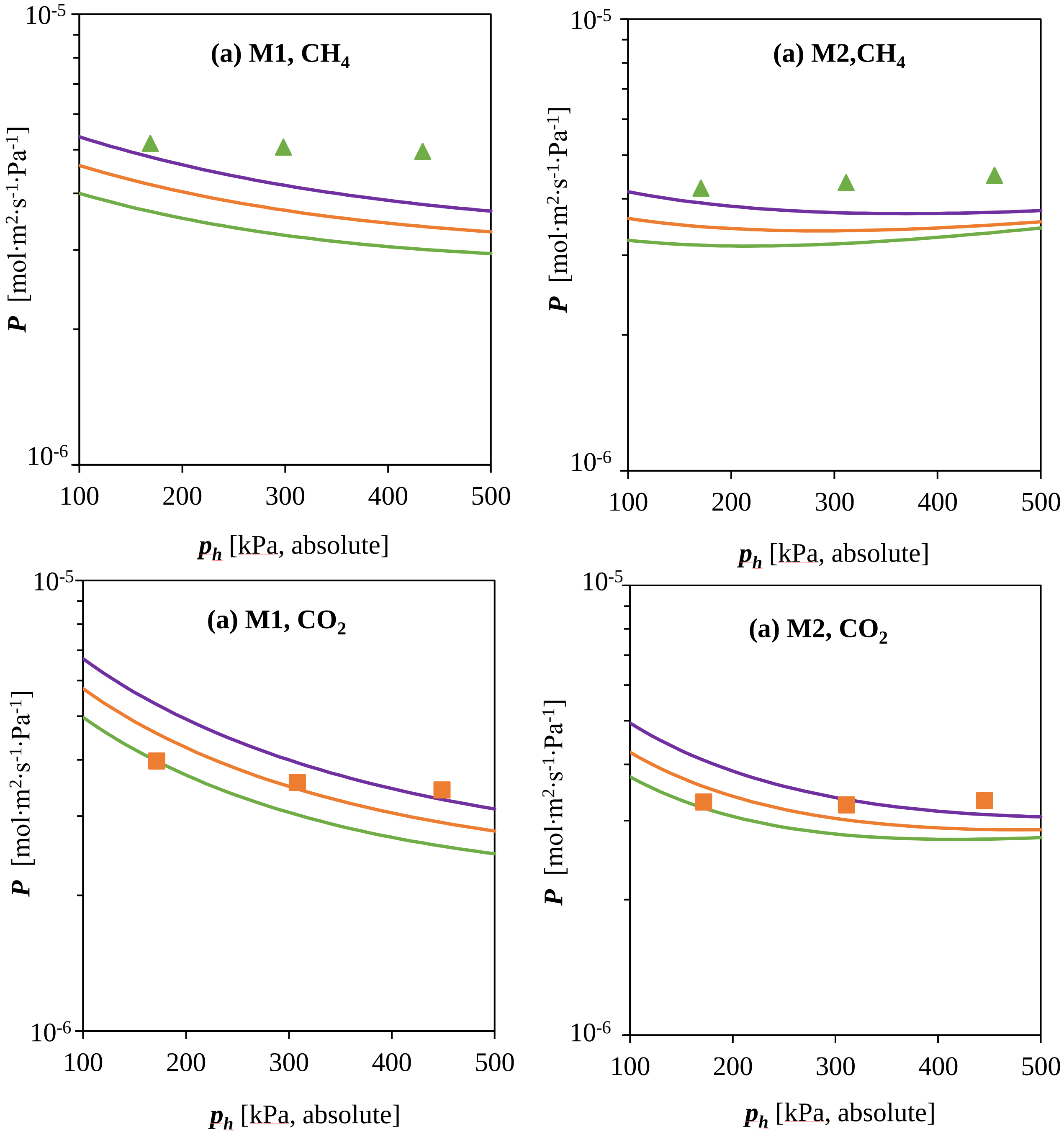

Figure 5.7. Experimentally determined and predicted permeances of CO_2 and CH_4 through calcined M1 and M2. Parameters x, d_d, y, and D_T as required to predict permeances have been determined using the 170 kPa (**green**), 300 kPa (**orange**), and 450 kPa (**purple**) feed pressure data values shown in Table 5.3 and 5.4. Permeate side pressures have been assumed to be 101.325 kPa.

5.5.0 CONCLUSIONS

The ultimate goal of this study was to propose a method that could be used to characterize zeolite membranes containing defects, and extract parameters, which quantify their intrinsic properties. These parameters have been denoted x, d_d, y, and D_{TN_2}, which describe the channel network of defects, the effective diameter of the defects, the zeolite crystal channel network, and the transport diffusivity of N_2. From these parameters, a set of equations which describe molecular transport in terms of simultaneous Knudsen and viscous flow through defects, as well as surface diffusion or Knudsen flow through zeolite channels (subject to the physicochemical properties of the zeolite and gas molecules) was developed. To demonstrate this model, two silicalite membranes, M1 and M2 were hydrothermally synthesized inside autoclaves with different liquid levels. These membranes were then characterized using the proposed method, which included measuring the permeances of He and N_2 gases in turn through each membrane at three different feed pressures, before and after calcination of the membrane.

Comparative analysis of permeances predicted using characteristic parameters from each feed pressure data set showed that the defect parameters x and d_d are coupled, and that their exact values were subject to uncertainty when they had been determined using the proposed method. As long as their relationship was maintained however, good predictions for defect transport at all pressure differentials were determined for He and N_2 gases. Zeolite parameters y and D_{TN_2} by comparison were more similar between membranes M1 and M2, and predicted He and N_2 transport through the calcined zeolite crystals of the membrane layer within experimental uncertainty at all pressure differentials. To evaluate the suitability of the proposed method to describe the molecular transport of gases which were not tested during membrane characterization, CH_4 and CO_2 permeance experiments were additionally conducted, and model predictions of their permeance compared to experimental permeances. These predictions did not perfectly describe the experimentally observed behaviour, however, they did show that the elements of the proposed equations are sufficiently detailed for practical purposes. Additionally, the parameters which describe CO_2 transport were found to be more sensitive to the feed pressure than those which describe CH_4 transport.

To summarize, the proposed method can be used to quantitatively describe the structure of zeolitic membranes given a limited number of in-situ gas permeation experiments. Further modifications to the proposed method would improve its accuracy, however, the current form of the proposed method can reasonably describe defective zeolitic membranes, and is sufficiently versatile that it is well suited for characterizing a wide variety of zeolite membrane types.

5.6.0 ACKNOWLEDGEMENTS

This research was financially supported by the Natural Sciences and Engineering Research Council of Canada (NSERC).

5.7.0 NOMENCLATURE

b	$[Pa^{-1}]$	Langmuir isotherm constant
d	[m]	Channel size
D_T	$[m^2\cdot s^{-1}]$	Transport diffusivity
J_d	$[mol\cdot m^{-2}\cdot s^{-1}]$	Defect flux
l	[m]	Effective length
M	$[kg\cdot mol^{-1}]$	Molecular weight
n	[-]	Number of defects per unit volume
P_i	$[mol\cdot m^{-2}\cdot s^{-1}\cdot Pa^{-1}]$	Permeance of gas i
P_d	$[mol\cdot m^{-2}\cdot s^{-1}\cdot Pa^{-1}]$	Defect permeance
P_z	$[mol\cdot m^{-2}\cdot s^{-1}\cdot Pa^{-1}]$	Zeolite permeance
p_h	[Pa]	Pressure at the high pressure side of the membrane

p_l	[Pa]	Pressure at the low pressure side of the membrane
q	[mol·kg^{-1}]	Surface loading
q^s	[mol·kg^{-1}]	Maximum surface loading
R	[m^3·Pa·K^{-1}·mol^{-1}]	Gas constant
T	[K]	Temperature
x	[m^{-1}]	Lumped parameter describing defect porosity over defect effective length ε_d / l_d
y	[m^{-1}]	Lumped parameter describing zeolite porosity over zeolite effective length ε_s / l_s

Subscripts

i, j	Gas component identifier
d	Defect
v	Viscous flow
K	Knudsen flow
z	Zeolite

Greek letters

α	[-]	Ideal selectivity
ε	[-]	Volume fraction
μ	[Pa·s^{-1}]	Dynamic viscosity
ρ	[kg·m^{-3}]	Zeolite density

Abbreviations

CH_4	Methane
CO_2	Carbon dioxide
F-	Bubble flow metes
H_2	Hydrogen
H_2O	Water

He	Helium
M1, M2	Membrane identifiers
MFC-	Mass flow controller
MS	Maxwell-Stefan
N_2	Nitrogen
NaY	Sodium Y Zeolite
NSERC	Natural Sciences and Engineering Research Council of Canada
P-	Pressure transducer
PFD	Process flow diagram
SF_6	Sulfur Hexafluoride
Si	Silica
SiO_2	Silica dioxide
T-	Thermocouple
TiO_2	Titanium dioxide
TPAOH	Tetra-propyl ammonium hydroxide

5.8.0 REFERENCES

[1] D. Ruthven, Principles of adsorption and adsorption processes, John Wiley and Sons, 1984.

[2] M. Pera-Titus, Porous inorganic membranes for CO_2 capture: Present and prospects, Chem. Rev. 114 (2014) 1413–1492. doi:10.1021/cr400237k.

[3] J.D. Figueroa, T. Fout, S. Plasynski, H. McIlvried, R.D. Srivastava, Advances in CO_2 capture technology—The U.S. Department of Energy's Carbon Sequestration Program, Int. J. Greenh. Gas Control. 2 (2008) 9–20. doi:10.1016/S1750-5836(07)00094-1.

[4] H. Maghsoudi, Defects of Zeolite Membranes: Characterization, Modification and Post-treatment Techniques, Sep. Purif. Rev. 45 (2016) 169–192.

doi:10.1080/15422119.2015.1103270.

[5] G. Pecanac, J. Malzbender, F. Pauly, M.L. Fontaine, P. Niehoff, S. Baumann, T. Beck, L. Singheiser, Mechanical characterization of ceramics by means of a 3D defect analysis, 41 (2015) 2411–2417. doi:10.1016/j.ceramint.2014.10.055.

[6] S. Gourdin, L. Marcin, M. Podgorski, M. Cherif, L. Carroz, Effective elastic properties and residual stresses in directionally solidified eutectic Al_2O_3/YAG/ZrO_2 ceramics estimated by finite element analysis, J. Mater. Sci. 52 (2017) 13736–13747. doi:10.1007/s10853-017-1479-6.

[7] M. Drobek, J. Motuzas, M. van Loon, R.W.J. Dirrix, R. a. Terpstra, A. Julbe, Coupling microwave-assisted and classical heating methods for scaling-up MFI zeolite membrane synthesis, J. Memb. Sci. 401–402 (2012) 144–151. doi:10.1016/j.memsci.2012.01.045.

[8] C. Bai, M.-D. Jia, J.L. Falconer, R.D. Noble, Preparation and separation properties of silicalite composite membranes, J. Membr. Scien. 1–2 (1995) 79–87. doi:10.1016/0376-7388(95)00049-I.

[9] W. Xiao, J. Yang, J. Lu, J. Wang, A novel method to synthesize high performance silicalite-1 membrane, Sep. Purif. Technol. 67 (2009) 58–63. doi:10.1016/j.seppur.2009.03.007.

[10] J.B. Lee, H.H. Funke, R.D. Noble, J.L. Falconer, High selectivities in defective MFI membranes, J. Memb. Sci. 321 (2008) 309–315. doi:10.1016/j.memsci.2008.05.004.

[11] J. Van Den Bergh, M. Mittelmeijer-Hazeleger, F. Kapteijn, Modeling Permeation of CO_2/CH_4, N_2/CH_4, and CO_2/Air Mixtures across a DD3R Zeolite Membrane, J. Phys. Chem. 114 (2010) 9379–9389. doi:10.1021/jp101075h.

[12] P.F. Lito, A.S. Santiago, S.P. Cardoso, B.R. Figueiredo, C.M. Silva, New expressions for single and binary permeation through zeolite membranes for different isotherm models, J. Memb. Sci. 367 (2011) 21–32. doi:10.1016/j.memsci.2010.10.034.

[13] R. Krishna, Describing the Diffusion of Guest Molecules Inside Porous Structures, J. Phys. Chem. 113 (2009) 19756–19781. doi:10.1021/jp906879d.

[14] T.Q. Gardner, J.L. Falconer, R.D. Noble, Adsorption and diffusion properties of zeolite membranes by transient permeation, Desalination. 149 (2002) 435–440. doi:10.1016/S0011-9164(02)00772-5.

[15] J. Kangas, L. Sandstrom, I. Malinen, J. Hedlund, J. Tanskanen, Maxwell–Stefan modeling of the separation of H_2 and CO_2 at high pressure in an MFI membrane, J. Memb. Sci. 435 (2013) 186–206. doi:10.1016/j.memsci.2013.02.026.

[16] A. Caravella, P.F. Zito, A. Brunetti, E. Drioli, G. Barbieri, Microporous and Mesoporous Materials A novel modelling approach to surface and Knudsen multicomponent diffusion through NaY zeolite membranes, Microporous Mesoporous Mater. 235 (2016) 87–99. doi:10.1016/j.micromeso.2016.07.049.

[17] P.F. Zito, A. Caravella, A. Brunetti, E. Drioli, G. Barbieri, Knudsen and surface diffusion competing for gas permeation inside silicalite membranes, J. Memb. Sci. 523 (2017) 456–469. doi:10.1016/j.memsci.2016.10.016.

[18] F. Jareman, J. Hedlund, D. Creaser, J. Sterte, Modelling of single gas permeation in real MFI membranes, J. Memb. Sci. 236 (2004) 81–89. doi:10.1016/j.memsci.2004.01.028.

[19] D. Kennedy, D. Carter, S. Wilson, B. Kruczek, F.H. Tezel, Pore plugging synthesis and characterization of silicalite-1 membranes using tubular TiO_2 supports: Effect of support pore size on membrane performance., Can. J. Chem. Eng. (2018). doi:0.1002/cjce.23095.

[20] J. Kärger, D.M. Ruthven, D.N. Theodorou, Diffusion in Nanoporous Materials, John Wiley and Sons, 2012.

[21] R.W. Baker, Membrane Technology and Applications, 3rd ed., Wiley, 2012.

[22] J. Dong, Y.S. Lin, M. Hu, R. Peascoe, E.A. Payzant, Template-removal-associated microstructural development of porous ceramic-supported MFI zeolite membranes,

Microporous Mesoporous Mater. 34 (2000) 241–253. doi:https://doi.org/10.1016/S1387-1811(99)00175-4.

[23] M.-D. Jia, K.-V. Peinemann, R.-D. Behling, Ceramic zeolite composite membranes., J. Memb. Sci. 82 (1993) 15–26. doi:10.1016/0376-7388(93)85089-F.

[24] J.M. Van De Graaf, F. Kapteijn, J.A. Moulijn, Permeation of weakly adsorbing components through a silicalite-1 membrane, Chem. Eng. Sci. 54 (1999) 1080–1092. doi:10.1016/S0009-2509(98)00326-1.

[25] X. Lin, J.L. Falconer, R.D. Noble, Parallel Pathways for Transport in ZSM-5 Zeolite Membranes, Chem. Mater. 10 (1998) 3716–3723. doi:10.1021/cm980484m.

[26] R.E. Kesting, A.K. Fritzsche, Polymeric Gas Separation Membranes, Wiley-Interscience, 1993.

[27] O. Talu, A.L. Myers, Reference potentials for adsorption of helium, argon, methane, and krypton in high-silica zeolites, Colloids Surfaces A Physicochem. Eng. Asp. 187–188 (2001) 83–93. doi:10.1016/S0927-7757(01)00628-8.

[28] R. Nagumo, H. Takaba, S. Suzuki, S. Nakao, Estimation of inorganic gas permeability through an MFI-type silicalite membrane by a molecular simulation technique combined with permeation theory, Microporous Mesoporous Mater. 48 (2001) 247–254. doi:10.1016/S1387-1811(01)00359-6.

[29] P. Malbrunot, D. Vidal, J. Vermesse, R. Chahine, T.K. Bose, Adsorbent Helium Density Measurement and Its Effect on Adsorption Isotherms at High Pressure, Langmuir. 13 (1997) 539–544. doi:10.1021/la950969e.

[30] A.B. Shelekhin, A.G. Dixon, Y.H. Ma, Theory of gas diffusion and permeation in inorganic molecular-sieve membranes, AIChE J. 41 (1995) 58–67. doi:10.1002/aic.690410107.

[31] J. Kärger, D.M. Ruthven, Diffusion in nanoporous materials: fundamental principles, insights and challenges, New J. Chem. 40 (2016) 4027–4048.

doi:10.1039/C5NJ02836A.

[32] S. Miachon, E. Landrivon, M. Aouine, Y. Sun, I. Kumakiri, Y. Li, O.P. Prokopová, N. Guilhaume, a. Giroir-Fendler, H. Mozzanega, J. A. Dalmon, Nanocomposite MFI-alumina membranes via pore-plugging synthesis. Preparation and morphological characterisation, J. Memb. Sci. 281 (2006) 228–238. doi:10.1016/j.memsci.2006.03.036.

[33] M. Anderson, H. Wang, Y.S. Lin, Inorganic membranes for carbon dioxide and nitrogen separation, Rev. Chem. Eng. 28 (2012) 101–121. doi:10.1515/revce-2012-0001.

[34] L. Tosheva, B. Mihailova, V. Valtchev, J. Sterte, Silicalite-1 macrostructures - preparation and structural features, Microporous Mesoporous Mater. 39 (2000) 91–101. doi:10.1016/S1387-1811(00)00179-7.

[35] P. Li, F.H. Tezel, Pure and binary adsorption of carbon dioxide and nitrogen on silicalite, J. Chem. Eng. Data. 53 (2008) 2479–2487. doi:10.1021/je7005902.

[36] P. Li, F.H. Tezel, Pure and Binary Adsorption Equilibria of Methane and Carbon Dioxide on Silicalite, 1 (2007) 3131–3153. doi:10.1080/01496390701512034.

[37] P. Li, F.H. Tezel, Pure and Binary Adsorption of Methane and Nitrogen by Silicalite, J. Chem. Eng. Data. 54 (2009) 8–15. doi:10.1021/je7005902.

[38] Y. Li, M. Pera-titus, G. Xiong, W. Yang, E. Landrivon, S. Miachon, J. Dalmon, Nanocomposite MFI-alumina membranes via pore-plugging synthesis : Genesis of the zeolite material, 325 (2008) 973–981. doi:10.1016/j.memsci.2008.09.030.

[39] W.J.W. Bakker, L.J.P. Van Den Broeke, F. Kapteijn, J. a Moulijn, Temperature Dependence of One-Component Permeation through a Silicalite-1 Membrane, AIChe J. 43 (1997) 2203–2214. doi:10.1002/aic.690430907.

[40] A.J. Burggraaf, Z. Vroon, K. Keizer, H. Verweij, Permeation of single gases in thin zeolite MFI membranes, J. Memb. Sci. 144 (1998) 77–86. doi:10.1016/S0376-7388(98)00036-2.

[41] C. Algieri, P. Bernardo, G. Golemme, G. Barbieri, E. Drioli, Permeation properties of a thin silicalite-1 (MFI) membrane, J. Memb. Sci. 222 (2003) 181–190. doi:10.1016/S0376-7388(03)00286-2.

[42] M. Noack, P. Kölsch, V. Seefeld, P. Toussaint, G. Georgi, J. Caro, Influence of the Si/Al-ratio on the permeation properties of MFI-membranes, Microporous Mesoporous Mater. 79 (2005) 329–337. doi:10.1016/j.micromeso.2005.01.004.

[43] D. Carter, D. Kennedy, F.H. Tezel, B. Kruczek, Characterization of Inorganic Silicalite - 1 Membrane to be used for the Separation of Greenhouse Gases, J. Fluid Flow Heat Mass Transf. 1 (2014) 43–47. doi:10.11159/jffhmt.2014.007.

[44] G.K. Papadopoulos, H. Jobic, D.N. Theodorou, Transport diffusivity of N_2 and CO_2 in silicalite: Coherent quasielastic neutron scattering measurements and molecular dynamics simulations, J. Phys. Chem. B. 108 (2004) 12748–12756. doi:10.1021/jp049265g.

[45] P. Ciavarella, H. Moueddeb, S. Miachon, K. Fiaty, J.A. Dalmon, Experimental study and numerical simulation of hydrogen/isobutane permeation and separation using MFI-zeolite membrane reactor, Catal. Today. 56 (2000) 253–264. doi:10.1016/S0920-5861(99)00283-7.

5.9.0 SUPPLEMENTARY MATERIAL

5.9.1 Feed and Permeate Side Pressures for He, N_2, CO_2, and CH_4

Due to the varied dimensions and characteristics of the defect and zeolite channels that are unique to each membrane, the relationship between feed pressure and permeate pressure varies from membrane to membrane. For each of the gases tested in this investigation, these relationships are shown in Fig. S.5.1.

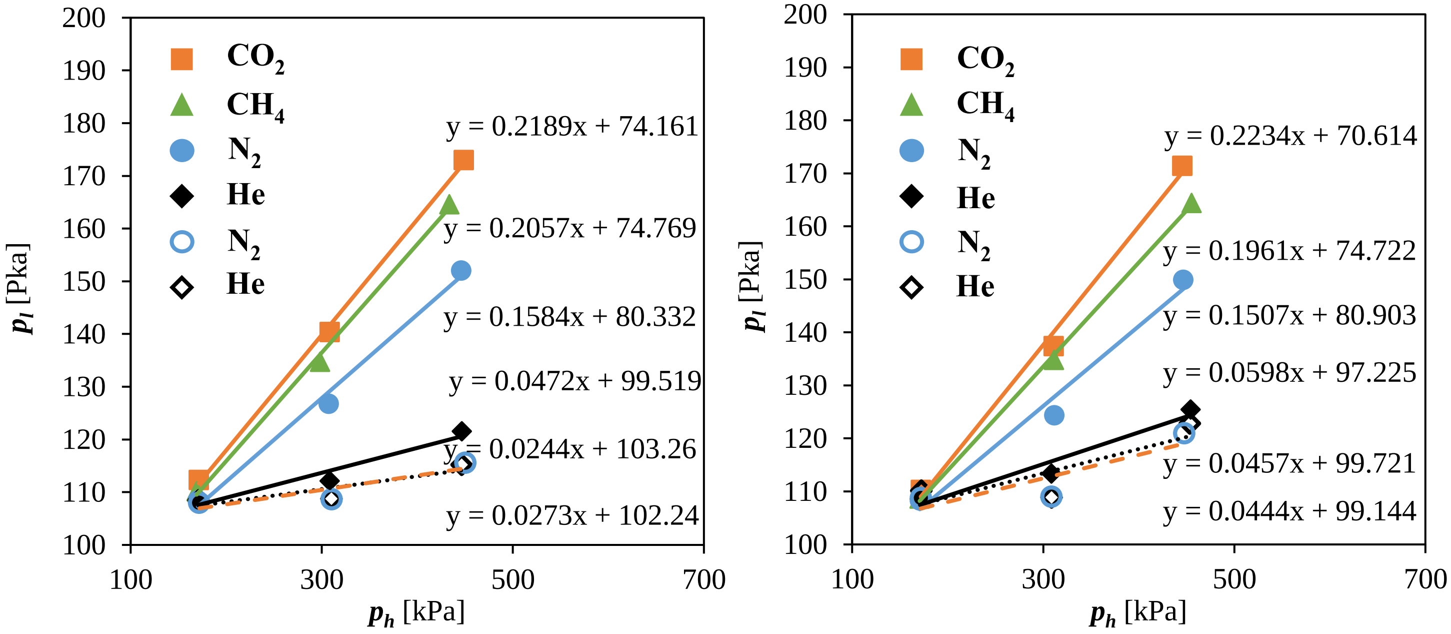

Figure S.5.1. Experimentally determined He, N_2, CO_2, and CH_4 feed pressure p_h, and permeate pressure p_l for M1 and M2. Unfilled points denote uncalcined membrane permeances, and filled points denote calcined membrane permeances. Permeation experiments were conducted at a temperature of 295 ± 2 K. Membrane length and area are 6.0 ± 0.1 cm, and 10.5 ± 0.1 cm^2 respectively.

5.9.2 CO_2 and CH_4 permeance predictions including permeate side pressure effects

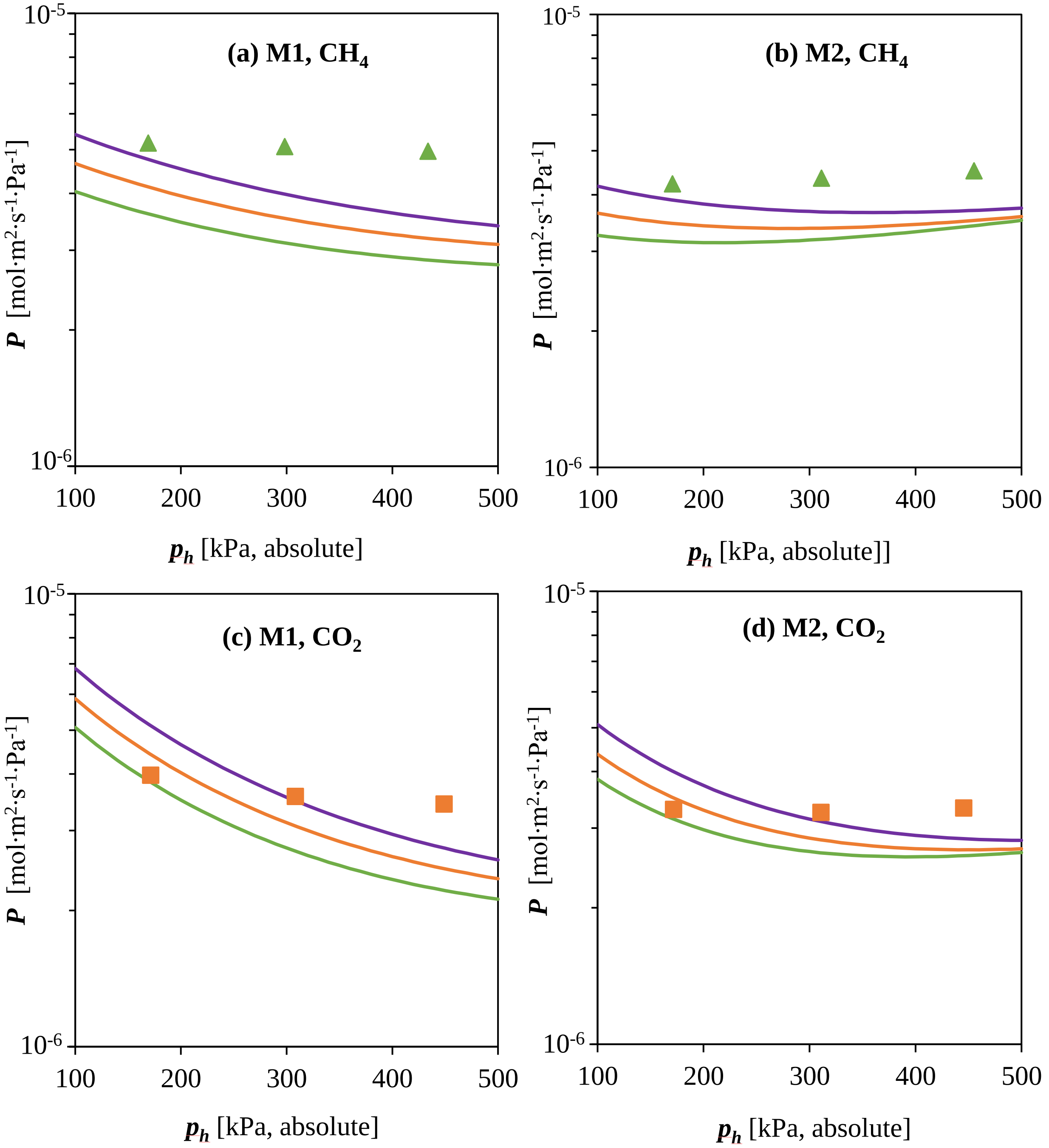

Figure S.5.2. Experimentally determined and predicted permeances of CO_2 and CH_4 through calcined M1 and M2. Parameters *x*, d_d, *y*, and D_T as required to predict permeances have been determined using the 170 kPa (**green**), 300 kPa (**orange**), and 450 kPa (**purple**) feed pressure data values shown in Table 5.3. Permeate side pressures as required for predictions have been calculated using the linear relationships shown in Figure S.5.1.

Chapter 6

Maxwell-Stefan Model Characterization of Silicalite Membranes Containing Viscous and Knudsen Sized Defects with CO_2 and N_2 Gas Mixtures

D. Carter[1], S. Al-Akwaa[1], B. Kruczek[1], F.H. Tezel[1] *
[1]University of Ottawa, Department of Chemical and Biological Engineering
161 Louis Pasteur, Ottawa, Ontario, CANADA, K1N 6N5
*Corresponding author

To be Submitted to: ***Journal of Membrane Science***

ABSTRACT

Although the goal of all membrane studies is to fabricate membranes without defects, to do so is very challenging. Newly fabricated membranes must therefore be characterized with consideration of their defects, which is also challenging due to the effects of different flow regimes through these defects on membrane performance. In this paper we therefore propose a method which allows discounting of defect flows in order to obtain the actual Maxwell-Stefan (MS) diffusivities and MS exchange coefficients from experimental results for defect containing zeolite membranes. These parameters describe the transport of gas molecules through zeolitic channels with consideration of adsorption phenomena and intermolecular interactions, which significantly affect gas mixture transport through zeolite membranes. To demonstrate the proposed method, the MS diffusivities and MS exchange coefficients of CO_2 and N_2 have been determined for two defect containing silicalite membranes. With the proposed method, we were able to observe a 44% decrease in the permeance of N_2 present in a binary gas mixture with CO_2 in comparison to pure N_2 permeance for gas transport through the zeolitic channels by surface diffusion only. When these binary surface diffusion permeances were used to determine CO_2 permeability and CO_2/N_2 permselectivity, a permeability of 91000 barrer, and permselectivity of 17 [-] were determined at the lowest total feed pressure investigated. These characteristics are notably above the Robeson upper bound. MS diffusivities of CO_2 and N_2; $Đ_{N_2}$ and $Đ_{CO_2}$, were found to be 7.26 – 8.33 x 10^{-8} $m^2 \cdot s^{-1}$, and 1.17 – 1.95 x 10^{-8} $m^2 \cdot s^{-1}$, respectively. Lastly, $Đ_{N_2/CO_2}$ and $Đ_{CO_2/N_2}$ exchange coefficients were determined, and $Đ_{N_2/CO_2}$ was found to be at least 1.38 times greater than $Đ_{CO_2/N_2}$ for both membranes, which challenges the Vignes correlation that is commonly used to describe exchange coefficients required to predict membrane performance using the MS model. The calculated performance characteristics are suitable for comparison of intrinsic properties of different types of zeolite membranes.

Keywords: Zeolites, Silicalite, Membranes, Surface Diffusion, Maxwell-Stefan

HIGHLIGHTS

- Silicalite membranes have been characterized using the Maxwell-Stefan model.
- Defect channel contributions to membrane performance have been excluded from the analysis.
- Maxwell-Stefan diffusivities and exchange coefficients for N_2 and CO_2 in silicalite membranes have been determined.

6.1.0 INTRODUCTION

6.1.1 Background

The incorporation of membrane technology for the separation of gas mixtures provides several opportunities for improving process efficiencies, flexibility, and control in comparison to other technologies such as cryogenic distillation and absorption [1]. Due to their modular nature, membrane processes can also be easily scaled to grow with processing plants, are mechanically simple as they do not contain many parts, and can respond quickly to changes in upstream or downstream conditions. The range of gas separation processes which can utilize membranes is similarly diverse and includes biogas or natural gas upgrading, flue gas treatment, and air separation.

Several different membrane types have been developed in response to the unique challenges posed by each separation application, and include polymeric, inorganic, and mixed matrix type membranes. In this manuscript, inorganic type membranes composed of zeolite crystals are of interest due to their higher thermal and chemical stability in comparison to the other membrane types [2]. The two most common ways to make zeolite membranes are the secondary growth method, and the pore plugging method, which have been described by others [1]. Membranes fabricated by the secondary growth method are composed of a uniform and selective zeolite crystal layer on top of a membrane support, and are fabricated in three stages. Firstly, zeolite crystals are grown in an autoclave. Next, these crystals are deposited onto the surface of a porous membrane support. Finally, the seeded membrane support undergoes hydrothermal synthesis of the zeolite crystal layer. Membranes fabricated by the pore plugging method are conversely made up of abutting zeolite crystals inside microporous ceramic membrane supports, which do not require seeding, and are grown in a single hydrothermal synthesis step. This simpler fabrication procedure is easier to reproduce than the more complex procedure for secondary growth membranes. Another important difference between membranes fabricated by the two methods is how they respond to changes in temperature, which occurs during membrane calcination to remove the template molecules from the zeolite crystal pores. Due to the different expansion coefficients of the membrane support and zeolite crystals, cracks in the membrane layer can be formed during this process, which are henceforth referred to as defects [3,4]. For pore plugged membranes, the consequences of defect formation can be less significant than for secondary growth membranes due to their 3D structure. In this way, defect pathways can be limited to a region of the selective membrane layer which does not necessarily create a continuous defect pathway across the membrane layer. So in order to realize the many beneficial attributes or pore plugged membranes, it is necessary to consider both the defect and zeolite pathways to characterize them and predict their performance.

To quantify the characteristics of zeolitic and defect channels in membranes, techniques such as permporometric and bubble point analyses have been developed by others. Although these techniques have been shown to accurately describe zeolitic membranes, they can be destructive to the membrane being analysed, and / or require specialized equipment which is not suitable for characterizing large membranes in-situ [5]. Alternatively, mass transport models have been proposed as they can be used to predict membrane performance based on a limited number of in-situ permeation experiments without destroying the membrane, and be applied to membranes of any size [6–8]. The most well known and proven model of this type is the Maxwell-Stefan (MS) model which has been well described by Krishna et al. [9]. In the MS model, the diffusivity of gas molecules, and exchange coefficients which describe molecular interactions can be determined with consideration of adsorption phenomena and isotherm data. Diffusivities are fundamental properties of molecular mass transport, and have been determined for different gases through various zeolites by others [9–11]. The MS model is therefore applicable to characterize defect-free zeolite membranes. On the other hand, the presence of defects in zeolite membranes is practically unavoidable. To address this limitation of the MS model due to a lack of reliable experimental data, a method has been proposed by the authors previously to quantify the physical characteristics of the defect and zeolite pathways. This method which has been included in this thesis is based on a limited number of in-situ, pure gas permeation experiments, and can be used to describe pure gas permeation through zeolite membranes [12].

In this study, the previously developed method has been used to characterize zeolite membranes based on CO_2/N_2 gas mixture separation experiments by assuming applicability of the MS transport model through the membrane's zeolite crystals. To demonstrate the proposed method, binary gas permeation experiments were conducted using a mixture of 15% CO_2 and 85% N_2 (which is similar to post combustion flue gas), using silicalite membranes. The contributions of viscous and Knudsen flow through defects to the experimentally determined performance have then been quantified, and excluded from the MS characterization analysis to account for structural differences between the two membranes. The binary gas mixture permeation experiments have also been conducted at different pressure differentials. In doing so, a range of operating conditions can be evaluated to test the limitations of the Vignes correlation. According to this correlation, MS exchange coefficients pairs are assumed to be equivalent to each other, which may significantly affect MS predictions when strong intermolecular interactions affect the transport of gas mixtures [13]. The Vignes correlation has therefore been challenged for some adsorbent-adsorbate systems such as using SAPO-34 and MFI by others, as these systems can sometimes exhibit phenomena where binary gas mixture separation performance is not well predicted by pure component behaviour. [14,15].

6.1.2 Molecular Transport Through Zeolite Membrane

To describe trans-membrane transport, it is necessary to consider the defect and zeolite channels separately as they are governed by different mass transfer mechanisms. Within each transport pathway, the permeance (pressure normalized flux) of each gas is dependent on the characteristics of the defect or zeolite pores, as well as the properties of the gas molecules.

For transport through defects, if the defects are sufficiently small in comparison to the mean free path of the gas molecules, Knudsen flow takes place. In this regime, gas molecules more frequently collide with the defect pore walls than other molecules, and lighter molecules in binary mixtures are preferentially transported over the heavier ones. For defects, whose pore size is greater than the mean free path of the gas molecules, and thus gas molecules collide more frequently with other gas molecules than with the defect wall, viscous flow dominates. In this regime, the molecular transport of each component is subject to the viscosity of the mixture, and there is no preferential transport of a molecular type. Both Knudsen and viscous flow occur simultaneously inside defect pores. Viscous and Knudsen flow permeances of component *i*, $\mathrm{P}_{V,i}$, and $\mathrm{P}_{K,i}$, can be described using equations *1* and *2*, respectively [1].

$$\mathrm{P}_{V,i} = \frac{\varepsilon_d}{l_d} d_d^2 \frac{(P_h + P_l)}{64\mu RT} \tag{1}$$

$$\mathrm{P}_{K,i} = \frac{\varepsilon_d}{l_d} d_d \frac{1}{3} \sqrt{\frac{8}{\pi M_{W,i} RT}} \tag{2}$$

where ε_d, l_d, and d_d are the defect porosity, effective path length in the defects, and the effective defect pore size, respectively. μ and M_W are the viscosity and molar weight, respectively. P_h and P_l are the total pressures at the high and low pressure sides of the membrane, respectively. T is the temperature, and R is the gas constant.

Due to the varied physico-chemical properties of gas molecules and zeolite pores, each type of gas has a different affinity for each type of zeolite crystal. Consequently, molecules with a greater affinity for the zeolite crystals of the membrane will be preferentially adsorbed, and transported in the direction of decreasing surface occupancy in accordance to Fick's law of diffusion [16]. Transport through zeolite crystals therefore proceeds according to the regime of surface diffusion, which is a function of synergistic adsorption and diffusion phenomena. In this investigation, it has been assumed that surface diffusion permeance of component *i*, $\mathrm{P}_{SD,i}$, can be described as the product of the zeolite crystal characteristics, adsorption capacity difference driving force, and transport diffusivity $D_{T,i}$ as shown in equation 3 [1,12,17]. This relationship is analogous to the solution diffusion model for gas transport across polymeric membranes, which describes permeance as the product of solubility and diffusivity.

$$\mathrm{P}_{SD,i} = \frac{\varepsilon_s}{l_s}\rho_s \frac{\left(q_{h,i} - q_{l,i}\right)}{\left(P_h - P_l\right)} D_{T,i} \tag{3}$$

where $q_{h,i}$, and $q_{l,i}$ are the amounts of component *i* adsorbed at the high and low pressure sides of the membrane, respectively. ε_s, and l_s are the silicalite channel porosity, and effective silicalite path length respectively. l_s includes tortuosity effects through the varied channel sizes and varied direction inside the porous zeolite structure. ρ_s, is the density of the silicalite adsorbent.

To determine MS diffusivity, it is necessary to determine the thermodynamic factor contribution to diffusivity from the Fickian diffusivity [16]. To this end, equation 3 can be re-written as a function of MS diffusivity Đ_i as shown in equation 4 for the transport of a pure gas.

$$\mathrm{P}_{SD,i} = \frac{\varepsilon_s}{l_s}\rho_s \frac{\left(q_{h,i} - q_{l,i}\right)}{\left(P_h - P_l\right)} \text{Đ}_\mathrm{i}\Gamma_i = \frac{\varepsilon_s}{l_s}\rho_s \frac{\left(q_{h,i} - q_{l,i}\right)}{\left(P_h - P_l\right)} \text{Đ}_\mathrm{i} \frac{d\ln(P)}{d\ln(q_i)} \tag{4}$$

where Đ_i is the MS diffusivity of *i*, and Γ_i is the thermodynamic factor.

For the pure gas transport of component *i* across a membrane, it is reasonable for many zeolite and gas types to assume that monolayer adsorption of gases occurs due to the narrow size of the zeolite's pores. The amounts of gas adsorbed can therefore be described by the Langmuir model which is shown in equation 5.

$$q_i = q_i^{sat} \frac{K_i P_i}{1 + K_i P_i} \tag{5}$$

Equation 4 can be multiplied by the pressure differential to convert permeance to molar flux J_i to yield equation 6 for adsorbed molecules.

$$J_i = \frac{\varepsilon_s}{l_s} \rho_s \text{Đ}_\text{i} \left(q_{h,i} - q_{l,i} \right) \frac{d \ln(P)}{d \ln(q_i)} \tag{6}$$

where q_i^{sat} is the saturation adsorption capacity for component *i*, and K_i is the Langmuir adsorption isotherm constant for component *i*. The values of K_i and q_i^{sat} can be obtained from pure component isotherms.

The general MS model equation for multicomponent gas transport is shown in equation 7 [18]. In this equation, the driving force for molecular transport is shown on the left hand side of the equation, and is expressed as the change in chemical potential of component *i*, μ_i, at two boundaries of the membrane. The first term on the right hand side of the equation represents the transport of component *i* subject to interactions with the channel walls only, and the second term represents the transport of component *i* subject to molecular interactions with other components in the mixture. This final term contains the exchange coefficient Đ_ij, which is a measure of the resistance exerted on component *i*, by component *j*. For the case of surface diffusion through a pore channel, displacement of adsorbed molecules is required for molecular transport in the direction of decreasing surface occupancy, which imparts resistance and slows down the rate of adsorption too. Given these phenomena, MS exchange coefficients can be interpreted as inverse drag coefficients [18].

$$-\nabla\mu_i = RT\frac{u_i}{Đ_\mathrm{i}} + RT\sum_{j=1,j\neq i}^{n}\theta_j\frac{u_i-u_j}{Đ_\mathrm{ij}} \tag{7}$$

where u_i is the velocity of *i*. θ_i is the fractional zeolite occupancy for component *i*.

Fractional coverages is expressed as follows:

$$\theta_i = \frac{q_i}{q_i^{sat}} \tag{8}$$

Velocities can be expressed in terms of the respective fluxes as follows:

$$u_i = \frac{J_i}{\rho_s q_i^{sat}\theta_i} = \frac{J_i}{\rho_s q_i} \tag{9}$$

When equation 7 is multiplied by θ_i/RT, and equations 8 and 9 are substituted into equation 7, equation 10 is obtained.

$$-\frac{\theta_i}{RT}\nabla\mu_i = \frac{1}{\rho_s}\left(\frac{J_i}{q_i^{sat}Đ_\mathrm{i}} + \sum_{j=1,j\neq i}^{n}\frac{q_jJ_i-q_iJ_j}{q_i^{sat}q_j^{sat}Đ_\mathrm{ij}}\right) \tag{10}$$

These equations have been described in detail by Krishna [18,19]. When the MS model is applied in this way to describe molecular transport across membranes, it is necessary to assume that the diffusion parameters $Đ_\mathrm{i}$ and $Đ_\mathrm{ij}$ do not vary along the direction of feed flow. This assumption is reasonable when the stage cut (ratio of permeate flow rate over feed flow rate) approaches to zero. The chemical potential gradient driving force can be related to fractional zeolite loading and a matrix of thermodynamic factors as shown in equation 11 for the transport of *i* that is present in a gas mixture with other components. The general equation for the elements of the thermodynamic factor matrix for the adsorbate-adsorbate interaction is shown in equation 12. If the amounts adsorbed for a binary mixture are assumed to be described according to the extended Langmuir model, which is shown in equation 13, the matrix of thermodynamic factors is given by equation 14 [18].

$$-\frac{\theta_i}{RT}\nabla\mu_i = \sum_{j=1}^{n}\Gamma_{ij}\nabla\theta_j \tag{11}$$

$$\Gamma_{ij} = \theta_i \frac{d \ln(p_i)}{d\theta_j} \tag{12}$$

$$q_1 = q_1^{sat} \frac{K_1 p_1}{1 + K_1 p_1 + K_2 p_2},\ q_2 = q_2^{sat} \frac{K_2 p_2}{1 + K_1 p_1 + K_2 p_2} \tag{13}$$

$$\Gamma = \begin{bmatrix} \dfrac{1-\theta_2}{1-\theta_1-\theta_2} & \dfrac{\theta_1}{1-\theta_1-\theta_2} \\ \dfrac{\theta_2}{1-\theta_1-\theta_2} & \dfrac{1-\theta_1}{1-\theta_1-\theta_2} \end{bmatrix} \tag{14}$$

Combining equations 10 and 11, and substituting equations 12 and 13 leads to equations 15 and 16 after rearrangements. To distinguish between pure and binary gas mixture fluxes, the binary gas mixture fluxes of components *1* and *2* have been denoted N_1 and N_2 [mol·m^{-2}·s^{-1}]. It should be emphasized that equations 15 and 16 are applicable for zero stage cut conditions, and that greater uncertainty is introduced at stage cuts greater than 0.

$$N_1 = -\frac{\varepsilon_s}{l_s} \rho_s q_1^{sat} \text{Đ}_1 \left[\frac{\left(\Gamma_{11} + \frac{\theta_1 \text{Đ}_2}{\text{Đ}_{21}} \Gamma_{11} + \frac{\theta_1 \text{Đ}_2}{\text{Đ}_{12}} \Gamma_{21} \right) \nabla \theta_1 + \left(\Gamma_{12} + \frac{\theta_1 \text{Đ}_2}{\text{Đ}_{21}} \Gamma_{12} + \frac{\theta_1 \text{Đ}_2}{\text{Đ}_{12}} \Gamma_{22} \right) \nabla \theta_2}{1 + \frac{\theta_2 \text{Đ}_1}{\text{Đ}_{12}} + \frac{\theta_1 \text{Đ}_2}{\text{Đ}_{21}}} \right] \tag{15}$$

$$N_2 = -\frac{\varepsilon_s}{l_s} \rho_s q_2^{sat} \text{Đ}_2 \left[\frac{\left(\Gamma_{21} + \frac{\theta_2 \text{Đ}_1}{\text{Đ}_{21}} \Gamma_{11} + \frac{\theta_2 \text{Đ}_1}{\text{Đ}_{12}} \Gamma_{21} \right) \nabla \theta_1 + \left(\Gamma_{22} + \frac{\theta_2 \text{Đ}_1}{\text{Đ}_{21}} \Gamma_{12} + \frac{\theta_2 \text{Đ}_1}{\text{Đ}_{12}} \Gamma_{22} \right) \nabla \theta_2}{1 + \frac{\theta_2 \text{Đ}_1}{\text{Đ}_{12}} + \frac{\theta_1 \text{Đ}_2}{\text{Đ}_{21}}} \right] \tag{16}$$

6.2.0 EXPERIMENTAL

6.2.1 Membrane Fabrication Procedure

To demonstrate the proposed characterization method, tubular Filtanium^{TM} supports from TAMI Industries (Nyons, France) were used to synthesize silicalite membranes by the pore plugging method. These supports are composed of TiO_2, have an active layer that is approximately 10 μm thick, with an average pore size of 0.45 μm. The membranes that have been used in this investigation, as well as details of the membrane fabrication procedure and support preparation steps have been described in more detail previously [12]. Two membranes have been fabricated and characterized in this study, which are referred to as M1 and M2.

To accommodate the synthesized membranes inside the membrane module that has been used during permeation experiments, the ends of the unfilled membrane supports have first been glazed with Aremco 617 from Aremco Products Inc (Valley Cottage, NY, USA). To fabricate the membranes, silicalite crystals have then been hydrothermally synthesized inside the active layer of the glazed membrane supports using a Teflon lined autoclave. The precursor solution that is required for the hydrothermal synthesis of silicalite is composed of 99.8 mol % purity silicon dioxide (SiO_2), 1 M tetrapropyl ammonium hydroxide (TPAOH), and deionized water (H_2O). The molar ratios of each component in this precursor solution are described in Table 6.1. After hydrothermal synthesis of the membranes, they were dried at 373 K for 20 hours, and calcined at 773 K for 4 hours. The heating and cooling rates for drying and calcination were 1 $K \cdot min^{-1}$. Table 6.1 shows that these membranes were fabricated identically, except for the free volume above the precursor solution in the autoclave during the hydrothermal synthesis, which was greater for M2 than M1. Although this free volume varied, both membranes were completely submerged during hydrothermal synthesis. SiO_2 and TPAOH were purchased from Sigma (Oakville, ON, Canada).

Table 6.1. Selected properties of the synthesis parameters for the membranes M1 and M2 that have been utilized in this study [12].

Membrane	**Hydrothermal Synthesis Preparation**			**Synthesis Round 1**			**Synthesis Interruption**		**Synthesis Round 2**			
	Precursor solution molar ratio Si : TPAOH : H_2O	Stirring time	Free Volume in Autoclave	Heating ramp	Hold Temp.	Hold time	Time	Cooling ramp	Heating ramp	Hold Temp.	Hold time	Cooling ramp
	[mol]	[h]	[% of total volume]	[$K \cdot min^{-1}$]	[K]	[h]	[h]	[$K \cdot min^{-1}$]	[$K \cdot min^{-1}$]	[K]	[h]	[$K \cdot min^{-1}$]
M1	1 : 0.45 : 27.8	72	< 1.0	1	443	12	11	1	1	443	72	1
M2	1 : 0.45 : 27.8	72	5.6	1	443	12	11	1	1	443	72	1

6.2.2 Gas Permeation Experiments

To evaluate the performance of the membranes fabricated in this study, in-situ gas permeation experiments have been conducted using the experimental setup whose process flow diagram is shown in Figure 6.1. In this setup, tubular silicalite membranes are contained inside a stainless steel module M that has been built in house at the University of Ottawa. With this module, a gas tight seal between the module and the membrane is created by axially compressing graphite gaskets, which then expand radially to completely cover the glazed ends of the membrane. Pure gases, or gas mixtures, can then be fed to the membrane inside the module at defined flow rates using mass flow controllers MFC1 and MFC2. The pressures of the retentate and permeate streams are measured using pressure transducers P1 and P2, respectively, and a pressure gradient as required for permeation across the membrane is induced by closing the metering valve V2. Feed flow rates can therefore be controlled using the mass flow controllers, and feed pressure is increased or decreased by opening or closing V2. The permeate stream is vented to a fume hood at approximately atmospheric pressure. The composition of the feed or permeate stream is determined using the Gas Chromatograph GC, and the stream of interest is directed to the GC as desired by valve V1. The flow rates of the permeate and retentate streams (or feed stream if directed by V1), are measured using bubble flow meters F1 and F2. Temperature has been controlled and set below room temperature by placing the system inside a fridge whose temperature is controlled with a digital thermostat control unit manufactured by Johnson Controls (Ottawa, ON, Canada). The in-line gas temperature has been measured using thermocouple T1. The composition of the retentate stream can be determined by mass balance as required.

To conduct pure gas permeation experiments, constant feed flow rates up to 10 L(STP)·min^{-1} are set using one of the mass flow controllers MFC 1 or MFC 2, which are then fed to the membrane. Feed side pressures from 170 kPa up to 450 kPa were then induced by closing V2, which resulted in permeate side pressures between 109 kPa and 170 kPa. At steady state, permeate flow rates were measured using F1. For the characterization method proposed in this study, pure gas permeation experiments have been conducted using

He and N_2 gases in turn prior to membrane calcination, and He, N_2, and CO_2 following membrane calcination.

To conduct binary gas mixture permeation experiments, feed flow rates of 3 ± 0.05 $L \cdot min^{-1}$ were used, and the gas mixture composition was maintained at 15 % ± 0.5 % CO_2 in a binary gas mixture with N_2. The total feed side pressures between 170 kPa and 450 kPa were also used, and permeate side pressures between 109 kPa and 170 kPa resulted. Feed flow rates and composition were measured at the start and end of each experiment. During experiments, permeate flow rates, permeate compositions, as well as feed and permeate side pressures were measured as a function of time. The experiments ended when all the measured operating conditions were constant.

He with a purity of 99.999%, N_2 with a purity of 99.998% and CO_2 with a purity of 99.99% have been used and were purchased in gas cylinders from Linde, (Missisauga, ON, Canada). The mass flow controllers have operating ranges of 0 – 1000 $ml(STP) \cdot min^{-1}$ (MFC1) and 0 – 10 $L(STP) \cdot min^{-1}$ (MFC2), are of Bronkhorst and MKS make, and were purchased from Hoskin (Burlington, ON, Canada), and MKS (Andover, MA, USA), respectively. The pressure transducers are of Cole Parmer make (Montreal, QC, Canada), and thermocouple was purchased from Omega, (Laval, QC, Canada). The gas chromatograph is made up of an HP 5730A oven temperature programmer (Ottawa, ON, Canada), and a Gow Mac 40 series detector (Bethlehem, PA, USA).

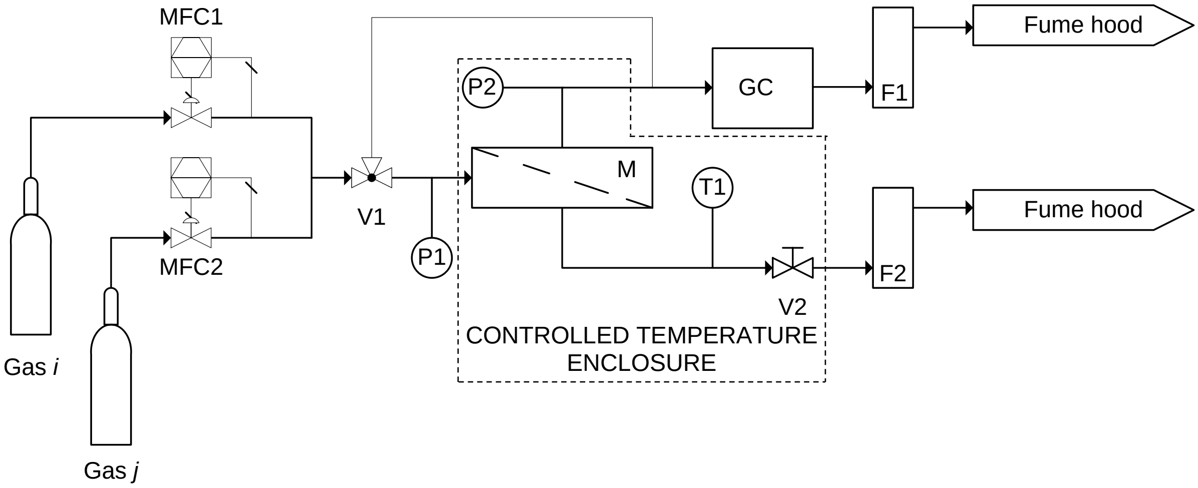

Figure 6.1. Process flow diagram showing the setup that has been used in this study to conduct gas permeation experiments. MFC1 and MFC2 are mass flow controllers, P1 and P2 are pressure transducers, T1 is a thermocouple, and F1 and F2 are bubble flow meters. V1 is a 3 way ball valve, and V2 is a metering valve. M is the module housing the membrane, and GC is the gas chromatograph.

6.2.3 Procedure for MS Characterization of Zeolite Membranes

The proposed characterization method draws upon literature data, as well as the results from in-situ gas permeation experiments to determine MS diffusivities $Đ_1$ and $Đ_2$ for pure components, as well as MS exchange coefficients $Đ_{12}$ and $Đ_{21}$ for the components of a binary gas mixture. To determine these parameters in the proposed method, it is necessary to first determine the parameters ε_d/l_d , d_d , ε_s/l_s , and $D_{T,i}$, which describe characteristics of the membrane, and the characteristics of each flow regime that contributes to gas mixture transport across the membrane. These flow rates for viscous, Knudsen, and surface diffusion regimes are referred to as Q_{PV}, Q_{PK}, and Q_{PSD}, respectively. In characterizing these regimes, the compositions of each regime are also determined.

In the proposed method, the following assumptions have been made, which are in common with the study conducted by Carter et al. [12]. Firstly, it has been assumed that the tubular membranes used in this study are analogous to flat, rectangular membranes. This assumption is reasonable as the thickness of the active layer of both membranes is approximately 10 µm, which is several orders of magnitude less than the diameter of the whole tubular support which is 0.55 ± 0.01 cm. The defects are modelled as uniformly sized cylindrical pores with an effective diameter that is equal to d_d, and the internal pore network of the silicalite crystals is assumed to be inaccessible to gas molecules prior to membrane calcination. He is therefore assumed to not be adsorbed by silicalite, which has been tested by others [20–22]. It has also been assumed that for the transport of adsorbing gases such as N_2 and CO_2, their transport is dominated by surface diffusion. This assumption has been found to be reasonable for CO_2 and N_2 by Shelekhin et al. [23] inside molecular sieve silica membranes, which have a structure similar to the silicalite membranes used in this work. Also, the gas mixture composition on the high pressure side of the membrane is assumed to be the arithmetic average of the feed and retentate compositions.

The schematic diagram showing the steps taken in this study for the characterization of the membranes and their dependencies to each other is shown in Figure 6.2. In this method there are four characterization steps, which are described in following paragraphs.

The physical characteristics of the membrane are first determined based on the results of pure gas permeation experiments conducted at the same feed pressure using He and N_2 prior to, and following membrane calcination. The feed pressures are chosen to be as close as possible to the feed pressures that will be used in the binary gas mixture permeation experiments. After the determination of He and N_2 permeances for pure gas systems, P_{He} and P_{N_2}, respectively before calcination, equations 17 and 18 are solved simultaneously using the constants shown in Table 6.2 to determine the unknowns ε_d / l_d, and d_d, from the results of the uncalcined He and N_2 permeation experiments.

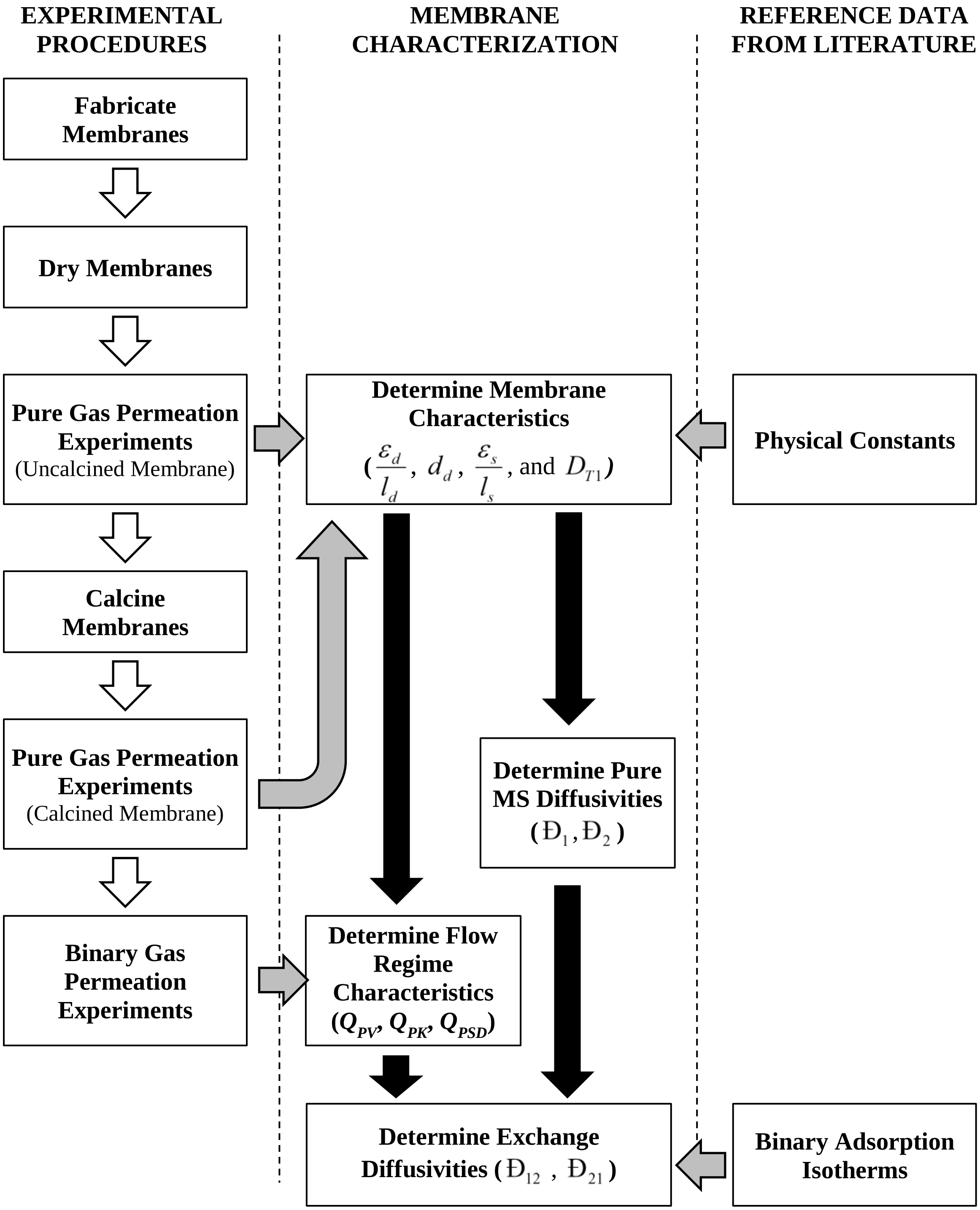

Figure 6.2. Schematic diagram showing the four characterization steps and their dependencies. These characterization steps are the determination of membrane characteristics, the determination of pure MS diffusivities, the determination of flow regime characteristics, and the determination of exchange diffusivities. The procedure to determine membrane characteristics was described previously and uses pure He and N_2 gases [12].

Equations 19 and 20 give the permeances of He and N_2, respectively, after calcination of the membrane. For He, viscous flow and Knudsen flow in defect pores and Knudsen flow in silicalite pores are considered, since He is assumed to be not adsorbed in silicalite pores. For N_2, viscous flow and Knudsen flow in defect pores and surface diffusion in silicalite pores are considered, since N_2 is adsorbed by silicalite. After the determination of pure gas permeations of He and N_2 after calcination, equation 19 is solved to determine d_d , and equation 20 is then solved to determine D_{TN_2} [12].

$$\mathrm{P}_{He} = \frac{\varepsilon_d}{l_d} d_d^2 \frac{(P_h + P_l)}{64\mu_{\mathrm{He}}\mathrm{RT}} + \frac{\varepsilon_d}{l_d} d_d \frac{1}{3}\sqrt{\frac{8}{\pi M_{WHe} RT}} \tag{17}$$

$$\mathrm{P}_{N_2} = \frac{\varepsilon_d}{l_d} d_d^2 \frac{(P_h + P_l)}{64\mu_{\mathrm{N_2}}\mathrm{RT}} + \frac{\varepsilon_d}{l_d} d_d \frac{1}{3}\sqrt{\frac{8}{\pi M_{WN_2} RT}} \tag{18}$$

$$\mathrm{P}_{He} = \frac{\varepsilon_d}{l_d} d_d^2 \frac{(P_h + P_l)}{64\mu_{\mathrm{He}}\mathrm{RT}} + \frac{\varepsilon_d}{l_d} d_d \frac{1}{3}\sqrt{\frac{8}{\pi M_{WHe} RT}} + \frac{\varepsilon_s}{l_s} d_s \frac{1}{3}\sqrt{\frac{8}{\pi M_{WHe} RT}} \tag{19}$$

$$\mathrm{P}_{N_2} = \frac{\varepsilon_d}{l_d} d_d^2 \frac{(P_h + P_l)}{64\mu_{\mathrm{N_2}}\mathrm{RT}} + \frac{\varepsilon_d}{l_d} d_d \frac{1}{3}\sqrt{\frac{8}{\pi M_{WN_2} RT}} + \frac{\varepsilon_s}{l_s} \rho_s \frac{(q_{h,i} - q_{l,i})}{(P_h - P_l)} D_{TN_2} \tag{20}$$

For membranes M1 and M2, equations 17 - 20 have been solved and reported by Carter et al. [12] as shown in Table 6.3.

Table 6.2. Constant parameters required for demonstration of the proposed characterization method using silicalite zeolite membranes at temperature T = 295 ± 2K. The adsorption and diffusion properties are taken from [24].

Property		He	N_2	CO_2
M_W	[kg·mol^{-1}]	0.004	0.028	0.044
µ	[Pa·s^{-1}]	1.973×10^{-5}	1.755×10^{-5}	1.473×10^{-5}
q^{sat}	[mol·kg^{-1}]	-	1.930	4.490
K	[Pa^{-1}]	-	0.072	0.301
$D_T / D_{T,N_2}$	[-]	-	1	0.35 ± 0.01

Table 6.3. Characteristic values for membranes M1 and M2 when experiments have been conducted at a feed pressure of approximately 300 kPa [12]. Permeation experiments were conducted at a temperature of 295 ± 2 K. Both membranes have a length of 6.0 ± 0.1 cm, and an area of 10.5 ± 0.1 cm^2.

Membrane	Characteristic Parameter			
	Đ_{21}	d_d	$\boldsymbol{d}_{d}$	D_{T,N_2}
M1	0.76 ± 0.25	1.8 ± 0.6 x 10^{-6}	10000 ± 2700	1.1 ± 0.3 10^{-7}
M2	0.63 ± 0.29	2.9 ± 1.3 x 10^{-6}	7600 ± 6600	1.0 ± 1.0 10^{-7}

After determining the fluxes for pure gas experiments, and knowing the values of ε_s / l_s, and the pure gas adsorption isotherms, pure MS diffusivities Đ_1 and Đ_1 were determined using equation 6. These pure gas experiments have been carried out at feed pressures between 170 kPa and 450 kPa for N_2 and CO_2 after membrane calcination. Then, values of Đ_1 and Đ_2 have been correlated with average fractional coverages determined from the high and low pressure side conditions using equations 5 and 8. The adsorption parameters required for these equations are shown in Table 6.2.

To determine the flow regime contributions to binary gas mixture transport, it is necessary to divide the total membrane into subsegments for viscous, Knudsen, and surface diffusion flow, which occur simultaneously as shown in Figure 6.3. The retentate flow rate Q_R and retentate composition x_R, are determined by mass balance from the measured flow rates Q_F and Q_P, and compositions x_F and y of the feed and permeate streams, respectively. Fluxes for each gas are determined next using equation 21.

$$N_1 = \frac{Q_P y}{A_m} \tag{21}$$

where A_m is the membrane area.

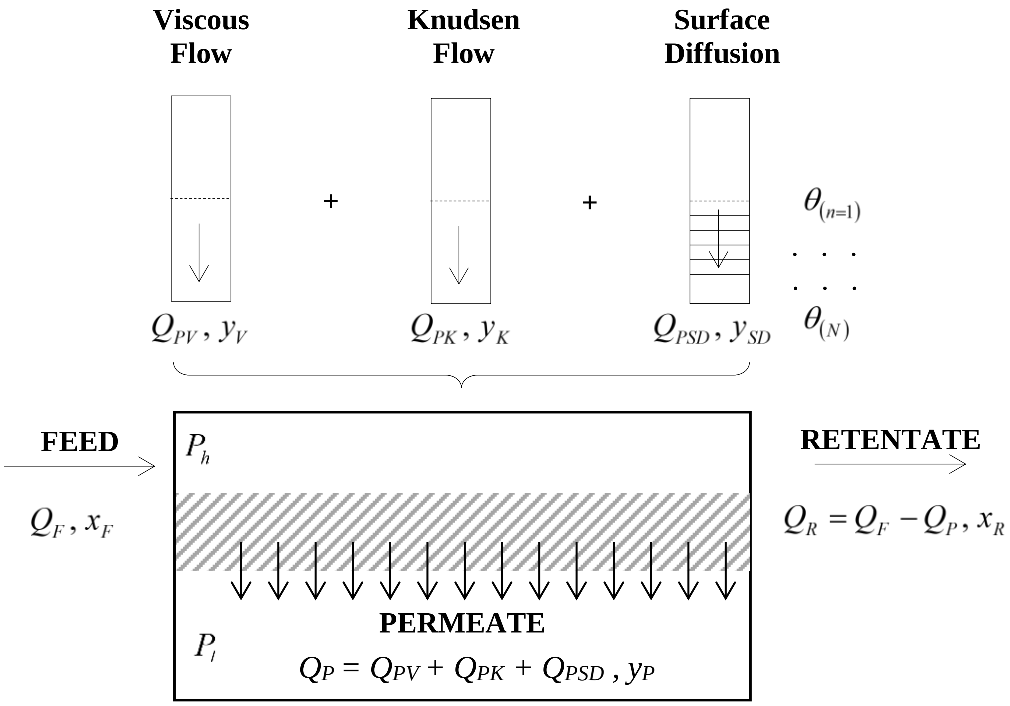

Figure 6.3. Schematic diagram showing the three flow regimes of viscous, Knudsen, and surface diffusion flow which describe the transport of gas molecules through an assumed rectangular membrane system. The feed and retentate stream flow rates are denoted Q_F and Q_R, and the permeate stream flow rates are denoted Q_{PV}, Q_{PK}, and Q_{PSD}, for Viscous flow, Knudsen flow, and Surface Diffusion flow contributions to total permeate flow Q_P respectively. Their compositions are x_F, x_R, y_V, y_K, y_{SD}, and y_P respectively. Feed and permeate side pressures are denoted P_h and P_l respectively. θ_n is the loading at position *n*, where subscripts *n* refer to segments in the radial direction for surface diffusion flow.

The Knudsen permeances of gases *1* and *2* are then determined using equation 2 with ε_d / l_d and d_d from Table 6.3, and the ideal Knudsen selectivity $\alpha^*_{Ki/j}$ is determined using the general ideal selectivity equation 22. To calculate the Knudsen flow contribution, first transport equation 23 for component *1* is divided by transport equation 24 for component *2*, and then the resulting equation is re-arranged resulting in the quadratic form for y_K as shown in equation 25. In this form, the pseudo permeate composition for Knudsen flow y_K can then be solved for explicitly, given the Knudsen ideal selectivity, high and low side total pressures, and the experimentally determined high pressure side retentate composition x_R. Knudsen fluxes for components *1* and *2* can then be determined by multiplying their

Knudsen permeances by their respective partial pressure differences given y_K as shown in equation 26.

$$\alpha^*_{K1/2} = \frac{\mathrm{P}_1}{\mathrm{P}_2} \tag{22}$$

$$Q_{PK} y_K = \mathrm{P}_{K1} A_m \left[P_h x_R - P_l y_K \right] \tag{23}$$

$$Q_{PK} (1 - y_K) = \mathrm{P}_{K2} A_m \left[P_h (1 - x_R) - P_l (1 - y_K) \right] \tag{24}$$

$$\left\{1 - \alpha^*_{K1/2}\right\} y_K^2 + \left\{ \frac{P_h}{P_l} \left[1 + x_R \left(\alpha^*_{K1/2} - 1\right)\right] + \alpha^*_{K1/2} - 1 \right\} y_K + \left\{ -\alpha^*_{K1/2} \frac{P_h}{P_l} x_R \right\} = 0 \tag{25}$$

$$N_{K1} = \mathrm{P}_{K1} \left[P_h x_R - P_l y_K \right] \tag{26}$$

The viscosity of the gas mixture at the high pressure side retentate composition x_R is then calculated from tabulated values at the experimental temperature, and then the viscous permeance of both gases *1* and *2* are determined using equation 1. As was the case for Knudsen fluxes, viscous fluxes can be determined by multiplying the viscous permeances by the partial pressure difference for components *1* and *2* where $y_V = x_R$, since viscous flow is non-selective.

By mass balance and method of differences between the overall, Knudsen, and viscous fluxes, surface diffusion fluxes for components *1* and *2* can be determined. The pseudo permeate composition for surface diffusion transport y_{SD} can then be found using equation 27.

$$y_{SD} = \frac{N_{SD1}}{N_{SD1} + N_{SD2}} \tag{27}$$

To determine the MS exchange coefficients $Đ_{12}$ and $Đ_{21}$ for the components of a binary gas mixture, the procedure shown in Figure 6.4 is followed. In this procedure, appropriate adsorption isotherms are first used to determine the average fractional coverages of components *1* and *2* at the high and low pressure sides of the membrane using equation 8. For the non-ideal CO_2-N_2-silicalite system, models such as the extended

Langmuir and IAST are unreliable. It has however been shown that the adsorption of CO_2 in this system is practically unaffected by the presence of N_2 at all gas mixture compositions, whereas the amount of N_2 adsorbed at equilibrium in the presence of CO_2 is significantly reduced [25,26]. The amounts of adsorbed CO_2 have therefore been determined assuming pure component adsorption behaviour with the Langmuir model where partial pressures of CO_2 replace total pressures. The amounts of adsorbed N_2 have then been determined using the binary adsorption isotherms published by Kennedy and Tezel, [26]. It should be noted that these binary adsorption isotherms have not been used to describe the amount of adsorbed CO_2 since they were determined at a greater temperature than the experimental permeation experiments (299 K in comparison to 295 K). This difference in temperature does not significantly affect the adsorption behaviour of N_2, but it does affect CO_2 due to the relatively greater amount of adsorbed molecules, and heat of adsorption of CO_2.

Next, an iterative method is used to change initial guesses for $Đ_{12}$ and $Đ_{21}$, such that the average fractional coverages at the high and low pressure sides of the membrane are described by equations 28 and 29, which are obtained from equations 15 and 16 subject to the constants A – F shown in equations 30 – 35. Note that $\nabla\theta_1$ and $\nabla\theta_2$ in equations 15 and 16 are re-written as $d\theta_1/dl$ and $d\theta_2/dl$ in equations 28 and 29, where the membrane thickness l is divided into N segments of fixed thickness dl. Starting at the high pressure side of the membrane which corresponds to the first segment where n = 1, equations 28 - 35 are used to calculate the change in surface occupancy through each segment n as shown in Figure 6.3. In these equations, values of $Đ_1$ and $Đ_2$ for pure components are used that correspond to the average amount adsorbed for components *1* and *2*, respectively, as described by the relationship between fractional occupancy and $Đ$ determined previously using equations 5, 6 and 8. The changed surface occupancies of the segment n are then used as the input surface occupancies for subsequent segment, n+1. These surface occupancy changes are determined for all segments until the low pressure side surface occupancies have been calculated.

$$\frac{d\theta_2}{dl} = \left[\frac{\frac{CD}{F} - A}{B - \frac{CE}{F}} \right] \tag{28}$$

$$\frac{d\theta_1}{dl} = -\left[\frac{D - E\frac{d\theta_2}{dl}}{F} \right] \tag{29}$$

Where dl [m] is the thickness of radial segment n.

$$A = \frac{N_2\left(1 + \theta_2 \frac{Đ_1}{Đ_{12}} + \theta_1 \frac{Đ_2}{Đ_{21}}\right)}{\rho_s q_2^{sat} Đ_2} \tag{30}$$

$$B = \frac{1-\theta_1}{1-\theta_1-\theta_2} + \left(\theta_2 \frac{Đ_1}{Đ_{12}} \frac{1-\theta_1}{1-\theta_1-\theta_2}\right) + \left(\theta_2 \frac{Đ_1}{Đ_{21}} \frac{\theta_1}{1-\theta_1-\theta_2}\right) \tag{31}$$

$$C = \frac{\theta_2}{1-\theta_1-\theta_2} + \left(\theta_2 \frac{Đ_1}{Đ_{12}} \frac{\theta_2}{1-\theta_1-\theta_2}\right) + \left(\theta_2 \frac{Đ_1}{Đ_{21}} \frac{1-\theta_2}{1-\theta_1-\theta_2}\right) \tag{32}$$

$$D = \frac{N_1\left(1 + \theta_2 \frac{Đ_1}{Đ_{12}} + \theta_1 \frac{Đ_2}{Đ_{21}}\right)}{\rho_s q_1^{sat} Đ_1} \tag{33}$$

$$E = \frac{\theta_1}{1-\theta_1-\theta_2} + \left(\theta_1 \frac{Đ_2}{Đ_{21}} \frac{\theta_1}{1-\theta_1-\theta_2}\right) + \left(\theta_1 \frac{Đ_2}{Đ_{12}} \frac{1-\theta_1}{1-\theta_1-\theta_2}\right) \tag{34}$$

$$F = \frac{1-\theta_2}{1-\theta_1-\theta_2} + \left(\theta_1 \frac{Đ_2}{Đ_{21}} \frac{1-\theta_2}{1-\theta_1-\theta_2}\right) + \left(\theta_1 \frac{Đ_2}{Đ_{12}} \frac{\theta_2}{1-\theta_1-\theta_2}\right) \tag{35}$$

The fractional coverages obtained at the low pressure side of the segment which have been determined by using equations 28 and 29 are then compared to the same fractional coverages that were determined experimentally. The differences between these fractional coverages are then minimized by changing the guessed values of $Đ_{12}$ and $Đ_{21}$, and repeating the iterative procedure as shown in Figure 6.4.

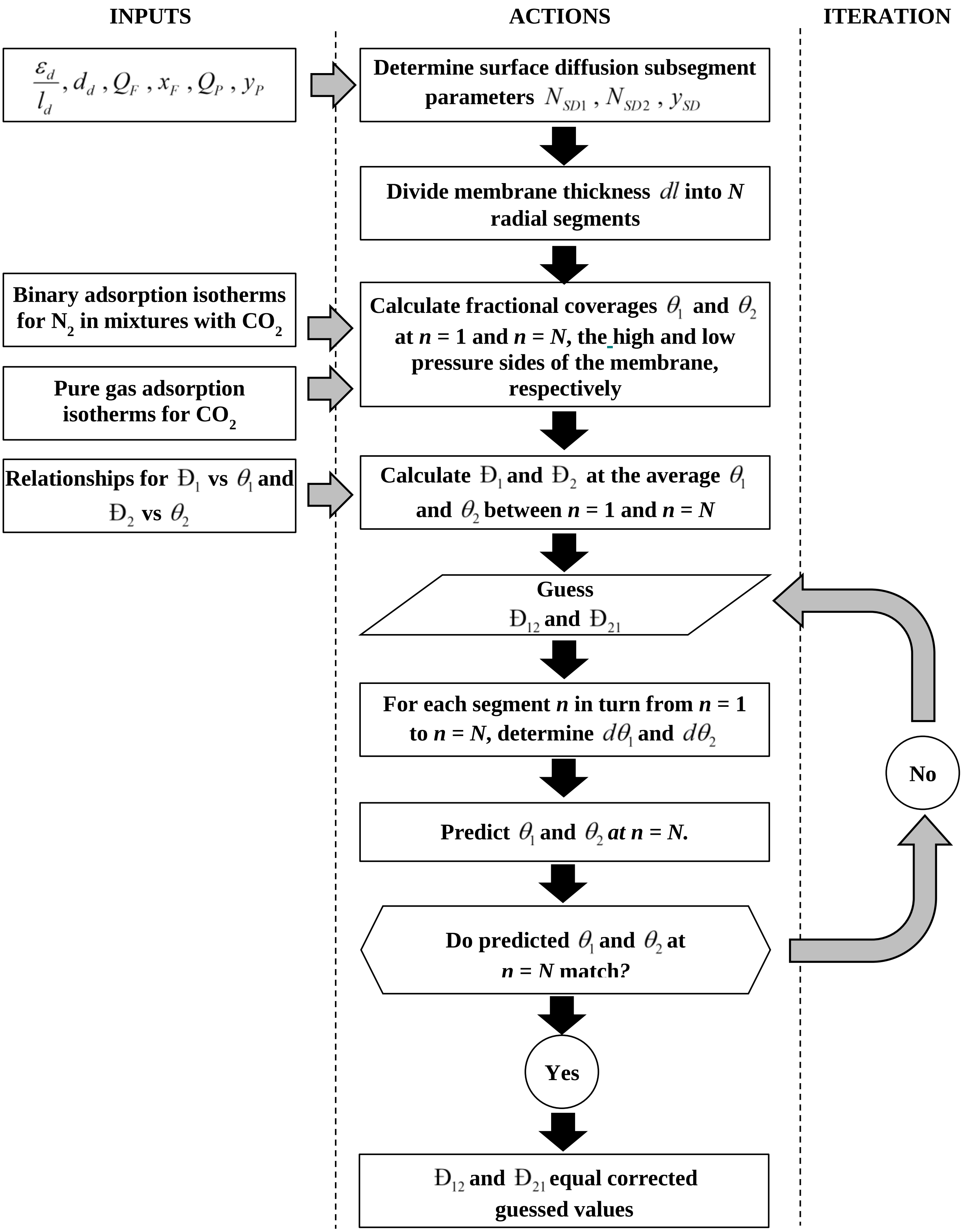

Figure 6.4. Schematic diagram showing the steps and dependencies between parameters to calculate MS exchange diffusivities, $Đ_{12}$ and $Đ_{12}$.

6.3.0 RESULTS AND DISCUSSION

6.3.1 Experimentally Determined Permeation Performance

The overall permeances of CO_2 and N_2, as well as the permeate compositions that have been determined from the binary gas permeation experiments at various pressure differentials are shown in Figure 6.5 for both membranes M1 and M2. From these permeances and permeate compositions, the effects of viscous, Knudsen, and surface diffusion flow can be evaluated to compare the performance of the different membranes in general.

From Figure 6.5, similar component permeances for both CO_2 and N_2 gases through M1 and M2 can be observed. CO_2 permeances between 1.49 and 7.09 x 10^{-5} $mol \cdot m^{-2} \cdot s^{-1} \cdot Pa^{-1}$, and N_2 permeances between 1.81 and 2.26 x 10^{-6} $mol \cdot m^{-2} \cdot s^{-1} \cdot Pa^{-1}$ were observed. It was also observed that the permeance of CO_2 is greater compared to N_2 through M1 than M2, whilst the permeance of N_2 is practically the same for M1 and M2. Consequently, the overall membrane selectivity α_{CO_2/N_2} is greater for M1 than M2. Since CO_2 is preferentially transported over N_2 only in the regime of surface diffusion for silicalite membranes, total membrane permeance must be dominated by surface diffusion transport through zeolite crystals. Since the membrane supports are similar for M1 and M2, this means that a greater volume of silicalite crystals must be present inside M1 compared to M2. In this situation, the available pathways for gas transport by surface diffusion are increased, and the defect pathways are simultaneously reduced. This behaviour agrees with values of d_d shown in Table 6.3, which is greater for M1 than M2, and the findings of the study using pure gases only [12]. With respect to the reduced permeance of CO_2 that can be observed as a function of partial pressure differential, this behaviour agrees with equation 3 for membrane transport dominated by surface diffusion flow. For surface diffusion transport across silicalite membranes, the driving force is the adsorption capacity difference between the high and low pressure sides of the membrane. Due to the non-linear shape of the CO_2 isotherms in silicalite, the surface occupancy gradient decreases with increasing partial pressure difference across the membrane. This causes the decrease in permeance for that gas with increasing partial pressure differential.

Since the adsorption isotherm for pure N_2 is practically linear at the experimental temperature, N_2 permeances should be independent of pressure differential. The observed increase in permeance of N_2 as partial pressure differential increases can therefore be attributed to the contributions of defect transport by viscous flow, which increase with pressure differential.

From Figure 6.5b, distinctly greater permeate compositions have been determined experimentally for M1 in comparison to M2. For both membranes, a maximum CO_2 concentration in the permeate can be observed at a pressure differential of approximately 190 kPa for both membranes. This maximum can be attributed to viscous flow contributions to total flux becoming more dominant than surface diffusion flux at higher pressure differentials, since viscous flux is non-selective and increases with pressure differential. The experimentally determined maximum concentration of CO_2 in the permeate is 23.7 and 20.2 mol% CO_2 for M1 and M2, respectively, for a feed mixture of 15 mol% CO_2.

6.3.2 Analysis of Calculated Surface Diffusion Permeances and Diffusivities

The characteristic parameters shown in Table 6.3 have been used in combination with equation 3 to first determine the pure N_2 and CO_2 surface diffusion permeances for M1 and M2, and they are shown in Figure 6.6a. The characteristic parameters shown in Table 6.3 have then been used to determine the Knudsen and viscous flow permeances of N_2 and CO_2 in binary gas mixtures using experimental binary gas permeation data and equations 22 – 26. The surface diffusion permeances of N_2 and CO_2 in binary gas mixtures have then been determined by subtracting the Knudsen and viscous flow permeances from the experimental data, and are shown in Figure 6.6b. From these permeances, MS diffusivities and MS exchange coefficients can be calculated. They are expected to be similar for the two membranes studied since the structure of zeolite channels does not vary between different membranes.

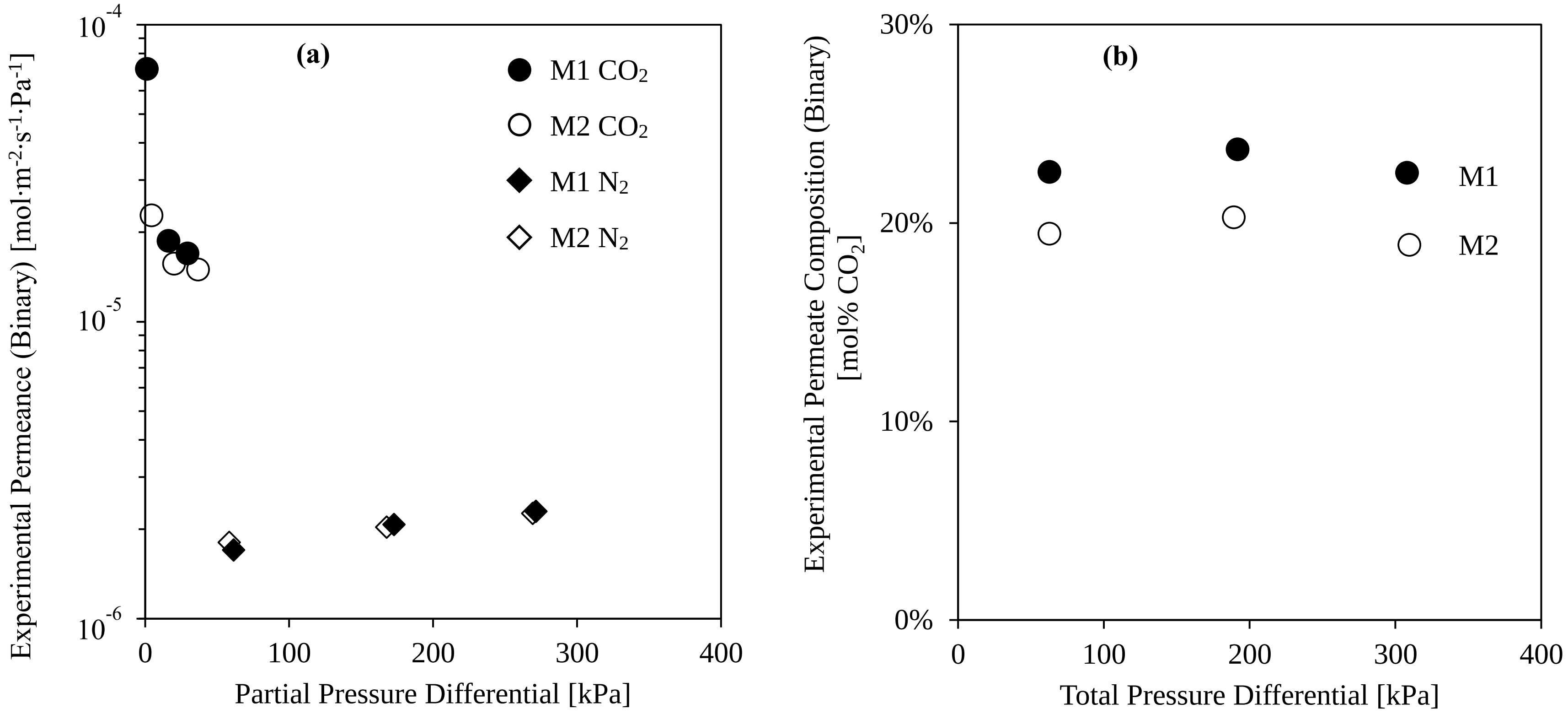

Figure 6.5. Gas mixture separation performance of membranes M1 and M2. A feed mixture composed of 15.0 % ± 0.5 % CO_2 in a binary gas mixture with N_2 was used, at a total flow rate of 3.00 ± 0.05 L·min^{-1}. Feed side pressure was controlled, and permeate side pressure was between 109 kPa and 170 kPa and found to increase with permeate flow rate. Experiments were conducted at a temperature of 295 ± 2 K. Both membranes have a length of 6.0 ± 0.1 cm, and an area of 10.5 ± 0.1 cm^2.

It should first be mentioned that although 3 binary gas mixture permeation experiments have been conducted using membranes M1 and M2, only 2 of the surface diffusion permeances for M1 are shown in Figure 6.6b and in subsequent plots. We were unable to determine the characteristic parameters for the lowest pressure differential investigated due to the strong dependence of q_{CO_2} on pressure below pressures of 150 kPa. At the pressure and composition conditions for this data set, the surface occupancy of CO_2 at the high pressure side of the membrane has been calculated to be less than the surface occupancy of CO_2 at the low pressure side. This would not happen in reality, and so any results that would be generated from this incorrect prediction has not been presented. Due to the greater contribution of defects to membrane transport for M2 than M1, the surface diffusion contribution to total membrane permeance is lower for M2 in comparison to M1. Consequently, the permeate composition is also lower for M2 in comparison to M1, and the partial pressure differences for CO_2 through M2 are lower than the partial pressure differences for M1 at equivalent total pressure differences. For M1, the average feed side compositions were found to be 15.0%, 14.3% and 13.6% when the total feed side pressures were 170 kPa, 300 kPa, and 450 kPa. For M2, the average feed side compositions were found to be 14.9%, 14.4%, and 14.0% when the total feed side pressures were 170 kPa, 300 kPa, and 450 kPa.

From the binary gas mixture surface diffusion permeances shown in Figure 6.6b, CO_2 permeances can be seen to increase as partial pressure difference is minimised as observed in Figure 6.5a. CO_2 permeance of M1 in Figure 6.6b is greater than that of M2, however, it can also be seen that N_2 permeance is significantly reduced for M1 in comparison to M2. This difference can be attributed to the differences between the defect and zeolite channels of M1 and M2. By discounting Knudsen and viscous flow, the N_2 permeances of M1 and M2 shown in Figure 6.6a are no longer as similar as they are in Figure 6.5a, as more N_2 is transported by Knudsen and viscous flow through M2 than M1. This relative trend is of practical use for evaluating novel membranes, but also demonstrates a way to quantify the contributions of defects to membrane permeance, which enables more reliable prediction of membrane performance.

The pure gas surface diffusion permeances of CO_2 and N_2 are shown in Figure 6.6a for M1 and M2. For both M1 and M2, the permeances for CO_2 are reasonably similar for pure and binary gas mixtures, whereas the permeances of N_2 for binary gas mixtures are smaller than the permeances of pure N_2. This difference in N_2 permeances can be attributed to pore blocking phenomena, which has been described qualitatively by others previously [27]. Pore blocking occurs for binary gas mixture adsorption systems when one component is more strongly adsorbed than the other, but has a much lesser diffusivity. Consequently, the more mobile but less strongly adsorbed species is excluded from adsorption sites more than would be expected based on Langmuirian adsorption phenomena. Unlike other studies, the permeances demonstrated in this study attempt to quantify the effects of pore blocking on the permeance of the more weakly adsorbed but more mobile species, in this case N_2. To this end and according to Figures 6.6a and 6.6b, the binary permeances of N_2 have decreased as much as 44% and 31% for M1 and M2, respectively, in comparison to pure gas permeances.

To determine gas permeabilities and CO_2/N_2 permselectivities, the binary gas surface diffusion permeances have been multiplied by the crystal pathway lengths of 1.7 µm and 2.3 µm for M1 and M2, respectively, as determined by Carter et al. [12]. This information has then been used to place the performance of both membranes at each set of operating conditions on the Robeson plot shown in Figure 6.7. The CO_2 permeabilities of M1 and M2 are notably among the most permeable of all membranes plotted by Robeson [28] at the operating conditions tested. The permselectivities that have been determined based on these permeabilties all fall below the upper bound line, except for one point which has been determined using M2 at a total feed pressure of 170 kPa. The CO_2 permeability and CO_2/N_2 permselectivity for this data point are 91000 barrer and 17 [-], respectively. The exceptional position of this data point above the upper bound line can be attributed to CO_2 blocking the zeolite pores and therefore limiting the transport of N_2 to a significant extent. The resulting data point exceeds the upper bound where the others do not due to the much lower partial pressure of CO_2 in comparison to N_2. Consequently, the surface diffusion permeance of CO_2 in the presence of N_2 is maximized to a greater extent than N_2, as shown in Figure

6.6b. Similarly, exceptional CO_2 permeability and CO_2/N_2 permselectivity for M1 would be expected at the lowest total pressure given surface diffusion permeance results.

The other membranes in the Robeson plot which are limited by the upper bound are predominantly polymeric membranes, and transport through them is described by the solution diffusion model. In this model, no intermolecular interactions are considered [1], and therefore, similar phenomena to pore blocking do not exist which could result in similarly excellent CO_2 permeability and CO_2/N_2 permselectivity like M2. It should be mentioned that the pathway lengths used to determine CO_2 and N_2 permeabilties assume that the active layer of the membrane support is completely plugged with silicalite crystals, which contradicts the observed presence of defects. M1 and M2 do however show clear selectivities for CO_2 over N_2, which is indicative that the defect pathway flow regimes of Knudsen and viscous flow have been overcome by the silicalite pathway flow regime of surface diffusion. The volume fraction of the active layer occupied by silicalite crystals therefore approaches complete plugging, and the assumption of complete plugging is reasonable to determine the maximum silicalite pathway length given the experimentally determined results. As this assumption becomes less valid due to greater volume fractions of defects, the estimated membrane thickness and resulting permeabilities are over-estimated.

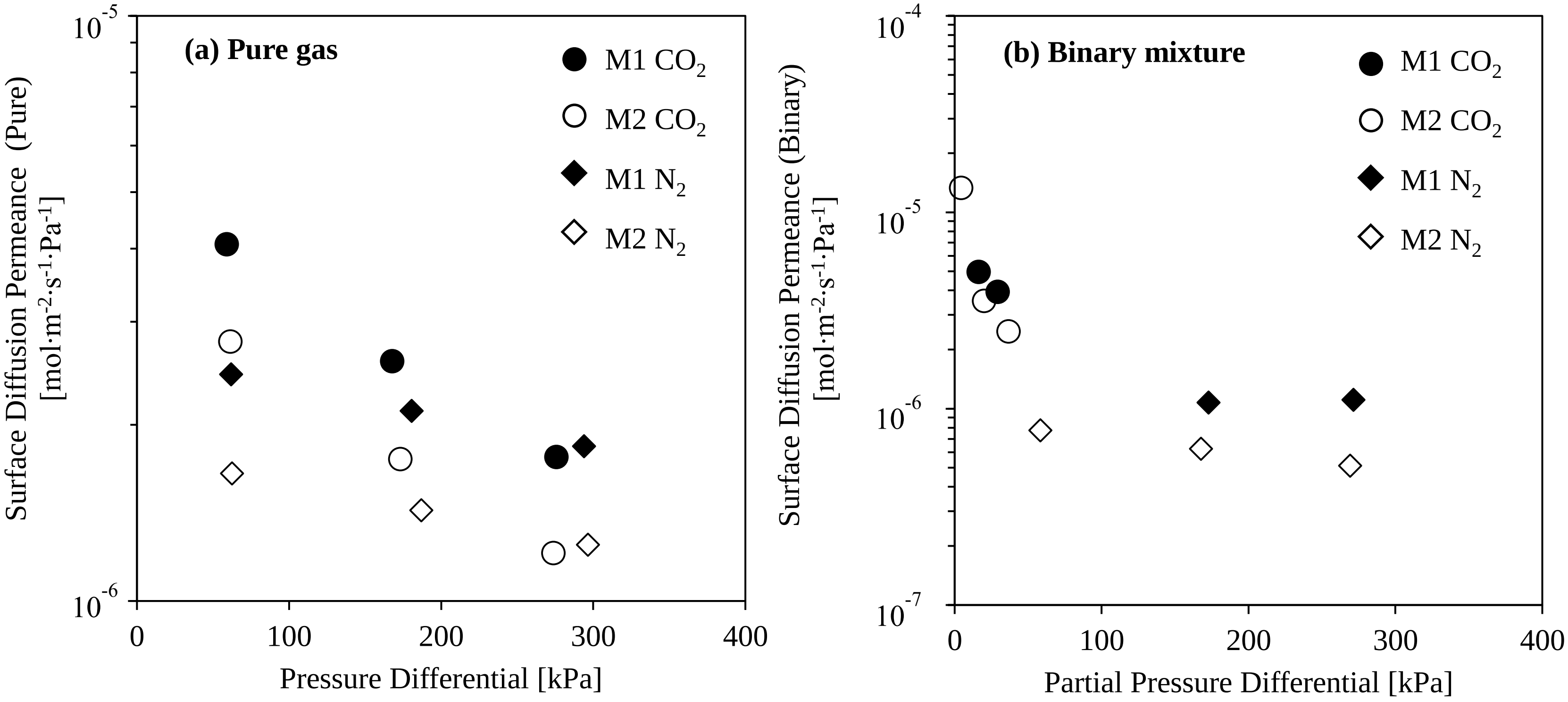

Figure 6.6. Pure and binary gas mixture surface diffusion permeances of CO_2 and N_2 through membranes M1 and M2. Defect contributions to membrane permeance have been discounted using the characteristic parameters shown in Table 6.3 in combination with experimental data to calculate these permeances. For binary gas mixture permeation experiments, a feed mixture composed of 15.0 % ± 0.5 % CO_2 in a binary gas mixture with N_2 was used at a flow rate of 3.00 ± 0.05 $L \cdot min^{-1}$. Feed gas flow rate was increased as required at the start of each pure gas permeation experiment to maintain a stage cut less than 50%. Feed side pressure was controlled, and permeate side pressure was found to increase with permeate flow rate between 109 kPa and 170 kPa. Pressure differentials were as indicated. Experiments were conducted at a temperature of 295 ± 2 K. Both membranes have a length of 6.0 ± 0.1 cm, and an area of 10.5 ± 0.1 cm^2.

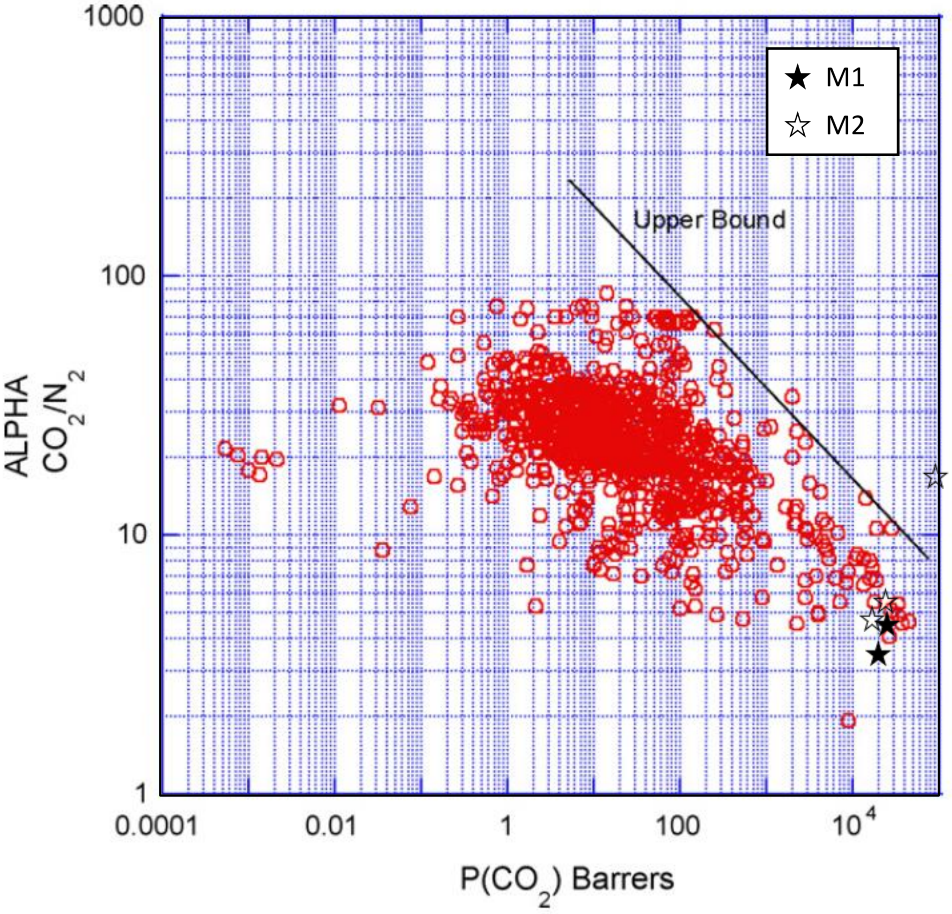

Figure 6.7. Upper bound correlation for CO_2/N_2 with the CO_2 permeability and CO_2/N_2 permselectivity from [28] with surface diffusion transport contributions for M1 and M2 added. For binary gas mixture permeation experiments, a feed mixture composed of 15.0 % ± 0.5 % CO_2 in a binary gas mixture with N_2 was used at a flow rate of 3.00 ± 0.05 $L\cdot min^{-1}$. Feed gas flow rate was increased as required at the start of each pure gas permeation experiment to maintain a stage cut less than 50%. Feed side pressure was controlled, and permeate side pressure was found to increase with permeate flow rate between 109 kPa and 170 kPa. Experiments were conducted at a temperature of 295 ± 2 K. Both membranes M1 and M2 have a length of 6.0 ± 0.1 cm, and an area of 10.5 ± 0.1 cm^2.

Figure 6.8a shows a very strong trend between the MS diffusivity, and the average amount of adsorbed CO_2 and N_2. MS diffusivities have been plotted in this way so that amounts adsorbed at the binary gas permeation experiment boundary conditions can be correlated with these results, which were determined using pure gas permeation data. There does not appear to be a significant difference between the MS diffusivities determined using

M1 and M2 at similar conditions, which is expected since MS diffusivities are intrinsic properties of zeolite crystals. It should be mentioned that there is a notable 25% difference in the value of d_d for M1 in comparison to M2. This finding suggests that the proposed method effectively takes into account the varied physical structure of different membranes. For the purposes of characterizing novel membranes, MS diffusivities can therefore be determined easily for surface diffusion flow through membranes given the parameters and equations described in this study. From these results, the trend in MS diffusivity of CO_2 as loading approaches 0 cannot be extrapolated with a high degree of certainty, although the MS diffusivities of N_2 suggests that this extrapolation is reasonable. Figure 6.8a also shows that the MS diffusivity of N_2 is greater than that of CO_2 at all investigated conditions, which is consistent with the results of others in the literature. The range of MS diffusivities; 7.26 – 9.33 x 10^{-8} $m^2 \cdot s^{-1}$, and 1.17 – 1.95 x 10^{-8} $m^2 \cdot s^{-1}$ for $Đ_{N_2}$ and $Đ_{CO_2}$, respectively, are within an order of magnitude of the intrinsic diffusion coefficients and corrected diffusivities reported elsewhere [17,29,30]. It should be noted that the diffusivities reported by others have not been corrected with consideration of adsorption phenomena and isotherm data. However, they are most similar to the MS diffusivities calculated in this study as zeolite loading approaches 0 [17,29,30]. Diffusivities are strongly dependent on temperature and pressure conditions, as well as the presence of intra-crystalline defects, and therefore variation within an order of magnitude is reasonable.

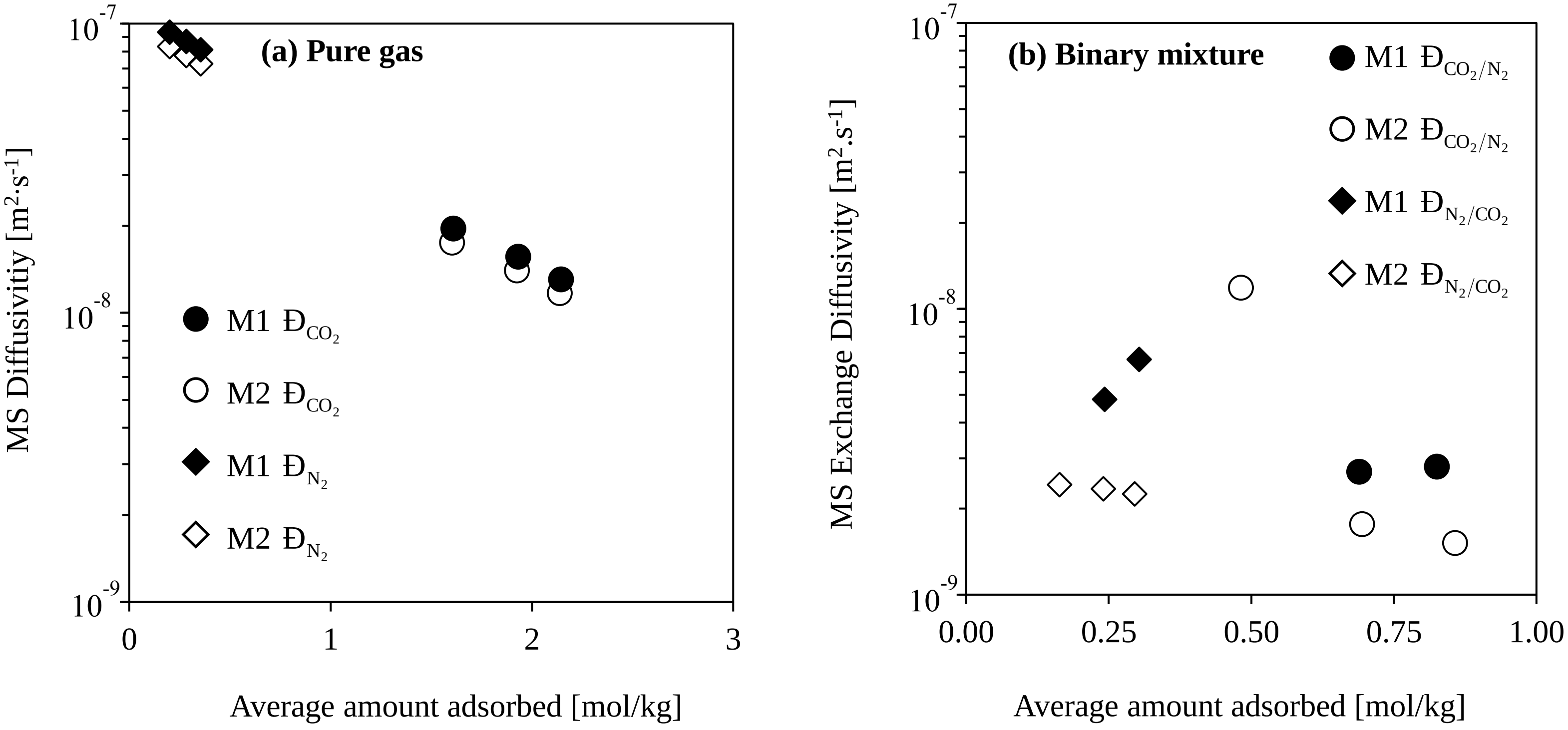

Figure 6.8. (a) Pure component MS diffusivities of CO_2 and N_2, and (b) exchange coefficients for CO_2/N_2 and N_2/CO_2 determined for binary gas system using surface diffusion gas permeation data from experiments conducted using membranes M1 and M2. Defect contributions to membrane permeance have been discounted using the characteristic parameters shown in Table 6.2 in combination with experimental data to calculate these diffusivities and exchange coefficients. For binary gas mixture permeation experiments, a feed mixture was composed of 15.0 % ± 0.5 % CO_2 in a binary gas mixture with N_2 was used at a flow rate of 3.00 ± 0.05 $L \cdot min^{-1}$. Feed gas flow rate was increased as required at the start of each pure gas permeation experiment to maintain a stage cut less than 50%. Feed side pressure was controlled, and permeate side pressure was found to increase with permeate flow rate between 109 kPa and 170 kPa. Pressure differentials were as indicated. Experiments were conducted at a temperature of 295 ± 2 K. Both membranes have a length of 6.0 ± 0.1 cm, and an area of 10.5 ± 0.1 cm^2.

Figure 6.8b shows the MS exchange coefficients $Đ_{CO_2/N_2}$ and $Đ_{N_2/CO_2}$ as functions of the average amount of adsorbed molecules between the high and low pressure sides of the membrane for CO_2 and N_2, respectively. High exchange coefficients are indicative that intermolecular interactions significantly affect molecular transport. For $Đ_{N_2/CO_2}$, this would mean that the transport of N_2 is subject to significant resistance from molecules of CO_2. On the one hand, it has been shown in many studies that the resistance imparted between different types of molecules on each other is equal, and can alternatively be expressed as $Đ_{12} = Đ_{21}$. For adsorbent-adsorbate systems, which do not exhibit pore blocking phenomena, and whose multicomponent adsorption behaviour can be described by the extended Langmuir model, this assumption is reasonable and is known as the Vignes correlation. For the present investigation; however, the MS exchange diffusivities shown in Figure 6.8b challenge the Vignes correlation.

Figures 6.8a and 6.8b show that diffusion of N_2 in the mixture, $Đ_{N_2/CO_2}$, is much smaller than the diffusion of N_2 in a pure system, $Đ_{N_2}$. This reduction between the pure component and binary mixture diffusivities is much more pronounced for N_2 than the reduction for CO_2 ($Đ_{CO_2/N_2}$ relative to $Đ_{CO_2}$). These relationships show that the presence of CO_2 blocks the pores of silicalite, and slows down N_2, which in turn leads to reduced N_2 permeances. This pore blocking by CO_2, and a reduction in the permeance of N_2 can be observed and quantified, whereby greater selectivities of CO_2 over N_2 are realised in binary gas mixture experiments, relative to studies using pure gases.

Figure 6.8b shows that for both M1 and M2, the exchange coefficients $Đ_{N_2/CO_2}$ are greater than $Đ_{CO_2/N_2}$ for all experiments except in the lowest pressure differential experiment that has been conducted using M2. The observed discrepancy in this trend by M2 could be attributed to the sensitivity of the proposed method when the concentration gradient of CO_2 is minimized, as the exchange coefficient $Đ_{N_2/CO_2}$ is consistent with the values determined at higher pressure differentials. The exchange coefficient $Đ_{CO_2/N_2}$ at higher pressure differentials however, is not. When this data set is excluded, the greatest exchange coefficients for M1 are 6.66 and 2.81 x 10^{-9} $m^2 \cdot s^{-1}$ for $Đ_{N_2/CO_2}$ and $Đ_{CO_2/N_2}$

respectively. For M2, the greatest exchange coefficients are 2.43 and 1.76 x 10^{-9} $m^2 \cdot s^{-1}$ for $Đ_{N_2/CO_2}$ and $Đ_{CO_2/N_2}$, respectively. These coefficients should be similar to each other as they both describe transport by surface diffusion flow only, however, this discrepancy can be attributed to the assumptions made to determine the characteristic parameters shown in Table 6.3. As the variation between the exchange coefficients $Đ_{N_2/CO_2}$ and $Đ_{CO_2/N_2}$ increases, intermolecular interactions can be considered to more significantly affect the transport of gas molecules. For M1 and M2, $Đ_{N_2/CO_2}$ was found to be 2.37 and 1.38 times greater than $Đ_{CO_2/N_2}$, respectively. These variations between exchange coefficients are therefore indicative of significant intermolecular interactions, and challenge the Vignes correlation, where the MS exchange diffusivities of the components of a binary mixture are assumed to be equal i.e $Đ_{12} = Đ_{21}$.

Based on the limited number of characteristic tests that were conducted in this study, as the average amount adsorbed tends to zero, $Đ_{N_2/CO_2}$ and $Đ_{CO_2/N_2}$ appear to perhaps converge. These results suggest that the Vignes correlation could be reasonably used when the average amount adsorbed approaches to 0. However, the average amount adsorbed approaches to 0 at high temperatures, and when pressure is reduced. Neither of these conditions are suitable for separating gas mixtures by surface diffusion through zeolite membranes. Therefore, predictions based on Vignes correlated conditions are of limited practical use for separating CO_2 and N_2 gases using silicalite membranes.

These exchange coefficients additionally indicate that as a greater proportion of flow proceeds according to the regime of surface diffusion, intermolecular interactions play an increasingly important role in predicting membrane performance. This reasoning is straightforward and has been made qualitatively in the past. However, the present study for the first time, to the best knowledge of the authors, has quantified these interactions for defect containing membranes at different operating conditions. In previous studies, it has simply been assumed that exchange coefficients are an intrinsic property of the zeolite crystals, even though there has been no way to distinguish between effects caused by variations in zeolite crystal packing, and the influence of defects. For defect free membranes, which contain uniform selective layer thicknesses, this assumption is reasonable. For pore plugged membranes which contain varied amounts of zeolite crystals in their selective layer, the structural complexity of the selective membrane layer almost unequivocally rejects this assumption.

Since only surface diffusion transport through silicalite channels is shown in Figure 6.8b, these findings can be compared with adsorption and diffusion studies using single crystals. To this end, the greater exchange coefficients of $Đ_{\mathrm{N_2/CO_2}}$ in comparison to $Đ_{\mathrm{CO_2/N_2}}$ can be related to the reduction in transport diffusivities of CO_2 as a function of loading that have been measured by Carter et al using Infra-Red Microimaging with a single crystal of silicalite [25].

6.4.0 CONCLUSIONS

In the present study, MS diffusivities and exchange coefficients, which describe the transport of a binary mixture of CO_2 and N_2 through two silicalite membranes containing Knudsen and viscous sized defects have been characterised. This has been achieved by firstly discounting the Knudsen and viscous flow contributions to binary gas mixture permeation using mass transport equations, and the characteristic parameters which describe the structure of these membranes as determined in a previous study. The remaining surface diffusion contribution to binary gas mixture permeation have then been plotted on a Robeson plot, and used in combination with the MS model to determine MS diffusivities $Đ_{CO_2}$ and $Đ_{N_2}$ for pure components, as well as the exchange coefficients $Đ_{\mathrm{N_2/CO_2}}$ and $Đ_{\mathrm{CO_2/N_2}}$ in the binary system.

For the silicalite membranes that have been characterized in this study, the surface diffusion permeances of CO_2 present in a binary gas mixture with N_2 were found to be similar to those found for pure CO_2, whereas the permeances of N_2 present in a binary gas mixture with CO_2 were observed to decrease as much as 44% compared to those found for pure N_2. The adsorption of N_2 in silicalite is therefore significantly reduced in the presence of CO_2 [26]. The surface diffusion permeances that have been determined in this study therefore demonstrate that the proposed method can be used to quantify the effects of pore blocking phenomena for non-ideal adsorbent membrane systems. Furthermore, when these surface diffusion permeances are converted into CO_2 permeability and CO_2/N_2 permselectivities, the greatest values obtained were 91000 barrer, and 17 [-] respectively. This performance is above the Robeson upper bound, and reflects the significance of pore blocking phenomena at low total feed pressures for this system of CO_2, N_2, and silicalite. The MS diffusivities of CO_2 and N_2 in the absence of Knudsen and viscous flow contributions were also determined, and found to be 7.26 – 9.33 x 10^{-8} $m^2 \cdot s^{-1}$, and 1.17 – 1.95 x 10^{-8} $m^2 \cdot s^{-1}$ for Đ_{N_2} and Đ_{CO_2} respectively. Thus, the utility of the proposed method for characterising defect containing membranes has additionally been demonstrated. Finally, exchange coefficients have been determined which quantify the intermolecular interactions between N_2 and CO_2 at the conditions investigated in this study. The results observed reject the Vignes correlation as $\text{Đ}_{\mathrm{N_2/CO_2}}$ was found to be more than 1.38 times greater than $\text{Đ}_{\mathrm{CO_2/N_2}}$ for both membranes. Although the exchange coefficients that were determined for the two membranes did not have similar values, $\text{Đ}_{\mathrm{N_2/CO_2}}$ was found to be greater than $\text{Đ}_{\mathrm{CO_2/N_2}}$ for both membranes, which is indicative that the diffusivity of N_2 is more significantly affected by the presence of CO_2 than CO_2 is by the presence of N_2.

6.5.0 ACKNOWLEDGEMENTS

This research was financially supported by the Natural Sciences and Engineering Research Council of Canada (NSERC).

6.6.0 NOMENCLATURE

A, B, C, D, E, F	[-]	MS model constants
A_m	$[m^2]$	Membrane Area
D_T	$[m^2 \cdot s^{-1}]$	Transport diffusivity
d_d	[m]	Effective defect size

J_i	[mol·m^{-2}·s^{-1}]	Flux of pure component *i*
K	[Pa^{-1}]	Langmuir adsorption isotherm constant
l_d	[m]	Effective defect path length
l_s	[m]	Effective silicalite path length
l	[m]	Membrane thickness
M_W	[kg·mol^{-1}]	Molecular weight
N_i	[mol·m^{-2}·s^{-1}]	Flux of component *i* in a binary gas mixture
N	[-]	Number of radial segments
P_K	[mol·m^{-2}·s^{-1}·Pa^{-1}]	Knudsen permeance
P_{SD}	[mol·m^{-2}·s^{-1}·Pa^{-1}]	Surface diffusion permeance
P_V	[mol·m^{-2}·s^{-1}·Pa^{-1}]	Viscous permeance
P_h	[Pa]	Total pressure at high pressure side of membrane
P_l	[Pa]	Total pressure at low pressure side of membrane
p_{h1}	[Pa]	Partial pressure at high pressure side of membrane of component 1
p_{l1}	[Pa]	Partial pressure at low pressure side of membrane of component 1
Q	[mol·s^{-1}]	Flow rate
q_h	[mol·kg^{-1}]	Amount of molecules adsorbed at the high pressure side of the membrane

$q_{l,}$	[mol·kg^{-1}]	Amount of molecules adsorbed at the low pressure side of the membrane
q_i^{sat}	[mol·kg^{-1}]	Amount of component *i* adsorbed at saturation
R	[J·mol^{-1}·K^{-1}]	Gas constant
T	[K]	Temperature
u	[m·s^{-1}]	Velocity
x	[-]	Mole fraction of CO_2 in the high pressure side of the membrane
y	[-]	Mole fraction of CO_2 in the low pressure permeate side of the membrane

Subscripts

d	Defects
F	Feed side
h	High pressure side
$i,\ j, 1, 2$	Components
K	Knudsen
l	Low pressure side
n	Radial segment identifier
P	Permeate side
R	Retentate side
s	Silicalite
SD	Surface diffusion

V	Viscous

Greek and Latin letters

$\alpha^{*}_{1/2}$	[-]	Ideal selectivity
ε_s	[-]	Silicalite volume fraction
ε_d	[-]	Defect volume fraction
θ	[-]	Fractional zeolite occupancy
ρ_s	[kg·m^{-3}]	Density of silicalite
Γ_i	[-]	Thermodynamic factor for pure component *i*
µ	[Pa·s^{-1}]	Viscosity
μ	[Pa·s^{-1}]	Chemical potential of component *i*
$Đ_i$	[m^2·s^{-1}]	Maxwell-Stefan diffusivity of *i*
$Đ_{12}$	[m^2·s^{-1}]	MS Exchange coefficient for resistance imparted by component 2 on component 1

Abbreviations

CO_2	Carbon Dioxide
F-	Bubble Flow Meter
GC	Gas Chromatograph
H_2O	Water
He	Helium
M-	Membrane Identifier
MFC-	Mass Flow Controller

MFI	Mordenite Framework Inverted
MS	Maxwell-Stefan
N_2	Nitrogen
NSERC	National Sciences and Engineering Research Council of Canada
P-	Pressure Transducer
PFD	Process Flow Diagram
SAPO-34	Silicoaluminophosphate Zeolite
SiO_2	Silica Dioxide
T-	Thermocouple
TiO_2	Titanium Oxide
TPAOH	Tetra-Propyl Ammonium Hydroxide
V-	Valve

6.7.0 REFERENCES

[1] R.W. Baker, Membrane Technology and Applications, 3rd ed., Wiley, 2012.

[2] R. Mallada, M. Menendez, Inorganic Membranes: Synthesis, Characterization, and Applications, Elsevier, 2008.

[3] F. Jareman, C. Andersson, J. Hedlund, The influence of the calcination rate on silicalite-1 membranes, Microporous Mesoporous Mater. 79 (2005) 1–5. doi:10.1016/j.micromeso.2004.10.032.

[4] J. Dong, Y.S. Lin, M. Hu, R. Peascoe, E.A. Payzant, Template-removal-associated microstructural development of porous ceramic-supported MFI zeolite membranes, Microporous Mesoporous Mater. 34 (2000) 241–253. doi:https://doi.org/10.1016/S1387-1811(99)00175-4.

[5] H. Maghsoudi, Defects of Zeolite Membranes: Characterization, Modification and Post-treatment Techniques, Sep. Purif. Rev. 45 (2016) 169–192. doi:10.1080/15422119.2015.1103270.

[6] A. Caravella, P.F. Zito, A. Brunetti, E. Drioli, G. Barbieri, Microporous and Mesoporous Materials A novel modelling approach to surface and Knudsen multicomponent diffusion through NaY zeolite membranes, Microporous Mesoporous Mater. 235 (2016) 87–99. doi:10.1016/j.micromeso.2016.07.049.

[7] F. Jareman, J. Hedlund, D. Creaser, J. Sterte, Modelling of single gas permeation in real MFI membranes, J. Memb. Sci. 236 (2004) 81–89. doi:10.1016/j.memsci.2004.01.028.

[8] T.Q. Gardner, J.L. Falconer, R.D. Noble, Adsorption and diffusion properties of zeolite membranes by transient permeation, Desalination. 149 (2002) 435–440. doi:10.1016/S0011-9164(02)00772-5.

[9] R. Krishna, J.M. Van Baten, M. Stefan, Unified Maxwell – Stefan description of binary mixture diffusion in micro - and meso -porous materials, Chem. Eng. Sci. 64 (2009) 3159–3178. doi:10.1016/j.ces.2009.03.047.

[10] J. Van Den Bergh, M. Mittelmeijer-hazeleger, F. Kapteijn, Modeling Permeation of CO_2/CH_4, N_2/CH_4, and CO_2/Air Mixtures across a DD3R Zeolite Membrane, J. Phys. Chem. 114 (2010) 9379–9389. doi:10.1021/jp101075h.

[11] P.F. Lito, A.S. Santiago, S.P. Cardoso, B.R. Figueiredo, C.M. Silva, New expressions for single and binary permeation through zeolite membranes for different isotherm models, J. Memb. Sci. 367 (2011) 21–32. doi:10.1016/j.memsci.2010.10.034.

[12] D. Carter, S. Al-Akwaa, F.H. Tezel, B. Kruczek, In-Situ Characterization of Inorganic Membranes Subject to Viscous, Knudsen and Surface Dffusion Flow Regimes. Submitted to, J. Memb. Sci. (2019).

[13] A. Vignes, Diffusion in binary solutions: Variation of Diffusion Coefficient with Composition, Ind. Eng. Chem. Fundam. 5 (1966) 189–199.

doi:10.1021/i160018a007.

[14] S. Li, J.L. Falconer, R.D. Noble, SAPO-34 membranes for CO_2/CH_4 separation, J. Memb. Sci. 241 (2004) 121–135. doi:10.1016/j.memsci.2004.04.027.

[15] R. Krishna, S. Li, J.M. van Baten, J.L. Falconer, R.D. Noble, Investigation of slowing-down and speeding-up effects in binary mixture permeation across SAPO-34 and MFI membranes, Sep. Purif. Technol. 60 (2008) 230–236. doi:10.1016/j.seppur.2007.08.012.

[16] J. Kärger, D.M. Ruthven, D.N. Theodorou, Diffusion in Nanoporous Materials, John Wiley and Sons, 2012.

[17] W.J.W. Bakker, L.J.P. Van Den Broeke, F. Kapteijn, J.A. Moulijn, Temperature Dependence of One-Component Permeation through a Silicalite-1 Membrane, AIChe J. 43 (1997) 2203–2214. doi:10.1002/aic.690430907.

[18] R. Krishna, A unified approach to the modelling of intraparticle diffusion in adsorption processes, Gas Sep. Purif. 7 (1993) 91–104. doi:10.1016/0950-4214(93)85006-H.

[19] R. Krishna, Diffusion of binary mixtures across zeolite membranes: Entropy effects on permeation selectivity, Int. Commun. Heat Mass Transf. 28 (2001) 337–346. doi:10.1016/S0735-1933(01)00239-1.

[20] O. Talu, A.L. Myers, Reference potentials for adsorption of helium, argon, methane, and krypton in high-silica zeolites, Colloids Surfaces A Physicochem. Eng. Asp. 187–188 (2001) 83–93. doi:10.1016/S0927-7757(01)00628-8.

[21] R. Nagumo, H. Takaba, S. Suzuki, S. Nakao, Estimation of inorganic gas permeability through an MFI-type silicalite membrane by a molecular simulation technique combined with permeation theory, Microporous Mesoporous Mater. 48 (2001) 247–254. doi:10.1016/S1387-1811(01)00359-6.

[22] P. Malbrunot, D. Vidal, J. Vermesse, R. Chahine, T.K. Bose, Adsorbent Helium Density Measurement and Its Effect on Adsorption Isotherms at High Pressure, Langmuir. 13 (1997) 539–544. doi:10.1021/la950969e.

[23] A.B. Shelekhin, A.G. Dixon, Y.H. Ma, Theory of gas diffusion and permeation in inorganic molecular-sieve membranes, AIChE J. 41 (1995) 58–67. doi:10.1002/aic.690410107.

[24] D. Kennedy, D. Carter, S. Wilson, B. Kruczek, F.H. Tezel, Pore plugging synthesis and characterization of silicalite-1 membranes using tubular TiO_2 supports: Effect of support pore size on membrane performance., Can. J. Chem. Eng. (2018). doi:0.1002/cjce.23095.

[25] D. Carter, F.H. Tezel, B. Kruczek, J. Kärger, D. Ruthven, R. Marthala, C. Chmelik, Isotherms and Transport Diffusivities of CO_2 in CO_2/N_2 Mixtures with Silicalite Determined Using Infra-Red Microimaging. Submitted to, MICROPOROUS MESOPOROUS Mater. (2019).

[26] D. Kennedy, F. Handan Tezel, Improved method for determining binary adsorption isotherms by using concentration pulse chromatography: Adsorption of CO_2 and N_2 by silicalite at different pressures, Adsorption. 20 (2014) 189–199. doi:10.1007/s10450-013-9562-z.

[27] L. Sandström, E. Sjöberg, J. Hedlund, Very high flux MFI membrane for CO_2 separation, J. Memb. Sci. 380 (2011) 232–240. doi:10.1016/j.memsci.2011.07.011.

[28] L.M. Robeson, The upper bound revisited, 320 (2008) 390–400. doi:10.1016/j.memsci.2008.04.030.

[29] P.F. Zito, A. Caravella, A. Brunetti, E. Drioli, G. Barbieri, Knudsen and surface diffusion competing for gas permeation inside silicalite membranes, J. Memb. Sci. 523 (2017) 456–469. doi:10.1016/j.memsci.2016.10.016.

[30] G.K. Papadopoulos, H. Jobic, D.N. Theodorou, Transport diffusivity of N_2 and CO_2 in silicalite: Coherent quasielastic neutron scattering measurements and molecular dynamics simulations, J. Phys. Chem. B. 108 (2004) 12748–12756. doi:10.1021/jp049265g.

Chapter 7

This chapter is based on:

Optimization of Silicalite Membrane Fabrication Procedure, and Gas Permeation Module Design and Development

ABSTRACT

Although the fabrication of perfect membranes should be the objective of every study that investigates the performance of novel membranes, it is also important to ensure that the procedures that are used to evaluate membrane quality are robust, and repeatable. In this research, silicalite membranes composed of abutting zeolite crystals whose nanoporous channels are of a similar size to gas molecules have been synthesized inside microporous ceramic membrane supports using pore plugging method. It is therefore of the utmost importance in this research to be certain that gases permeating through the membranes that have been fabricated proceed predominantly through the zeolite crystal pores of the selective membrane active layer, and that this layer is not bypassed. In pursuit of ensuring that the method used to characterize newly fabricated membranes is robust and reproducible, three different types of membrane module have been fabricated, and the sealing method of integrating membranes into the module is carefully investigated. These modules have utilized polymer epoxies, teflon fittings, specialty glazing compounds, and specially cut graphite gaskets. The best membrane performance has been found using a module which utilizes Torr seal epoxy to integrate the ceramic membrane into the module, however, this type of arrangement cannot be regenerated, and slowly poisons the incorporated membrane with time. On the other hand, the most reproducible membrane module utilizes a specialty glazing solution in combination with graphite gaskets, but this arrangement results in bypassing of the membrane layer from consumption of the glaze on top of the membrane support due to the harsh chemical conditions involved during membrane synthesis in the autoclave. Although changes to the membrane module have been implemented throughout this research, the best membrane fabrication procedure was

found to include an interruption during hydrothermal synthesis, and a minimized headspace above the synthesis solution in the autoclave during membrane fabrication.

Several challenges exist for researchers to address in this field. The most important one among them is how to combine the best attributes of the different module and different membrane sealing methods, and that has been the focus of the present investigation.

7.1.0 OPTIMIZATION OF MEMBRANE FABRICATION

By modifying the membrane synthesis conditions, it is intended to fabricate membranes which contain a layer of zeolite crystals that is both thin, and continuous. Such membranes contain no defect pathways through which gas transport may occur according to Knudsen or viscous flow regimes. This lack of defect pathways maximizes the selectivity of the membrane. By minimizing the zeolite membrane thickness, the resistance to gas transport is minimized, and gas permeance is maximized [1]. When both objectives are met, highly selective and permeable membranes can be fabricated, which reduces the number of membranes that are required for a separation process.

There are two methods, which are commonly used to fabricate zeolite membranes, 1) the secondary growth method, and 2) the in-situ crystallization method, also known as the pore plugging method. In the pore plugging method, zeolite crystals are intergrown inside a microporous support in a single synthesis step to create a selective layer of abutting zeolite crystals. With the secondary growth method however, seed crystals are grown separately, deposited onto a porous membrane support, and finally subjected to a second growth step, which aims to create a continuous crystal layer on top of the microporous support [2]. Defect pathways which compromise membrane performance can be created in both membrane types, and have different characteristics due to the configuration of the crystal layer. In secondary growth membranes, continuous defect pathways across the membrane are likely to be formed. In pore plugged membranes however, defect pathways proceed around the zeolite crystals and membrane support pores. In this situation, defect pathways in pore plugged membranes may not necessarily create a continuous pathway across the membrane. The selectivity of pore plugged membranes is therefore, less sensitive to the presence of defects in comparison to secondary growth membranes. All membranes in this research were synthesized by the pore plugging method.

To hydrothermally synthesize silicalite crystals inside the pores of a membrane support, a precursor solution composed of a silica source, water, and a templating agent are combined with membrane supports inside an autoclave. A cradle was designed to keep the tubular supports in an upright position. 4 tubular supports were used in each batch of synthesis in the autoclave. The autoclave is then sealed, and the temperature of the autoclave is increased using an oven. This caused a pressure increase in the sealed autoclave. As temperature and pressure inside the autoclave increase, molecules of Silica and the templating agent begin to diffuse into the active layer of the membrane support. Molecules of Si and O_2 then form SiO_4 tetrahedra, which are attracted to each other and form pentasil units made up of pentasil rings. These pentasil units grow around templating agents to become pentasil chains, and eventually crystals of silicalite [3]. Although crystals of silicalite are formed on all exposed surfaces of the membrane support, a selective layer of abutting crystals is readily formed in the membrane support's active layer since the pore size of this layer is the smallest, and requires the least and smallest number of crystals to become plugged. Temperature and pressure therefore contribute to the rate of crystal growth, and therefore the size and the number of crystals inside the membrane support as synthesis time increases [4–7]. For pore plugged membranes, the size of crystals is furthermore limited by the size of the active layer pores. Given the objective is to plug the membrane support pores completely, it is desirable to fabricate many small crystals to minimize the total volume of unfilled regions of the membrane support. Temperature, pressure and time must therefore all be optimized with consideration of the non-uniform pore structure of the membrane supports to fabricate the best possible membranes. These complex relationships are particularly difficult to study due to the caustic and volatile nature of the template solution molecule, tetra-propyl ammonium hydroxide (TPAOH) that is used to direct the synthesis of silicalite.

A summary of the different conditions that have been investigated are shown in Table 7.1. To fabricate the most defect free membranes as much as possible in this study, different membrane support pore sizes, molar compositions of the precursor solution, and number of interruptions during membrane synthesis were varied. Also, it was attempted to measure the autoclave fill level, as well as the pressure during membrane synthesis using a custom made autoclave to investigate how these variables affect membrane structure. These two characteristics have not been investigated at the temperatures and pressures used in this study to the best of our knowledge. The effect of membrane support pore size is notably absent from this chapter, as it is described in detail in Chapter 3.

In addition to the membrane characteristics and synthesis parameters that were investigated for each membrane batch, the permeation tests that have been conducted with each membrane are summarized by corresponding coloured cells. Blue cells indicate that pure gas permeation tests have been conducted with the membrane, and orange cells indicate that binary gas mixture permeation tests have been conducted with the membrane. Not all of the permeation test results have been featured in this thesis. Therefore, the membranes whose results have been presented are identified by green cells, and the corresponding chapter has been identified in the adjacent column.

Table 7.1. Summary of membrane fabrication conditions undertaken in this research. Membrane batch codes PP 19, 20, 23, and 24 are a part of a different study and so are not shown.

Membrane details							**Synthesis conditions**			
Code	Support pore size [μm]	ID	Experiments conducted		Featured in Thesis		Autoclave Type	Precursor solution composition [mol]	Interruptions	Autoclave fill level
			Pure	Binary		Chapter		SiO_2:TPAOH:H_2O		
CONTROL	0.3	(1)	🟦		🟩	3	N/A	N/A	N/A	N/A
	0.45	(2)	🟦		🟩	3				
	0.8	(3)	🟦		🟩	3				
	1.4	(4)	🟦		🟩	3 , 7				
PP12	0.3	(1)	🟦	🟧			Parr 4748	1:0.5:27.8	0	80 - 100%
	0.3	(2)	🟦	🟧						
	0.3	(3)	🟦	🟧	🟩	7				
	0.3	(4)	🟦	🟧						
PP13	0.2	(1)					Parr 4748	1:0.5:27.8	0	80 - 100%
	0.3	(2)								
	1.4	(3)								
	-									
PP14	0.8	(1)	🟦	🟧	🟩	3 , 7	Parr 4748	1:0.45:27.8	1	80 - 100%
	0.2	(2)	🟦		🟩	7				
	0.14	(3)	🟦							
	0.3	(4)	🟦		🟩	3 , 7				

Membrane details							**Synthesis conditions**			
Code	Support pore size	ID	Experiments conducted		Featured in Thesis		Autoclave Type	Precursor solution composition [mol]	Interruptions	Autoclave fill level
	[µm]		Pure	Binary		Chapter		SiO_2:TPAOH:H_2O		
PP15	0.45	(1)	🟦	🟧	🟩	3	Parr 4748	1:0.45:27.8	1	80 - 100%
	0.3	(2)	🟦		🟩	3				
	0.8	(3)	🟦	🟧	🟩	2 , 3				
	1.4	(4)	🟦		🟩	3				
PP16	0.3	(1)	🟦		🟩	3	Parr 4748	1:0.45:27.8	1	> 95%
	0.45	(2)	🟦		🟩	3				
	1.4	(3)	🟦		🟩	3				
	0.8	(4)								
PP17	0.8	(1)	🟦				Parr 4748	1:0.45:27.8	1	> 95%
	1.4	(2)								
	0.45	(3)	🟦	🟧						
	-									
PP18	0.3	(1)					Parr 4748	1:0.45:27.8	1	> 99%
	0.45	(2)	🟦							
	0.8	(3)	🟦							
	1.4	(4)								
PP21	0.3	(3)					Custom Autoclave - has gold fitting and tubing	1:0.47:29.3	1	~ 30%
	0.45	(2)								
	0.8	(1)	🟦		🟩	7				
	1.4	(4)								

Membrane details							**Synthesis conditions**			
Code	Support pore size [μm]	ID	Experiments conducted Pure	Binary	Featured in Thesis	Chapter	Autoclave Type	Precursor solution composition [mol] SiO_2:TPAOH:H_2O	Interruptions	Autoclave fill level
PP22	0.3	(3)					Custom Autoclave - soln exposed to internal fitting	1:0.45:25.6	1	~ 30%
	0.45	(2)								
	0.8	(1)	🟦							
	1.4	(4)								
PP25	0.3	(1)	🟦		🟩	7	Custom Autoclave - soln exposed to internal fitting	1:0.45:27.6	1	~ 30%
	0.3	(2)	🟦							
	0.3	(3)								
	0.3	(4)								
PP26	0.8	(1)	🟦		🟩	7	Custom Autoclave - soln exposed to internal fitting	1:0.54:34.1	1	~ 30%
	0.8	(2)	🟦		🟩	7				
	0.45	(3)	🟦							
	0.45	(4)								
PP27	0.8	(1)					Custom Autoclave - new beaker lid	1:0.45:27.6	1	~ 38%
	0.8	(2)								
	0.45	(3)	🟦							
	0.45	(4)								

Membrane details							**Synthesis conditions**			
Code	Support pore size [μm]	ID	Experiments conducted		Featured in Thesis		Autoclave Type	Precursor solution composition [mol]	Interruptions	Autoclave fill level
			Pure	Binary		Chapter		SiO_2:TPAOH:H_2O		
PP28	0.8	(1)	🟦				Custom Autoclave - new beaker lid	1:0.45:26.4	1	~ 38%
	0.8	(2)								
	0.45	(3)	🟦		🟩	7				
	0.45	(4)	🟦							
PP29	0.8	(1)	🟦				Parr 4748	1:0.45:27.8	1	~ 80%
	0.8	(2)								
	0.45	(3)	🟦	🟧						
	0.45	(4)	🟦	🟧						
PP30	0.45	(1)	🟦	🟧	🟩	7	Parr 4748	1:0.45:26.4	1	~ 80%
	0.45	(2)	🟦							
	0.8	(3)	🟦							
	0.8	(4)								
PP31	0.45	(1)	🟦				Parr 4748	1:0.45:26.4	2	~ 85%
	0.45	(2)	🟦							
	0.45	(3)	🟦		🟩	7				
	0.45	(4)	🟦	🟧						
PP32	0.45	(1)					Parr 4748	1:0.45:27.8	1	~ 94%
	0.45	(2)	🟦							
	0.45	(3)	🟦							
	0.45	(4)	🟦	🟧	🟩	5, 6, 7				

Membrane details							**Synthesis conditions**			
Code	Support pore size [μm]	ID	Experiments conducted Pure	Binary	Featured in Thesis	Chapter	Autoclave Type	Precursor solution composition [mol] SiO_2:TPAOH:H_2O	Interruptions	Autoclave fill level
PP33	0.45	(1)	🟦	🟧	🟩	5, 6, 7	Parr 4748	1:0.45:27.8	1	> 99%
	0.45	(2)	🟦		🟩	7				
	0.45	(3)								
	0.45	(4)	🟦							
PP34	0.45	(1)	🟦				Parr 4748	1:0.45:27.8	1	~ 97%
	0.45	(2)								
	0.45	(3)								
	0.45	(4)								

7.1.1 Molar Composition of Precursor Solution and Interruptions During Hydrothermal Synthesis

The molar composition of the precursor solution has been studied by many other researchers in the literature [8–11]. Therefore, it has not been investigated in this thesis to a great extent. To effectively plug membrane support pores, a precursor solution composition is required which allows for 1) seeding and growth of zeolite crystals, and 2) diffusion of template and zeolite building block molecules into the membrane support pores to replenish the consumed molecules. According to Li et al. [12] this optimum precursor solution molar ratio is 1 : 0.45 : 27.8 for SiO_2 : TPAOH : H_2O, and has been predominately used in this work as shown in Table 7.1. The molar composition that was used for membranes in the first 2 batches; PP 12 – PP 13, was used by the previous student, who worked on this project, and is 1 : 0.5 : 27.8 for SiO_2 : TPAOH : H_2O [13]. In the following 5 batches; PP 14 - 18, the molar ratio of 1 : 0.45 : 27.8 for SiO_2 : TPAOH : H_2O was used. The difference in performance that was observed when switching from the former to the latter molar composition is shown in Figure 7.1.

Figure 7.1 shows that the He permeance of PP 12 0.3 (3), which was fabricated using the molar ratio of 1 : 0.5 : 27.8 for SiO_2 : TPAOH : H_2O is slightly less than the He permeance of PP 14 0.3 (4), which was fabricated using the molar ratio of 1 : 0.45 : 27.8 SiO_2 : TPAOH : H_2O. The N_2/He selectivity of PP 14 0.3 is remarkably different in comparison to PP 12 0.3 (3) in that the former is selective to N_2 while the latter is selective to He. These observed permeances are indicative of comparatively less crystal growth in PP 12 0.3 (3). It should be mentioned however, that membrane PP 12 0.3 (3) was quenched to cool the autoclave following hydrothermal synthesis. Therefore, it is likely that by cooling the autoclave quickly in this way, defects were formed due to the different rates of thermal expansion of the silicalite crystals and the membrane support. Subsequent membranes were therefore fabricated using the molar ratio of 1 : 0.45 : 27.8 SiO_2 : TPAOH : H_2O. It was hoped that a larger support pore size would make better membranes if the procedure was repeated. This investigation has been described in detail in Chapter 3.

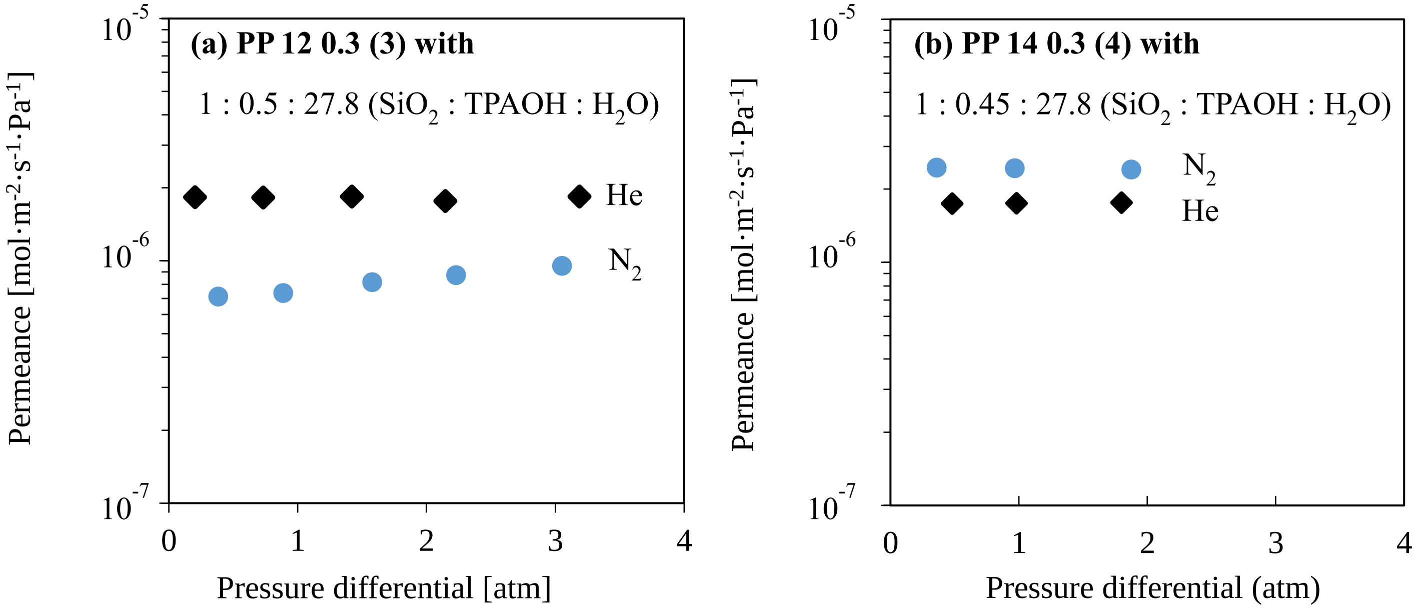

Figure 7.1. Effect of precursor solution molar composition on permeances of He and N_2. Both membranes were tested using module 1 with the high and low pressure sides of the membrane sealed using a generic epoxy. (a) He and N_2 pure gas permeances of membrane PP 12 0.3 (3) which was fabricated using the precursor molar composition ratio 1 : 0.5 : 27.8 for SiO_2 : TPAOH : H_2O. (b) He and N_2 pure gas permeances of membrane PP 14 0.3 (4) which was fabricated using the precursor molar composition ratio 1 : 0.45 : 27.8 for SiO_2 : TPAOH : H_2O.

In addition to optimizing the precursor solution for hydrothermal synthesis, Li et al. have reported that an interruption during hydrothermal synthesis results in improved plugging of the membrane active layer [12]. During an interruption, hydrothermal synthesis is paused by reducing the autoclave temperature and therefore pressure partway through synthesis, thus slowing down the rate of crystal growth. Sufficient time is then allowed for zeolite crystal reactants to diffuse into the spaces between the recently formed zeolite crystals. When the autoclave temperature and hydrothermal synthesis then resume, it is expected that rapid growth of small crystals will begin again, plugging any unoccupied regions of the active layer with zeolite crystals. Membranes fabricated in batches PP 14 and onwards have therefore included an interruption to improve zeolite packing density inside newly fabricated membranes.

A comparison of the permeances of membranes fabricated with 1 interruption (batch PP 30) and 2 interruptions (PP 31) are shown in Figure 7.2.

Figure 7.2 unexpectedly shows no N_2/He selectivity for PP 31 0.45 (3), even though its He permeance is similar to the He permeance of PP 30 0.45 (1). These results are indicative that significant defect pathways are present in the active layer of membrane PP 31 0.45 (1). Since the most significant difference between membranes fabricated in batch PP 30 and PP 31 is the second round of hydrothermal synthesis, the much poorer selectivity was likely caused by the additional heating and cooling process between rounds of hydrothermal synthesis. In this case, additional defects can be attributed to the different thermal coefficients of linear expansion for the zeolite crystals and the membrane support. Consequently, small defect pathways may have been formed during membrane heating, which are not closed during the cooling phase. This explanation is supported by the presence of viscous flow through PP 31 0.45 (3), which causes both He and N_2 permeances to increase with pressure.

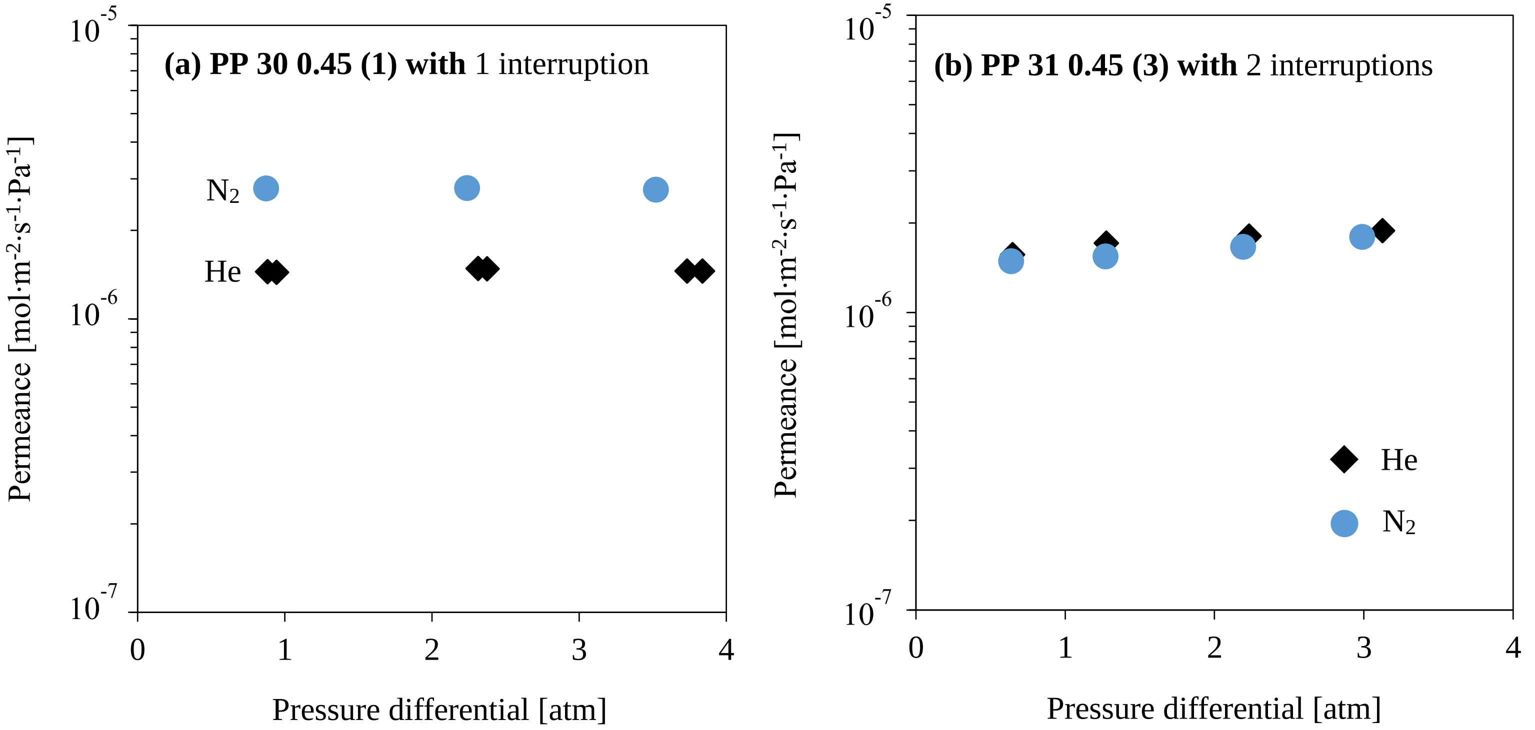

Figure 7.2. Effect of number of interruptions during hydrothermal synthesis on permeances of He and N_2. Both membranes were tested using module 1. Membrane PP 30 0.45 (1) was sealed using generic epoxy, whereas PP 31 0.45 (3) was sealed using Torrseal. (a) He and N_2 pure gas permeances of membrane PP 30 0.45 (1) which was fabricated using the precursor molar composition ratio 1 : 0.45 : 26.4 SiO_2 : TPAOH : H_2O and 1 interruption during hydrothermal synthesis. (b) He and N_2 pure gas permeances of membrane PP 31 0.45 (3) which was fabricated using the precursor molar composition ratio 1 : 0.45 : 26.4 SiO_2 : TPAOH : H_2O and 2 interrupted hydrothermal synthesis rounds. Both membranes were tested using module 1.

Alternatively, there may be an effect caused by sealing the membrane PP 31 0.45 (3) with Torrseal as opposed to the generic epoxy for PP 30 0.45 (1). Since this was the first batch of membranes to be sealed with Torrseal, the application procedure was not very well refined when PP 31 0.45 (3) was sealed. This membrane may still be a good membrane, but if the axial faces of this membrane support were not completely sealed, the membrane may be bypassed during permeation experiments.

Now that graphite gasket containing membrane module has been developed (and is described in the next section), future membranes can be tested using this module, and characterized using the characterization method in chapter 5. Since this method requires testing uncalcined membranes, it is too late to test the membranes from batches PP 30 and 31, but a future study could take untested membranes, subject them to conditions which are expected to cause defects, and then be re-characterized.

7.1.2 Autoclave Fill Level

During hydrothermal synthesis, as the autoclave is filled with a greater volume of liquid, the headspace inside the autoclave is reduced, and any vaporized liquid will have a reduced volume to occupy. According to the ideal gas law and other equations of states, this means that pressure inside the autoclave will increase more in that case with temperature. At the same time, as pressure increases, the solubility of gases inside liquids increases, and their equilibrium concentration at a given temperature changes. Some studies have mentioned the autoclave fill level that was used, but these studies do not investigate the effects of different fill levels on membrane performance [8,11–13]. It has therefore been hypothesized that greater autoclave fill levels promote zeolite crystal formation inside pore plugged membranes, which improves their performance. This hypothesis is supported by the N_2 permeance trends shown in Figure 3.7 in Chapter 3 that were observed for membranes fabricated in batches PP 14 – PP16. In Chapter 3 membrane batches are denoted as A, B, and C for PP 14, PP15, and PP 16, respectively. Figure 3.7 shows that membranes fabricated in batch PP 16 (batch C) generally exhibit greater N_2 permeance in comparison to membranes fabricated in batches PP 15 and PP 14 (batch B and A, respectively). Cross referencing these results with Table 7.1 shows that although the autoclave fill level was not measured accurately for these membranes, it was more certain and likely greater for batch PP 16 (batch C, > 95%) in comparison to batches PP 14 and PP15 (batch A and B, 80 – 100%).

After these observations, the hypothesis that autoclave fill level affects membrane performance has been tested by fabricating three batches of membranes using different autoclave fill levels, which were more reliably measured for the first time with batch PP 32. The permeances of membranes fabricated at the highest measured autoclave fill level of more than 99% (PP33) and lowest measured autoclave fill level of 94% (PP32) are shown in Figure 7.3.

It should be emphasized that by increasing the autoclave fill level, the potential for an explosion becomes greater, and therefore this investigation could inherently be dangerous. In this study, the risk has been minimized by conducting the synthesis inside an oven, which is inside a fume hood with its sash lowered. This way, in the event of an explosion the vapors will be vented safely, and both the oven door and fumehood sash will protect any passers by from injury. The autoclave that has been used has also been inspected prior to each use to ensure that its structure is not compromised, and that it is in good working order.

Figure 7.3 shows that the permeances of N_2 at all feed pressures are greater for membrane PP 33 0.45 (1) in comparison to membrane PP 32 0.45 (4). Conversely, it shows that the permeances of He at all feed pressures are slightly greater for membrane PP 32 0.45 (4) in comparison to membrane PP 33 0.45 (1). The permeances of both gases increase as a function of feed pressure, which indicates that viscous flow contributions to membrane permeance are present in both membranes. Due to the presence of viscous flow, the greatest N_2/He selectivities are found at the lowest feed pressure, and are 1.83 and 1.44 for of PP 33 0.45 (1) and PP 32 0.45 (4) respectively. Although the permeances of each membrane are approximately similar, their varied selectivities indicate that there are fewer and/or smaller defects in PP 33 0.45 (1) in comparison to PP 32 0.45 (4). Since these two membranes were fabricated and tested at similar conditions, their varied performance can be attributed to their only distinguishing synthesis parameter, which is the autoclave fill level.

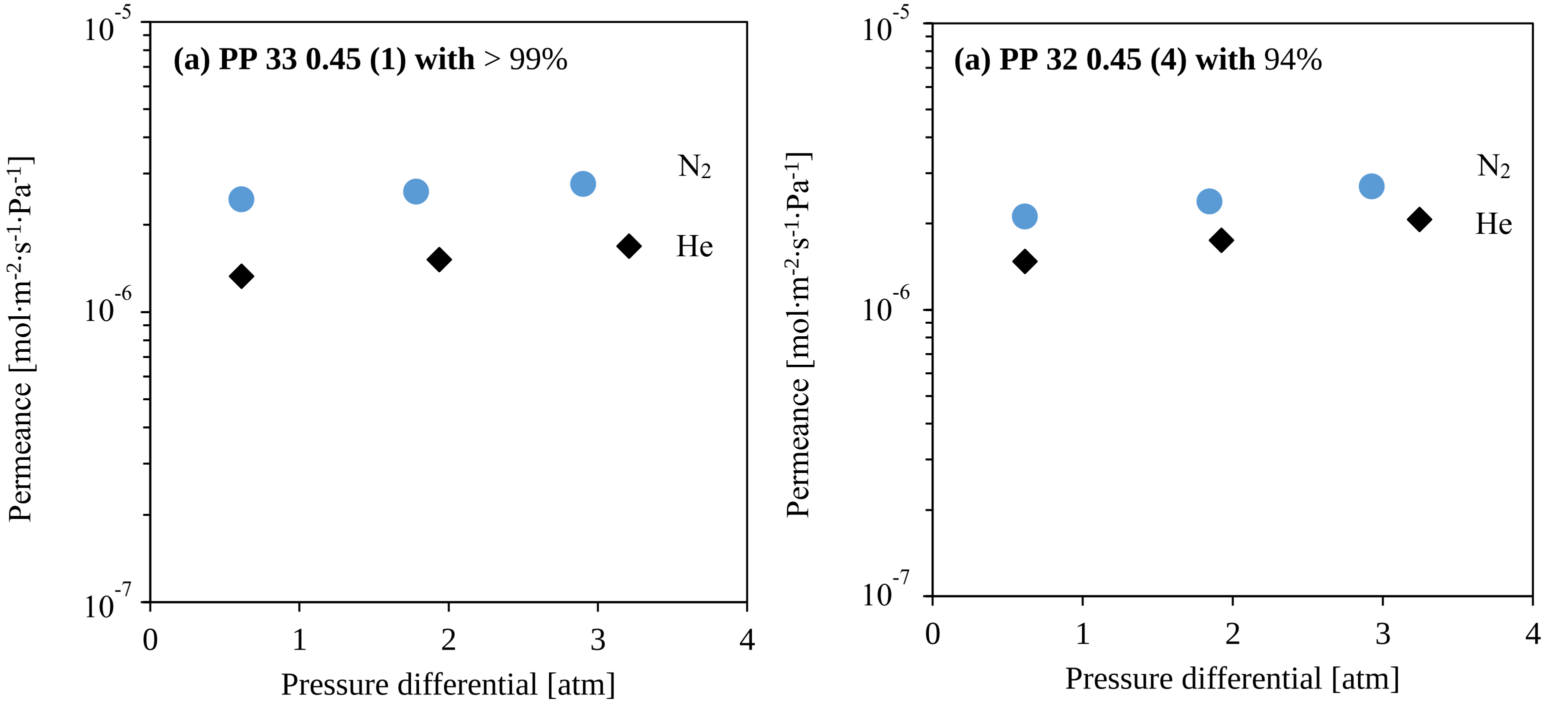

Figure 7.3. Effect of autoclave fill level on permeances of He and N_2. Both membranes were tested using module 3 with Aremco 617 glazed ends. (a) He and N_2 pure gas permeances of membrane PP 33 0.45 (1) which was fabricated using the precursor molar composition ratio 1 : 0.45 : 27.8 SiO_2 : TPAOH : H_2O, 1 interruption during hydrothermal synthesis, and an autoclave fill level of more than 99%. (b) He and N_2 pure gas permeances of membrane PP 32 0.45 (4) which was fabricated using the precursor molar composition ratio 1 : 0.45 : 27.8 SiO_2 : TPAOH : H_2O, 1 interruption during hydrothermal synthesis, and an autoclave fill level of 94%.

As shown in Table 7.1, the autoclave fill level is greater for batch PP 33 in comparison to batch PP 32. Since greater N_2 permeances and higher N_2/He ideal selectivities indicate more complete pore plugging of membrane support pores, the results shown in Figure 7.3 support the hypothesis that autoclave fill level promotes better zeolite crystal formation inside pore plugged membranes.

7.1.3 Parr Autoclave and Custom-made Autoclave

To the best of our knowledge, there are no published studies where the autoclave pressure during hydrothermal synthesis of silicalite membranes is measured. This is understandable as the introduction of a gauge or sensor to an autoclave also introduces additional complexity to the autoclave design, and possible places for the autoclave to leak at high pressures. Instead, a commercially available autoclave with a Teflon beaker insert is generally utilized, and the pressure inside the autoclave is reported as being autogenous. The autoclave that was used in this study to synthesize membranes was a model 4748 Acid Digestion bomb made by Parr instruments, and is shown in Figure 7.4a. To better describe and understand the synthesis conditions however, it was desired to measure pressure during hydrothermal synthesis, which could not be done with this autoclave. An alternative custom made autoclave was therefore designed and tested which contained few wetted stainless steel parts and is shown in Figures 7.4b-d. In addition to a Teflon O-ring sealed Teflon beaker insert, this autoclave contained a gold plated tube which was in contact with the synthesis solution, but allowed a connection to be made to a cross fitting which was connected to a pressure gauge, valve, and a rupture disc. Although a port for a pressure gauge could alternatively be integrated into the lid of the autoclave, the wetted parts of the pressure gauge would come into contact with the hydrothermal synthesis solution. Integrating a pressure gauge in this way would therefore result in simultaneously corroding the gauge and contaminating the synthesis solution.

Minor modifications to the custom autoclave were made following initial tests using water. It was found that the O-ring seal for the Teflon liner would compress excessively and leak vapour due to the combination of the high pressure and temperature inside the autoclave. A double O-ring design was therefore created. This design also leaked, and after several uses it was observed that the Teflon liner lid had compressed since Teflon is prone to creep at high temperatures when under stress. It was then necessary to replace the lid, and it became obvious that the gold plated tube connecting the autoclave to the pressure gauge would need to be replaced with the autoclave liner lid after every few batches. Although gold plating was good for chemical resistance reasons, it was impractical. The next model had a chamfered Teflon lid, which could be replaced easily and sealed with the Teflon beaker insert like the Parr 4748 autoclave. Instead of a gold plated tube connecting the autoclave to the pressure gauge, a Teflon fitting attached to a stainless steel line was used instead. For comparison with the permeances of PP 30 0.45 (1) shown in Figure 7.2a, the permeances of PP 28 0.45 (3), are shown in Figure 7.5. PP 28 0.45 (3) was fabricated using the custom autoclave with a similar precursor solution molar ratio to membranes fabricated in batch PP 30 with the Parr autoclave.

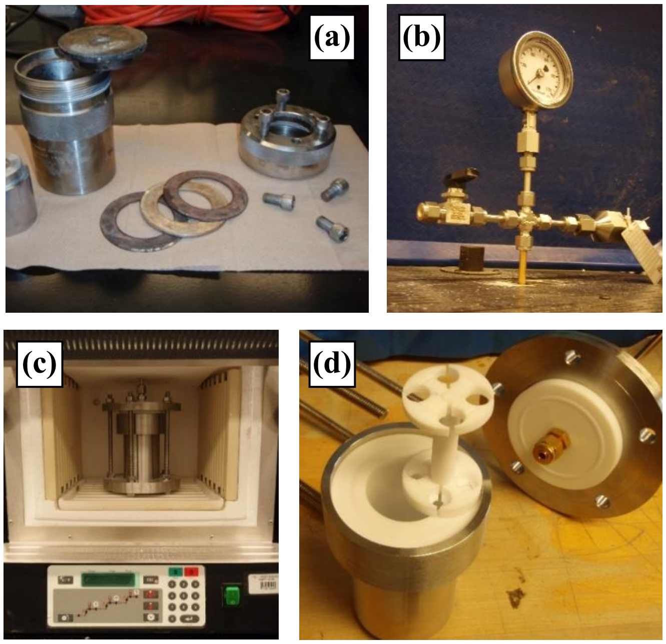

Figure 7.4. Pictures showing the autoclaves that have been used in this research. Figure 7.4a (top left) shows the Parr Instruments model 4748 autoclave. This autoclave utilizes Belleville spring washers which are compressed by cap screws to ensure that the Teflon liner of the autoclave remains sealed during heating and cooling. Chamfered Teflon lid and Teflon liner not shown. Figures 7.4b – d (top right, bottom left, and bottom right), show the rupture disc, vent valve, and pressure gauge assembly (b top right), the assembled custom autoclave inside the oven prior to hydrothermal synthesis (c bottom left), and the Teflon O ring sealed Teflon liner, Teflon membrane cradle, and gold plated tube which leads to the assembly shown in 7.4b (d bottom right).

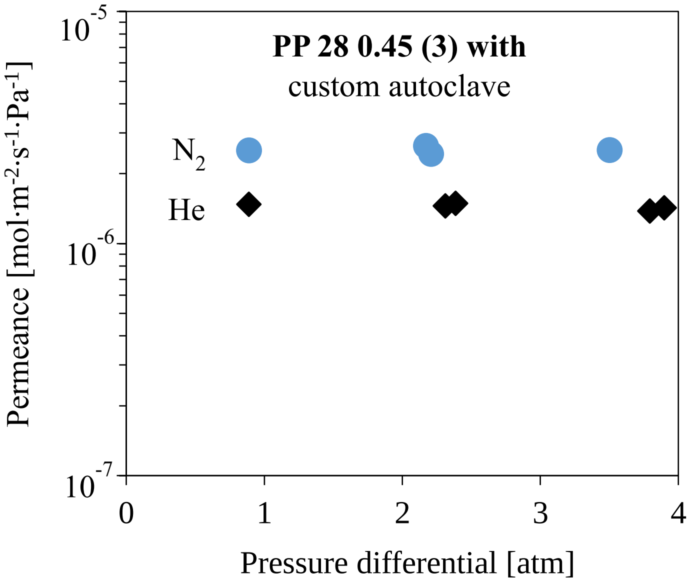

Figure 7.5. Influence of custom autoclave on permeances of He and N_2. The membrane was tested using module 1, and was sealed using generic epoxy. He and N_2 pure gas permeances of membrane PP 28 0.45 (3) which was fabricated using the precursor molar composition ratio 1 : 0.45 : 26.4 SiO_2 : TPAOH : H_2O and 1 interruption during hydrothermal synthesis.

The permeance of He and N_2 through PP 28 0.45 (3) shown in Figure 7.5 is similar to PP 30 0.45 (1) shown in Figure 7.2a. Although reproducing the membrane performance is a good achievement, the ideal selectivity of these membranes is only 1.7, and fabricating membranes with this autoclave was not very reproducible. Since the membranes fabricated using the custom autoclave were not as selective as the membranes fabricated using the Parr autoclave, the custom autoclave was therefore abandoned.

Several lessons have been learnt by fabricating and testing the custom autoclave, which do not need be repeated by another student wishing to investigate the effects of the autoclave further. In a future study, it would be worthwhile to minimize the volume of tubing and therefore headspace above the autoclave. Additionally, autoclaves with ports are commercially available, and although their wetted parts are stainless steel and not Teflon, it may be worthwhile using such an autoclave to determine the saturation pressure curve as a function of temperature for the precursor solution used to fabricate silicalite membranes. This curve would be subject to error as the caustic TPAOH would react with the stainless steel parts of the autoclave, but it would give a place to start from. Alternatively, a disposable autoclave liner could perhaps be used inside such an autoclave. Advances in single use bioreactors are becoming more sophisticated in the pharmaceutical industry (DisTek for example already sells disposable liners for bench scale bioreactors). This could perhaps be adapted to zeolite membrane manufacturing. Also, a Belleville or other spring washer should be implemented in a future autoclave design. This feature allows the lid of the autoclave to remain compressed and sealed against the lip of the Teflon insert when the stainless steel autoclave body expands more than the liner, and is a part of the Parr 4748 autoclave, likely for this reason.

7.2.0 MEMBRANE MODULE DESIGNS AND SEALING

Even with significant forethought and consideration, an iterative process was required to come up with a membrane module design that was able to form a gas tight seal between a ceramic membrane module and stainless steel tubes. Many examples of membrane modules are presented in the literature, which should theoretically make the choice of module design straightforward [14–21]. However, these investigations rarely discuss the intricacies of their membrane module designs. Furthermore, and to the best of our knowledge, these literature examples have never compared different membrane modules or disclosed the limitations of their membrane module.

During this research, a total of three different membrane modules, and several different sealing methods have been investigated and are compared to each other. It is therefore hoped that the knowledge presented here will save the time of others and be of assistance to them when they are selecting a membrane module and sealing method to meet their processing needs.

7.2.1 Module with Teflon Ferrules on Stainless Steel Tubing (Module 1)

Figure 7.6 shows a picture of the expanded membrane module 1, which utilizes Teflon ferrules to separate the high and low pressure sides of the membrane using Teflon ferrule fittings on stainless steel tubing. The module is made up of Swagelok fittings, which utilize stainless steel ferrules, except the connections to the membrane feed and retentate pressure lines, which utilize Teflon ferrules. In this way, the same module can be used with different membranes. The tubing, which is to be connected to the ceramic membrane support with a sealing method is made up of convoluted tubing welded to stainless steel adaptors and then tubing. Since convoluted tubing is flexible, a large axial face is made available for applying sealant, and it is not necessary to perfectly align the ceramic membrane support and stainless steel tubing for them to be concentric. These attributes mean that it is very easy to create a gas tight seal between the ceramic membrane support and stainless steel process lines for the connections to the rest of the set up.

Although Teflon ferrules creep and are deformed when subjected to repeated stresses, they can be replaced periodically. In doing so, the integrity of the seal formed between the Teflon ferrules and stainless steel tubing can be relied upon.

Figure 7.6. Picture showing how the membrane and stainless steel supports assembly is inserted into membrane module 1. Teflon ferrules and Swagelok fittings are used to separate the permeate stream from the feed and retentate streams. The membrane shown in this picture has been attached to the stainless steel tubing of the feed and retentate lines using generic epoxy.

Generic epoxies

To attach the ceramic membrane support to the convoluted tubing of the feed and retentate pressure lines, 2-Ton epoxy made by Devcon (Danvers, MA, USA), and then Perma Poxy made by Permatex (Solon, OH, USA) were used. The brand of epoxy was changed midway through the research as a vendor, which sold 2-Ton epoxy could not be found once our supply ran out. Figure 7.7 shows what the epoxy looks like when cured. Perma poxy was purchased as it is similar to 2-Ton's epoxy, although it is recognized that the two epoxies are likely to have differences in their exact composition. In this context, the similar epoxy was made up of a "hardener" component, and a "resin" component, which are to be mixed for a few minutes before application to the surfaces to be bonded. The composition of the epoxies made by each manufacturer are protected as trade secrets, but it can be seen in the following plots that this information is irrelevant as the performance of membranes attached to stainless steel supports using such an epoxy changes with time. Any experiments that have been conducted using membranes, which have been subjected to such an epoxy therefore, cannot be reproduced, and use of such epoxy is not recommended. Since these generic epoxies are however able to effectively attach ceramic membranes to stainless steel tubes, they were used exclusively for testing membranes in batches PP 12 – PP 16. These epoxies were then used sporadically to test membranes in batches PP 17 – PP 30 as a reference in comparison to the other attachment methods that were investigated.

Epoxy was first applied onto the convoluted tubing and membrane support's axial faces, and the two axial faces were then brought into contact with each other. In this way, a mechanically weak bond was created to concentrically align the convoluted tubing with the membrane as well as possible. After a few hours had elapsed, the membrane and stainless steel tubes were set to rotate radially, and more epoxy was applied to the membrane support and convoluted tubing joint, while the assembly spun at less than 30 rpm to create a more lasting bond. This spinning action was responsible for the even coating of epoxy that can be seen in Figure 7.7.

Figure 7.7. Picture showing a membrane attached to the stainless steel tubing of the feed and retentate lines using epoxy.

Figure 7.8 shows the permeances of He and N_2 that were measured using membrane PP 14 0.2 (2) which was attached to stainless steel feed and retentate pressure lines using epoxy, and were determined 12 months apart.

From this figure it can be seen that the permeance of He as well as N_2 for PP 14 0.2 (2) have decreased substantially between May 2014 and May 2015. Additionally, the ideal selectivity of N_2/He has decreased slightly in this time from 2.75 to 2.70. The simultaneous reduction of the ideal selectivity and the permeance could indicate that the pores of the silicalite crystals, which make up the membrane, have become blocked. In this scenario, the surface diffusion contribution to overall permeance would have decreased, and the defect transport contribution to overall permeance become more significant. Thus, the N_2/He ideal selectivity has reduced in the direction of Knudsen selectivity, which favours He over N_2. The cause of this blockage is reasoned to have come from the evaporated epoxy solvent, which is used to dissolve the polymers in both the Perma poxy and 2 Ton epoxies. Although the exact solvents, which have been used in the epoxies are protected trade secrets, solvents are typically long chained molecules with significant dipole moments. Such attributes are clear indicators that adsorption would occur with silicalite, and would additionally be very strongly bonded. Although the rate of evaporation of off-gassed solvents from the epoxy is very small, it would accumulate inside the crystals of the silicalite membrane and eventually become significant. As the silicalite crystal layer is only 10 microns thick, a large amount of solvent would not be required to poison the membrane.

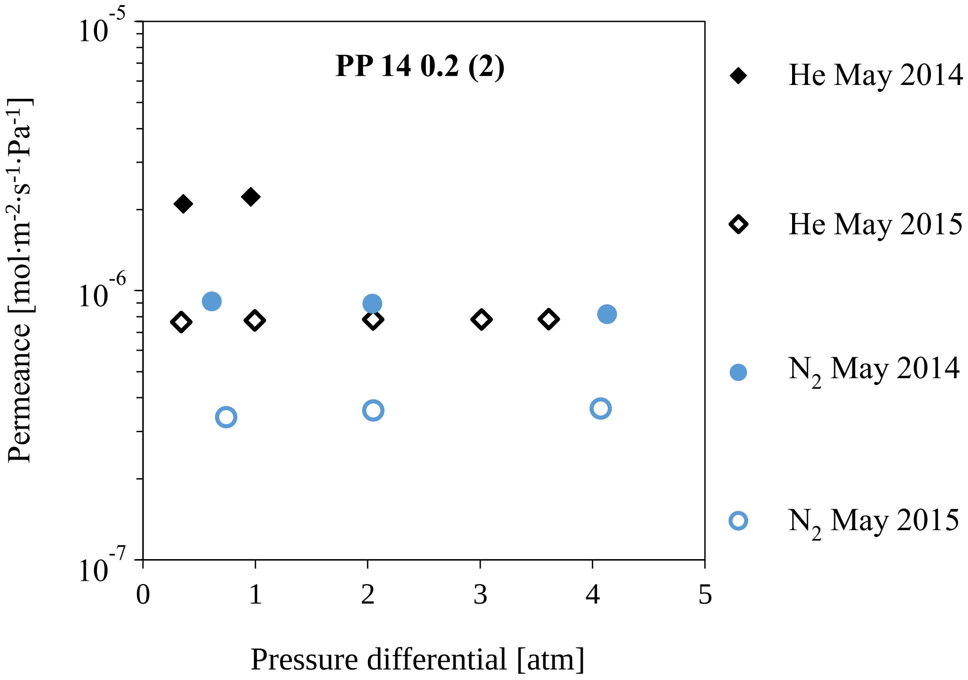

Figure 7.8. Effect of time on permeances of He and N_2. This membrane was tested using module 1 and generic epoxy. He and N_2 pure gas permeances of membrane PP 14 0.2 (2) determined in May 2014 and May 2015. He and N_2 pure gas permeances of membrane PP 14 0.2 (2) which was fabricated using the precursor molar composition ratio 1 : 0.45 : 27.8 SiO_2 : TPAOH : H_2O and 1 interruption during hydrothermal synthesis.

Torrseal

Given the simultaneous reduction in the permeance and selectivity when the generic epoxy was used, an alternative epoxy has been investigated. When selecting a second type of epoxy to test, it was additionally considered that the epoxy would off-gas a significantly lesser amount of molecules, and would be able to be regenerated at as high a temperature as possible. From these criteria, Torrseal epoxy which is made by Agilent (Santa Clara, CA, USA) was identified. Torrseal is commonly used in low pressure vacuum conditions where low off-gassing is required, and can be heated up to 120 °C. This epoxy has been used to attach the membrane support to the stainless steel tubing as shown in Figure 7.9.

Figure 7.9. Picture showing a membrane attached to the stainless steel tubing of the feed and retentate lines using Torrseal.

Similarly to the 2 Ton and Perma poxy epoxies, the Torrseal hardener and resin polymers were mixed for a few minutes before Torrseal was applied to the membrane. As for the other epoxies, Torrseal was then applied to the membrane and convoluted tubing axial faces, which were then brought into contact with each other, and left to cure for several hours which created a mechanically weak bond. Additional Torrseal was later applied to the outer faces of the convoluted tubing and membrane support to reinforce the bond between the two materials while the pieces were stationary. Since Torrseal is much tackier than the other epoxies, it could not be set to spin, and its bond is less smooth than for the other epoxies. PP 33 0.45 (2) has notably been tested using module 1 with Torrseal, as well as the most recently developed module, and is discussed in section 7.3.0. Other membranes in batches PP 31 – PP 34 have also been tested using module 1 with Torrseal, although their results are not all shown in this thesis.

To thermally regenerate a membrane that has been exposed to moisture or other compounds, and therefore discount contamination of the zeolite crystals in future trials, the membrane and module should be be heated up to the minimum purge temperature. For zeolite 5A, which is similar to silicalite, the minimum purge temperature for moisture and air is is 300 °C [22]. This temperature is therefore recommended for regenerating silicalite membranes, and is unfortunately beyond the 120 °C melting point of Torrseal.

For applications that do not require high temperature regeneration, Torrseal was found to be an ideal material for binding ceramic to stainless steel and creating a gas tight seal. In this study, the regeneration of the membranes between experiments for different adsorbing gases were carried out by He purge at room temperature.

7.2.2 Module with Teflon ferrules on Ceramic Membrane Support (Module 2)

Figure 7.10 shows a picture of the expanded membrane module 2, which utilizes Teflon ferruled fittings to bond the high and low pressure sides of the membrane tubing to the ceramic membrane support. The module is made up of Swagelok fittings, which utilize stainless steel ferrules, and similar to module 1, utilizes Teflon ferrules for the connections to the membrane feed and retentate pressure lines so that the same module can be used with different membranes.

Figure 7.10. Picture showing how the membrane and stainless steel supports assembly is inserted into membrane module 2. Teflon ferrules and Swagelok fittings are used to separate the permeate stream from the feed and retentate streams. The membrane is also been attached to the stainless steel tubing of the feed and retentate lines using Swagelok fittings and Teflon ferrules.

For the ceramic membrane support to be sealed by the Teflon ferrules inside module 2, it is necessary to apply an impermeable sealant to the axial faces of the membrane support, as well as approximately 1 cm of the outside face. A schematic illustration of these faces is shown in Figure 7.11a. In doing so, no gas should bypass the selective zeolite membrane layer. The types of sealant, which have been used for this purpose can either be applied prior to membrane synthesis, or after membrane synthesis. In the case of sealants applied prior to membrane synthesis, it is necessary for the sealant to withstand temperatures up to 500 °C, the temperature of membrane calcination, as well as the caustic conditions inside the autoclave during hydrothermal synthesis without leaching. Alternatively, sealants applied after membrane synthesis do not need to withstand the conditions inside the autoclave during hydrothermal synthesis, but do need to withstand temperatures up to 500 °C to be characterized according to the method described in chapter 5. Prior to 2017, the standard operating procedure for characterizing membranes did not require conducting permeation tests before membrane calcination, and so sealants applied after membrane synthesis were evaluated to withstand regeneration temperatures up to 100 °C, which is sufficient to dry the membrane. It is recognized that a regeneration temperature below 300 °C is less than ideal, but in combination with a purge gas stream of He it was hoped that a temperature of 100 °C would be sufficient to desorb most contaminants from the zeolite pores.

One of the most durable and impermeable seal types is glass, which can be coated onto ceramic membrane supports of any shape and size as glass particles suspended in a solvent solution. Once applied to a membrane support, the solvents can be evaporated, and the glass particles fuse together at a sufficiently high temperature. A picture of a membrane whose ends have been glazed is shown in Figure 7.11b.

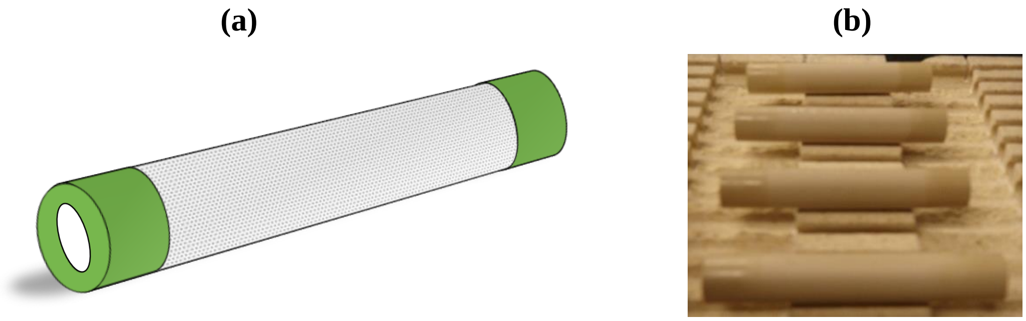

Figure 7.11. Details of membrane module 2. (a) Schematic showing the faces where an impermeable coating needs to be applied to membrane supports that are used with module 2. The coated areas are shown in green. (b) A picture of Aremco 617 coated membranes. Their coated ends appear glossy and a different colour in comparison to the middle of the membrane supports.

Aremco 617, with and without silicon rubber

Aremco 617 which is made by Aremco (Valley Cottage, NY, USA) is a special type of laboratory grade glazing compound, which has been used in other inorganic membrane studies when membranes have been subjected to harsh chemical conditions [23,24]. This glaze solution contains suspended glass particles in several different solvents such that the glaze solution can be diluted in water as needed to be applied to the membrane support evenly, and then cured at varied temperatures to fuse the glass particles together. These curing temperatures go as high as 875 °C. Therefore, Aremco 617 must be applied prior to membrane synthesis since the thermal stability of silicalite is between 700 °C and 1100 °C depending on the quality of crystals fabricated [25]. Since the solvents of the Aremco 617 solution are removed when the glaze is cured, off-gassing inside the membrane is not possible for Aremco 617 coated membranes. Additionally, it is necessary to apply several thin coats of Aremco 617 to form an impermeable glaze layer to minimize the formation of gas bubbles inside the glaze, which would otherwise crack during curing. In this investigation, 2 coats were found to be satisfactory for creating an impermeable seal. This was determined by covering all outside faces of an unfilled non-selective membrane support with Aremco 617, and measuring He permeance at multiple pressures. The results of this investigation are shown in Table 7.2. Several membranes from batches PP 17 – PP 25 were tested using module 2 and Aremco sealing, with and without silicon rubber.

Table 7.2 firstly shows that a membrane sealed inside Module 1 with a generic epoxy, or module 2 with no glaze or additional sealant on its ends can be used to measure the permeance of an unfilled membrane support within 5% of each other. This variation is within the experimental error of 9% for permeances as shown in Appendix 1. Given this result, permeances measured using module 2 can be reasoned to be similar to those measured using module 1. The observed reductions in He permeance of Aremco 617 coated supports can therefore be attributed to the number of coats of Aremco 617 that have been applied to the membrane support. Table 7.2 shows that when a single coat of Aremco 617 is applied to an unfilled membrane support, He permeance decreases by an order of magnitude in comparison to an unfilled membrane support without any Aremco 617 application. When two coats of Aremco were applied, He permeance was then below the minimum detectable permeance value of 10^{-9} $mol \cdot m^{-2} \cdot s^{-1} \cdot Pa^{-1}$, which is indicative that the membrane support was impermeable. These experiments were considered to be successful, and subsequent membranes were coated with 3 coats of Aremco 617 prior to membrane synthesis to achieve good membrane coverage, despite the increased time and labour requirement.

Table 7.2. He pure gas permeances of unfilled membrane supports with a pore size of 1.4 μm. Module 1 with the generic epoxy (2-Ton) over the axial membrane support faces, and module 2 with up to 2 coats of Aremco 617 over the entire outer surface of the membrane support have been used to incorporate the membrane supports into the module.

Module	Sealant	He Permeance $[mol \cdot m^{-2} \cdot s^{-1} \cdot Pa^{-1}]$
1	Generic Epoxy (axial faces only)	8.29×10^{-5}
2	None	8.99×10^{-5}
2	1 x Aremco 617 (axial faces and outer surface)	5.83×10^{-6}
2	2 x Aremco 617 (axial faces and outer surface)	$< 10^{-9}$

The permeances and selectivities of membranes that were tested using module 2 were not however, as favourable as the membranes that were fabricated previously. Figure 7.12 shows the He and N_2 permeances of membrane PP 21 0.8 (1), which was tested using Module 2 with Aremco 617 sealing, and membrane PP 14 0.8 (1) which was tested using module 1 and the generic epoxy.

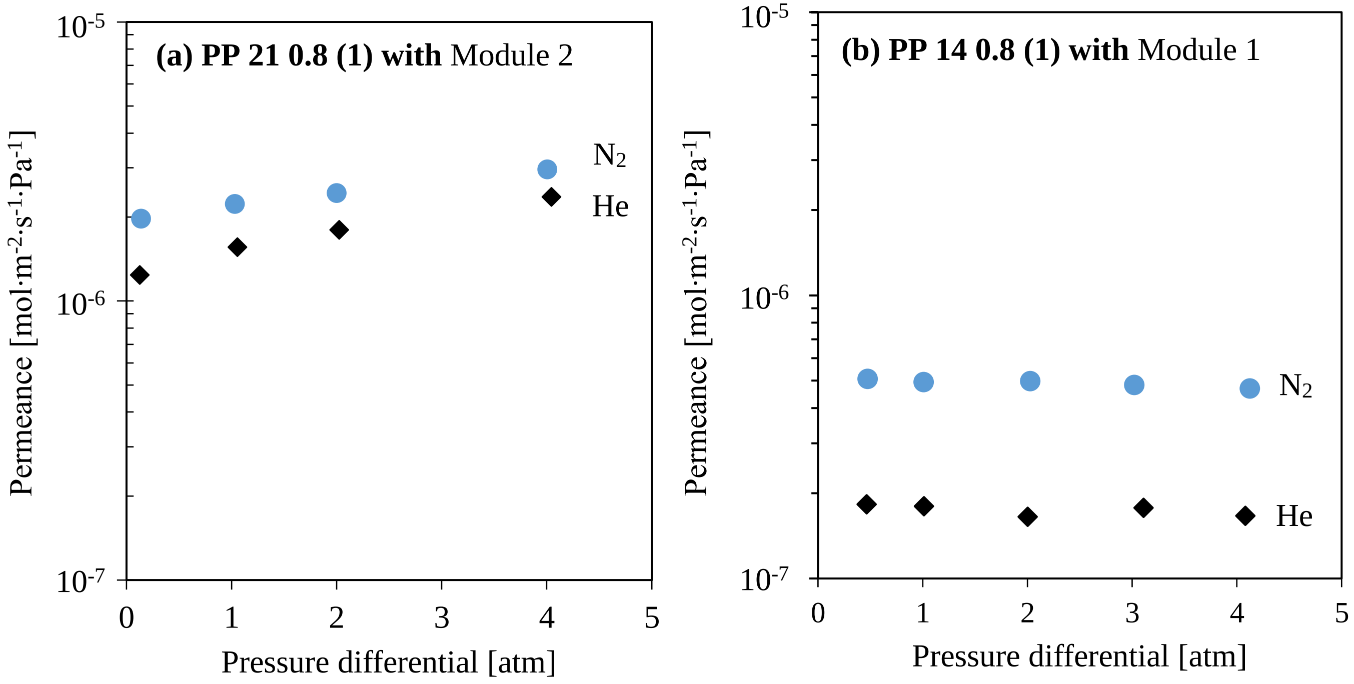

Figure 7.12. Effect of modules 1 and 2, as well as changes to membrane fabrication method over time on permeances of He and N_2. PP 21 0.8 (1) was tested using module 2 and sealed using Aremco 617 and Teflon ferrules, whereas PP 14 0.8 (1) was tested using module 1 and was sealed using generic epoxy. (a) He and N_2 pure gas permeances of membrane PP 21 0.8 (1) determined in March 2016. This membrane was fabricated inside the custom made autoclave, using the precursor molar composition ratio 1:0.47:29.3 SiO_2 : TPAOH : H_2O and with 1 interruption during hydrothermal synthesis. (b) He and N_2 pure gas permeances of membrane PP 14 0.8 (1) determined in August 2013. This membrane was fabricated inside the Parr autoclave, using the precursor molar composition ratio 1:0.45:27.8 SiO_2 : TPAOH : H_2O and with 1 interruption during hydrothermal synthesis.

Figure 7.12 shows that although the He and N_2 permeances are greater for PP 21 0.8 (1) in comparison to PP 14 0.8 (1), its selectivities are less. Furthermore, Figure 7.12a shows that both He and N_2 permeance through PP 21 0.8 (1) increase with feed pressure, which is indicative of viscous flow and larger defects, which were not typically observed for membranes fabricated previously. Such performance is undesirable and was unexpected given the results of the pure gas permeation experiments conducted using completely sealed membrane supports as shown in Table 7.2. It was soon discovered that the Teflon ferrules had creeped due to the induced stress of the module fittings. Therefore the number of times the Teflon ferrules were re-used was reduced, and the ferrules were inspected prior to use to make sure that they were still sufficiently well shaped. Despite this precaution, subsequently tested membranes which were coated with Aremco 617 glaze showed viscous flow contributions to membrane permeance. Although the autoclave type, module, sealing method, and precursor molar composition are all different between PP 21 0.8 (1) and PP 14 0.8 (1), the continued observation of viscous flow in subsequently tested membranes using module 2 suggested that the sealing method was more significantly responsible for viscous flow.

A silicon rubber was then applied over the Aremco 617 coating to create an additional barrier to viscous flow permeation due to an improper seal between the Teflon ferrules and the Aremco 617 coated membrane ends. Although silicon rubber is not impermeable like Aremco 617, such rubbery polymers have much lower permeabilities than zeolitic membranes. Therefore, their contribution to membrane permeance was considered to be reasonably negligible. A picture showing membrane PP 25 0.3 (1) coated with silicon rubber on top of Aremco 617 is shown in Figure 7.13. Both silicon rubber and Teflon can withstand temperatures in excess of 170 °C, and so the addition of silicon rubber would not be the limiting factor for membrane regeneration inside module 2. The addition of silicon rubber did however, present difficulty as its application increases the diameter of the membrane supports, and if the Teflon ferrules were then forced onto the membrane support too roughly, the silicon rubber coating would peel off, and thus be rendered useless. Despite this difficulty in assembling the module when silicon rubber is applied, some membranes were tested and found to contain no viscous flow sized defects, and additionally had reasonably good ideal selectivities for N_2/He.

A more significant concern was however encountered when the module was disassembled one day; the compressive stress of Teflon in the radial direction had sheared off the ends of the membrane through the silicon rubber and Aremco 617. In the membrane shown in Figure 7.13, a clear line can be seen in the picture on the right hand side where the Teflon ferrules sheared through the silicon rubber. Although a torque wrench could be used to tighten the module fittings using only fresh Teflon ferrules to ensure repeated sealing of the membrane, without shearing off the ends, it was decided that it would be better to investigate an alternative solution that would be more robust.

Figure 7.13. Picture showing membrane PP 25 0.3 (1) whose end faces have been coated with silicon rubber on top of Aremco 617. The right hand side picture shows the vertical line where a Teflon ferrule cut at the silicon rubber.

Minwax

As an alternative to Aremco 617, Minwax Polycrylic which is made by Sherwin Williams (Cleveland, OH, USA) was investigated as a post calcination treatment for synthesized membranes. An unfilled membrane support was again completely covered as was done for Aremco 617, however, only one coat of undiluted Minwax was required to reduce the permeance of He through the membrane support such that no permeance could be measured. Although this performance is ideal, Minwax is only stable up to a temperature of 40 °C, at which point it off-gasses significant amounts of VOCs (including alkyl propanols, ethylene glycol, glycol ether, and n-methyl pyrrolidone), which would poison the zeolite crystals of the membrane. This type of sealing is not a practical solution, and was not tested with any silicalite membranes.

Tremclad

Tremclad high heat enamel which is made by Rust-Oleum (Vernon Hills, IL, USA) is sold as a coating for fireplaces, wood stoves, and barbecues, which once cured is claimed to be able to tolerate temperatures up to 350 °C. It was initially assumed that an enamel for barbecues must not off-gas significantly, if at all, as the cured sealant is rated for food exposure conditions. These attributes are ideally suited for sealing the ends of the membrane supports used in this investigation. Tremclad may furthermore offer additional strength such that the Teflon ferrules used in module 2 would not shear the ends of a membrane coated with Tremclad. Pictures showing membranes PP 26 0.8 (1) and PP 26 0.8 (2) whose support ends are coated with Tremclad after exposure to higher temperatures of different duration are shown in Figure 7.14a and 7.14b, respectively. Given the observable cracked appearance of membrane PP 26 0.8 (1) which had been exposed to 250 °C, it is not recommended that membranes coated with Tremclad are subjected to such temperatures. Furthermore, the burn marks that can be observed on PP 26 0.8 (2) from exposure to 300 °C indicate that Tremclad enamel not only off-gases, but off-gases components that autoignite above 250 °C, since there were no sparks inside the membrane module.

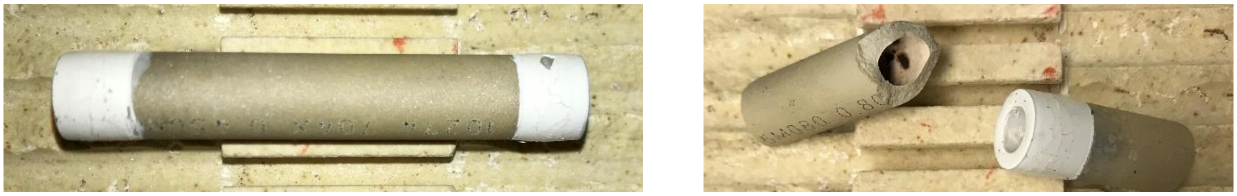

(a) PP 26 0.8 (1)

(b) PP 26 0.8 (2)

Figure 7.14. (a) Picture showing membrane PP 26 0.8 (1) whose end faces have been coated with Tremclad after being exposed to 250 °C for 48 hours. (b) Membrane PP 26 0.8 (2) which had been exposed to 300 °C for 4 hours).

Since 300 °C regeneration therefore was not possible with Tremclad coated membranes, they were not investigated further. Given the failure of sealants applied prior to and following membrane calcination, an alternative module design was therefore investigated.

7.2.3 Module with Graphite Gaskets on Ceramic Membrane Support (Module 3)

The third and final module to be fabricated was designed after conducting a literature search to see what types of modules had been used successfully by others, and then analyzing these designs, given the firsthand knowledge of different module and membrane sealing techniques that had been learnt during this study. Although some fairly recent studies were still conducted using epoxied membrane supports, which have been proven to be undesirable in this investigation, a popular type of membrane – module seal design utilized polymer O rings in combination with glazing compounds such as Aremco 617 [17,20,21,26]. O ring sealed designs are capable of withstanding temperatures up to 256 °C if Kalrez O-rings are used [17], but are susceptible to burst if the high pressure side of the membrane axially pushes the O-ring beyond the glazed sections of the membrane support. In this scenario, there is insufficient friction force induced by compressing the O-ring radially to prevent the O-ring from bursting. In other studies, compressed graphite rings are used to seal the membrane, however, it does not seem readily apparent how such rings would compress to form a seal between the membrane module and ceramic membrane support as they are made from graphite ribbon that has already been pressed inside a die at high pressure [14,19]. These module designs however, seemed to be the most promising, as graphite, unlike polymeric materials, can be heated above 500 °C, and does not creep or out-gas solvents. A module that was most similar to the module designed by Gu et al [18] was therefore developed, which utilized graphite gaskets that were purchased from McMaster Carr (Elmhurst, IL, USA).

This third module is composed of three main parts; one centre bored tube (also containing shoulders to accommodate graphite gaskets) with welded stainless steel discs for flange mounts, and two outside flange pieces, which compress the graphite gaskets when tightened into the flange mounts with bolts. Each of the three parts contains a 1/8” Swagelok compression fitting so that the feed, retentate, and permeate sides of the membrane module can be easily connected to the permeation setup shown in Figure 5.1, in chapter 5. The seal between the membrane module and ceramic membrane support notably do not use Swagelok fittings. The graphite that is used to form a seal with the ceramic membrane support is a compressible graphite that can be purchased in sheets from McMaster Carr (Elmhurst, IL, USA). From these sheets of graphite, gaskets, which fit snugly on top of the membrane support, and inside the specifically cut out space for them inside the centre bored module section have been fabricated using a CNC milling machine. This module is shown in Figure 7.15.


(a)
(b)

Figure 7.15. (a) Picture showing the assembled module 3. (b) Picture showing the incorporation of the membrane and gaskets into the membrane module 3, 7.15b (right).

Aremco 617 without silicon rubber

To create a seal between the ceramic membrane support and the graphite gaskets, it was necessary to seal the membrane faces as shown in Figure 7.11a, and so Aremco 617 was used for this purpose as before. No silicon rubber is needed, as when the graphite gaskets are compressed in the axial direction by tightening the flange bolts, the gaskets expand in the radial direction to form perfect seals over the glazed sections of the membrane support. To prove that this type of sealing arrangement is reproducible, several different membranes have been subjected to pure gas permeation experiments using He at the range of conditions shown in Table 7.3. As well as membranes PP 32 0.45 (4) and PP

33 0.45 (1) which are featured in Table 7.3, other membranes fabricated in batches PP 32 – PP 34 have been tested using Module 3 and Aremco 617 without silicon rubber.

Table 7.3. He permeances at 295 K for PP 32 0.45 (4) and PP 33 0.45 (1) at a feed pressure of 170 ± 2 kPa and permeate side pressure of 100 ± 2 kPa before and after exposure to the indicated gases, and the indicated thermal regeneration regimes. All permeation experiments were conducted using module 3, and the graphite gaskets were replaced in after thermal regeneration process, and prior to the measurement of He permeance at conditions 4 and 6. Condition 6 was not tested for membrane PP 33 0.45 (1).

Condition	He Permeance	
	$[mol \cdot m^{-2} \cdot s^{-1} \cdot Pa^{-1}]$	
	PP 32 0.45 (4)	PP 33 0.45 (1)
1) After Drying	9.42×10^{-7}	4.27×10^{-7}
2) After Calcination	1.80×10^{-6}	1.32×10^{-6}
3) After CH_4 exposure	1.75×10^{-6}	1.28×10^{-6}
4) After 300 °C regeneration	1.95×10^{-6}	1.32×10^{-6}
5) After CO_2 exposure	1.93×10^{-6}	1.46×10^{-6}
6) After 300 °C regeneration	1.93×10^{-6}	-

Table 7.3 shows that despite the varied He permeances of each membrane due to their unique structures, He permeance can be reproduced within experimental error (which is 9% and is detailed in Appendix A.1) following various circumstances using module 3 with graphite gaskets and membranes whose ends have been sealed with Aremco 617. The thermal regeneration regimes that are indicated in Table 7.3 were conducted on membranes that were removed from the module, heated up and cooled down inside an oven, and then re-installed inside the module using uncompressed gaskets. With this procedure, there are many opportunities for the membrane structure to be compromised. Most notably, replacement of the gaskets means that a new seal which may not be as efficient as the previous seal is made, but there is also adsorption of atmospheric moisture, which occurs in the time between taking the membrane out of the oven, and installing it inside the membrane module. Also, every time the membrane is heated up and cooled down, there are new opportunities for defects to form due to the different thermal expansion coefficients of the membrane support and zeolite crystals [27,28]. Despite these conditions, He

permeances remain practically constant as stated previously. Additionally, Table 7.3 shows that regeneration of the membrane up to a temperature of 300 °C can be carried out with this module to recover the originally determined permeances of a membrane within the experimental error. These permeances may in fact have differed due to changes in the membrane structure as mentioned previously. However, this module has the capability to test for these changes more accurately than any of the other modules investigated. To this end, an inline air heater will be installed by the next student to regenerate membranes without needing to replace the membrane gaskets or expose the membrane to atmospheric conditions.

7.3.0 COMPARISON BETWEEN RECENTLY FABRICATED AND ORIGINAL MEMBRANES

Despite all of the modifications to the membrane fabrication and characterization procedures that have been undertaken throughout this study, there is one very important question, which has remained unanswered: "Why is the selectivity of newly fabricated membranes inferior to the membranes fabricated at the start of this research." The greatest N_2/He selectivity that has been observed was 2.75, which was achieved using PP 14 0.2 (2). Other membranes with similar selectivities are shown in Chapter 3.

This membrane was fabricated early on in this research, and no membrane after batch PP 16 has since been as selective as that membrane. Of course, since fabricating that membrane, the generic epoxy has no longer been used, and the characterization method module and sealing mechanism are likely responsible for the reduced performance. Although this reduced performance is undesirable, the newly fabricated membranes, which have been tested using module 3 with Aremco 617 and graphite gaskets have been shown to perform reproducibly well and can be thermally regenerated, which could not be claimed for the previously fabricated membrane modules. To test this hypothesis, the permeance of He and N_2 through PP 33 0.45 (2) was first measured inside module 3 with Aremco 617 and graphite gaskets. Then, the membrane was attached to stainless steel tubes using

Torrseal epoxy and incorporated into module 1. With this module, its He and N_2 permeances were re-measured. The results of these tests are shown in Figure 7.16.

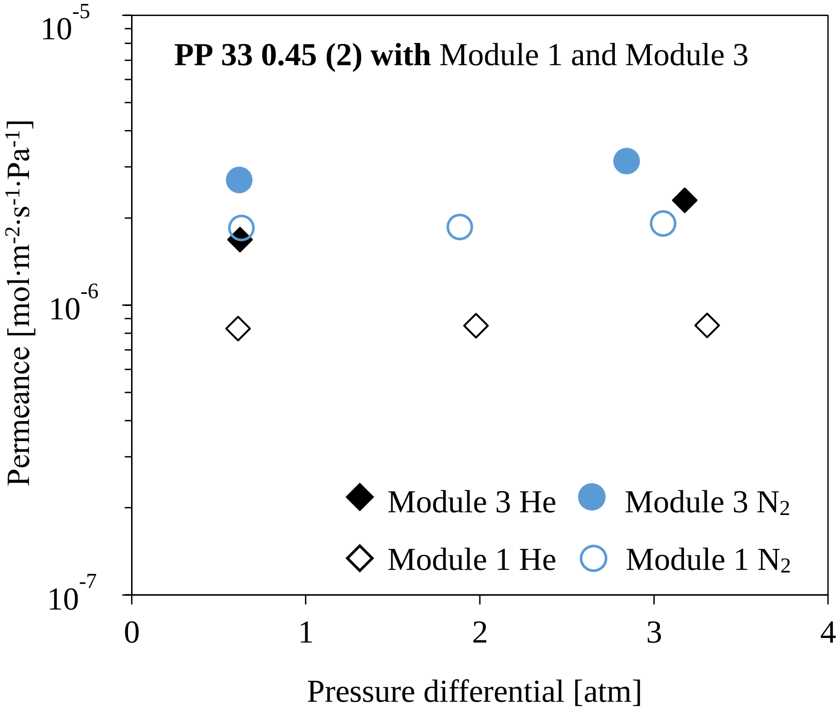

Figure 7.16. Effect of modules 1 and 3 on the permeances of He and N_2. The membrane was tested with module 1 using Torrseal epoxy, and also with module 3 using Aremco 617 glaze with graphite gaskets. He and N_2 permeances of membrane PP 33 0.45 (2) which was fabricated using the precursor molar composition ratio 1 : 0.5 : 27.8 SiO_2 : TPAOH : H_2O and 1 interruption during hydrothermal synthesis

Figure 7.16 shows that viscous flow contributes to the permeance of He and N_2 when module 3 with Aremco 617 sealed ends is used. When module 1 with Torrseal epoxy is used however, the viscous flow contribution to He and N_2 permeance can be eliminated. Permeances of He and N_2 are consequently lower when module 1 with Torrseal epoxy is used. By eliminating the viscous flow contribution to membrane permeance, the N_2/He selectivity increases from 1.60 to 2.23. This new selectivity is comparable to that of PP 14 0.2 (2) and others in Chapter 3. This behaviour can likely be attributed to the Aremco 617 coatings at the axial faces of the membrane having likely been consumed during hydrothermal synthesis. When these membranes are incorporated into module 3, gases have then bypassed the selective membrane layer by going through the created defects of the axial membrane faces. This consumption reaction has been observed for many years and studied well for glass when submerged in other basic and caustic aqueous solutions [29,30]. Since the hydrothermal synthesis solution that is used to fabricate membranes is very basic and caustic, it is likely that the cured Aremco 617 glaze has been partially consumed during hydrothermal synthesis, although no visual observations could be made to confirm this hypothesis. By using Torrseal, these axial face defects have been plugged, and so this bypassed contribution to overall permeance is not observed. The newly fabricated membranes are therefore likely to be well plugged too.

One of the consequences of this finding is that although the permeances of membranes tested using module 3 are reproducible, their measured performance is subject to defect contributions to permeance that do not compromise the selective membrane layer. Therefore, the effects of different experimental techniques to fabricate ideal membrane are difficult to measure, since although these axial face defects can be plugged with Torrseal, Torrseal can never be completely removed. Any time effects on membrane performance therefore, can never be discounted, or reversed if a membrane has been altered using Torrseal. Of course, characterization models can be developed to describe these additional defects, however, it is still necessary to eliminate these defects to utilize zeolite membranes for industrial processes.

Arguably the most important challenge for future research in this area is to therefore improve the method of integrating zeolite membranes into modules. Module 3 is far superior to the other modules with respect to reproducibly testing membrane performance. Therefore the identification of an alternative glaze solution, which can withstand hydrothermal synthesis conditions, or can be cured at a temperature which the zeolite can withstand, would be potential solutions. Perhaps a UV cured polymer, which does not off-gas gases that are poisonous to the zeolite could be used instead of Aremco 617. Alternatively, a silicon rubber gasket, which covers the axial faces of the membranes and could be used in addition to, or instead of the graphite gaskets. Silicon rubber can be heated up to appropriate temperatures for zeolite membrane regeneration, however, its durability is less than that of graphite, and so its structural integrity would need to be routinely tested.

Silicon rubber can also off-gas VOC's, which would then require membrane regeneration to be removed. At the same time, repeated regeneration cycles would make the silicon rubber become brittle and porous, and so the regeneration regime could be an additional cause of viscous flow sized defects. Since other researchers have been able to utilize glazes such as Aremco 617 successfully, maybe it is necessary to fabricate a thicker layer of Aremco 617. Or, perhaps the consumption of Aremco 617 is accelerated as the autoclave headspace is reduced due to the increased pressure and saturation pressure of TPAOH inside the autoclave. In this case, a compromise between zeolite crystal growth inside the membrane support pores, and sealing of the axial membrane faces would need to be realized to optimize membrane performance. Alternatively, borosilicate glass could be investigated, as the borosilicate glass is more resistant to chemical attack.

7.4.0 CONCLUSIONS

Three different membrane modules have been investigated in this research to integrate microporous membrane supports, which have then been further investigated by utilizing alternative sealing methods that are compatible with each module. The first module utilized different epoxies to attach ceramic membranes to stainless steel tubes, which were then integrated into the module using teflon ferrules. Of the two different epoxies that were investigated, Torrseal was found to be the best, and was able to integrate well fabricated membranes to measure permeances of He and N_2 which gave an ideal selectivity for N_2/He greater than 2. Unfortunately, this arrangement is incompatible with necessary in situ regeneration of the membrane at 300 °C. Module 2 required applying a glaze solution to the membrane support prior to membrane synthesis which was cured at a temperature of 875 °C. Then upon the cured glaze, Teflon ferrules were applied to integrate the membrane support into the module. Other alternatives to Aremco 617 were investigated, however, they either poisoned the membrane with time, or were incompatible with in situ regeneration of the membrane at 300 °C. Additionally, this module exerted sufficient force in the axial direction from the Teflon ferrules that the ends of the ceramic membrane support were sheared off, and so this module is not recommended for future studies. Module 3 also utilized Aremco 617 to glaze the membrane support, but instead utilized graphite gaskets on top of the Aremco 617 layer to integrate the membrane into the module. This arrangement is compatible with 300 °C regeneration conditions, did not poison the membrane with time, and can reproducibly measure membrane permeances following removal of the membrane from the module. The disadvantage of this module is that Aremco 617 is likely consumed during membrane synthesis, which creates additional defect pathways for gas transport. Although membrane testing with this arrangement is reproducible, its results therefore do not reflect true membrane layer performance.

Membrane fabrication was also optimized in this study by investigating the effects of precursor solution concentration and number of interruptions during membrane synthesis to a limited extent. It was also intended to measure and control pressure during this process using a custom made autoclave, however, the autoclave did not function as well as the commercially available autoclave. Membrane synthesis therefore resumed using the commercially available autoclave for the membranes fabricated later in this research. This investigation found that good membranes could be fabricated using the optimized synthesis solution molar ratio found by others, and that there appears to be a relationship between autoclave fill level and membrane quality. The mechanism responsible for ideal membrane performance in this case is unknown since autoclave pressure could not be measured during synthesis, and there is no saturation pressure data available for TPAOH at the temperature used to synthesize silicalite membranes to the best of our knowledge. Regardless, a relationship likely exists which could be limited by the rate of diffusion of TPAOH into the pores of the membrane support, which is worthy of further investigation.

It is therefore recommended that future research is conducted to combine the beneficial attributes of modules 1 and 3 so that superior membranes can be reliably characterized in the future. Also, more fundamental data should be collected with respect to temperatures, pressures, and solubilities of SiO_2 in TPAOH and water. In doing so, changes in membrane performance can be attributed reliably to hydrothermal synthesis conditions, and modifications to membrane fabrication methods quickly discounted or adjusted based on their expected changes to the synthesis conditions. Finally, a rigorous analysis using membranes fabricated in batches with more varied autoclave fill levels is required to prove the hypothesis that autoclave fill level promotes better zeolite crystal formation inside pore plugged membranes, which is recommended for a future study.

7.5.0 ABBREVIATIONS

H_2O	Water
He	Helium
N_2	Nitrogen
O_2	Oxygen
Si	Silica
SiO_2	Silica dioxide
TiO_2	Titanium hydroxide
TPAOH	Tetra-propyl ammonium hydroxide

7.6.0 REFERENCES

[1] R.W. Baker, Membrane Technology and Applications, 3rd ed., Wiley, 2012.

[2] M. Anderson, H. Wang, Y.S. Lin, Inorganic membranes for carbon dioxide and nitrogen separation, Rev. Chem. Eng. 28 (2012) 101–121. doi:10.1515/revce-2012-0001.

[3] J. Čejka, A. Corma, S. Zones, Zeolites and Catalysis: Synthesis, Reactions and Applications, 2010. doi:10.1002/9783527630295.

[4] J.N. Watson, L.E. Iton, R.I. Keir, J.C. Thomas, T.L. Dowling, J.W. White, TPA−Silicalite Crystallization from Homogeneous Solution: Kinetics and Mechanism of Nucleation and Growth, J. Phys. Chem. B. 101 (1997) 10094–10104. doi:10.1021/jp971531l.

[5] Y.Q. Deng, S.F. Yin, C.T. Au, Preparation of nanosized silicalite-1 and its application in vapor-phase Beckmann rearrangement of cyclohexanone oxime, Ind.

Eng. Chem. Res. 51 (2012) 9492–9499. doi:10.1021/ie3001277.

[6] K. Iwakai, T. Tago, H. Konno, Y. Nakasaka, T. Masuda, Preparation of nano-crystalline MFI zeolite via hydrothermal synthesis in water/surfactant/organic solvent using fumed silica as the Si source, Microporous Mesoporous Mater. 141 (2011) 167–174. doi:10.1016/j.micromeso.2010.11.001.

[7] A.I. Lupulescu, J.D. Rimer, Supplementary Materials for In Situ Imaging of Silicalite-1 Surface Growth Reveals the Mechanism of Crystallization Movies S1 and S2, Science (80-.). 344 (2014) 729–733. doi:10.1126/science.1250984.

[8] Y. Peng, H. Lu, Z. Wang, Y. Yan, Microstructural optimization of MFI-type zeolite membranes for ethanol-water separation, J. Mater. Chem. A. 2 (2014) 16093–16100. doi:10.1039/c4ta02837f.

[9] M. Noack, P. Kölsch, R. Schäfer, P. Toussaint, I. Sieber, J. Caro, Preparation of MFI membranes of enlarged area with high reproducibility, Microporous Mesoporous Mater. 49 (2001) 25–37. doi:10.1016/S1387-1811(01)00396-1.

[10] M.A. Snyder, M. Tsapatsis, Hierarchical nanomanufacturing: From shaped zeolite nanoparticles to high-performance separation membranes, Angew. Chemie - Int. Ed. 46 (2007) 7560–7573. doi:10.1002/anie.200604910.

[11] S. Miachon, E. Landrivon, M. Aouine, Y. Sun, I. Kumakiri, Y. Li, O.P. Prokopová, N. Guilhaume, a. Giroir-Fendler, H. Mozzanega, J. a. Dalmon, Nanocomposite MFI-alumina membranes via pore-plugging synthesis. Preparation and morphological characterisation, J. Memb. Sci. 281 (2006) 228–238. doi:10.1016/j.memsci.2006.03.036.

[12] Y. Li, M. Pera-titus, G. Xiong, W. Yang, E. Landrivon, S. Miachon, J. Dalmon, Nanocomposite MFI-alumina membranes via pore-plugging synthesis : Genesis of the zeolite material, 325 (2008) 973–981. doi:10.1016/j.memsci.2008.09.030.

[13] M. Tawalbeh, Silicalite-1 Membranes Synthesis, Characterization, CO_2/N_2 Separation and Modeling, 2013.

[14] A. Giroir-Fendler, J. Peureux, H. Mozzanega, J.A. Dalmon, Characterization of a Zeolite Membrane for Catalytic Membrane Reactor Application, Stud. Surf. Sci. Catal. 101 (1996) 127–136.

[15] W.J.W. Bakker, L.J.P. Van Den Broeke, F. Kapteijn, J. a Moulijn, Temperature Dependence of One-Component Permeation through a Silicalite-1 Membrane, AIChe J. 43 (1997) 2203–2214. doi:10.1002/aic.690430907.

[16] C. Algieri, P. Bernardo, G. Golemme, G. Barbieri, E. Drioli, Permeation properties of a thin silicalite-1 (MFI) membrane, J. Memb. Sci. 222 (2003) 181–190. doi:10.1016/S0376-7388(03)00286-2.

[17] A.J. Burggraaf, Z. Vroon, K. Keizer, H. Verweij, Permeation of single gases in thin zeolite MFI membranes, J. Memb. Sci. 144 (1998) 77–86. doi:10.1016/S0376-7388(98)00036-2.

[18] X. Gu, J. Dong, T.M. Nenoff, D.E. Ozokwelu, Separation of p-Xylene from Multicomponent Vapor Mixtures using Tubular MFI Zeolite Membranes, Stud. Surf. Sci. Catal. 170 (2007) 949–954. doi:10.1016/S0167-2991(07)80944-X.

[19] S. Abate, C. Genovese, S. Perathoner, G. Centi, Performances and stability of a Pd-based supported thin film membrane prepared by EPD with a novel seeding procedure. Part 1-Behaviour in H_2:N_2 mixtures, Catal. Today. 145 (2009) 63–71. doi:10.1016/j.cattod.2008.06.024.

[20] M. Drobek, J. Motuzas, V. Durand, M. Duchateau, C. Charmette, A. Hertz, C. Loubat, A. Julbe, Evaluation of a new supercritical CO_2-assisted deposition method for preparing gas selective polymer/zeolite composite membranes, J. Memb. Sci. 429 (2013) 428–435. doi:10.1016/j.memsci.2012.11.058.

[21] X. Dong, H. Wang, Z. Rui, Y.S. Lin, Tubular dual-layer MFI zeolite membrane reactor for hydrogen production via the WGS reaction: Experimental and modeling studies, Chem. Eng. J. 268 (2015) 219–229. doi:10.1016/j.cej.2015.01.046.

[22] R.T. Yang, Adsorbents: Fundamentals and Applications, John Wiley and Sons, 2003.

[23] R. Sari, Z. Yaakob, M. Ismail, W.R.W. Daud, L. Hakim, Palladium-alumina composite membrane for hydrogen separator fabricated by combined sol-gel, and electroless plating technique, Ceram. Int. 39 (2013) 3211–3219. doi:10.1016/j.ceramint.2012.10.006.

[24] A.L. Vincent, J.L. Luo, K.T. Chuang, A.R. Sanger, Promotion of activation of CH_4 by H_2S in oxidation of sour gas over sulfur tolerant SOFC anode catalysts, Appl. Catal. B Environ. 106 (2011) 114–122. doi:10.1016/j.apcatb.2011.05.014.

[25] S.P. Zhdanov, N.N. Feoktistova, N.I. Kozlova, M.M. Piryutko, Silicalites and their thermal stability, Bull. Acad. Sci. USSR Div. Chem. Sci. 34 (1985) 2467–2472. doi:10.1007/BF00953007.

[26] X. Lin, J.L. Falconer, R.D. Noble, Parallel Pathways for Transport in ZSM-5 Zeolite Membranes, Chem. Mater. 10 (1998) 3716–3723. doi:10.1021/cm980484m.

[27] S. Choi, J.H. Drese, C.W. Jones, Adsorbent materials for carbon dioxide capture from large anthropogenic point sources, ChemSusChem. 2 (2009) 796–854. doi:10.1002/cssc.200900036.

[28] L. Tosheva, B. Mihailova, V. Valtchev, J. Sterte, Silicalite-1 macrostructures - preparation and structural features, Microporous Mesoporous Mater. 39 (2000) 91–101. doi:10.1016/S1387-1811(00)00179-7.

[29] L.L. Hench, Characterization of Glass Corrosion and Durability, J. Non. Cryst. Solids. 19 (1975) 27–39. doi:doi:10.1016/B978-0-7204-0419-7.50005-6.

[30] R.W. Douglas, T.M.M. El-Shamy, Reactions of Glasses with Aqueous Solutions, J. Am. Ceram. Soc. 50 (1967) 1–8. doi:10.1111/j.1151-2916.1967.tb14960.x.

Chapter 8

Conclusions, Contributions to Original Knowledge, and Recommendations for Future Work

8.1.0 SYNOPSIS

A summary of the contributions of each chapter to achieving the three main objectives, and one sub-objective of this thesis is as follows.

For the objective to fabricate defect free silicalite membranes, it was necessary to not only fabricate several different membranes under different synthesis conditions and evaluate their quality, but also be certain that the measured performance results were reliable, and reproducible. The work in Chapters 2, 3, 5, and 7 have therefore contributed to the investigation of this objective. In Chapter 2 (Characterization of Inorganic Silicalite-1 Membrane to be Used for the Separation of Greenhouse Gases), the performance of a single promising membrane is presented. This study demonstrates the different transport phenomena that affect gas transport through silicalite membranes, and therefore establishes that adsorption and diffusion phenomena should be considered to assess membrane quality. In Chapter 3 (Pore Plugging Synthesis and Characterization of Silicalite-1 Membranes Using Tubular TiO_2 Supports: Effect of Support Pore Size on Membrane Performance), the performances of 9 different membranes which were fabricated in three separate batches were analyzed to identify optimum fabrication conditions. In Chapter 7 (Optimization of Silicalite Membrane Fabrication Procedure, and Gas Permeation Module Design and Development), the conditions that were investigated to optimize the fabrication of new membranes, including those which are not present in Chapters 2, 3, 5 and 6 of this thesis, have been summarized. Also, the various issues that were encountered to assess the reliability of the measured performance results due to module and sealing issues are presented in this chapter. Some of these issues are responsible for creating defects in newly fabricated membranes. In Chapter 5 (In-Situ Characterization of Inorganic Membranes Subject to Viscous, Knudsen and Surface Diffusion Flow Regimes), the lessons learned from Chapter 7 were used to fabricate and test membranes whose performance is reproducible, despite their less desirable performance in comparison to some of the membranes in Chapter 3. Although defect free membranes were not fabricated, many tools and techniques were developed in this work which other researchers can use to achieve this objective in the future.

For the next objective to characterize the structure of defect containing membranes using a limited number of in-situ permeation tests, the method presented in Chapter 5 was developed. In this method, parameters which describe the structure of the characterized membrane are determined, from which more complex models can be applied to design membrane processes. Additionally, these parameters can be used to direct optimization studies as differences in the structure of fabricated membranes can be related to crystallization phenomena and membrane synthesis conditions. This characterization method relies on diffusion ratios that have been determined from uptake experiments using beds of packed crystals which have been presented in Chapter 3, and the method was validated by comparing membrane performance predictions with experimental results using CH_4 and CO_2.

For the final objective to determine characteristic Maxwell-Stefan (MS) diffusivities and exchange diffusivities of defect containing silicalite membranes, the method presented in Chapter 6 (Maxwell-Stefan Model Characterization of Silicalite Membranes Containing Viscous and Knudsen Sized Defects with CO_2 and N_2 gas mixtures) was developed. In this method, the MS model is used, as well as the method presented in Chapter 5 to firstly quantify defect contributions to membrane transport, and then exclude them from MS analysis. In doing so, intrinsic characteristics for membranes composed of silicalite are determined. To validate this method, the characteristic diffusivities were compared to experimentally determined diffusivities using Infra-Red Micro-imaging (IRM), which is described in Chapter 4 (Equilibrium Isotherms and Transport Diffusivities for CO_2 and CO_2/N_2 Mixtures in Silicalite measured by Infra-Red Micro-imaging). IRM has not been used to determine this information for the system of silicalite-CO_2-N_2 before, and therefore this work was a sub objective of this thesis. Although uptake methods using beds of crystals, and molecular simulation models exist which can alternatively be used to determine diffusivities, these models are subject to many assumptions in comparison to IRM analysis using a single crystal. Unlike uptake methods using beds of crystals, thermal effects, as well as inter-crystal diffusion resistances do not influence the results determined using IRM and do not need to be discounted. And unlike molecular simulation models, accurate parameters which describe the force field inside zeolite crystals with complex geometries are not required with IRM since the uptake of molecules inside the crystal is measured. As a result of these benefits, meaningful diffusivities were determined with IRM given a limited number of assumptions, and reasonable agreement between diffusivities determined using the method in Chapter 6 and IRM. The method developed in Chapter 6 can also be applied to other pore plugged membrane types, with other gas pairs, and is a powerful method for designing membrane processes.

8.2.0 CONCLUSIONS

The pore plugging method was used to fabricate silicalite-1 membranes inside tubular TiO_2 ceramic membrane supports, which had 10-µm thick porous active layer with defined average pore sizes between 0.2 and 1.4 µm. Additionally, the effects of autoclave fill level, precursor molar composition, and interruptions in heat treatments on membrane performance were investigated. From these experiments the best performance was typically achieved using membranes whose average pore size was either 0.45 or 0.8 µm, using a precursor molar composition of 1: 0.45 : 27.8 SiO_2 : TPAOH : H_2O, with the autoclave filled to a level more than 80% of its volume with the solution, and with a single interruption in heat treatment. At these conditions, ideal selectivities for N_2/He were found to be between 1.8 and 2.8, which indicates that surface diffusion was a dominant transport mechanism in these membranes.

It was later found that membrane performance deteriorated with time, and therefore, alternative modules and sealing methods were designed and tested that could withstand regeneration temperatures between 120 ºC and 300 ºC. This investigation showed that the best performance was observed when using Torrseal epoxy to integrate the inorganic membranes into a metal permeation module, although using Torrseal limits the maximum regeneration temperature to 120 ºC. Alternatively, a different permeation module was designed, which utilizes graphite gaskets to integrate membranes whose ends have been glazed. In this thesis, membranes were removed from the module and regenerated at 300 ºC inside an oven. This module could however, be used with an inline gas heater to regenerate inorganic membranes in-situ, and at temperatures up to 300 ºC. Gas permeation experiments were found to be reproducible following regeneration at 300 ºC inside an oven with this module, however, the ideal selectivities for N_2/He of membranes tested using this module ranged from 1.2 – 1.7. The reason for this reduced performance was attributed to consumption of the glaze compound at the axial membrane faces, which led to gas molecules bypassing the membrane layer during permeation tests. This behaviour was proven by first measuring the permeances of He and N_2 through a membrane whose ends had been sealed with Aremco 617 using the graphite sealed module. The membrane was then removed from the module, Torrseal applied to the glazed surfaces of the membrane, and the He and N_2 permeances re-measured using the Torrseal compatible module. As expected for membranes whose defects had been covered by Torrseal, He and N_2 permeances using the Torrseal compatible module were less than permeances measured using the Aremco 617 and graphite sealed module, and the membrane was more selective for N_2/He.

In addition to evaluating membrane quality based on ideal selectivities, an alternative method was developed to describe the volume fraction, effective length, and the size of the selective and non-selective channels of membranes. This method does not destroy or contaminate the analyzed membrane, and utilizes a limited number of in-situ gas permeation experiments before and after membrane calcination using the graphite sealed module. This method was validated in two ways. Firstly, by comparing permeance predictions for the gases used to characterize the membrane (He and N_2) at untested feed pressures, with experimental permeances. Then, this method was further validated by comparing permeance predictions for untested gases (CO_2 and CH_4) with experimental ones. In combination with the characterization parameters determined using the proposed method, the Maxwell-Stefan model was used to determine diffusivities $Đ_{N_2}$, $Đ_{CO_2}$ and exchange coefficients $Đ_{N_2/CO_2}$ and $Đ_{CO_2/N_2}$ for silicalite crystals in membranes containing defects. In this way, the surface diffusion transport through zeolite crystals was distinguished from defect transport contributions to total permeance. Additionally, these predicted diffusivities were compared to diffusivities measured using Infra-Red micro-imaging inside a single zeolite crystal at the University of Leipzig, which were in reasonable agreement with each other.

The research undertaken in this thesis therefore addresses the macro scale challenges with separating gas mixtures using zeolite membranes, and links their performance to the physico-chemical characteristics of single zeolite crystals. With this knowledge, the quality of newly fabricated membranes can be quantified using meaningful characteristics, and their performance at untested conditions can be predicted.

8.3.0 CONTRIBUTIONS TO ORIGINAL KNOWLEDGE

- In this work, a novel method for characterizing newly fabricated zeolite membranes containing viscous and Knudsen flow sized defects has been developed. Unlike other characterization methods, this method requires the results of a limited number of in-situ gas permeation measurements, and does not damage the structure of the membrane like other existing techniques such as permporometry and polymer sphere permeation experiments.
- For the first time, defect flow contributions have been discounted from binary gas mixture permeation results, and the MS diffusivities and exchange coefficients related to molecular transport through zeolite crystals are calculated.
- For the first time, the diffusivities of pure CO_2, as well as CO_2 present in gas mixtures with N_2, has been measured using a single crystal of silicalite by Infra-Red Micro-imaging. Also for the first time, CO_2 adsorption isotherms of silicalite for CO_2 present in mixtures with N_2 have been measured using Infra-Red Micro-imaging.

8.4.0 RECOMMENDATIONS FOR FUTURE WORK

- To enable regeneration of membranes without exposing them to atmospheric gases, an in situ heater to regenerate membranes at 300 ºC should be installed.
- To reduce thermal stress which can cause defects in the membrane during calcination at 500 °C, the minimum temperature for TPAOH removal should be determined. Also,

drying and calcining membranes should be carried out inside a convection oven or tubular furnace, in an atmosphere that is free of moisture to ensure controlled heating and cooling of the membrane.

- To ensure that the selective layer is not bypassed during permeation tests, an alternative glaze to Aremco 617 should be found which could be used to integrate ceramic supported zeolite membranes into the graphite sealed module. The ideal material is resistant to alkali attack at high temperatures, does not off gas polar components (or off gassed molecules can be removed by thermal regeneration), does not excessively expand at high temperatures, and creates a hermetic coating. Borosilicate glass, porcelain, UV cured polymers, specialized cements, or an alternative material that is already in use by another specialization should be tried. Additionally, a method should be set up to test these sealants quickly, and without wasting membranes.
- To better control the permeate side pressure during permeation experiments so that the permeance of different gases can be compared at equivalent feed and permeate side pressures, the length of the permeate stream vent line should be reduced. This could be achieved by moving the setup into a fume hood if it is desired to continue to test flammable gases such as CH_4, or alternatively, tests could be designed which use non-flammable gases.
- To evaluate the hypothesis that autoclave fill level affects the quality of zeolite membranes, an autoclave should be developed which contains a port that a pressure gauge can be attached to. From the measured pressures, correlations between membrane quality and the consumption of TPAOH to direct zeolite synthesis can be made. This autoclave should contain a chemically resistant liner, and a hydrophobic filter between the autoclave and a pressure gauge so that pressure can be monitored during membrane synthesis without the risk of caustic vapors attacking the gauge mechanism or reacting with exposed metal surfaces. The autoclave should also include a mechanism to keep the autoclave sealed during cooling periods, such as a Belleville or wave spring washer, like commercially available autoclaves.
- To link membrane performance with the characteristic parameters determined using the proposed characterization method, fundamental data to describe the autoclave conditions during hydrothermal synthesis should also be determined. Ideally, the

solubility of SiO_2 in mixtures with H_2O and TPAOH, and the saturation pressure curve for TPAOH would be established.

- To increase the concentration of the selected component in the permeate stream and improve membrane performance, gas permeation experiments should be conducted below room temperature where adsorption affinities are stronger. This will also increase the surface occupancy gradient across the membrane, which will make it easier to characterize membranes using the Maxwell-Stefan model. These colder temperatures exist for several months of the year in Canada, and it would not be unreasonable for a membrane system to be located outside at a processing plant. The setup is currently capable of temperatures as low as 4 ºC, and immersion cooling of the feed gas stream using liquid nitrogen cooling could possibly be used to lower the temperature further.
- To further improve the accuracy of membrane characteristics determined using the Maxwell-Stefan model, and complement low temperature zeolite membrane permeation tests, binary isotherms for N_2 and CO_2 in mixtures at 3 different temperatures below room temperature should be determined. Although this data has been determined near room temperature (26°C), models and assumptions are required to extrapolate this information to current experimental temperatures of 20 – 24 °C, which is a source of uncertainty.

Appendix 1

Error Analysis for In Situ Characterization

The defect characterization model equations are as follows.

$$P_{He,U} = xd_d^2 \frac{(p_h + p_l)}{64\mu_{He} RT} + xd_d \frac{1}{3}\sqrt{\frac{8}{\pi M_{He} RT}} \tag{1}$$

$$P_{N_2,U} = xd_d^2 \frac{(p_h + p_l)}{64\mu_{N_2} RT} + xd_d \frac{1}{3}\sqrt{\frac{8}{\pi M_{N_2} RT}} \tag{2}$$

$$P_{He} = xd_d^2 \frac{(p_h + p_l)}{64\mu_{He} RT} + (xd_d + yd_z)\frac{1}{3}\sqrt{\frac{8}{\pi M_{He} RT}} \tag{3}$$

$$P_{N_2} = xd_d^2 \frac{(p_h + p_l)}{64\mu_{N_2} RT} + xd_d \frac{1}{3}\sqrt{\frac{8}{\pi M_{N_2} RT}} + y\left(\frac{q_h - q_l}{p_h - p_l}\right)\rho D_T \tag{4}$$

Where unknowns x, d_d, y, and D_T are solved for given the experimentally determined pressure and permeate flow rates (as required to determine permeances) of He and N_2 gases through the membrane before and after membrane calcination.

The uncertainties of each unknown parameter have been determined using standard error equations, which are as follows.

$$\Delta(x \pm y) = \sqrt{\Delta x^2 + \Delta y^2} \tag{5}$$

$$\Delta(xy) = xy\sqrt{\left(\frac{\Delta x}{x}\right)^2 + \left(\frac{\Delta y}{y}\right)^2} \tag{6}$$

$$\Delta\left(\frac{x}{y}\right) = \frac{x}{y}\sqrt{\left(\frac{\Delta x}{x}\right)^2 + \left(\frac{\Delta y}{y}\right)^2} \tag{7}$$

A sample calculation for the determination of errors pertaining to the calculation of characteristic parameters at the lowest pressure differential investigated is shown to demonstrate the error analysis procedure.

Appendix 1 **– Error Analysis for In Situ Characterization**

The experimentally determined parameters are shown in Table A.1.1.

Table A.1.1. Experimentally determined pressure and permeate flow rate values. Pressure uncertainties are equal to 0.5 psi for the feed side pressures, and 0.1 psi for the permeate side pressures. Flow rate time uncertainties are the maximum variation in times measured in comparison to the mean determined from at least 5 measurements. All experiments were conducted at a temperature of 295 ± 1.5 ºK.

Zeolite crystal state	**Gas**	**Pressures**				**Flow rates**		
		Feed side p_h	**Uncert.**	**Permeate side p_l**	**Uncert.**	**Bubble flow meter (BFM) volume**	**Time for film to cross BFM volume**	**Uncert.**
		[Pa]	**[Pa]**	**[Pa]**	**[Pa]**	**[cc]**	**[s]**	**[s]**
Uncalcined	He	171203	3447	108461	689	9	13.152	0.1
	N_2	171976	3447	107992	689	9	16.724	0.1
Calcined	He	170458	3447	108516	689	90	43.222	0.1
	N_2	170300	3447	108426	689	90	23.556	0.1

Pressure differential uncertainty is therefore:

$$\begin{aligned} \Delta(p_h - p_l) &= \sqrt{3447^2 + 689^2} \\ \Delta(p_h - p_l) &= 3515\ Pa \end{aligned} \tag{8}$$

To determine permeances, membrane area A_m is also required, which is a function of membrane diameter D and length L which were measured with calipers, and are calculated as follows.

$$\begin{aligned} D &= 0.551 \pm 0.008\, cm \\ L &= 6.035 \pm 0.005\, cm \\ A_m &= \pi DL = \pi .0.551.6.035 \\ A_m &= 10.447\, cm^2 = 0.001045 m^2 \end{aligned} \tag{9}$$

The membrane area uncertainty is therefore:

$$\Delta(A_m) = 0.001045\sqrt{\left(\frac{0.008}{0.551}\right)^2 + \left(\frac{0.005}{6.035}\right)^2}$$
$$\Delta(A_m) = 1.52.10^{-5}\ m^2 \tag{10}$$

From the data in Table A.1.1, permeate flow rates can be determined by dividing bubble flow meter (BFM) volume by the time taken for the film to cross the BFM volume. Permeate flow rates for He and N_2 prior to and following membrane calcination are therefore as follows.

$$V_{pHe,U} = \frac{0.000009\ m^3}{13.152 \pm 0.1\ s} = 6.843.10^{-7} \pm 6.843.10^{-7}\sqrt{\left(\frac{0.1}{13.152}\right)^2}$$
$$V_{pHe,U} = 6.843.10^{-7} \pm 5.203.10^{-9}\ \frac{m^3}{s} \tag{11a}$$

$$V_{pN_2,U} = \frac{0.000009\ m^3}{16.724 \pm 0.1\ s} = 5.381.10^{-7} \pm 5.381.10^{-7}\sqrt{\left(\frac{0.1}{16.724}\right)^2}$$
$$V_{pN_2,U} = 5.381.10^{-7} \pm 3.218.10^{-9}\ \frac{m^3}{s} \tag{11b}$$

$$V_{pHe} = \frac{0.00009\ m^3}{43.222 \pm 0.1\ s} = 2.082.10^{-6} \pm 2.082.10^{-6}\sqrt{\left(\frac{0.1}{43.222}\right)^2}$$
$$V_{pHe} = 2.082.10^{-6} \pm 4.818.10^{-9}\ \frac{m^3}{s} \tag{11c}$$

$$V_{pN_2} = \frac{0.00009\ m^3}{23.556 \pm 0.1\ s} = 3.821.10^{-6} \pm 3.821.10^{-6}\sqrt{\left(\frac{0.1}{23.556}\right)^2}$$
$$V_{pN_2} = 3.821.10^{-6} \pm 1.622.10^{-8}\ \frac{m^3}{s} \tag{11d}$$

The permeate flow rates determined using equation 11 can then be converted to standard temperature values but not standard temperature and pressure (STP) as the pressure at the permeate side BFM pressure was not measured. If it is reasoned that the permeate side BFM pressure is 1 psi above atmospheric pressure, and has an uncertainty of 1 psi, the STP uncertainty can however be calculated. This has been done in equation 12 which follows.

$$V_{pHe,U} = \frac{6.843.10^{-7}\ \frac{m^3}{s}}{295.15\ K}.273.15\ K$$

$$V_{pHe,U} = 6.333.10^{-7} \pm 6.333.10^{-7}\sqrt{\left(\frac{6895}{108220}\right)^2 + \left(\frac{5.203.10^{-9}}{6.843.10^{-7}}\right)^2 + \left(\frac{1.5}{295.15}\right)^2} \tag{12a}$$

$$V_{pHe,U} = 6.333.10^{-7} \pm 4.076.10^{-8}\ \frac{m^3}{s}$$

$$V_{pN_2,U} = \frac{5.381.10^{-7}\ \frac{m^3}{s}}{295.15\ K}.273.15\ K$$

$$V_{pN_2,U} = 4.980.10^{-7} \pm 4.980.10^{-7}\sqrt{\left(\frac{6895}{108220}\right)^2 + \left(\frac{3.218.10^{-9}}{5.381.10^{-7}}\right)^2 + \left(\frac{1.5}{295.15}\right)^2} \tag{12b}$$

$$V_{pN_2,U} = 4.980.10^{-7} \pm 3.197.10^{-8}\ \frac{m^3}{s}$$

$$V_{pHe} = \frac{2.082.10^{-6}\ \frac{m^3}{s}}{295.15\ K}.273.15\ K$$

$$V_{pHe} = 1.927.10^{-6} \pm 1.927.10^{-6}\sqrt{\left(\frac{6895}{108220}\right)^2 + \left(\frac{4.817.10^{-9}}{2.082.10^{-6}}\right)^2 + \left(\frac{1.5}{295.15}\right)^2} \tag{12c}$$

$$V_{pHe} = 1.927.10^{-6} \pm 1.232.10^{-7}\ \frac{m^3}{s}$$

$$V_{pN_2} = \frac{3.821.10^{-6}\ \frac{m^3}{s}}{295.15\ K}.273.15\ K$$

$$V_{pN_2} = 3.536.10^{-6} \pm 3.536.10^{-6}\sqrt{\left(\frac{6895}{108220}\right)^2 + \left(\frac{1.622.10^{-8}}{3.821.10^{-6}}\right)^2 + \left(\frac{1.5}{295.15}\right)^2} \tag{12d}$$

$$V_{pN_2} = 3.536.10^{-6} \pm 2.265.10^{-7}\ \frac{m^3}{s}$$

The permeate flow rates can then be converted to molar flow rates, and then fluxes using equation 13.

$$J_{He,U}=\frac{6.333.10^{-7}\ \frac{m^3}{s}.\frac{1000\ l}{m^3}.\frac{1mol}{22.4\ l}}{0.001045\ m^2}$$

$$J_{He,U}=2.706.10^{-2}\pm 2.706.10^{-2}.\sqrt{\left(\frac{4.076.10^{-8}}{6.333.10^{-7}}\right)^2+\left(\frac{1.52.10^{-5}}{0.001045}\right)^2} \tag{13a}$$

$$J_{He,U}=2.706.10^{-2}\pm 1.790.10^{-3}\ \frac{mol}{m^2s}$$

$$J_{N_2,U}=\frac{4.980.10^{-7}\ \frac{m^3}{s}.\frac{1000\ l}{m^3}.\frac{1mol}{22.4\ l}}{0.001045\ m^2}$$

$$J_{N_2,U}=2.128.10^{-2}\pm 2.128.10^{-2}.\sqrt{\left(\frac{3.197.10^{-8}}{4.980.10^{-7}}\right)^2+\left(\frac{1.52.10^{-5}}{0.001045}\right)^2} \tag{13b}$$

$$J_{N_2,U}=2.128.10^{-2}\pm 1.401.10^{-3}\ \frac{mol}{m^2s}$$

$$J_{He}=\frac{1.927.10^{-6}\ \frac{m^3}{s}.\frac{1000\ l}{m^3}.\frac{1mol}{22.4\ l}}{0.001045\ m^2}$$

$$J_{He}=8.235.10^{-2}\pm 8.235.10^{-2}.\sqrt{\left(\frac{1.232.10^{-7}}{1.927.10^{-6}}\right)^2+\left(\frac{1.52.10^{-5}}{0.001045}\right)^2} \tag{13c}$$

$$J_{He}=8.235.10^{-2}\pm 5.400.10^{-3}\ \frac{mol}{m^2s}$$

$$J_{N_2}=\frac{3.356.10^{-6}\ \frac{m^3}{s}.\frac{1000\ l}{m^3}.\frac{1mol}{22.4\ l}}{0.001045\ m^2}$$

$$J_{N_2}=1.511.10^{-1}\pm 1.511.10^{-1}.\sqrt{\left(\frac{2.265.10^{-7}}{3.356.10^{-6}}\right)^2+\left(\frac{1.52.10^{-5}}{0.001045}\right)^2} \tag{13d}$$

$$J_{N_2}=1.511.10^{-1}\pm 9.930.10^{-1}\ \frac{mol}{m^2s}$$

From the fluxes and pressures, permeances can then be calculated using equation 14.

$$P_{He,U} = \frac{2.706.10^{-2}\ .\dfrac{mol}{m^2 s}}{171203 - 108461\ Pa}$$

$$P_{He,U} = 4.313.10^{-7} \pm 4.313.10^{-7}.\sqrt{\left(\frac{1.790.10^{-3}}{2.706.10^{-2}}\right)^2 + \left(\frac{3515}{62743}\right)^2} \tag{14a}$$

$$P_{He,U} = 4.313.10^{-7} \pm 3.734.10^{-8}\ \frac{mol}{m^2 sPa}$$

$$P_{N_2,U} = \frac{2.128.10^{-2}\ .\dfrac{mol}{m^2 s}}{171976 - 107992\ Pa}$$

$$P_{N_2,U} = 3.326.10^{-7} \pm 3.326.10^{-7}.\sqrt{\left(\frac{1.401.10^{-3}}{2.128.10^{-2}}\right)^2 + \left(\frac{3515}{63984}\right)^2} \tag{14b}$$

$$P_{N_2,U} = 3.326.10^{-7} \pm 2.852.10^{-8}\ \frac{mol}{m^2 sPa}$$

$$P_{He} = \frac{8.235.10^{-2}\ .\dfrac{mol}{m^2 s}}{170458 - 108516\ Pa}$$

$$P_{He} = 1.329.10^{-6} \pm 1.329.10^{-6}.\sqrt{\left(\frac{5.400.10^{-3}}{8.235.10^{-2}}\right)^2 + \left(\frac{3515}{61942}\right)^2} \tag{14c}$$

$$P_{He} = 1.329.10^{-6} \pm 1.153.10^{-7}\ \frac{mol}{m^2 sPa}$$

$$P_{N_2} = \frac{1.511.10^{-1}\ .\dfrac{mol}{m^2 s}}{170300 - 108426\ Pa}$$

$$P_{N_2} = 2.442.10^{-6} \pm 2.442.10^{-6}.\sqrt{\left(\frac{9.930.10^{-3}}{1.151.10^{-1}}\right)^2 + \left(\frac{3515}{61874}\right)^2} \tag{14d}$$

$$P_{N_2} = 2.442.10^{-6} \pm 2.121.10^{-7}\ \frac{mol}{m^2 sPa}$$

To solve for unknowns x and d_d analytically, constants $C_{V,He}$, $C_{K,He}$, C_{V,N_2}, and C_{K,N_2} are defined as shown below. Next, equations 1a and 2a are divided by each other to eliminate *x*, and then the resulting equation 15 is divided on both sides by d_d to determine d_d using equation 16.

$$C_{VHe} = \left\{ \frac{1}{64\mu_{He}RT} \right\}$$

$$C_{VHe} = \frac{1}{64.1.97.10^{-5}\,Pas\;8.314\,\frac{m^3Pa}{molK}\,295.15K} = 0.3232 \pm 0.3232\sqrt{\left(\frac{1.5}{295.15}\right)^2}$$

$$C_{VHe} = 0.3232 \pm 0.0016\,\frac{mol}{m^3Pa^2s}$$

$$C_{KHe} = \left\{ \frac{1}{3}\sqrt{\frac{8}{\pi M_{He}RT}} \right\}$$

$$C_{KHe} = \frac{1}{3}\sqrt{\frac{8}{3.14.0.004\,\frac{kg}{mol}.\frac{mPas^2}{kg}\,8.314\,\frac{m^3Pa}{molK}\,295.15K}} = 0.1697 \pm 0.1697\sqrt{\left(\frac{1.5}{295.15}\right)^2}$$

$$C_{KHe} = 0.1697 \pm 0.0009\,\frac{mol}{m^2Pas}$$

$$C_{VN_2} = \left\{ \frac{1}{64\mu_{N_2}RT} \right\}$$

$$C_{VN_2} = \frac{1}{64.1.76.10^{-5}\,Pas\;8.314\,\frac{m^3Pa}{molK}\,295.15K}$$

$$C_{VN_2} = 0.3618 \pm 0.3618\sqrt{\left(\frac{1.5}{295.15}\right)^2}$$

$$C_{VN_2} = 0.3618 \pm 0.0018\,\frac{mol}{m^3Pa^2s}$$

$$C_{KN_2} = \left\{ \frac{1}{3}\sqrt{\frac{8}{\pi M_{N_2}RT}} \right\}$$

$$C_{KN_2} = \frac{1}{3}\sqrt{\frac{8}{3.14.0.028\,\frac{kg}{mol}.\frac{mPas^2}{kg}\,8.314\,\frac{m^3Pa}{molK}\,295.15K}} = 0.0642 \pm 0.0642\sqrt{\left(\frac{1.5}{295.15}\right)^2}$$

$$C_{KN_2} = 0.0642 \pm 0.0003\,\frac{mol}{m^2Pas}$$

Appendix 1 – Error Analysis for In Situ Characterization

$$P_{He,U} = xd_d^2 \frac{(p_h + p_l)}{64\mu_{He} RT} + xd_d \frac{1}{3}\sqrt{\frac{8}{\pi M_{He} RT}} \tag{1}$$

$$P_{He,U} = xd_d^2 \left(p_h + p_l\right)_{He,U} C_{VHe} + xd_d C_{KHe}$$

$$P_{He,U} = x\left\{ d_d^2 \left(p_h + p_l\right)_{He,U} C_{VHe} + d_d C_{KHe} \right\} \tag{1a}$$

$$P_{N_2,U} = xd_d^2 \frac{(p_h + p_l)}{64\mu_{N_2} RT} + xd_d \frac{1}{3}\sqrt{\frac{8}{\pi M_{N_2} RT}} \tag{2}$$

$$P_{N_2,U} = xd_d^2 \left(p_h + p_l\right)_{N_2,U} C_{VN_2} + xd_d C_{KN_2}$$

$$P_{N_2,U} = x\left\{ d_d^2 \left(p_h + p_l\right)_{N_2,U} C_{VN_2} + d_d C_{KN_2} \right\} \tag{2a}$$

$$\frac{P_{He,U}}{P_{N_2,U}} = \frac{d_d^2 \left(p_h + p_l\right)_{He,U} C_{VHe} + d_d\ C_{KHe}}{d_d^2 \left(p_h + p_l\right)_{N_2,U} C_{VN_2} + d_d\ C_{KN_2}} \tag{1a/2a}$$

$$P_{He,U}\left\{ d_d^2 \left(p_h + p_l\right)_{N_2,U} C_{VN_2} + d_d C_{KN_2} \right\} = P_{N_2,U}\left\{ d_d^2 \left(p_h + p_l\right)_{He,U} C_{VHe} + d_d C_{KHe} \right\} \tag{15}$$

$$P_{He,U} d_d \left(p_h + p_l\right)_{N_2,U} C_{VN_2} + P_{He,U} C_{KN_2} = P_{N_2,U} d_d \left(p_h + p_l\right)_{He,U} C_{VHe} + P_{N_2,U} C_{KHe}$$

$$d_d \left\{ P_{He,U} \left(p_h + p_l\right)_{N_2,U} C_{VN_2} - P_{N_2,U} \left(p_h + p_l\right)_{He,U} C_{VHe} \right\} = P_{N_2,U} C_{KHe} - P_{He,U} C_{KN_2}$$

$$d_d = \frac{P_{N_2,U} C_{KHe} - P_{He,U} C_{KN_2}}{P_{He,U} \left(p_h + p_l\right)_{N_2,U} C_{VN_2} - P_{N_2,U} \left(p_h + p_l\right)_{He,U} C_{VHe}} \tag{16}$$

To simplify the error analysis for d_d, equation 16 can be divided into 4 terms; *i* – *iv*.

$$i = P_{N_2,U} C_{KHe} = 3.326.10^{-7}\ \frac{mol}{m^2 sPa}.0.1697\frac{mol}{m^2 sPa}$$

$$i = 5.646.10^{-8} \pm 5.646.10^{-8}\sqrt{\left(\frac{2.852.10^{-8}}{3.326.10^{-7}}\right)^2 + \left(\frac{0.0009}{0.1697}\right)^2}$$

$$i = 5.646.10^{-8} \pm 4.849.10^{-9}\ \frac{mol^2}{m^4 s^2 Pa^2}$$

$$ii = P_{He,U} C_{KN_2} = 4.313.10^{-7}\ \frac{mol}{m^2 sPa}.0.0642\frac{mol}{m^2 sPa}$$

$$ii = 2.767.10^{-8} \pm 2.767.10^{-8}\sqrt{\left(\frac{3.734.10^{-8}}{4.313.10^{-7}}\right)^2 + \left(\frac{0.0003}{0.0642}\right)^2}$$

$$ii = 2.767.10^{-8} \pm 2.400.10^{-9}\ \frac{mol^2}{m^4 s^2 Pa^2}$$

$$iii = P_{He,U}\left(p_h + p_l\right)_{N_2,U} C_{VN_2} = 4.313.10^{-7}\ \frac{mol}{m^2 sPa}.(171976 + 107992 Pa).0.3618\frac{mol}{m^3 Pa^2 s}$$

$$iii = 0.0438 \pm 0.0438\sqrt{\left(\frac{3.734.10^{-8}}{4.313.10^{-7}}\right)^2 + \left(\frac{3515}{279968}\right)^2 + \left(\frac{0.0018}{0.3618}\right)^2}$$

$$iii = 0.0438 \pm 0.0038\frac{mol^2}{m^5 s^2 Pa^2}$$

$$iv = P_{N_2,U}\left(p_h + p_l\right)_{He,U} C_{VHe} = 3.326.10^{-7}\ \frac{mol}{m^2 sPa}.(171203 + 108461 Pa).0.3232\frac{mol}{m^3 Pa^2 s}$$

$$iv = 0.0300 \pm 0.0300\sqrt{\left(\frac{2.852.10^{-8}}{3.326.10^{-7}}\right)^2 + \left(\frac{3515}{279664}\right)^2 + \left(\frac{0.0016}{0.3232}\right)^2}$$

$$iv = 0.0300 \pm 0.0026\frac{mol^2}{m^5 s^2 Pa^2}$$

The subtraction operations for equation 16 can then be conducted as follows for the numerator 16a, and denominator 16b.

$$i - ii = 5.646.10^{-8}\ \frac{mol^2}{m^4 s^2 Pa^2} - 2.767.10^{-8}\ \frac{mol^2}{m^4 s^2 Pa^2} \pm \sqrt{\left(4.849.10^{-9}\right)^2 + \left(1.400.10^{-9}\right)^2}$$

$$i - ii = 2.878.10^{-8} \pm 5.410.10^{-9}\ \frac{mol^2}{m^4 s^2 Pa^2}$$

(16a)

$$iii - iv = 0.0438\frac{mol^2}{m^5 s^2 Pa^2} - 0.0300\frac{mol^2}{m^5 s^2 Pa^2} \pm \sqrt{(0.0038)^2 + (0.0026)^2}$$
$$iii - iv = 0.0138 \pm 0.0046\frac{mol^2}{m^5 s^2 Pa^2} \tag{16b}$$

d_d can then be determined by substituting 16a and 16b into equation 16.

$$d_d = \frac{i - ii}{iii - iv} = \frac{2.878.10^{-8}\,\dfrac{mol^2}{m^4 s^2 Pa^2}}{0.0138\,\dfrac{mol^2}{m^5 s^2 Pa^2}}$$
$$d_d = 2.089.10^{-6} \pm 2.089.10^{-6}\sqrt{\left(\frac{5.410.10^{-9}}{2.878.10^{-8}}\right)^2 + \left(\frac{0.0046}{0.0138}\right)^2}$$
$$d_d = 2.089.10^{-6} \pm 8.056.10^{-7}\,m$$

d_d can next be substituted into equation 2a, which once rearranged into equation 2b can then include lumped terms *v* and *vi*, and finally be used to calculate *x*.

$$x = \frac{P_{N_2,U}}{d_d^2\,(p_h + p_l)_{N_2,U}\,C_{VN_2} + d_d C_{KN_2}} \tag{2b}$$

$$v = d_d^2 (p_h + p_l)_{N_2,U} C_{VN_2} = \left(2.089.10^{-6}\right)^2 m^2.(171976 + 107992\,Pa).0.3618\frac{mol}{m^3 Pa^2 s}$$
$$v = 3.939.10^{-7} \pm 3.939.10^{-7}\sqrt{2.\left(\frac{8.056.10^{-7}}{2.089.10^{-6}}\right)^2 + \left(\frac{3515}{279968}\right)^2 + \left(\frac{0.0018}{0.3618}\right)^2}$$
$$v = 3.939.10^{-7} \pm 2.149.10^{-7}\frac{mol}{msPa}$$
$$vi = d_d C_{KN_2} = 2.089.10^{-6}\,m.0.0642\frac{mol}{m^2 sPa}$$
$$vi = 3.546.10^{-7} \pm 3.546.10^{-7}\sqrt{\left(\frac{8.056.10^{-7}}{2.089.10^{-6}}\right)^2 + \left(\frac{0.0003}{0.0642}\right)^2}$$
$$vi = 3.546.10^{-7} \pm 1.367.10^{-7}\frac{mol}{msPa}$$

$$v+vi=3.939.10^{-7}\,\frac{mol}{msPa}+3.546.10^{-7}\,\frac{mol}{msPa}$$
$$v+vi=7.485.10^{-7}\pm\sqrt{\left(2.149.10^{-7}\right)^2+\left(1.367.10^{-7}\right)^2}$$
$$v+vi=7.485.10^{-7}\pm 2.547.10^{-7}\,\frac{mol}{msPa}$$

Calculation of *x*.

$$x=\frac{P_{N_2U}}{v+vi}=\frac{3.326.10^{-7}\,\frac{mol}{m^2sPa}}{7.485.10^{-7}\,\frac{mol}{msPa}}=0.576\pm0.576\sqrt{\left(\frac{2.852.10^{-5}}{3.326.10^{-7}}\right)^2+\left(\frac{2.547.10^{-7}}{7.485.10^{-7}}\right)^2}$$
$$x=0.576\pm0.202\,\frac{1}{m}$$

To calculate the uncertainty of *y*, the equation to describe He permeance through the calcined membrane P_{He}, is calculated by rearranging equation A.3 as follows, and then for greater clarity, the terms of the resulting equation, equation A.3a have been denoted *vii* – *ix* and analyzed.

$$\begin{aligned}P_{He}&=xd_d^2\,\frac{\left(p_h+p_l\right)}{64\mu_{He}RT}+xd_d\,\frac{1}{3}\sqrt{\frac{8}{\pi M_{He}RT}}+yd_z\,\frac{1}{3}\sqrt{\frac{8}{\pi M_{He}RT}}\\ y&=\frac{P_{He}}{d_zC_{KHe}}-\frac{xd_d^2\left(p_h+p_l\right)_{He}}{d_zC_{VHe}C_{KHe}}-\frac{xd_d}{d_z}\end{aligned}\qquad\text{(A.3)}$$

$$vii=\frac{P_{He}}{d_zC_{KHe}}=\frac{1.329.10^{-6}\,\frac{mol}{m^2sPa}}{5.5.10^{-10}\,m\;0.1697\,\frac{mol}{m^2sPa}}$$
$$vii=14239.031\pm14239.031\sqrt{\left(\frac{1.153.10^{-7}}{1.329.10^{-6}}\right)^2+\left(\frac{0.0009}{0.1697}\right)^2}$$
$$vii=14239.031\pm1237.641\frac{1}{m}$$

$$viii = \frac{xd_d^2\left(p_h + p_l\right)_{He}C_{VHe}}{d_z C_{KHe}}$$

$$viii = \frac{0.576\,\frac{1}{m}\left(2.089.10^{-6}\right)^2 m.m\,\left(170458 + 108516\right)Pa\;0.3232\,\frac{mol}{m^3 sPa^2}}{5.5.10^{-10}\,m\;0.1697\,\frac{mol}{m^2 sPa}}$$

$$viii = 2428.231 \pm 2428.231\sqrt{\left(\frac{0.202}{0.576}\right)^2 + 2\left(\frac{8.056.10^{-7}}{2.089.10^{-6}}\right)^2 + \left(\frac{3515}{278974}\right)^2 + \left(\frac{0.0016}{0.3232}\right)^2 + \left(\frac{0.0009}{0.1697}\right)^2}$$

$$viii = 2428.231 \pm 1574.859\,\frac{1}{m}$$

$$ix = \frac{xd_d}{d_z} = \frac{0.576\frac{1}{m}\,2.089.10^{-6}\,m}{5.5.10^{-10}\,m} = 2187.753 \pm 2187.753\sqrt{\left(\frac{0.202}{0.576}\right)^2 + \left(\frac{8.056.10^{-7}}{2.089.10^{-6}}\right)^2}$$

$$ix = 2187.753 \pm 1140.753\frac{1}{m}$$

y can then be calculated from vii – ix.

$$y = vii - viii - ix = 14239.031\frac{1}{m} - 2428.231\frac{1}{m} - 2187.753\frac{1}{m} = 9623.048$$

$$y = 9623.048 \pm \sqrt{1237.641^2 + 1574.859^2 + 1140.371^2}$$

$$y = 9623.048 \pm 2304.861\frac{1}{m}$$

Similarly to the calculation of *y*, to calculate the uncertainty of D_{TN_2} the equation to describe N_2 permeance through the calcined membrane P_{N_2}, is calculated by rearranging equation A.4 as follows, and then for greater clarity, the terms of the resulting equation, equation A.4a have been denoted *x-xiii* and analyzed.

$$P_{N_2} = xd_d^2\frac{\left(p_h + p_l\right)}{64\mu_{N_2}RT} + xd_d\,\frac{1}{3}\sqrt{\frac{8}{\pi M_{N_2}RT}} + y\left(\frac{q_h - q_l}{p_h - p_l}\right)\rho D_{TN_2} \qquad \text{(A.4)}$$

$$D_{TN_2} = \frac{P_{N_2}}{xi} - \frac{xd_d^2\left(p_h + p_l\right)_{N_2}C_{VN_2}}{xi} - \frac{xd_d C_{KN_2}}{xi}$$

Amounts adsorbed q_h and q_l are first calculated, and then the parameter *xi* which will be included in the parameters *xii* – *xiv*.

$$q_{hN_2} = q^s \frac{bp_h}{1+bp_h} = 1.930\frac{mol}{kg}\frac{0.072\frac{1}{Pa}170300Pa}{1+0.072\frac{1}{Pa}170300Pa} = 0.242\frac{mol}{kg}$$

$$q_{lN_2} = q^s \frac{bp_l}{1+bp_l} = 1.930\frac{mol}{kg}\frac{0.072\frac{1}{Pa}108426Pa}{1+0.072\frac{1}{Pa}108426Pa} = 0.165\frac{mol}{kg}$$

$$xi = y\left(\frac{q_h - q_l}{p_h - p_l}\right)\rho = 9623.048\frac{1}{m}\left(\frac{0.242\frac{mol}{kg} - 0.165\frac{mol}{kg}}{170300Pa - 108426Pa}\right)1800\frac{kg}{m^3}$$

$$xi = 21.556 \pm 21.556\sqrt{\left(\frac{2304.861}{9623.048}\right)^2 + \left(\frac{3515}{61874}\right)^2}$$

$$xi = 21.556 \pm 5.306\frac{mol}{m^4 Pa}$$

$$xii = \frac{P_{N_2}}{xi} = \frac{2.442.10^{-6}\,\frac{mol}{m^2 sPa}}{21.556\,\frac{mol}{m^4 Pa}} = 1.133.10^{-7} \pm 1.133.10^{-7}\sqrt{\left(\frac{2.121.10^{-7}}{2.442.10^{-6}}\right)^2 + \left(\frac{5.3062}{21.556}\right)^2}$$

$$xii = 1.133.10^{-7} \pm 2.957.10^{-8}\,\frac{m^2}{s}$$

$$xiii = \frac{xd_d^2\left(p_h + p_l\right)_{N_2} C_{V\backslash N_2}}{xi}$$

$$xiii = \frac{0.576\,\frac{1}{m}\left(2.089.10^{-6}\right)^2 m.m\,\left(170300 + 108426\right)Pa\;0.3618\,\frac{mol}{m^3 sPa^2}}{21.556\,\frac{mol}{m^4 Pa}}$$

$$xiii = 1.176.10^{-8} \pm 1.176.10^{-8}\sqrt{\left(\frac{0.202}{0.576}\right)^2 + 2\left(\frac{8.056.10^{-7}}{2.089.10^{-6}}\right)^2 + \left(\frac{3515}{278726}\right)^2 + \left(\frac{0.0018}{0.3618}\right)^2 + \left(\frac{5.3062}{21.556}\right)^2}$$

$$xiii = 1.176.10^{-8} \pm 8.157.10^{-9}\,\frac{m^2}{s}$$

$$xiv = \frac{xd_d C_{KN_2}}{xi} = \frac{0.576\,\frac{1}{m}\,2.089.10^{-6}\,m\;0.0642\,\frac{mol}{m^2 sPa}}{21.556\,\frac{mol}{m^4 Pa}}$$

$$xiv = 3.584.10^{-9} \pm 3.584.10^{-9}\sqrt{\left(\frac{0.202}{0.576}\right)^2 + \left(\frac{8.056.10^{-7}}{2.089.10^{-6}}\right)^2 + \left(\frac{0.0003}{0.0642}\right)^2 + \left(\frac{5.3062}{21.556}\right)^2}$$

$$xiv = 3.584.10^{-9} \pm 2.066.10^{-9}\,\frac{m^2}{s}$$

D_{TN_2} can then be calculated from *xii* – *xiv*.

$$D_{TN_2} = xii - xiii - xiv = 1.133.10^{-7}\,\frac{m^2}{s} - 1.176.10^{-8}\,\frac{m^2}{s} - 3.584.10^{-9}\,\frac{m^2}{s}$$

$$D_{TN_2} = 9.794.10^{-8}\,\frac{m^2}{s}$$

$$D_{TN_2} = 9.794.10^{-8} \pm \sqrt{\left(2.957.10^{-8}\right)^2 + \left(8.157.10^{-9}\right)^2 + \left(2.066.10^{-9}\right)^2}$$

$$D_{TN_2} = 9.794.10^{-8} \pm 3.074.10^{-8}\,\frac{m^2}{s}$$

Appendix 2

Derivation of Maxwell-Stefan Equations

The following derivation is for the determination of self and exchange diffusivities of two components; *i* and *j* that are present in a binary mixture, and fed to an adsorbent membrane using the Maxwell-Stefan (MS) model. A representation of the MS model is shown in Figure A.2.1. According to this model, the feed side and permeate side compositions must be single values. To this end, the average feed side and permeate side compositions from experimental data are used. The most reliable diffusivities are therefore found at zero stage cut conditions when the deviations from the average composition values are minimized. This model assumes that there is no back mixing or pressure drop on the retentate and permeate sides of the membrane, and that the experimental data has been collected at steady state. Additionally, the surface coverage at the boundary conditions is calculated by fitting adsorption data from binary adsorption isotherms to the Langmuir model, and using the Langmuir model as required. More specifically, adsorption capacities are taken from binary adsorption isotherms at the composition of interest, and are then plotted as a function of partial pressure. By utilizing binary adsorption isotherms instead of pure component isotherms, more reasonable characteristic diffusivities are obtained. Although tubular membranes are used, their diameter is two orders of magnitude larger than the membrane thickness. The curvature of the membrane has therefore been neglected, and the geometry of the membrane layer assumed to be rectangular. The following derivation equations can be found in the PhD thesis of Muhammad Tawalbeh, the previous PhD student for this project (M. Tawalbeh, Silicalite-1 Membranes Synthesis, Characterization, CO_2/N_2 Separation and Modeling, 2013).

Appendix 2 – Derivation of Maxwell-Stefan Equations

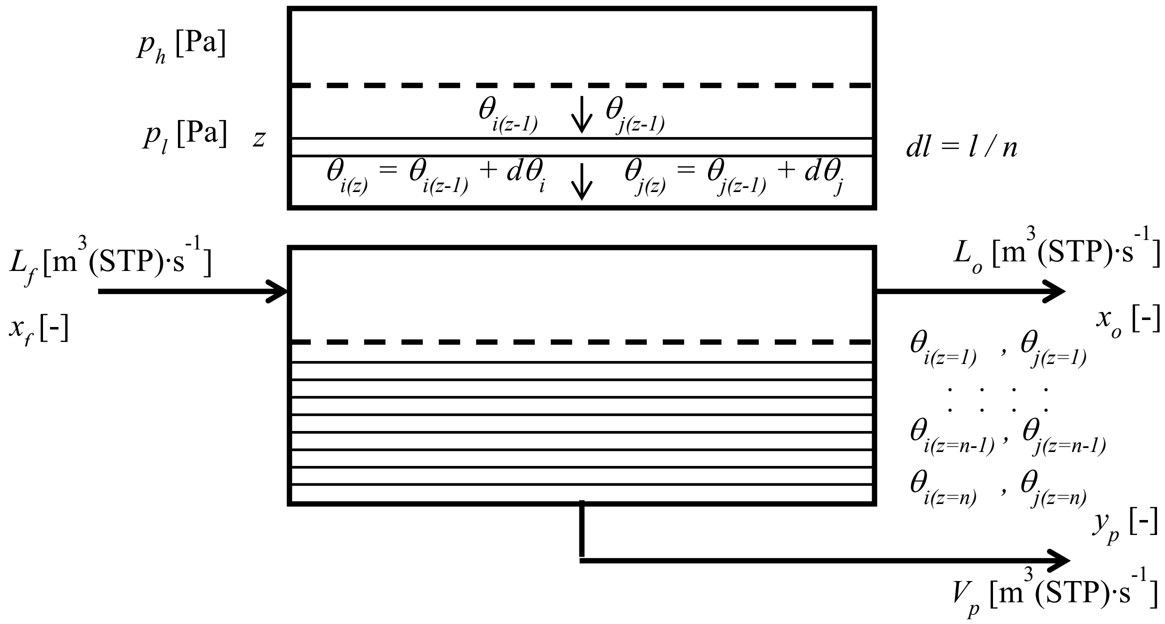

Figure A.2.1. Schematic showing the iterative procedure used to calculate the self and exchange diffusivities for two gases separated using an adsorptive membrane using the MS model.

The principal equations to be derived are:

$$J_i = \frac{Đ_i \varepsilon \rho_s q_i^{\max}}{\tau l} \ln\left(\frac{1 + K_i p_{ih}}{1 + K_i p_{il}}\right) \tag{1}$$

$$\frac{d\theta_j}{dl} = \frac{\frac{CD}{F} - A}{B - \frac{CE}{F}} \tag{2}$$

$$\frac{d\theta_i}{dl} = -\frac{D - E\frac{d\theta_j}{dl}}{F} \tag{3}$$

Where *A, B, C, D, E,* and *F* are as follows:

$$A = \frac{N_j\left(1 + \theta_j \frac{Đ_i}{Đ_{ij}} + \theta_i \frac{Đ_j}{Đ_{ji}}\right)}{\rho_s q_j^{\max} Đ_j} \tag{4}$$

$$B = \Gamma_{jj} + \left(\theta_j \frac{\text{Đ}_{\mathrm{i}}}{\text{Đ}_{\mathrm{ij}}} \Gamma_{jj} \right) + \left(\theta_j \frac{\text{Đ}_{\mathrm{i}}}{\text{Đ}_{\mathrm{ji}}} \Gamma_{ij} \right) \tag{5}$$

$$C = \Gamma_{ji} + \left(\theta_j \frac{\text{Đ}_{\mathrm{i}}}{\text{Đ}_{\mathrm{ij}}} \Gamma_{ji} \right) + \left(\theta_j \frac{\text{Đ}_{\mathrm{i}}}{\text{Đ}_{\mathrm{ji}}} \Gamma_{ii} \right) \tag{6}$$

$$D = \frac{N_i \left(1 + \theta_j \frac{\text{Đ}_i}{\text{Đ}_{ij}} + \theta_i \frac{\text{Đ}_j}{\text{Đ}_{ji}} \right)}{\rho_s q_i^{\max} \text{Đ}_i} \tag{7}$$

$$E = \Gamma_{ij} + \left(\theta_i \frac{\text{Đ}_{\mathrm{j}}}{\text{Đ}_{\mathrm{ji}}} \Gamma_{ij} \right) + \left(\theta_i \frac{\text{Đ}_{\mathrm{j}}}{\text{Đ}_{\mathrm{ij}}} \Gamma_{jj} \right) \tag{8}$$

$$F = \Gamma_{ii} + \left(\theta_i \frac{\text{Đ}_{\mathrm{j}}}{\text{Đ}_{\mathrm{ji}}} \Gamma_{ii} \right) + \left(\theta_i \frac{\text{Đ}_{\mathrm{j}}}{\text{Đ}_{\mathrm{ij}}} \Gamma_{ji} \right) \tag{9}$$

Derivation of Eq. 1.

Eq. 1 is used to calculate the self-diffusivities of each gas inside the membrane. This is equivalent to the diffusivity of gas molecules subject to interactions from molecules of the same type, as well as with the adsorbent material. The results from single gas permeance experiments are therefore used.

The general flux of a component *i* can be written as follows.

$$J_i = u_i c_i \tag{10}$$

where J_i [mol·m^{-2}·s^{-1}] is the pure gas molar flux of component *i*, u_i [m·s^{-1}] is the velocity of component *i* through the membrane, and c_i [mol·m^{-3}] is the molar concentration of component *i*. For the membranes used in this study, mass transport proceeds inside the pores of silicalite, and so density and adsorption capacity can be substituted for c_i as follows.

$$J_i = u_i \rho_s q_i \tag{11}$$

where ρ_s [kg·m^{-3}] is the density of silicalite, and q_i [mol·kg^{-1}] is the adsorption capacity of component *i*.

The driving force for a diffusive process is chemical potential μ, and is opposed by frictional forces. The general diffusive flux of a component *i* can therefore be written as follows.

$$fu_i = -\frac{d\mu_i}{dl} \tag{12}$$

where *f* [J·s·mol^{-1}·m^{-2}] is a friction coefficient, and μ_i [J·mol^{-1}] is the chemical potential of component *i*. dl is the membrane thickness of a segment over which chemical potential is measure

Given the assumption of ideal gas behaviour, Eq. 12 can be expanded as follows.

$$fu_i = \frac{d}{dl}\left(\mu_i^0 + RT \ln p_i\right) \tag{13}$$

where and μ^0_i [J·mol^{-1}] is the chemical potential of component *i* at standard conditions; which is true for the permeate side, *R* [8.314 J·mol^{-1}·K^{-1}] is the gas constant, *T* [K] is the experimental temperature, and p_i [atm] is the partial pressure of component *i*, which is equivalent to the total pressure for a pure gas.

Eq. 13 can be rearranged and substituted into Eq. 11 as follows.

$$u_i = -\frac{RT}{f}\frac{d\ln p_i}{dl} \tag{14}$$

$$J_i = -\frac{RT}{f}\frac{d\ln p_i}{dl}\rho_s q_i \tag{15}$$

Since adsorption capacity q_i [mol·kg^{-1}] is a function of partial pressure, and different at the feed and permeate sides of the membrane, the change can be expressed as shown in Eq. 21, and substituted into Eq. 15 as follows.

$$d\ln q_i = \frac{dq_i}{q_i} \tag{16}$$

$$J_i = -\rho_s \frac{RT}{f} \frac{d \ln p_i}{d \ln q_i} \frac{dq_i}{dl} \tag{17}$$

where $d\ln p_i$ divided by $d\ln q_i$ represents the gradient of the equilibrium isotherm in logarithmic co-ordinates.

Given the following relationships for Fickian transport diffusivity D_i [$m^2 \cdot s^{-1}$] and Maxwell-Stefan (MS) self diffusivitiy $Đ_i$ [$m^2 \cdot s^{-1}$]; where MS self-diffusivity is equivalent to the corrected transport diffusivity, Eq. 17 can be re-written as follows.

$$D_i = \frac{RT}{f} \frac{d \ln p_i}{d \ln q_i} \tag{18}$$

$$Đ_i = \frac{RT}{f} \tag{19}$$

$$J_i = -\rho_s D_i \frac{dq_i}{dl} = -\rho_s Đ_{\mathrm{i}} \frac{d \ln p_i}{d \ln q_i} \frac{dq_i}{dl} \tag{20}$$

Whereas Fickian diffusivities are a lumped parameter that includes deviation from ideal gas conditions, MS diffusivities are separate from thermodynamic effects. MS diffusivities are therefore preferable for characterizing adsorptive membrane performance as the driving force for gas permeation in an adsorptive membrane is adsorption capacity difference, which is a function of temperature. The relationship between Fickian and MS diffusivities is therefore as follows.

$$D_i = Đ_{\mathrm{i}} \frac{d \ln p_i}{d \ln q_i} = Đ_{\mathrm{i}} \Gamma \tag{21}$$

where Γ [-] represents the thermodynamic correction factor to MS diffusivity that is included in the Fickian diffusivity. Given the logarithmic relationship shown in Eq. 16 for q_i, which also applies to p_i, Γ can be re-written as follows.

$$\Gamma = \frac{d \ln p_i}{d \ln q_i} = \frac{q_i}{p_i} \frac{dp_i}{dq_i} \tag{22}$$

Eq. 22 can then be substituted into Eq. 20 as follows.

$$J_i = -\rho_s \text{Đ}_\text{i} \frac{q_i}{p_i} \frac{dp_i}{dq_i} \frac{dq_i}{dl} = -\rho_s \text{Đ}_\text{i} \frac{q_i}{p_i} \frac{dp_i}{dl} \tag{23}$$

For a pure gas, the Langmuir adsorption model is reasonable, and so can be substituted into Eq. 23 as follows.

$$q = q_i^{sat} \frac{K_i p_i}{1 + K_i p_i} \tag{24}$$

$$J_i = -\rho_s \text{Đ}_\text{i} \left(q_i^{sat} \frac{K_i p_i}{1 + K_i p_i} \right) \frac{dp_i}{p_i dl} \tag{25}$$

where K_i [Pa^{-1}] and $q^{sat}{}_i$ [mol·kg^{-1}] are the Langmuir adsorption coefficient and saturation capacity respectively.

Eq. 25 can then be integrated from z = 0 to l as follows.

$$J_i = -\rho_s q_i^{sat} \text{Đ}_\text{i} \ln\left(\frac{1 + K_i p_{hi}}{1 + K_i p_{li}} \right) \tag{26}$$

where p_{hi} [Pa], and p_{li} [Pa], are the feed side and permeate side partial pressures of component *i* respectively.

Eq. 26 can then be further developed to account for ε [-], the porosity of the membrane support active layer, and well as τ [-], the tortuosity of the pores of silicalite, and *l* [m], the membrane thickness. In this form, the MS self-diffusivity for a component *i* can be calculated.

$$J_i = \frac{-\rho_s \varepsilon q_i^{sat} \text{Đ}_\text{i}}{\tau l} \ln\left(\frac{1 + K_i p_{hi}}{1 + K_i p_{li}} \right) \tag{1}$$

Derivation of Eqs. 2 - 9.

MS self-diffusivities alone cannot be used to describe the transport of gas mixtures through an adsorptive membrane. It is therefore necessary to calculate MS exchange diffusivities which account for inter-molecular interactions. This is accomplished by fitting binary gas permeation experimental data to the MS equations using known surface occupancies at the boundary conditions of the membrane. Once the surface occupancies at the boundary conditions have been calculated, the membrane can be divided into a number of segments z [-], and the surface occupancy profile as a function of membrane thickness calculated. This is accomplished by assuming that the outputs for a segment are the inputs for the subsequent segment. By therefore guessing values for MS exchange diffusivities, and generating the surface occupancy profile, an iterative method can then be used to change values of exchange diffusivities, and generate new surface occupancy profiles which converge to the experimentally known permeate surface occupancy.

The generalized MS equation can first be used to describe the mass transport by diffusion through an adsorptive membrane and is as follows.

$$-\nabla\mu_i = RT\frac{u_i}{\text{Đ}_i} + RT\sum_{\substack{j=1\\ j\neq 1}}^{n}\theta_j\frac{u_i - u_j}{\text{Đ}_{ij}} \tag{27}$$

where $\nabla\mu_i$ [J·mol^{-1}], is the isothermal driving force as a function of chemical potential for component *i*, θ_j [-], is the surface occupancy of component *j*, and $Đ_{ij}$ [m^2·s^{-1}], is the MS Exchange diffusivity of component *i* subject to interactions with component *j*. The first term on the right hand side of Eq. 27 represents the resistance to mass transport exerted by other molecules of component *i* and adsorbent silicalite. The second term on the right represents the resistance to mass transport of component *i* exerted by molecules of component *j*.

Eq. 27 can then be rearranged, and multiplied by θ_j [-] as follows.

$$-\frac{\theta_i}{RT}\nabla\mu_i = \frac{\theta_i u_i}{\text{Đ}_i} + \sum_{\substack{j=1\\ j\neq 1}}^{n}\theta_i\theta_j\frac{u_i - u_j}{\text{Đ}_{ij}} \tag{28}$$

Given the relationships between adsorption capacity and surface occupancy as shown below, Eq. 29 and 30 can be substituted into Eq. 28 as follows.

$$\theta_i = \frac{q_i}{q_i^{sat}} \tag{29}$$

$$\theta_j = \frac{q_j}{q_j^{sat}} \tag{30}$$

$$-\frac{\theta_i}{RT}\nabla\mu_i = \frac{q_i u_i}{\mathrm{q}_\mathrm{i}^\mathrm{sat}\,Đ_i} + \sum_{\substack{j=1\\ j\neq 1}}^{n} q_i q_j \,\frac{u_i - u_j}{\mathrm{q}_\mathrm{i}^\mathrm{sat}\mathrm{q}_\mathrm{j}^\mathrm{sat}\,Đ_{ij}} \tag{31}$$

where q_i^{sat} [mol·kg^{-1}], is the maximum saturation capacity of the adsorbent for component *i*.

Given the relationship between surface occupancies and fluxes shown in Eq. 33, Eq 31 can be modified as follows.

$$J_i = \rho_s q_i^{sat}\theta_i = \rho_s q_i u_i \tag{32}$$

$$u_i = \frac{N_i}{\rho_s q_i^{sat}\theta_i} = \frac{N_i}{\rho_s q_i} \tag{33}$$

$$-\frac{\theta_i}{RT}\nabla\mu_i = \frac{1}{\rho_s}\frac{N_i}{\mathrm{q}_\mathrm{i}^\mathrm{sat}\,Đ_i} + \sum_{\substack{j=1\\ j\neq 1}}^{n}\frac{q_j N_i - q_i N_i}{\mathrm{q}_\mathrm{i}^\mathrm{sat}\mathrm{q}_\mathrm{j}^\mathrm{sat}\,Đ_{ij}} \tag{34}$$

where N_i [mol·m^{-2}·s^{-1}], is the molar flux of component *i* when present in a binary gas mixture.

Eq. 34 can then be simplified by relating the surface occupancies using a matrix of thermodynamic correction factors as follows.

$$\frac{\theta_i}{RT}\nabla\mu_i = \sum_{\substack{j=1\\ j\neq 1}}^{n}\Gamma_{ij}\nabla\theta_j \tag{35}$$

where Γ_{ij} [-] is the thermodynamic correction factor for I in the presence of j, and has the following relationships with other properties.

$$\Gamma_{ij} = \theta_i\frac{\partial \ln p_i}{\partial\theta_j} = \frac{\theta_i}{p_i}\frac{\partial p_i}{\partial\theta_j} \tag{36}$$

Where the partial derivatives are defined by adsorption equilibrium between p_i and θ_i. Γ_{ij} can therefore also be represented as follows.

$$\Gamma_{ij} = \left(\frac{q_j^{sat}}{q_i^{sat}}\right)\frac{q_i}{p_i}\frac{\partial p_i}{\partial q_j} \tag{37}$$

Eq. 34 can then be combined with Eq. 35 as follows.

$$\sum_{j=1}^{n}\Gamma_{ij}\nabla\theta_j = -\frac{1}{\rho_s}\left(\frac{N_i}{\mathrm{q}_\mathrm{i}^\mathrm{sat}\,\text{Đ}_i}+\sum_{\substack{j=1\\ j\neq 1}}^{n}\frac{q_jN_i-q_iN_j}{\mathrm{q}_\mathrm{i}^\mathrm{sat}\mathrm{q}_\mathrm{j}^\mathrm{sat}\,\text{Đ}_{ij}}\right) \tag{38}$$

Eq. 38 can then be written for two components as follows.

$$\Gamma_{ii}\nabla\theta_i+\Gamma_{ij}\nabla\theta_j = -\frac{1}{\rho_s}\left(\frac{N_i}{\mathrm{q}_\mathrm{i}^\mathrm{sat}\,\text{Đ}_i}+\frac{q_jN_i-q_iN_j}{\mathrm{q}_\mathrm{i}^\mathrm{sat}\mathrm{q}_\mathrm{j}^\mathrm{sat}\,\text{Đ}_{ij}}\right) \tag{39}$$

$$\Gamma_{ji}\nabla\theta_i+\Gamma_{jj}\nabla\theta_j = -\frac{1}{\rho_s}\left(\frac{N_j}{\mathrm{q}_\mathrm{j}^\mathrm{sat}\,\text{Đ}_j}+\frac{q_iN_j-q_jN_i}{\mathrm{q}_\mathrm{i}^\mathrm{sat}\mathrm{q}_\mathrm{j}^\mathrm{sat}\,\text{Đ}_{ji}}\right) \tag{40}$$

Eq. 39 and 40 can be solved simultaneously, which is represented by the matrix which follows.

$$\begin{bmatrix}\Gamma_{ii} & \Gamma_{ij}\\ \Gamma_{ji} & \Gamma_{jj}\end{bmatrix}\begin{pmatrix}\nabla\theta_i\\ \nabla\theta_j\end{pmatrix} = -\frac{1}{\rho_s}\begin{bmatrix}\dfrac{q_j}{\mathrm{q}_\mathrm{i}^\mathrm{sat}\mathrm{q}_\mathrm{j}^\mathrm{sat}\,\text{Đ}_{ij}}+\dfrac{1}{\mathrm{q}_\mathrm{i}^\mathrm{sat}\,\text{Đ}_i} & -\dfrac{q_i}{\mathrm{q}_\mathrm{i}^\mathrm{sat}\mathrm{q}_\mathrm{j}^\mathrm{sat}\,\text{Đ}_{ij}}\\ -\dfrac{q_j}{\mathrm{q}_\mathrm{i}^\mathrm{sat}\mathrm{q}_\mathrm{j}^\mathrm{sat}\,\text{Đ}_{ji}} & \dfrac{q_i}{\mathrm{q}_\mathrm{i}^\mathrm{sat}\mathrm{q}_\mathrm{j}^\mathrm{sat}\,\text{Đ}_{ji}}+\dfrac{1}{\mathrm{q}_\mathrm{j}^\mathrm{sat}\,\text{Đ}_j}\end{bmatrix}\begin{pmatrix}N_i\\ N_j\end{pmatrix} \tag{41}$$

Eq. 41 can alternatively be expressed in vector notation as follows.

$$-\rho_s[\Gamma](\nabla\theta)=[B'](N) \tag{42}$$

where B’ can be represented by the matrix which follows.

$$[B']=\begin{bmatrix}\dfrac{q_j}{\mathrm{q}_\mathrm{i}^\mathrm{sat}\mathrm{q}_\mathrm{j}^\mathrm{sat}\,\text{Đ}_{ij}}+\dfrac{1}{\mathrm{q}_\mathrm{i}^\mathrm{sat}\,\text{Đ}_i} & -\dfrac{q_i}{\mathrm{q}_\mathrm{i}^\mathrm{sat}\mathrm{q}_\mathrm{j}^\mathrm{sat}\,\text{Đ}_{ij}}\\ -\dfrac{q_j}{\mathrm{q}_\mathrm{i}^\mathrm{sat}\mathrm{q}_\mathrm{j}^\mathrm{sat}\,\text{Đ}_{ji}} & \dfrac{q_i}{\mathrm{q}_\mathrm{i}^\mathrm{sat}\mathrm{q}_\mathrm{j}^\mathrm{sat}\,\text{Đ}_{ji}}+\dfrac{1}{\mathrm{q}_\mathrm{j}^\mathrm{sat}\,\text{Đ}_j}\end{bmatrix} \tag{43}$$

Eq. 43 can then be further simplified by substitution of Eq. 29 and 30 as follows.

$$[B'] = \begin{bmatrix} \frac{\theta_j}{Đ_{ij}} + \frac{1}{Đ_i} & -\frac{\theta_i}{Đ_{ij}} \\ -\frac{\theta_j}{Đ_{ji}} & \frac{\theta_i}{Đ_{ji}} + \frac{1}{Đ_j} \end{bmatrix} \begin{bmatrix} \frac{1}{q_i^{sat}} & 0 \\ 0 & \frac{1}{q_j^{sat}} \end{bmatrix} \tag{44}$$

Eq. 43 can additionally be simplified as follows by utilizing the inverse q^{sat} matrix as shown.

$$[B'] = [B][q^{sat}]^{-1}$$

(45)

The elements of Eq. 45 are as follows.

$$[B] = \begin{bmatrix} \frac{\theta_j}{Đ_{ij}} + \frac{1}{Đ_i} & -\frac{\theta_i}{Đ_{ij}} \\ -\frac{\theta_j}{Đ_{ji}} & \frac{\theta_i}{Đ_{ji}} + \frac{1}{Đ_j} \end{bmatrix} \tag{46}$$

$$[q^{sat}]^{-1} = \begin{bmatrix} \frac{1}{q_i^{sat}} & 0 \\ 0 & \frac{1}{q_j^{sat}} \end{bmatrix} \tag{47}$$

The inverse of matrix [B’] can be calculated as shown in Eq. 48, and then used to solve for binary mixture fluxes as shown in Eq. 49.

$$[B']^{-1} = [B]^{-1}[q^{sat}] \tag{48}$$

$$(N) = -\rho_s [B']^{-1}[\Gamma](\nabla\theta)$$

$$(N) = -\rho_s [q^{sat}][B]^{-1}[\Gamma](\nabla\theta) \tag{49}$$

The inverse of a general matrix [a] can be found using Eq. 50 and 51 which follow.

$$[a] = \begin{bmatrix} a_{11} & a_{12} \\ a_{21} & a_{22} \end{bmatrix}$$

$$[a]^{-1}=\frac{1}{Det[a]}\begin{bmatrix} a_{22} & -a_{12} \\ -a_{21} & a_{11}\end{bmatrix} \tag{50}$$

$$Det[a]=a_{11}\times a_{22}-a_{12}\times a_{21} \tag{51}$$

The inverse of [B] can therefore be calculated as required for Eq. 49 and has the following form.

$$[B]^{-1}=\frac{\begin{bmatrix} \frac{\theta_i}{Đ_{ji}}+\frac{1}{Đ_j} & \frac{\theta_i}{Đ_{ij}} \\ \frac{\theta_j}{Đ_{ji}} & \frac{\theta_j}{Đ_{ij}}+\frac{1}{Đ_i}\end{bmatrix}}{\frac{\theta_i}{Đ_i Đ_{ji}}+\frac{\theta_j}{Đ_j Đ_{ij}}+\frac{\theta_i}{Đ_i Đ_j}} \tag{52}$$

Eq. 52 can then be simplified as follows.

$$[B]^{-1}=\frac{\begin{bmatrix} Đ_i & 0 \\ 0 & Đ_j\end{bmatrix}\begin{bmatrix} 1+\frac{\theta_i Đ_j}{Đ_{ji}} & \frac{\theta_i Đ_j}{Đ_{ij}} \\ \frac{\theta_j Đ_i}{Đ_{ji}} & 1+\frac{\theta_j Đ_i}{Đ_{ij}}\end{bmatrix}}{\frac{\theta_i Đ_j}{Đ_{ji}}+\frac{\theta_j Đ_i}{Đ_{ij}}+1} \tag{53}$$

Eq. 53 can then be substituted into Eq. 49 in order to describe the flux of a two component system as follows.

$$\begin{pmatrix} N_i \\ N_j \end{pmatrix}=\frac{\begin{bmatrix} q_i^{sat} & 0 \\ 0 & q_j^{sat}\end{bmatrix}\begin{bmatrix} Đ_i & 0 \\ 0 & Đ_j\end{bmatrix}\begin{bmatrix} 1+\frac{\theta_i Đ_j}{Đ_{ji}} & \frac{\theta_i Đ_j}{Đ_{ij}} \\ \frac{\theta_j Đ_i}{Đ_{ji}} & 1+\frac{\theta_j Đ_i}{Đ_{ij}}\end{bmatrix}\begin{bmatrix} \Gamma_{ii} & \Gamma_{ij} \\ \Gamma_{ji} & \Gamma_{jj}\end{bmatrix}\begin{pmatrix} \nabla\theta_i \\ \nabla\theta_j \end{pmatrix}}{\frac{\theta_i Đ_j}{Đ_{ji}}+\frac{\theta_j Đ_i}{Đ_{ij}}+1} \tag{54}$$

Eq. 54 can then undergo dot matrix multiplication to generate the flux equations for component *i* and *j* as follows as a function of thermodynamic factors, adsorption isotherm properties, and surface occupancies.

$$N_i = -\rho_s q_i^{sat}\text{Đ}_i \times \left[\frac{\left(\Gamma_{ii} + \frac{\theta_i \text{Đ}_j}{\text{Đ}_{ji}} \Gamma_{ii} + \frac{\theta_i \text{Đ}_j}{\text{Đ}_{ij}} \Gamma_{ji} \right) \nabla \theta_i + \left(\Gamma_{ij} + \frac{\theta_i \text{Đ}_j}{\text{Đ}_{ji}} \Gamma_{ij} + \frac{\theta_i \text{Đ}_j}{\text{Đ}_{ij}} \Gamma_{jj} \right) \nabla \theta_j}{\frac{\theta_i \text{Đ}_j}{\text{Đ}_{ji}} + \frac{\theta_j \text{Đ}_i}{\text{Đ}_{ij}} + 1} \right] \tag{55}$$

$$N_j = -\rho_s q_j^{sat}\text{Đ}_j \times \left[\frac{\left(\Gamma_{jj} + \frac{\theta_j \text{Đ}_i}{\text{Đ}_{ij}} \Gamma_{jj} + \frac{\theta_j \text{Đ}_i}{\text{Đ}_{ji}} \Gamma_{ij} \right) \nabla \theta_j + \left(\Gamma_{ji} + \frac{\theta_j \text{Đ}_i}{\text{Đ}_{ij}} \Gamma_{ji} + \frac{\theta_j \text{Đ}_i}{\text{Đ}_{ji}} \Gamma_{ii} \right) \nabla \theta_i}{\frac{\theta_i \text{Đ}_j}{\text{Đ}_{ji}} + \frac{\theta_j \text{Đ}_i}{\text{Đ}_{ij}} + 1} \right] \tag{56}$$

The thermodynamic factors as required for Eq. 55 and 56 are as defined by Eq. 38. By then assuming that the single site extended Langmuir model Eq. 57 is applicable, the thermodynamic correction factors can be expressed as functions of surface occupancies. The complete list of thermodynamic factors is as follows.

$$q_i = \frac{q_i^{sat} K_i p_i}{1 + \sum_{k=1}^{n} K_k p_k} \tag{57}$$

$$\Gamma_{ii} = \left(\frac{q_i^{sat}}{q_i^{sat}} \right) \frac{q_i}{p_i} \frac{\partial p_i}{\partial q_i} = \frac{1 - \theta_j}{1 - \theta_i - \theta_j} \tag{58}$$

$$\Gamma_{ij} = \left(\frac{q_j^{sat}}{q_i^{sat}} \right) \frac{q_i}{p_i} \frac{\partial p_i}{\partial q_j} = \frac{\theta_i}{1 - \theta_i - \theta_j} \tag{59}$$

$$\Gamma_{ji} = \left(\frac{q_i^{sat}}{q_j^{sat}} \right) \frac{q_j}{p_j} \frac{\partial p_j}{\partial q_i} = \frac{\theta_j}{1 - \theta_i - \theta_j} \tag{60}$$

$$\Gamma_{jj} = \left(\frac{q_j^{sat}}{q_j^{sat}} \right) \frac{q_j}{p_j} \frac{\partial p_j}{\partial q_j} = \frac{1 - \theta_i}{1 - \theta_i - \theta_j} \tag{61}$$

Diffusion occurs in the direction of decreasing surface occupancy from the feed to permeate side of the membrane, the following equations; Eq. 62 and 63, as well as Eq. 58 – 61, can be substituted into Eq. 55 and 56 as follows.

$$\nabla \theta_i = \frac{d\theta_i}{dl} \qquad (62)$$

$$\nabla q_i = \frac{dq_i}{dl} \qquad (63)$$

$$N_i = -\rho_s q_i^{sat} \text{Đ}_i \left\{ \frac{\left[\frac{1-\theta_j}{1-\theta_i-\theta_j} + \left(\frac{\theta_i \text{Đ}_j}{\text{Đ}_{ji}} \frac{1-\theta_j}{1-\theta_i-\theta_j}\right) + \left(\frac{\theta_i \text{Đ}_j}{\text{Đ}_{ij}} \frac{\theta_j}{1-\theta_i-\theta_j}\right)\right]\frac{d\theta_i}{dl} + \left[\frac{\theta_i}{1-\theta_i-\theta_j} + \left(\frac{\theta_i \text{Đ}_j}{\text{Đ}_{ji}} \frac{\theta_i}{1-\theta_i-\theta_j}\right) + \left(\frac{\theta_i \text{Đ}_j}{\text{Đ}_{ij}} \frac{1-\theta_i}{1-\theta_i-\theta_j}\right)\right]\frac{d\theta_2}{dl}}{\frac{\theta_i \text{Đ}_j}{\text{Đ}_{ji}} + \frac{\theta_j \text{Đ}_i}{\text{Đ}_{ij}} + 1} \right\} \tag{64}$$

$$N_j = -\rho_s q_j^{sat} \text{Đ}_j \left\{ \frac{\left[\frac{1-\theta_i}{1-\theta_i-\theta_j} + \left(\frac{\theta_j \text{Đ}_i}{\text{Đ}_{ij}} \frac{1-\theta_i}{1-\theta_i-\theta_j}\right) + \left(\frac{\theta_j \text{Đ}_i}{\text{Đ}_{ji}} \frac{\theta_i}{1-\theta_i-\theta_j}\right)\right]\frac{d\theta_j}{dl} + \left[\frac{\theta_j}{1-\theta_i-\theta_j} + \left(\frac{\theta_j \text{Đ}_i}{\text{Đ}_{ij}} \frac{\theta_j}{1-\theta_i-\theta_j}\right) + \left(\frac{\theta_j \text{Đ}_i}{\text{Đ}_{ji}} \frac{1-\theta_j}{1-\theta_i-\theta_j}\right)\right]\frac{d\theta_i}{dl}}{\frac{\theta_i \text{Đ}_j}{\text{Đ}_{ji}} + \frac{\theta_j \text{Đ}_i}{\text{Đ}_{ij}} + 1} \right\} \tag{65}$$

Eq. 64 and 65 can then be further simplified as follows.

$$-\frac{N_i\left(\frac{\theta_i \text{Đ}_j}{\text{Đ}_{ji}} + \frac{\theta_j \text{Đ}_i}{\text{Đ}_{ij}} + 1\right)}{\rho_s q_i^{sat} \text{Đ}_\text{i}} = \left\{ \begin{array}{l} \left[\frac{1-\theta_j}{1-\theta_i-\theta_j} + \left(\frac{\theta_i \text{Đ}_j}{\text{Đ}_{ji}} \frac{1-\theta_j}{1-\theta_i-\theta_j}\right) + \left(\frac{\theta_i \text{Đ}_j}{\text{Đ}_{ij}} \frac{\theta_j}{1-\theta_i-\theta_j}\right)\right]\frac{d\theta_i}{dl} + \\ \left[\frac{\theta_i}{1-\theta_i-\theta_j} + \left(\frac{\theta_i \text{Đ}_j}{\text{Đ}_{ji}} \frac{\theta_i}{1-\theta_i-\theta_j}\right) + \left(\frac{\theta_i \text{Đ}_j}{\text{Đ}_{ij}} \frac{1-\theta_i}{1-\theta_i-\theta_j}\right)\right]\frac{d\theta_2}{dl} \end{array} \right\} \tag{66}$$

$$\frac{-N_j\left(\frac{\theta_i \text{Đ}_j}{\text{Đ}_{ji}} + \frac{\theta_j \text{Đ}_i}{\text{Đ}_{ij}} + 1\right)}{\rho_s q_j^{sat} \text{Đ}_j} = \left\{ \begin{array}{l} \left[\frac{1-\theta_i}{1-\theta_i-\theta_j} + \left(\frac{\theta_j \text{Đ}_i}{\text{Đ}_\text{ij}} \frac{1-\theta_i}{1-\theta_i-\theta_j}\right) + \left(\frac{\theta_j \text{Đ}_i}{\text{Đ}_\text{ji}} \frac{\theta_i}{1-\theta_i-\theta_j}\right)\right]\frac{d\theta_j}{dl} + \\ \left[\frac{\theta_j}{1-\theta_i-\theta_j} + \left(\frac{\theta_j \text{Đ}_i}{\text{Đ}_{ij}} \frac{\theta_j}{1-\theta_i-\theta_j}\right) + \left(\frac{\theta_j \text{Đ}_i}{\text{Đ}_{ji}} \frac{1-\theta_j}{1-\theta_i-\theta_j}\right)\right]\frac{d\theta_i}{dl} \end{array} \right\} \tag{67}$$

where the right hand sides of Eq. 66 and 67 are not matrices.

Eq. 66 can then be re-arranged in order to have the form of an ODE for the change in surface occupancy of component *i* as a function of a change in membrane thickness as follows.

$$\frac{d\theta_i}{dl}=\left\{\frac{-\dfrac{N_i\left(\dfrac{\theta_i\text{Đ}_j}{\text{Đ}_{ji}}+\dfrac{\theta_j\text{Đ}_i}{\text{Đ}_{ij}}+1\right)}{\rho_s q_i^{sat}\text{Đ}_\mathrm{i}}-\left[\dfrac{\theta_i}{1-\theta_i-\theta_j}+\left(\dfrac{\theta_i\text{Đ}_j}{\text{Đ}_{ji}}\dfrac{\theta_i}{1-\theta_i-\theta_j}\right)+\left(\dfrac{\theta_i\text{Đ}_j}{\text{Đ}_{ij}}\dfrac{1-\theta_i}{1-\theta_i-\theta_j}\right)\right]\dfrac{d\theta_2}{dl}}{\left[\dfrac{1-\theta_j}{1-\theta_i-\theta_j}+\left(\dfrac{\theta_i\text{Đ}_j}{\text{Đ}_{ji}}\dfrac{1-\theta_j}{1-\theta_i-\theta_j}\right)+\left(\dfrac{\theta_i\text{Đ}_j}{\text{Đ}_{ij}}\dfrac{\theta_j}{1-\theta_i-\theta_j}\right)\right]}\right\} \tag{68}$$

Eq. 68 can then be substituted into Eq. 67 as follows.

$$\frac{-N_j\left(\dfrac{\theta_i\text{Đ}_j}{\text{Đ}_{ji}}+\dfrac{\theta_j\text{Đ}_i}{\text{Đ}_{ij}}+1\right)}{\rho_s q_j^{sat}\text{Đ}_j}=\left\{\begin{array}{l}\left[\dfrac{1-\theta_i}{1-\theta_i-\theta_j}+\left(\dfrac{\theta_j\text{Đ}_i}{\text{Đ}_\mathrm{ij}}\dfrac{1-\theta_i}{1-\theta_i-\theta_j}\right)+\left(\dfrac{\theta_j\text{Đ}_i}{\text{Đ}_\mathrm{ji}}\dfrac{\theta_i}{1-\theta_i-\theta_j}\right)\right]\dfrac{d\theta_j}{dl}+\left[\dfrac{\theta_j}{1-\theta_i-\theta_j}+\left(\dfrac{\theta_j\text{Đ}_i}{\text{Đ}_{ij}}\dfrac{\theta_j}{1-\theta_i-\theta_j}\right)+\left(\dfrac{\theta_j\text{Đ}_i}{\text{Đ}_{ji}}\dfrac{1-\theta_j}{1-\theta_i-\theta_j}\right)\right]\times\\ \dfrac{-\dfrac{N_i\left(\dfrac{\theta_i\text{Đ}_j}{\text{Đ}_{ji}}+\dfrac{\theta_j\text{Đ}_i}{\text{Đ}_{ij}}+1\right)}{\rho_s q_i^{sat}\text{Đ}_\mathrm{i}}-\left[\dfrac{\theta_i}{1-\theta_i-\theta_j}+\left(\dfrac{\theta_i\text{Đ}_j}{\text{Đ}_{ji}}\dfrac{\theta_i}{1-\theta_i-\theta_j}\right)+\left(\dfrac{\theta_i\text{Đ}_j}{\text{Đ}_{ij}}\dfrac{1-\theta_i}{1-\theta_i-\theta_j}\right)\right]\dfrac{d\theta_2}{dl}}{\left[\dfrac{1-\theta_j}{1-\theta_i-\theta_j}+\left(\dfrac{\theta_i\text{Đ}_j}{\text{Đ}_{ji}}\dfrac{1-\theta_j}{1-\theta_i-\theta_j}\right)+\left(\dfrac{\theta_i\text{Đ}_j}{\text{Đ}_{ij}}\dfrac{\theta_j}{1-\theta_i-\theta_j}\right)\right]}\end{array}\right\} \tag{69}$$

where the right hand side of Eq. 69 is not a matrix.

Eq. 69 can then be written as a function of multiple parameters called $A - F$ in the format shown as follows.

$$-A=\left[B\frac{d\theta_j}{dl}+C\left(\frac{-D-E\frac{d\theta_j}{dl}}{F}\right)\right] \tag{70}$$

The parameters $A - F$ can then be written as required for 4 – 9.

$$A=\frac{N_j\left(1+\theta_j\frac{Đ_i}{Đ_{ij}}+\theta_i\frac{Đ_j}{Đ_{ji}}\right)}{\rho_s q_j^{\max} Đ_j} \tag{4}$$

$$B=\frac{1-\theta_i}{1-\theta_i-\theta_j}+\left(\theta_j\frac{Đ_\mathrm{i}}{Đ_\mathrm{ij}}\frac{1-\theta_i}{1-\theta_i-\theta_j}\right)+\left(\theta_j\frac{Đ_\mathrm{i}}{Đ_\mathrm{ji}}\frac{\theta_i}{1-\theta_i-\theta_j}\right) \tag{5}$$

$$C=\frac{\theta_j}{1-\theta_i-\theta_j}+\left(\theta_j\frac{Đ_\mathrm{i}}{Đ_\mathrm{ij}}\frac{\theta_j}{1-\theta_i-\theta_j}\right)+\left(\theta_j\frac{Đ_\mathrm{i}}{Đ_\mathrm{ji}}\frac{1-\theta_j}{1-\theta_i-\theta_j}\right) \tag{6}$$

$$D=\frac{N_i\left(1+\theta_j\frac{Đ_i}{Đ_{ij}}+\theta_i\frac{Đ_j}{Đ_{ji}}\right)}{\rho_s q_i^{\max} Đ_i} \tag{7}$$

$$E=\frac{\theta_i}{1-\theta_i-\theta_j}+\left(\theta_i\frac{Đ_\mathrm{j}}{Đ_\mathrm{ji}}\frac{\theta_i}{1-\theta_i-\theta_j}\right)+\left(\theta_i\frac{Đ_\mathrm{j}}{Đ_\mathrm{ij}}\frac{1-\theta_i}{1-\theta_i-\theta_j}\right) \tag{8}$$

$$F=\frac{1-\theta_j}{1-\theta_i-\theta_j}+\left(\theta_i\frac{Đ_\mathrm{j}}{Đ_\mathrm{ji}}\frac{1-\theta_j}{1-\theta_i-\theta_j}\right)+\left(\theta_i\frac{Đ_\mathrm{j}}{Đ_\mathrm{ij}}\frac{\theta_j}{1-\theta_i-\theta_j}\right) \tag{9}$$

Eq. 70 can then be expressed as an ODE for the change in surface occupancy of component *j* as the membrane thickness change as required for Eq. 2.

$$-A=\left[B\frac{d\theta_j}{dz}-\frac{CD}{F}-\frac{CE\frac{d\theta_j}{dl}}{F}\right] \tag{71}$$

$$-A+\frac{CD}{F}=\left(B-\frac{CE}{F}\right)\frac{d\theta_j}{dl} \qquad (72)$$

$$\frac{d\theta_j}{dl}=\frac{\frac{CD}{F}-A}{B-\frac{CE}{F}} \qquad (2)$$

Eq. 4 – 9 can also be substituted into Eq. 68 in order to form the ODE for the change in surface occupancy of component *i* as the membrane thickness changes as required for Eq. 3.

$$\frac{d\theta_i}{dl}=-\frac{D-E\frac{d\theta_j}{dl}}{F} \qquad (3)$$

Appendix 3

Determination of the Adsorption Isotherms and Transport Diffusivities of Gases in Mixtures Inside Zeolitic Crystals Using Infra-Red Micro-Imaging

D. Carter[1], F.H. Tezel[1], B. Kruczek[1], J. Karger[2], C. Chmelik[2]*.

[1]University of Ottawa, Department of Chemical and Biological Engineering
161 Louis Pasteur, Ottawa, Ontario, Canada K1N 6N5
[2]University of Leipzig, Department of Interface Physics
Linnestrasse 5, Leipzig, Germany, 04103
*Corresponding author

To be submitted to: *Methods X*

ABSTRACT

In the following method, the varied regions of Infra-Red (IR) light absorption by guest molecules inside a zeolitic crystal are measured and quantified to determine binary adsorption isotherms and transport diffusivities. This has been achieved using a vacuum capable setup which includes an Infra-Red Microscope (IRM) and Fourier Transform Infra-Red Spectrometer (FTIR). By utilizing IR light and FTIR spectroscopy, this method can be used to describe the behavior of low concentrations of relatively fast molecules inside zeolitic crystals as an alternative to chromatographic pulse methods. To demonstrate the capabilities of this method, binary adsorption isotherms and transport diffusivities of CO_2 in mixtures composed of CO_2 and N_2 inside silicalite have been determined. From the fundamental measurements determined using this method, complex gas separation processes such as swing adsorption and multi stage membrane systems can be designed for novel zeolite materials. This method can also be used to develop models for complex adsorption and diffusion systems, and validate sophisticated molecular simulation models.

Appendix 3 – Determination of Adsorption Isotherms and Transport Diffusivities of Gases in Mixtures Inside Zeolitic Crystals Using Infra-Red Micro-Imaging

Keywords: Zeolite Characterization, Silicalite, Infra-Red Micro-imaging, Adsorption, Diffusion.

A.3.1.0 METHOD DETAILS

A.3.1.1 Equipment and Materials

The experimental setup that was used in this method consists of two stainless steel gas reservoirs, several pressure transducers, a turbomolecular pump, and multiple gate valves that were connected to a quartz sample cell containing the zeolite crystal to be characterized. The quartz cell of this system was placed on the stage of an Infra-Red Microscope (IRM), which was connected to a Fourier Transform Infra-Red Spectrometer (FTIR) in order to measure the amount of Infra-Red (IR) light absorbed by the sample crystal under different experimental conditions. This setup can be seen in Figure A.3.1. Additionally, convoluted vacuum tubing and VCO type fittings have been used so that the quartz cell can be removed from the stage of the IRM and placed inside a portable tubular furnace without disconnecting the quartz cell from the setup. The IRM and FTIR devices that were used in this method are the Hyperion 3000, and Vertex 80V models respectively, which are made by Bruker (Ettlingen, Germany). The portable furnace was a Carbolite MTF 12/38/400 made by Carbolite Gero Ltd (Neuhasen, Germany), and the turbomolecular pump was a Highcube 80 made by Pfeifer (Asslar, Germany).

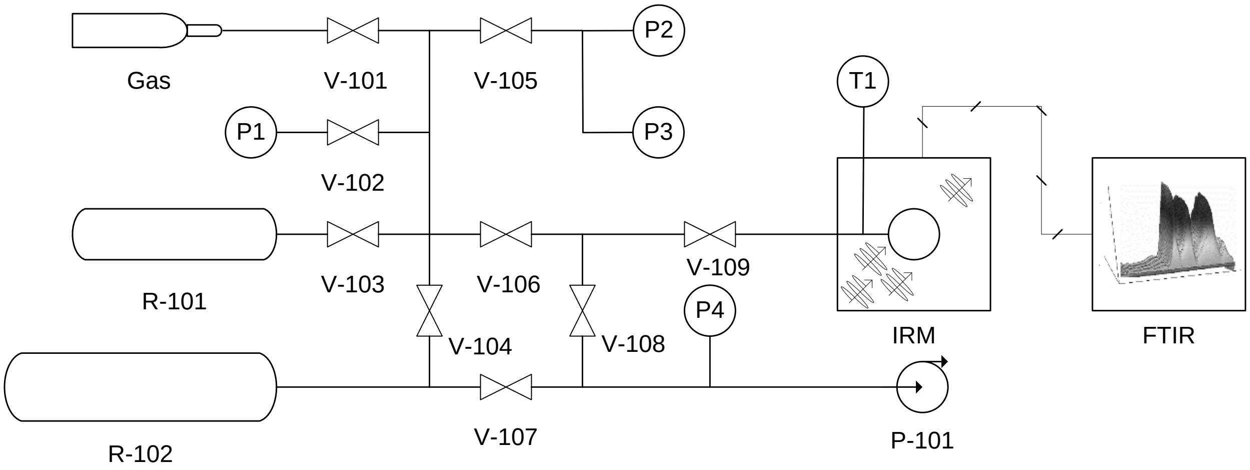

Figure A.3.1. A schematic showing the experimental setup that was used in this method. P1 – P4 are pressure transducers, and T1 is a K type thermocouple which can be used to measure room temperature in the vicinity of the quartz cell. V-101 - V-109 are gate valves. R-101 and R-102 are stainless steel reservoirs, and P-101 is a vacuum pump. The regeneration furnace is not shown. The pressure transducers are made by Pfeifer (Asslar, Germany) and have operating ranges of 0.1 – 1100 kPa (APR 266), 1 x 10^{-4} – 1.1 kPa (CMR 363), 1 x 10^{-2} – 110 kPa (CMR 361), and 5 x 10^{-8} – 100 kPa (PKR 251) for P1 – P4 respectively. The gas reservoirs R-101 and R-102 are made from 316 stainless steel, and have capacities of 0.473 L and 3.785 L, respectively.

A.3.1.2 Experimental Method

The following method has been used to characterize various combinations of zeolite crystals and gas mixtures, and has been developed from the work of Chmelik et al [1,2].

1. The zeolite crystal to be characterized was placed inside a quartz sample cell and connected to the experimental setup. The quartz cell was then placed inside the portable tubular furnace, valves V-101 to V-109 were opened, and the system evacuated using vacuum pump P-101. During evacuation, the quartz cell was subjected to temperature of 400 °C. Once evacuated, the quartz cell was removed from the portable oven and placed onto the stage of the IRM. V-101 to V-109 were then closed.
2. For pure gas uptake experiments, reservoir R-102 was then filled from the gas cylinder up to the desired maximum experimental pressure as measured by P1 by

opening V-101, V-102, and V-104. An additional amount of gas was then added to R-102 in order to compensate for the system volume at the maximum pressure. V-101, V-102 and V-104 were then closed. For gas mixture uptake experiments at room temperature, ideal gas behavior has been assumed, and the partial pressure of each gas as a fraction of the total gas pressure was manipulated in order to fill R-102 with a predetermined molar composition. Since there is only one sample gas port in the setup shown in Figure A.3.1, it was necessary to re-evacuate the process lines after the second cylinder had been connected to the system. This was done by opening V-101, V-106, and V-108. Once the process lines were re-evacuated, V-101, V-106, and V-108 were closed.

3. Gas uptake experiments to determine transport diffusivities were then conducted according to the following procedure:
    - 3.1. The IRM was first operated in optical mode, and its IR laser was focused on the zeolite crystal. The IRM was then switched to IR transmittance mode, and the IR transmittance spectrum of the crystal was determined. This spectrum was the reference spectrum.
    - 3.2. Reservoir R-101 was filled with gas from R-102 by opening V-103 as well as V-105, and then slowly opening V-104 until the desired pressure was reached. V-104 was then closed. For a step change in pressure from 0 to 10 kPa, R-101 was filled with gas from R-102 until the pressure measured by P3 was observed to be 10.2 kPa (where 0.2 kPa of pressure was required to compensate for the sample cell volume in order to reach a final pressure of approximately 10 kPa in the system).
    - 3.3. The FTIR was set to continuously determine IR transmittance spectra of the bulk gas phase and crystal, which was subjected to a step change in pressure by quickly opening V-109. Spectra were continuously determined until equilibrium had been realized, which was confirmed by observing that the IR transmittance spectra did not change with time. These spectra were analyzed subject to the reference spectrum determined in step 3.1.
4. The amounts of gas adsorbed by the zeolite crystal at equilibrium were then determined according to the following procedure:

4.1. The FTIR was used to determine the IR transmittance spectra of the bulk gas phase and crystal at equilibrium.

4.2. The IRM was switched back to optical mode, and the quartz cell was translocated on the IRM stage such that the IRM laser was focused on a region of the quartz cell where no crystal was present. The IRM was then switched back to IR transmittance mode, and the IR transmittance spectra of this space, which describes the bulk gas phase only, were determined. The equilibrium spectra determined in step 4.1 were analyzed given the reference spectra of both the crystal as determined in step 3.1, and the bulk gas phase as determined in this step; step 4.2.

4.3. The IRM was again switched back to optical mode, and the quartz cell was translocated back to its original location such that the IR laser was focused on the zeolite crystal as before. V-109 was then closed.

5. Steps 3 and 4 were repeated for all pressure steps of interest.

A.3.1.3 Analysis of Experimental Data

From the IR transmittance spectra (I) that were obtained in steps 3 and 4, IR absorption spectra (A) were determined. This has been achieved by dividing the reference spectrum (I_0) by each transmittance spectrum, and then taking its logarithm in accordance with the Beer-Lambert law [3], as described by Equation 1 [4]. Given IR absorption spectra, the molecular bonds of guest molecules and zeolitic crystals can be distinguished from each other according to their different bands in IR absorbance spectra. These different bands can be observed as IR absorption spectra peaks, and were quantified by integration.

$$A = log\left(\frac{I_0}{I}\right) \tag{1}$$

In order to determine transport diffusivities from IRM data, the previously published method by Chmelik et al has been used [1,2]. In this method, time dependent IR absorbance spectra peaks from step 3 corresponding to the guest molecules of interest have been integrated. Relative uptake as a fraction of complete uptake was then determined based on these integrals, and was used in combination with an appropriate analytical expression in order to find the transport diffusivity of the guest molecules by regression analysis. Analytical expressions which describe the diffusion of guest molecules inside different shapes such as slabs, spheres, and cylinders have been published by Crank and can be applied to appropriately shaped crystals as required [5].

In order to generate binary adsorption isotherms from experimental data using IRM, the relationship between guest molecule IR absorbance and molar gas concentration was correlated to generate a calibration curve. For ideal systems, a single literature adsorption isotherm value can be used to generate the required calibration curve in accordance with the Beer-Lambert law, which describes absorbance as a linear function of path length and concentration [3]. For non-ideal systems, IR absorption spectra peak integrals pertaining to the guest molecules at numerous pressures can be correlated to literature isotherms to generate the required calibration curve.

A.3.2.0 METHOD VALIDATION

This method has been validated using a crystal of silicalite with pure CO_2 gas, and gas mixtures composed of CO_2 and N_2. In this investigation, the silicalite crystal was cuboid shaped, and had height, width, and length dimensions of 510 µm, 490 µm, and 1200 µm, respectively. This crystal was fabricated according to a similar method to the one published by Kida et al using quartz as the silica source [6]. The CO_2 and N_2 gases that were used for pure gas and gas mixture experiments had purities of 99.998%, and were purchased from Sigma (Schnelldorf, Germany). Adsorption isotherms and transport diffusivities were found for CO_2 only and not for N_2 due to the limitations of IRM not being able to measure fast diffusing molecules which do not absorb IR light at room temperature such as N_2. These results have been published elsewhere [7].

Order of experiments and crystal regeneration conditions for silicalite and mixtures composed of CO_2/N_2 were as follows:

I. The zeolite crystal was first regenerated by removing all adsorbed species from its structure under a vacuum pressure of less than 10^{-4} mbar at a temperature of 450

°C for 11 hours as described in step 1 of the experimental method section. Heating and cooling temperature rates of 5 °C per minute were used.

II. A gas mixture composed of 15% / 85% CO_2 / N_2 was prepared, and gas uptake and amounts adsorbed at equilibrium were investigated for CO_2 at pressure steps of 10 kPa from 0 – 100 kPa, and then pressure steps of 25 kPa from 100 kPa to 250 kPa. Pure N_2 was not investigated due to its poor absorption of IRM light at the experimental conditions.

III. The zeolite crystal was regenerated at room temperature by removing all adsorbed species from its structure under a vacuum of less than 10^{-4} mbar.

IV. Step II and then III were repeated in turn for gas mixtures composed of 30% / 70%, 50% / 50%, 70% / 30%, 85% / 15% CO_2 / N_2,and then 100% CO_2.

Three days were required to characterize the zeolite crystal in this way, and so the crystal was regenerated as described in step I overnight in between experiments.

Figures A.3.2 – A.3.4 show the calibration curve, binary adsorption isotherms, and transport diffusivities for CO_2 inside silicalite at various compositions and pressures with N_2 in silicalite.

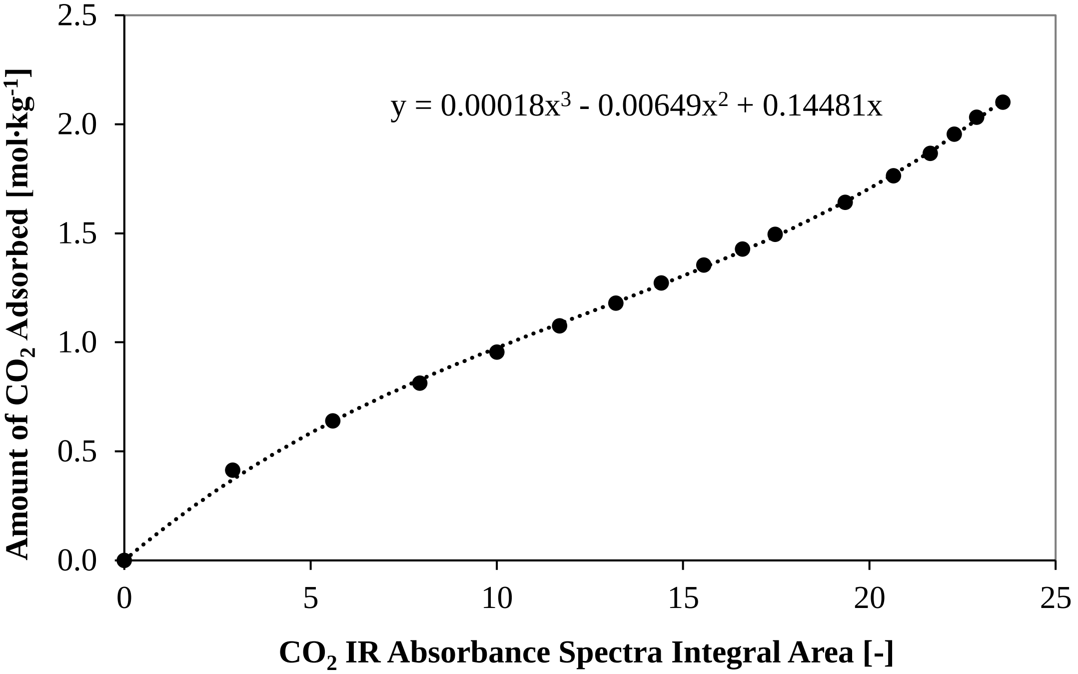

Figure A.3.2. Calibration curve describing the relationship between experimentally determined IR absorbance spectra which were integrated between wavelengths of 3550 and 3740 cm^{-1} for CO_2, and the amount of CO_2 adsorbed on silicalite. IR absorbance spectra were determined from experiments that were conducted at pressures between 0 kPa and 250 kPa using pure CO_2. The amounts of CO_2 adsorbed on silicalite have been taken from the isotherm data obtained by Li and Tezel [8]. Temperature effects have been accounted for by utilizing the temperature dependent Sips model for isotherm data at a temperature of 32 °C.

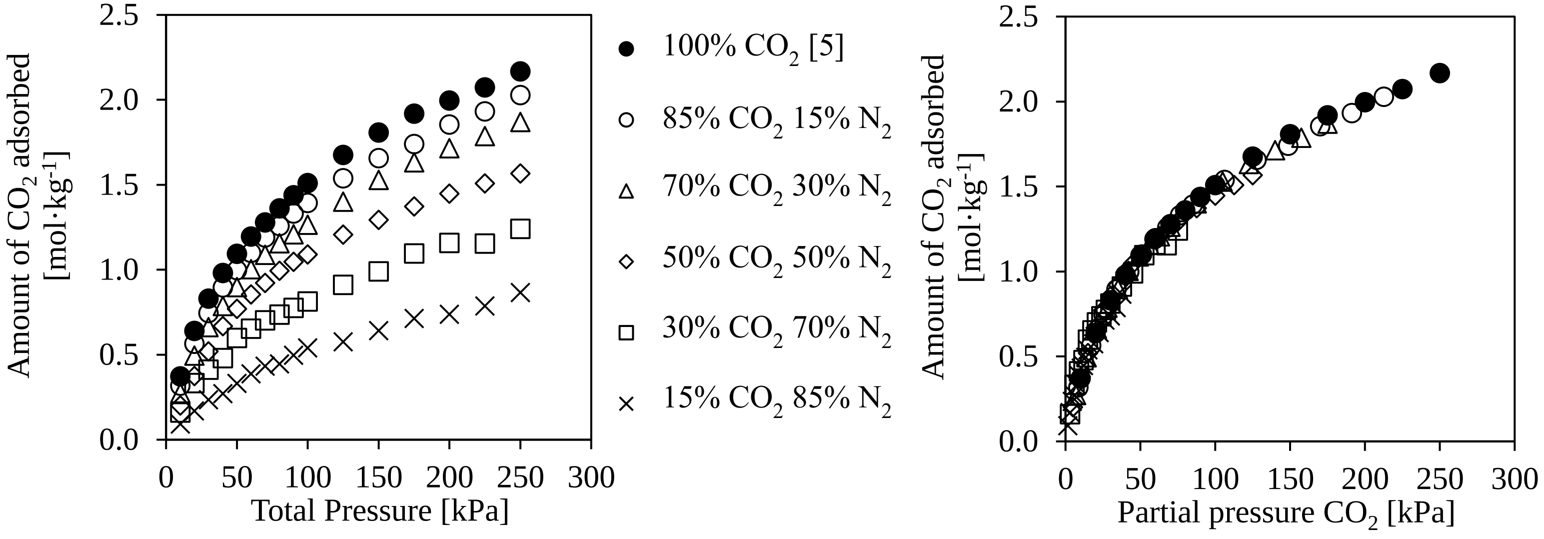

Figure A.3.3. Amount of CO_2 adsorbed at equilibrium on a single crystal of silicalite when present as a pure gas, and in binary CO_2 and N_2 mixtures, as a function of total pressure (a), and partial pressure (b). All of these experiments were conducted at 32 ± 2 °C.

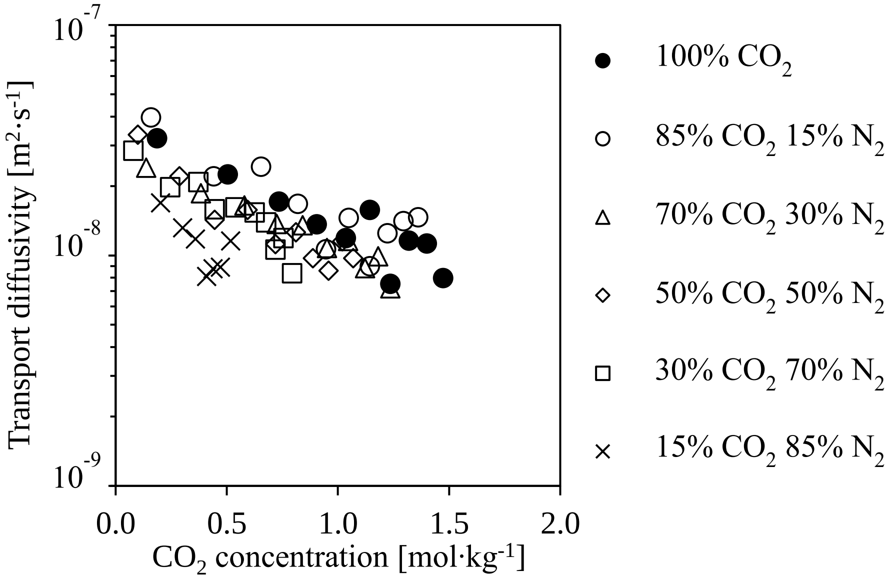

Figure A.3.4. CO_2 transport diffusivities expressed as a function of CO_2 concentration. Concentration in this figure refers to the average amount of CO_2 adsorbed between the initial and final pressures of the uptake experiment. Experiments were conducted at a temperature of 32 ± 2 °C and pressures between 0 and 100 kPa using a range of mixture compositions. The crystal was assumed to be cuboid shaped and infinitely long in order to determine transport diffusivity by regression analysis. The height, width, and length dimensions of the crystal were 510 µm, 490 µm, and 1200 µm respectively.

A.3.3.0 ACKNOWLEDGEMENTS

This research project was financially supported by German Science Foundation, the Natural Sciences and Engineering Research Council of Canada (NSERC), and the University of Ottawa Student Mobility program.

A.3.4.0 NOMENCLATURE

A	Absorbance spectra
APR 266	Pressure transducer model
CMR 361, 363	Pressure transducer models
CO_2	Carbon Dioxide
FTIR	Fourier Transform Infra-Red Spectroscopy

I	Transmittance spectra
I_0	Reference spectra
IR	Infra-Red
IRM	Infra-Red Microimaging
N_2	Nitrogen
PKR 251	Pressure transducer model
R	Reference spectra
T	Transmittance spectra

A.3.5.0 REFERENCES

[1] C. Chmelik, A. Varma, L. Heinke, D.B. Shah, J. Kärger, F. Kremer, U. Wilczok, W. Schmidt, Effect of surface modification on uptake rates of isobutane in MFI crystals: An infrared microscopy study, Chem. Mater. 19 (2007) 6012–6019. doi:10.1021/cm071632o.

[2] C. Chmelik, L. Heinke, P. Kortunov, J. Li, D. Olson, D. Tzoulaki, J. Weitkamp, J. Kärger, Ensemble measurement of diffusion: Novel beauty and evidence, ChemPhysChem. 10 (2009) 2623–2627. doi:10.1002/cphc.200900489.

[3] D.F. Swinehart, The Beer-Lambert Law, J. Chem. Educ. 39 (1962) 333. doi:10.1021/ed039p333.

[4] J. Kärger, D.M. Ruthven, D.N. Theodorou, Diffusion in Nanoporous Materials, John Wiley and Sons, 2012.

[5] J. Crank, The Mathematics of Diffusion, Oxford University Press, 1975.

[6] T. Kida, K. Kojima, H. Ohnishi, Synthesis of large silicalite-1 single crystals from two different silica sources, 30 (2004) 727–732. doi:10.1016/j.ceramint.2003.08.011.

[7] D. Carter, F.H. Tezel, B. Kruczek, J. Kärger, D. Ruthven, R. Marthala, C. Chmelik, Isotherms and Transport Diffusivities of CO_2 in CO_2/N_2 Mixtures with Silicalite Determined Using Infra-Red Microimaging. Submitted to,

MICROPOROUS MESOPOROUS Mater. (2018).

[8] P. Li, F.H. Tezel, Pure and binary adsorption of carbon dioxide and nitrogen on silicalite, J. Chem. Eng. Data. 53 (2008) 2479–2487. doi:10.1021/je7005902.

Appendix 4 – Investigation and Comparison of Mixed Matrix Membranes Composed of Polyimide Matrimid with ZIF-8, Silicalite, and SAPO-34

Appendix 4

The following manuscript has been published in the Journal of Membrane Science as shown below:

Investigation and Comparison of Mixed Matrix Membranes Composed of Polyimide Matrimid with ZIF – 8, Silicalite, and SAPO – 34

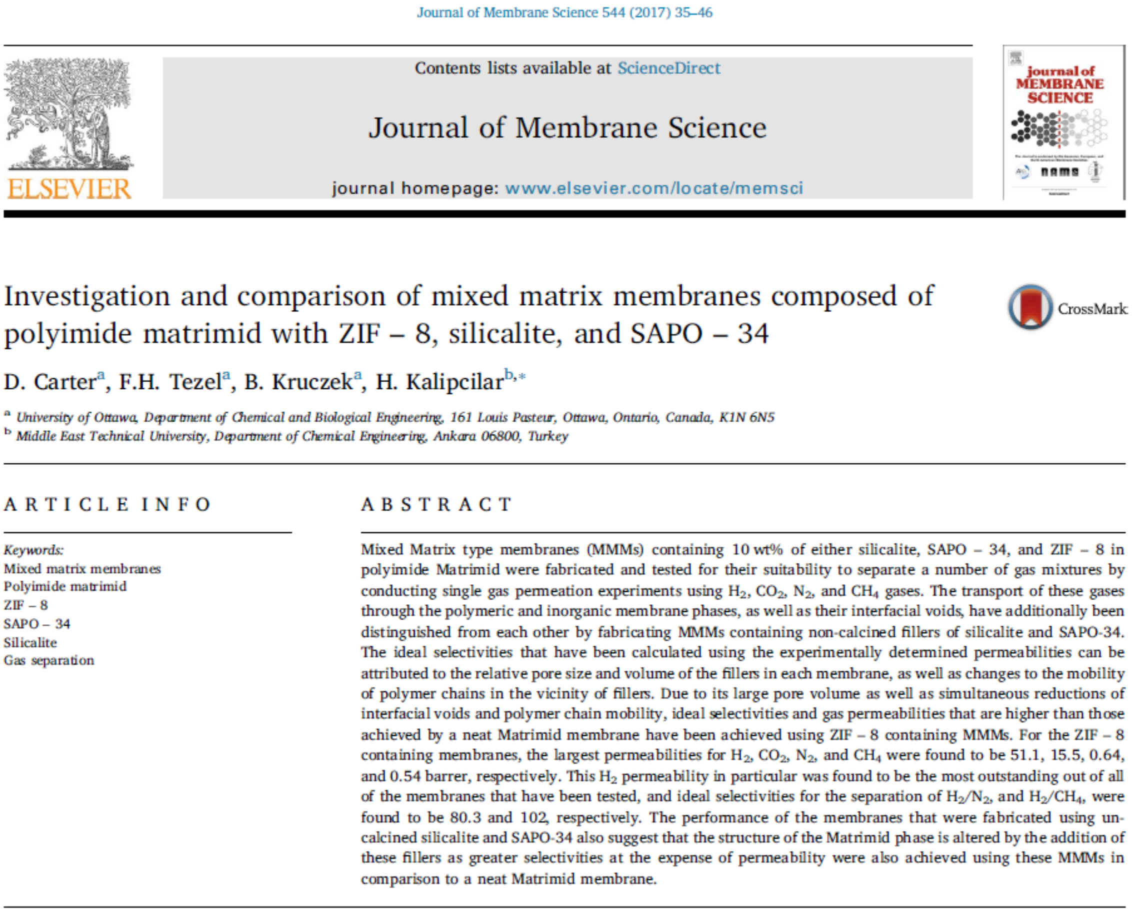

Journal of Membrane Science 544 (2017) 35–46

Contents lists available at ScienceDirect

Journal of Membrane Science

journal homepage: www.elsevier.com/locate/memsci

Investigation and comparison of mixed matrix membranes composed of polyimide matrimid with ZIF – 8, silicalite, and SAPO – 34

D. Carter[a], F.H. Tezel[a], B. Kruczek[a], H. Kalipcilar[b,*]

[a] *University of Ottawa, Department of Chemical and Biological Engineering, 161 Louis Pasteur, Ottawa, Ontario, Canada, K1N 6N5*
[b] *Middle East Technical University, Department of Chemical Engineering, Ankara 06800, Turkey*

ARTICLE INFO

Keywords:
Mixed matrix membranes
Polyimide matrimid
ZIF – 8
SAPO – 34
Silicalite
Gas separation

ABSTRACT

Mixed Matrix type membranes (MMMs) containing 10 wt% of either silicalite, SAPO – 34, and ZIF – 8 in polyimide Matrimid were fabricated and tested for their suitability to separate a number of gas mixtures by conducting single gas permeation experiments using H_2, CO_2, N_2, and CH_4 gases. The transport of these gases through the polymeric and inorganic membrane phases, as well as their interfacial voids, have additionally been distinguished from each other by fabricating MMMs containing non-calcined fillers of silicalite and SAPO-34. The ideal selectivities that have been calculated using the experimentally determined permeabilities can be attributed to the relative pore size and volume of the fillers in each membrane, as well as changes to the mobility of polymer chains in the vicinity of fillers. Due to its large pore volume as well as simultaneous reductions of interfacial voids and polymer chain mobility, ideal selectivities and gas permeabilities that are higher than those achieved by a neat Matrimid membrane have been achieved using ZIF – 8 containing MMMs. For the ZIF – 8 containing membranes, the largest permeabilities for H_2, CO_2, N_2, and CH_4 were found to be 51.1, 15.5, 0.64, and 0.54 barrer, respectively. This H_2 permeability in particular was found to be the most outstanding out of all of the membranes that have been tested, and ideal selectivities for the separation of H_2/N_2, and H_2/CH_4, were found to be 80.3 and 102, respectively. The performance of the membranes that were fabricated using un-calcined silicalite and SAPO-34 also suggest that the structure of the Matrimid phase is altered by the addition of these fillers as greater selectivities at the expense of permeability were also achieved using these MMMs in comparison to a neat Matrimid membrane.

Appendix 5

The following manuscript has been published in the Journal Desalination as shown below:

Characterization of Commercial RO Membranes for the Concentration of Ammonia Converted to Ammonium Sulfate from Anaerobic Digesters

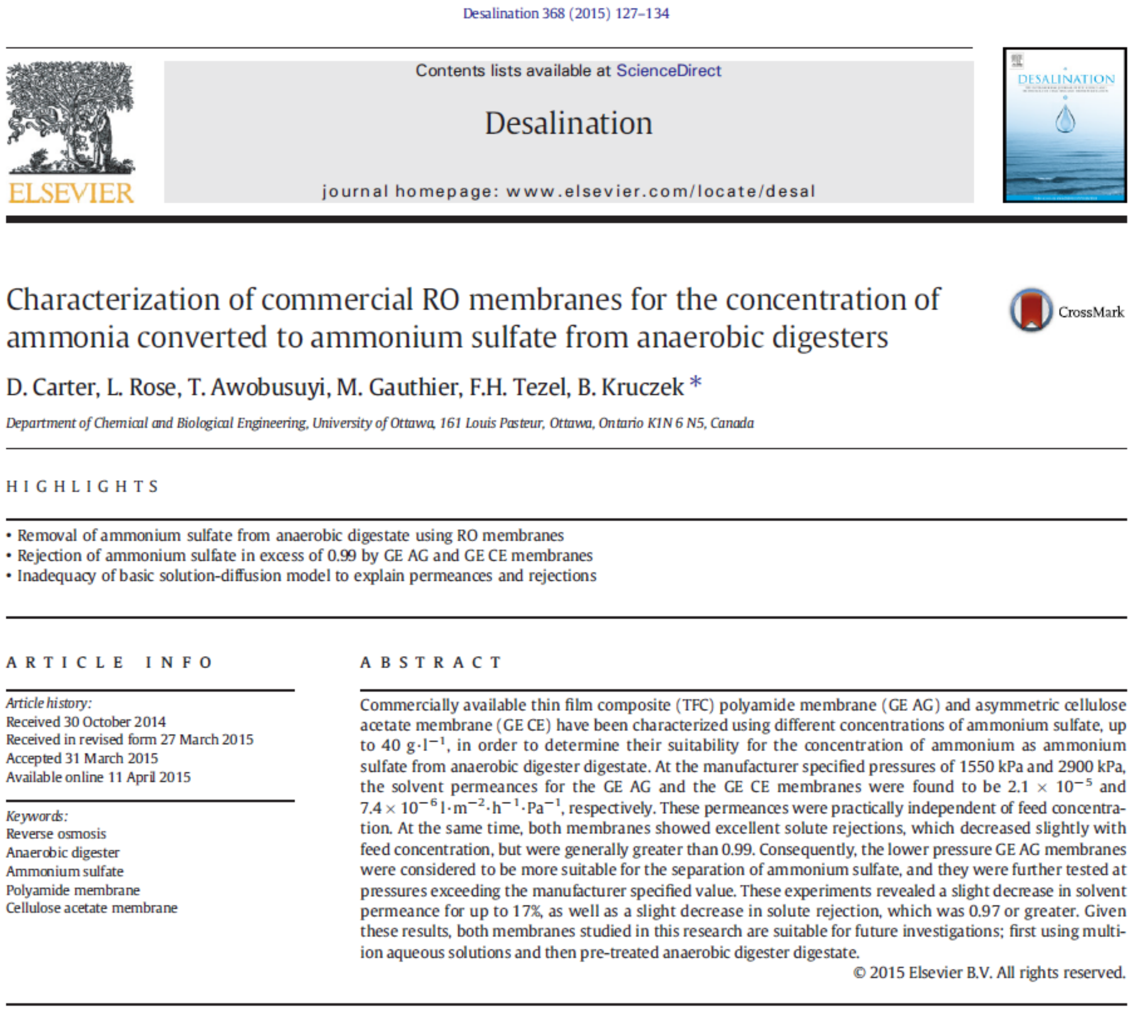

Desalination 368 (2015) 127–134

Contents lists available at ScienceDirect

Desalination

journal homepage: www.elsevier.com/locate/desal

Characterization of commercial RO membranes for the concentration of ammonia converted to ammonium sulfate from anaerobic digesters

D. Carter, L. Rose, T. Awobusuyi, M. Gauthier, F.H. Tezel, B. Kruczek *

Department of Chemical and Biological Engineering, University of Ottawa, 161 Louis Pasteur, Ottawa, Ontario K1N 6 N5, Canada

HIGHLIGHTS

- Removal of ammonium sulfate from anaerobic digestate using RO membranes
- Rejection of ammonium sulfate in excess of 0.99 by GE AG and GE CE membranes
- Inadequacy of basic solution-diffusion model to explain permeances and rejections

ARTICLE INFO

Article history:
Received 30 October 2014
Received in revised form 27 March 2015
Accepted 31 March 2015
Available online 11 April 2015

Keywords:
Reverse osmosis
Anaerobic digester
Ammonium sulfate
Polyamide membrane
Cellulose acetate membrane

ABSTRACT

Commercially available thin film composite (TFC) polyamide membrane (GE AG) and asymmetric cellulose acetate membrane (GE CE) have been characterized using different concentrations of ammonium sulfate, up to 40 $g \cdot l^{-1}$, in order to determine their suitability for the concentration of ammonium as ammonium sulfate from anaerobic digester digestate. At the manufacturer specified pressures of 1550 kPa and 2900 kPa, the solvent permeances for the GE AG and the GE CE membranes were found to be 2.1×10^{-5} and $7.4 \times 10^{-6}\ l \cdot m^{-2} \cdot h^{-1} \cdot Pa^{-1}$, respectively. These permeances were practically independent of feed concentration. At the same time, both membranes showed excellent solute rejections, which decreased slightly with feed concentration, but were generally greater than 0.99. Consequently, the lower pressure GE AG membranes were considered to be more suitable for the separation of ammonium sulfate, and they were further tested at pressures exceeding the manufacturer specified value. These experiments revealed a slight decrease in solvent permeance for up to 17%, as well as a slight decrease in solute rejection, which was 0.97 or greater. Given these results, both membranes studied in this research are suitable for future investigations; first using multi-ion aqueous solutions and then pre-treated anaerobic digester digestate.